Corrosion Protection of Friction Stir Welded Al 7075 Panel for use in Aerospace Applications using Cold Gas Dynamic Spray

By

Patrick Trahan

Thesis Submitted to the Department of Mechanical Engineering in Conformity with the Requirements for the Masters of Applied Sciences, Mechanical Engineering

University of Ottawa
Ottawa, ON, Canada
May 30, 2013

Abstract

The aerospace industry is constantly looking for methods to reduce the cost of flying their airplanes. These savings can come in many forms, one of them being cost savings attributed to fuel savings by either reducing the weight of the airplane or reducing the drag. Friction stir welding (FSW) was introduced as a means of joining previously unweldable Al 7075, a high-strength aluminum alloy commonly used in aerospace for its high specific strength. This eliminated the need for costly and time consuming rivets to be installed, firstly reducing the production cost of the airplane and secondly reducing the overall weight of the airplane therefore improving fuel consumption.

There are many factors at play in the process of producing FSW Al 7075, but the result of this process creates a weld joint that is more susceptible to corrosion than the rest of the panel. For this reason, FSW Al 7075 panel fail prematurely and must be replaced too often. The main goal of this project is, using cold gas dynamic spray, to create a metallic layer on top of an Al 7075 FSW joint to protect it against corrosion.

A series of 3 corrosion tests indicated that pure Al, among coatings of pure Al, Al 5038 and Al 7075, offered the best protection against corrosion. Al 5083 would also be a suitable material and should be used in applications where high bond strengths are required. Al 7075, although of the same alloy as the parent material, is not recommended for corrosion protection as it offered little advantage over the parent material.

In order to better understand the interaction of creating a coating after a hot welding process, several analyses were performed. These included deposition at multiple substrate temperatures as well as hardness and velocity measurements. Results indicate that some aluminum alloys are very sensitive to temperature, yielding better coatings at high substrate temperatures. Individual particle deposition tests reveal that these improvements do not occur at the substrate-coating interface.

Another portion of this project was dedicated to creating tensile specimens composed entirely of pure Al cold sprayed coatings. Several sets of samples were produced. Results indicate that pulling in the direction of nozzle travel direction yields UTS values 50% higher than pulling in the direction perpendicular to the direction of nozzle travel during coating deposition. Results after annealing seem to converge towards the same value. Finally, a new nozzle design was performed which should create a more efficient spraying process, resulting in cost savings for the industry.

Acknowledgments

There are a number of people that have contributed to the success of my thesis, both academically and personally. I would like to thank them for their continued support and guidance. First off, to my thesis supervisor, Bertrand Jodoin. Thank you Bert for you rigor and insightfulness throughout my project. You are a great researcher, teacher and mentor, and I will value what I what learned from you and from this learning experience as I take on new projects in my personal and professional life alike.

I would like to thank The Boeing Company for their continued support during this project. Their expertise and knowledge on all the aspects of this project was invaluable. Having access to some of their equipment incredibly accelerated the rate at which I was able to perform my experiments. Many thanks to Centerline for their continued support troubleshooting problems we sometimes had after pushing their system to the limits.

I would also like to thank the technicians from the Department of Mechanical Engineering machine shop at the University of Ottawa. Thank you James for doing the CNC work I couldn't do even after you taught me how to operate it, to Stan for his tools, his supervision and his help, and to John for providing a solution when no one else could! Thanks to Leo, Mike and Paul too! I appreciate all the work you all have done for me.

Many thanks to my numerous fellow students without whom this experience would never have been as much fun: Guillaume Archambault, Antoine Bacciochini, Mathieu Bolduc, Daniel Cormier, Guo DeLiang, Ruben Fernandez, Daniel MacDonald, Jean-Louis Pelletier, Samuel Leblanc-Robert and Tyler Samson. Not to mention the multiple coop students that came and left the lab during their semestrial stay, whose hard work was always appreciated, especially when I didn't feel like cleaning the powder feeder or CMP-ing coupons!

Last but not least, to the members of my immediate family. Thank you for the support and the encouragements in all the endeavours I pursued. To my girlfriend Mélissa, thank you so much for being in my life.

TABLE OF CONTENTS

List of Symbols

Nomenclature

A	Nozzle cross sectional area	[m^2]
a	Acceleration	[m/s^2]
c	Speed of sound	[m/s]
C	Sutherland gas constant	[K]
c_o	Speed of sound in vacuum	[m/s]
C_d	Drag coefficient	[Non-dimensional]
D	Diameter	[m]
D_h	Hydraulic diameter	[m]
f	Fanning factor	[Non-dimensional]
F_d	Drag force	[N]
k	Gas Dynamic: Specific heat ratio	[Non-dimensional]
k	Light Refraction: Gladstone-Dale Coefficient	[cm^3/g]
L	Nozzle length	[m]
m	Mass	[kg]
$\dot{m}$	Mass flow rate	[kg/s]
M	Mach number	[Non-dimensional]
n	Refraction index	[Non-dimensional]
P	Pressure	[Pa]
R	Gas constant	[J/kg$^{\cdot}$K]
r	Nozzle radius	[m]
Re	Reynolds number	[Non-dimensional]
T	Temperature	[K]
V	Velocity	[m/s]
x	Distance from powder injection point	[m]
Δx	Discrete interval distance	[m]
ε	Surface roughness	[µm]
λ	Sutherland constant	[µPa*s/K$^{-1/2}$]
ρ	Density	[kg/m^3]
$\rho_{\mathbf{b}}$	Bulk material density	[kg/m^3]

μ	Gas dynamic viscosity	[μPa*s]

Subscripts and Superscripts

$_{air}$	Air properties
*	Nozzle throat conditions
$_{o}$	Flow stagnation properties (Exception: c_o)
$_{p}$	Particle properties
$_{1,2,3\ldots}$	Property at point 1, 2, 3…

List of Acronyms

AA	Aluminum Alloy
AKA	Also Known As
APS	Air Plasma Spray
CFRP	Carbon Reinforced Plastic
CGDS	Cold Gas Dynamic Spraying
D-gun	Detonation-gun
DE	Deposition Efficiency
EDS	Energy Dispersive Spectroscopy
EMF	Electromotive Force
EXCO	EXfoliation COrrosion
FRP	Fibre Reinforced Plastic
FSW	Friction Stir Welding (or Friction Stir Weld)
GFRP	Glass Reinforced Plastic
GMAW	Gas Metal Arc Welding
GP	Guinier-Preston
GTAW	Gas Tungsten Arc Welding
HAZ	Heat Affected Zone
HVOF	High Velocity Oxygen/Fuel
LP	Low Pressure
LPCS	Low Pressure Cold Spray
LPPS	Low Pressure Plasma Spray
MIG	Metal Inert Gas
PGDS	Pulsed Gas Dynamic Spraying
RH	Relative Humidity
RPM	Revolution per Minute
SCFH	Standard Cubic Feet per Hour
SEM	Scanning Electron Microscope
SOD	Stand Off Distance
SST	Supersonic Spray Technology
TIG	Tungsten Inert Gas
TMAZ	Thermo-Mechanically Affected Zone
XRD	X-Ray Diffraction

List of Figures

List of Tables

1 Introduction

1.1 Background

The aerospace industry is on a constant path of improvement and innovation towards reducing the costs of producing airplanes while maintaining their effective service life, increasing time between service and increasing the comfort and amenities for the passengers. To achieve this, the airlines must integrate new cutting edge technologies that, through rigorous testing, have been shown to improve the quality of the assembly at a lower cost.

A perfect example of this is the recent replacement of steel or aluminum with fibre reinforced plastic (FRP) for the fuselage, wing and tail sections of the Boeing 787 Dreamliner aircraft [1]. (70% of the weight of this aircraft and its predecessor, the 777, is either aluminum or FRPs [2].) FRPs such a carbon (CFRP) or glass (GFRP) have a much greater strength-to-weight ratio than traditional aircraft materials such as aluminum alloys or steels. This means that the aircraft is lighter and therefore consumes less fuel. FRPs are less prone to environmental corrosion resulting in a lower aircraft maintenance cost. However, the installation process of these materials can be tedious. This is partially due to the fact that it is difficult to connect sections of aircraft-grade materials together.

The reason why aerospace materials cannot be joined easily is because of their composition. Most of the aluminum present on an aircraft is alloyed, resulting in mechanical properties that closely match that of steel for the same density as pure aluminum. Some of these alloys include but are not limited to aluminum alloy (AA) 7075 and 5083.

The issue of using these alloys as the main building block of aircrafts is the fact that it is very difficult to fuse two of these plates together. In most large-structure manufacturing, welding is used to join large metal pieces together. However, it is very difficult to join two aluminum plates because it forms a very resistant oxide layer almost instantly. To weld aluminum, an inert gas zone must be created around the weld joint to inhibit the formation of this oxide layer. This process applies only to pure aluminum. Welding some of the afore-mentioned alloys is even more difficult because of their alloying elements and heat treatments. In the extreme case of 2xxx and 7xxx series aluminum alloys, it is impossible to join two pieces together with typical welding methods because of hot cracking and stress-corrosion problems [3].

This is why rivets are used on most airplanes. Instead of welding two aluminum panels, they are riveted. However, riveting is a very costly process, and for many reasons. The rivets are aircraft grade, and typically very expensive. The process of riveting is extremely long since millions [4] of rivets must be installed on planes. At a total cost of 5-10$ per rivets, this is not a cost effective process [5].

Friction stir welding (FSW) is a new type of welding technique that solves aluminum alloy welding issues [3]. With FSW, it is possible to weld any type of aluminum alloys, even those like AA 7075 which are impossible to weld by any other means. This is the greatest advantage FSW has over other typical welding techniques. In some cases, it is even possible to weld different materials, such as copper and aluminum, together [6]. (A more in-depth welding review will be carried out in sections 2.4 and 2.5) FSW is a process developed very recently. However, it is already starting to appear in commercial aircrafts. Using friction stir welding instead of riveting can lead to instant savings in rivet material costs. There are also savings in operator time and engineering since FSW is a fairly rapid process with barely any clean-up required. Furthermore, because there are no longer millions of rivets on the fuselage, the drag coefficient of the airplane is reduced, resulting in long-term fuel savings. Finally, FSW can also save inspection cost since rivets need to be inspected regularly for defects or oxide formation around the rivet.

Since its appearance on aircrafts, an issue has arisen as to the corrosion resistance of FSW joints. Although the alloy retains most of its physical properties, it was noticed that FSW joints are less corrosion resistant than their parent material counterpart which in the long run would make this type of welding unusable for fuselage applications. A solution to this problem must be found in order to continue utilizing this welding technique on aircrafts.

1.2 Motivation of Research and General Objectives

Due to this issue at the FSW joint, this welding technique can only be used experimentally or must be maintained more frequently. This project was created in collaboration with The Boeing Company to help solve the issue of corrosion regarding Al 7075 FSW joints. The findings in this project will allow Boeing to install FSW panels and therefore reduce maintenance, materials and fuel costs without the need for frequent maintenance. Because of this alliance, there are certain limitations to the research that can be performed. These limitations will be discussed in section 3 and 4.

There are many ways to resolve this problem. The proposed solution is to create a metallic coating on top of an Al 7075 FSW joint to cover the poor corrosion resistant zone. The coating will be created using a low pressure cold gas dynamic spray system, or LP-CGDS system. A cold spray system will be used because these systems, unlike their thermal spray counterparts, do not affect the microstructure of the powder that is deposited on the surface (or of the material to be coated) and allow for a clean and efficient coating of small regions. (A full comparison will be carried out in section 2.2.) This project will aim to accomplish the following list of objectives:

- Identify the causes of the loss in corrosion resistance to ensure that producing a metallic coating is a viable solution;
- Determine the feasibility of spraying metallic particles onto Al 7075 by testing multiple system parameters;
- Modify the system parameters to optimize the coating produced;
- Spray coatings of various aluminum alloys onto Al 7075 and test their corrosion resistance via multiple testing standards and measuring methods;
- Compare the corrosion resistance of the various protective aluminum alloy coatings and compare them with the as-FSW panels' corrosion resistance; and
- Perform additional tests to deepen understanding of the CGDS process applied on a FSW joint.

1.3 Outline of the Thesis

The content of this thesis has been separated into 8 chapters. Chapter 1 will present a general introduction to the project, as to the main goals to be achieved during the research. It will present basic background information that will be discussed at in greater detail in later chapters.

Chapter 2 presents a review of the relevant literature and processes. This includes an in-depth view of CGDS and a brief summary of other thermal spray processes. These processes will then be compared. The same process will take place with FSW and other welding techniques. A review of the relevant AA 7075 information will then be presented, as well as a basic overview of corrosion principles. Finally, relevant solutions to FSW joint corrosion protection will be overviewed.

Chapter 3 will present the detailed research objectives. This represents an exhaustive analysis of the tasks that must be achieved in order to obtain the objectives that were set forth in section 1.2.

Chapter 4 will present the experimental research approach. This represents the means that have been taken to achieve each of the tasks presented in chapter 3. This includes the type of metallic powder used to create the coatings, the presentation of the research equipment, as well as material characterization techniques and current material performances.

Chapter 5 will go in depth in the type of powder used to produce the metallic coatings. This chapter will dive into the powder characterization such as particle geometry and size distribution. It will finish with a summary of the powder characterization.

Chapter 6 is where the experimental work begins and where the objectives set forth for this thesis are achieved. This includes understanding the corrosion behaviour of FSW joints, producing optimal metallic coatings and finally producing coatings and verifying their effectiveness at protecting FSW joint against corrosion. This is the main results chapter for the thesis.

Chapter 7 presents the first of two secondary objectives set that were aimed for in this thesis project. This set of secondary objectives involves testing the mechanical properties of the coating. This includes hardness testing, as well as adhesion and tensile tests.

Chapter 8 presents a rather interesting problem. During the experimental phase it was noticed that some powders are more difficult to spray than others. This can create a significant problem for commercial applications. A special section in this thesis has been reserved to investigate what is happening inside the critical components of the system and what can be done to improve the efficiency of the coating process.

Finally, the conclusion (chapter 9) will summarize the findings reported in this thesis and provide closing remarks on the present research work. Recommendation and suggestions for future work are presented in chapter 10.

2 Review of Relevant Literature and Processes

The following chapter presents a detailed review of the literature pertinent to this research project. Firstly, the CGDS technology and theory will be introduced, followed by a brief overview of other thermal spray processes and concluded by a comparison between the CGDS process and the other thermal spray processes. Secondly, the FSW process will be introduced, followed by other welding techniques. A comparison between FSW and these welding processes will be carried out. Thirdly and fourthly, a review of the relevant information concerning Al 7075 and corrosion principles will be respectively presented. Finally, a review of previous research in this field will be presented.

2.1 Cold Gas Dynamic Spraying (CGDS)

2.1.1 Brief Historical Background

The CGDS process is the most recent thermal spray process. It was accidentally discovered in the mid-1980’s following a supersonic flow tracing experiment ran by Anatolii Papyrin [7][8]. Small copper powder particles were used as tracing material. Papyrin noticed that beyond a certain speed, later dubbed “critical velocity”, the particles would adhere to the model rather than eroding it (see Figure 1). Papyrin then spent a few years pursuing this discovery and developing equipment specifically made for the purpose of depositing metallic particles to create a coating. In 1994 him and several colleagues filed a patent for the first cold spray equipment [9]. Many commercial variations of this machine now exist, and today CGDS is used in many different industrial applications around the world, including damage repair, corrosion protection and conductive layer repairs (used in lightning dissipation systems on airplanes for example) to name a few.

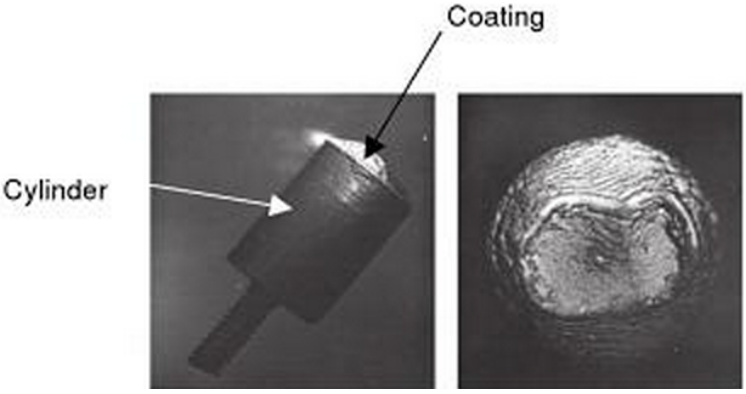

Figure 1. Photographs of the Coating Formed from Aluminum Particles on a Cylinder. M_∞=3.0, T_0=300K, d_{pm}=20 µm [8]

2.1.2 Process Overview

Figure 2 presents a schematic of how the process is completed. The main gas, also called propellant gas, is fed from a series of high-pressure gas bottles to the gas controller where its pressure is regulated. The gas then flows through the main tube, where it goes through the propellant gas heater. The temperature of the gas is controlled with the same afore-mentioned controller using a thermocouple placed at the heater exit.

The gas then flows through a de Laval nozzle which is a converging-diverging assembly consisting of an orifice (converging-diverging sections) and a nozzle (diverging section). (The smallest point in the cross section is called the throat) This assembly will accelerate the flow to supersonic velocities.

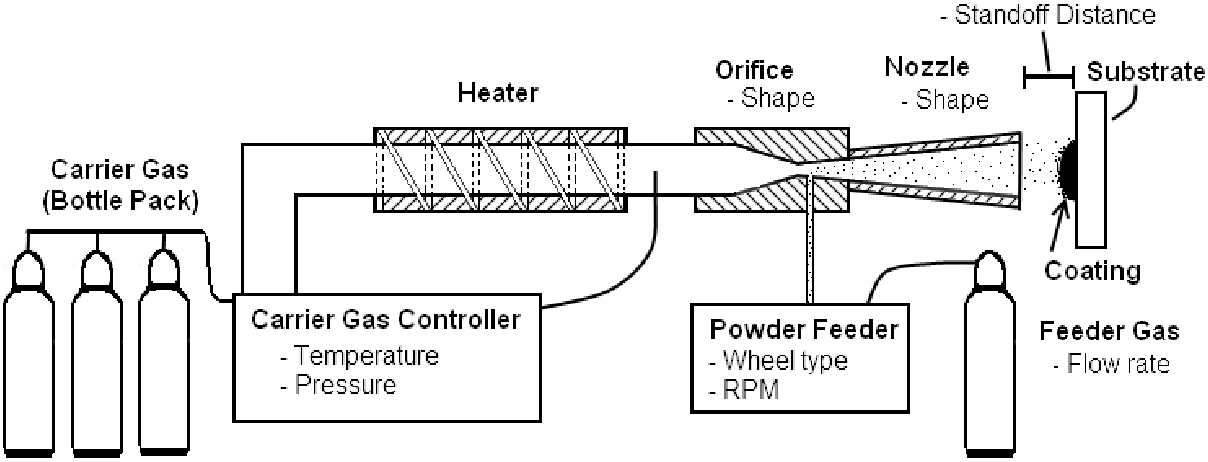

Figure 2: Cold Gas Dynamic Spray Process Outline. Equipment is labelled in Bold Font, and Variables are labelled in Normal Font

The powder is loaded into a powder feeder. A separate gas bottle is connected to the powder feeder to supply a gas flow (carrier gas flow) to transport the powder to the propellant gas flow. The feeder gas flow rate can also be adjusted. If the powder is injected after the throat (as pictured) the system is called “low pressure” since the powder injection point is at lower pressure. If the powder is injected before the throat this system is called “high pressure”.

Using this system and modifying its 6 variables accordingly (nozzle and orifice shape are fixed for the system), the deposition of each powder type can be individually optimized. In this case powder type represents the specific powder element, alloying, morphology and metallurgy. For example, copper powders come in many different shapes and sizes. A complete powder specification would be to specify pure copper powder (element and alloying), air atomized 0-125 µm size (morphology) standard grain (metallurgy).

2.1.3 Concept of Deposition Efficiency and Particle Critical Velocity

A very important parameter in the efficiency of the entire process is the deposition efficiency. Deposition efficiency is defined as the ratio of powder mass deposited on the substrate to the mass of powder injected in the nozzle. At a deposition efficiency of 100% all the powder coming from the powder feeder and injected into the nozzle is deposited onto the substrate. Lower deposition efficiencies indicate that some of the powder did not adhere to the substrate to form a coating. This results in a longer spray time to obtain the same coating thickness, resulting in losses in gas and electricity, as well as increased operator time.

Particle velocity highly affects deposition rate. A higher particle velocity results in a higher the deposition efficiency. (There are many factors influencing particle velocity, including propellant gas pressure and temperature, as well as De Laval nozzle geometry). Once injected in the nozzle, the particles will be accelerated by the gas flow until they hit the substrate. Theoretically, a minimum velocity is required for the particle to bond to the substrate. This minimum value is called critical velocity. The critical velocity changes depending on many factors including material (element and alloy), particle size and particle shape as well as particle impact temperature and substrate temperature. The critical velocity for many materials was measured experimentally to be between

150 and 900 m/s [10][11]. This was done considering the percentage of adhered particles. For pure copper and pure aluminum, critical velocities of 500-570 m/s and 660 m/s respectively have been established [12]. Once passed this minimum value the deposition efficiency will increase with increasing particle velocities. Figure 3 shows that the deposition efficiency will be low until the critical velocity (v_{crit}) where deposition efficiency increases drastically and rises asymptotically until a 100% DE is achieved.

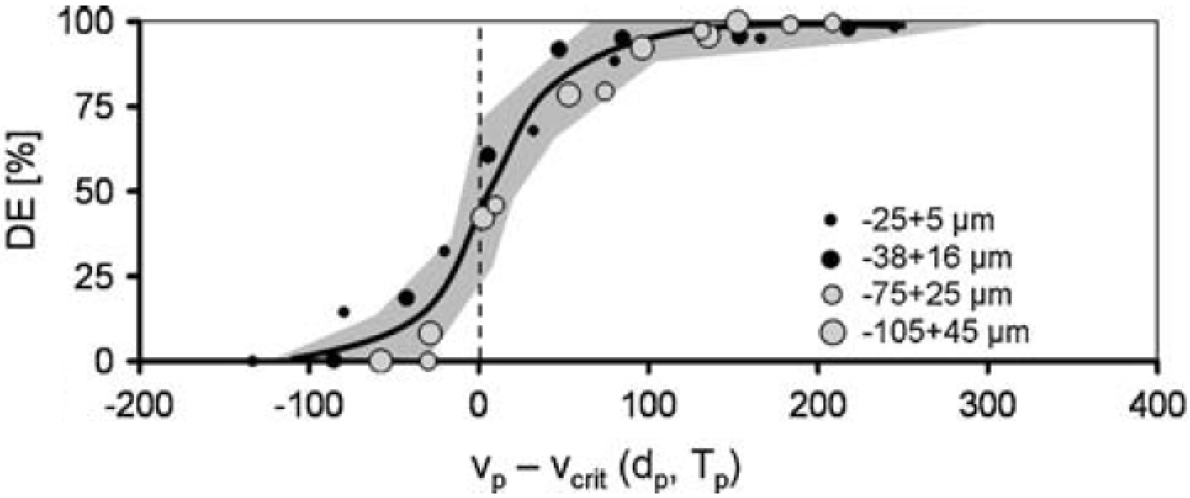

Figure 3. DE as a Function of the Impact Velocity [13]

2.1.4 Gas Dynamic Principles in CGDS

This section presents a brief introduction to gas dynamic principles relevant to CGDS. Mainly, these concepts can be applied to the relation between propellant gas pressure and temperature as it flows through the de Laval nozzle assembly. Please refer to the list of symbols on page ix.

Gas dynamics is the study of high speed compressible flows. In the case of air, compressibility must be taken into account once velocities reach a Mach number of 0.3. The Mach number M is the ratio of flow velocity V to local speed of sound C:

$$M = \frac{V}{C} \tag{1}$$

Where the speed of sound *C* is represented by the equation:

$$C = \sqrt{kRT} \tag{2}$$

where *k* is the specific heat ratio, *R* is the gas constant and *T* is the gas temperature. For air,

$$k_{air} = 1.4$$

$$R_{air} = 287 \frac{J}{kg \cdot K}$$

Therefore the speed of sound in air is a function of temperature:

$$C_{air} = 20.04\sqrt{T} \tag{3}$$

For air at 25^{o}C (298.15 K), the speed of sound is 346.1 m/s. In this case, compressibility would occur at a flow velocity of 103.8 m/s.

Equations can be developed to dictate how a compressible flow will behave. Analyzing an infinitesimal pressure wave, and making assumptions that there is a steady state steady flow process with a perfect gas in an adiabatic and reversible process (i.e. polytropic of the form $PV^{K} = 1$) with no shear forces, equations dictating how this flow will behave can be developed. These equations are the following:

$$\frac{T_o}{T} = 1 + \frac{(k-1)}{2} M^2 \tag{4}$$

$$\frac{P_o}{P} = \left(1 + \frac{(k-1)}{2} M^2\right)^{\frac{k}{k-1}} \tag{5}$$

$$\frac{\dot{m}}{A} = M\sqrt{\frac{k}{RT_o}}P_o\left(1+\frac{k-1}{2}M^2\right)^{-\frac{1}{2}} \tag{6}$$

In these equations, T_o is the stagnation temperature, P_o is the stagnation pressure, $\dot{m}$ is the mass flow rate in the nozzle and A is the cross-sectional area. Stagnation properties refer to the properties of the gas when the velocity is 0 m/s.

Stating that the location where the flow velocity is Mach 1 has an area of $A*$, equation (6) becomes:

$$\frac{A}{A^*} = \frac{1}{M}\left[\left(\frac{2}{k+1}\right)\left(1+\frac{(k-1)}{2}M\right)\right]^{k+1/2(k-1)} \tag{7}$$

Figure 4 shows equations (4) and (5) plotted as a function of Mach number. Figure 5 shows equation (7) plotted in the same way.

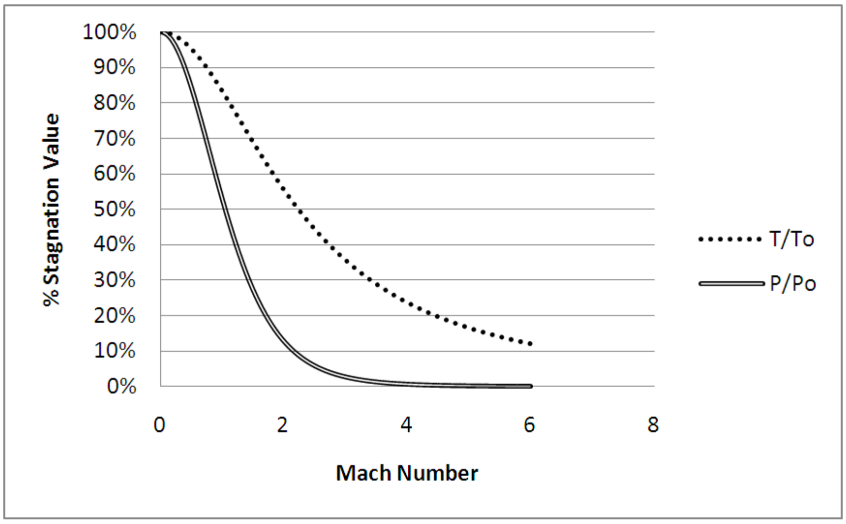

Figure 4. Plot of Temperature and Pressure Ratio with Increasing Mach Number

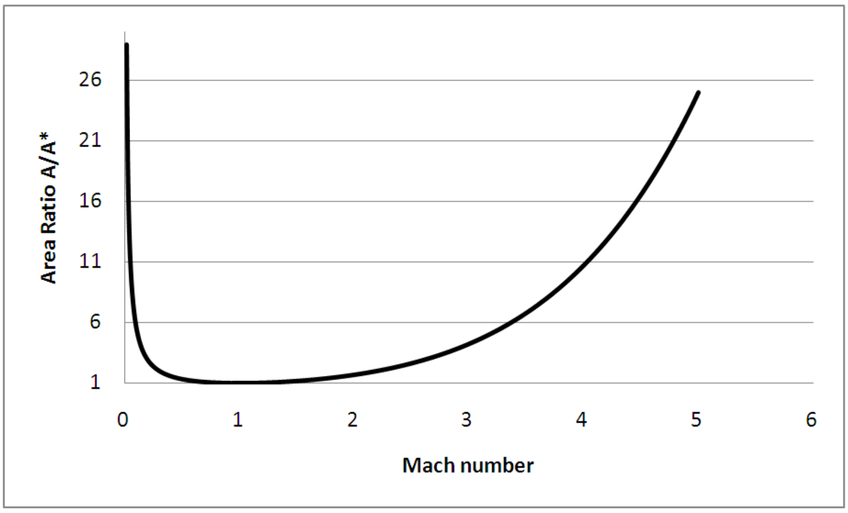

Figure 5. Plot of Area Ratio A/A* for Increasing Mach Number

Figure 4 shows that as the flow velocity increases, the pressure and temperature will drop, but at different rates. Figure 5 shows a few interesting features. First, the smallest cross section will be at Mach 1 and is called the throat. The shape of the nozzle (imagine the shape in the chart mirrored vertically) will resemble an hourglass, with the first half accelerating the flow to Mach 1, and the second half accelerating the flow past this value. Therefore, counter intuitively, to accelerate the flow past Mach 1 the cross section must increase. Another conclusion that can be made this figure is that for every area ratio, there is a subsonic and supersonic solution.

There are many ways to design a nozzle. One approach is to select a desired exit Mach number i.e. the desired velocity of the gas as it exits the nozzle. From this number, the required area ratio (equation (7)) and the stagnation pressure required assuming an exit pressure (back pressure) of 101.325 kPa (using equation (5)) can be determined. This design back pressure is the ideal pressure at which the air surrounding the nozzle exit should be at. The gas flow exits the nozzle at the design back pressure. Increasing the temperature will increase the energy of the flow (and the flow velocity). Changing the throat diameter will change the mass flow through the nozzle.

Although the theoretical design is now “complete”, it is of interest to us to analyze the effect of varying the stagnation pressure (i.e. pressure before flow is accelerated) and the back pressure to analyze their effect on the gas velocity. It is important to grasp the results of this sensitivity analysis in order to remain in the proper operating conditions, which are high gas velocities. The change in pressure is represented in Figure 6.

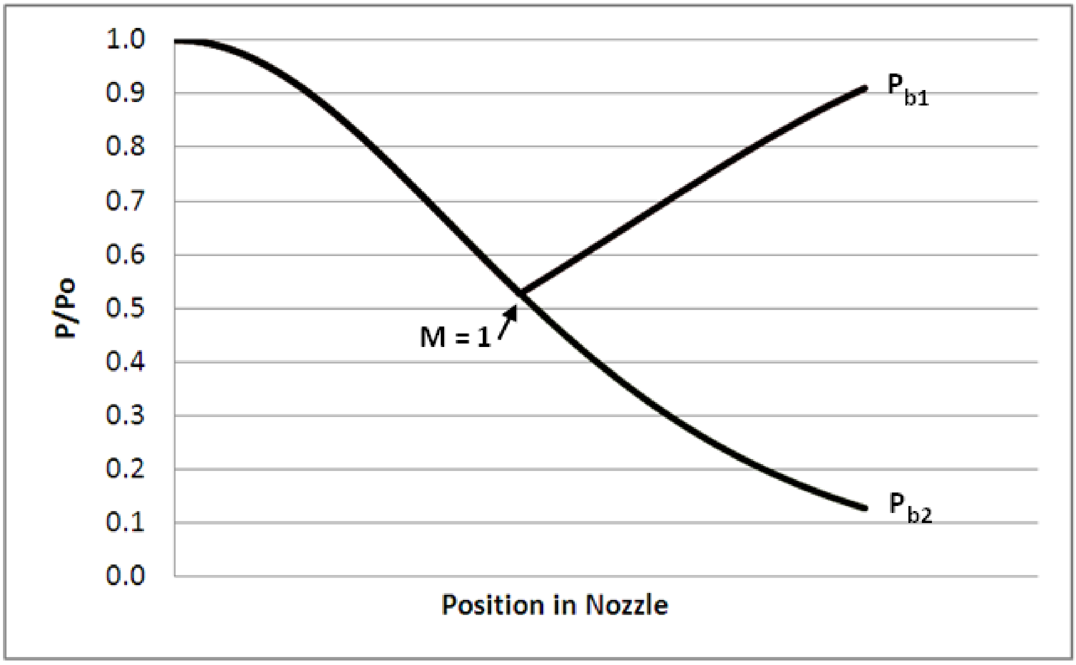

Figure 6. Change in Pressure with Position in Nozzle. Both Sonic and Subsonic Possibilities are Shown

If the back pressure is much too high (P_{b1} case) when compared to the stagnation pressure then the flow will remain subsonic. To find at which back pressure this will occur, the design Mach number's area ratio must be found, followed by the subsonic Mach number that has the same area ratio. This can be done using equation (7). Finally use equation (5) to find the back pressure knowing the stagnation pressure.

If the back pressure is as designed (P_{b2} case) then the flow will exit at supersonic velocities and the exit pressure will exactly match the back pressure. If the back pressure suddenly increases, the flow pressure will be lower than the back pressure. The gas is then in an overexpanded state. To rectify the situation shockwaves will form inside the nozzle to rectify the difference in pressure. Severe turbulence will occur because of this. Consult Figure 7 for a visual representation of this turbulence.

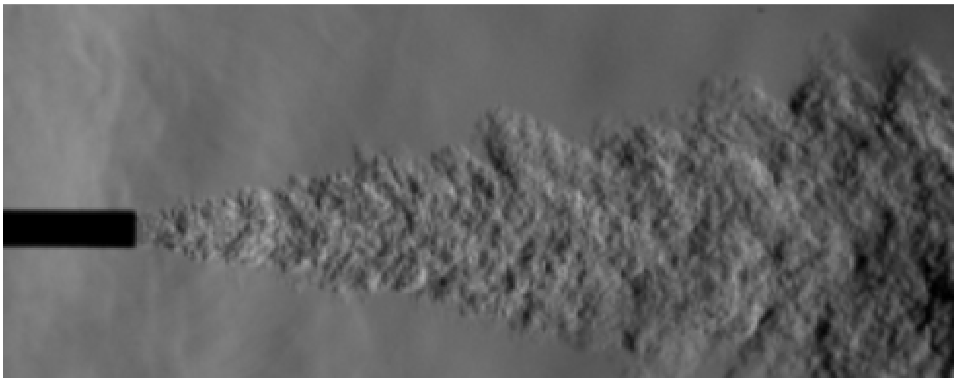

Figure 7. Over Expanded Flow showing Exit Turbulence.

If the back pressure suddenly drops, then the flow is in an under expanded state. Diamond expansion fans will be created outside the nozzle to correct for the pressure difference. It is always preferable to keep the flow in an underexpanded state since there are no shockwaves in this configuration. Expansion fans will keep the flow in a supersonic regime, allowing for faster gas velocities. An example of an underexpanded state is shown in Figure 8.

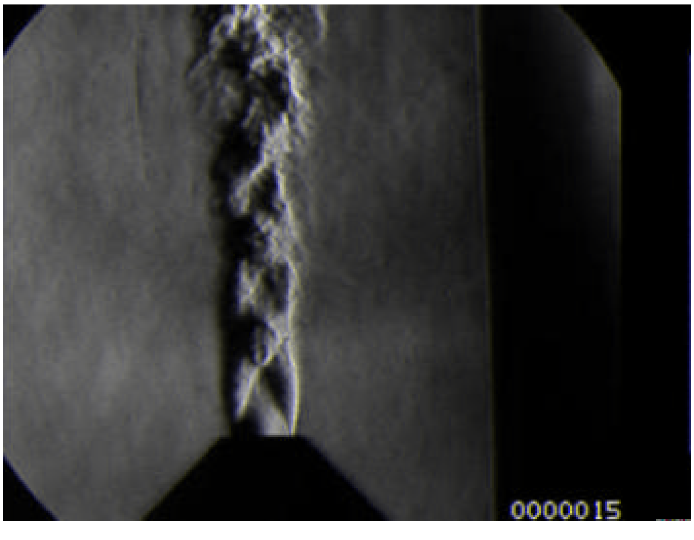

Figure 8. Underexpanded Flow Showing Diamond Shockwaves. Source: http://i.ytimg.com/vi/f_BAqv0Y6zg/0.jpg

This theory can be applied to a constant back pressure situation where the stagnation pressure varies. Increasing the stagnation pressure above the design point will create an underexpanded flow (preferable). Decreasing the pressure below the design point will create an overexpanded flow. Figure 9 shows this explanation.

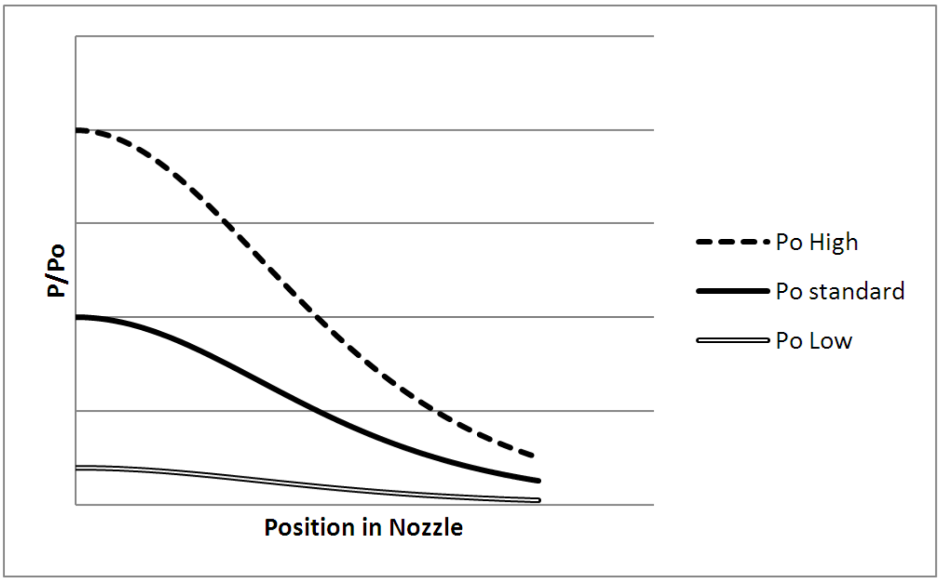

Figure 9. Effect of Increasing Stagnation Pressure on Exit Pressure, Showing an Underexpanded Flow for High Stagnation Pressure (P_o High), and an Overexpanded Flow for Low Stagnation Pressure (P_o Low)

Therefore, to the keep the flow in an underexpanded state, the stagnation pressure must be higher than the design stagnation pressure.

2.1.5 Bonding Mechanisms

This section describes how the incoming particles adhere to the substrate. While this is still a subject of debate, there are a two bonding mechanisms currently described for CGDS. The first is pure mechanical bonding. It occurs by plastic deformation of both the substrate and particle, leading to material interlocking producing mechanical strength [11].

A process that occurs readily in CGDS is called “adiabatic shear instability” commonly evaluated in processes such as explosive welding. The process occurs in rapid plastic deformation processes such as high velocity metallic particle impact. Due to the speed of the process, the heat generated in the deformation is concentrated at the particle/substrate interface. (This means there is no heat transfer to the rest of the particle) This allows local interface softening, allowing a sheer band to form and jet material outward in a process aptly called jetting. Theories indicate that this rapid shearing breaks the protective surface oxide layer allowing for a metal to metal contact, which provides good adhesion [11]. An example of a jetted particle is shown in Figure 10.

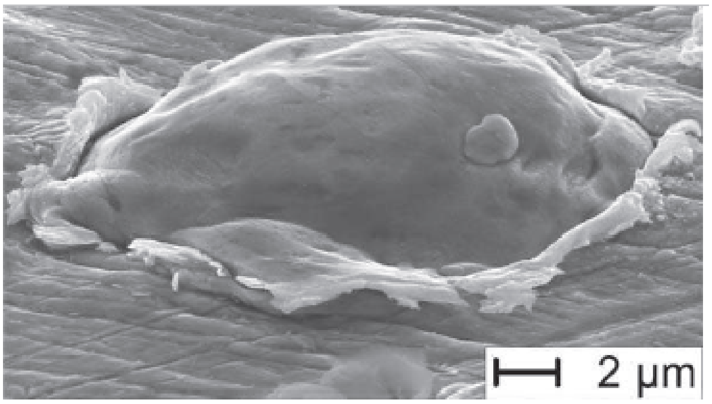

Figure 10. Scanning Electron Micrographs (Secondary Electron Mode) of Wipe Test Samples of Copper Particles on a Copper Substrate, Showing a Close-Up Image [12]

Jetted particles are a sign that there was adiabatic sheer instability at this particular coating / substrate interface. It is a sign that good mechanical bonding is in place. Secondly, it is also a sign of the second bonding mechanism discussed in CGDS: metallurgical bonding. In some case, it is suggested that the heat generated adiabatically could melt the interface, providing metallurgical bonding between the particle and the substrate. Figure 11 presents this case.

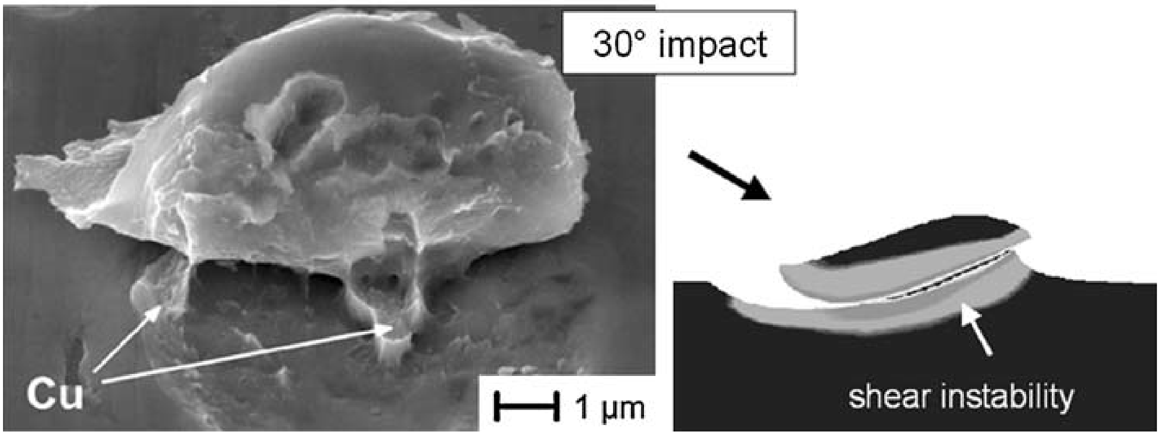

Figure 11. Location of Shear Instability Noting Regions of Metallurgical Bonding [13]

2.1.6 CGDS Advantages and Limitations

There are many advantages to the cold spray system. One of the most important features is that it is possible to conserve the original powder metallurgy e.g. nano-sized grains or special heat-treated alloys. This is very important when specific coating properties are required without having to modify the entire coated part. The coating porosity is also very low. Furthermore, because the particle must impact the substrate at high velocities, the coating area is restricted to the exit area of the nozzle, meaning there is no overspray outside of this zone. Cold spray coatings can therefore be deposited without masking as other thermal spray require. The system can also be made to be portable, making onsite repairs as possibility.

The CGDS process presents many advantages, but also has its limitations. Because mechanical deformation is required for CGDS coating to occur, some coatings cannot be formed with CGDS. For instance, high hardness materials such as ceramics (Al_2O_3, CrC, and WC) cannot be deposited with cold spray. Due to the high plastic deformation involved in the deposition process, the coating will be very hard, but it will also be brittle. For cases where a high toughness is required, CGDS coatings are not recommended.

As mentioned in section 2.1.2, there are two types of cold spray systems: high pressure and low pressure powder injection. The only difference between the two systems is that in the high pressure systems the powder is injected before the throat. This means that the particles stay longer in the nozzle assembly, and can therefore receive more thermal and kinetic energy from the propellant gas flow. This is beneficial for the coating quality; however this also means that the nozzle assembly is more prone to clogging and damage than a low-pressure system. This is due to the fact that the power must converge at the throat, impacting on the walls of the nozzle before being accelerated in the diverging section.

2.2 Other Thermal Spray Processes

The purpose of this section is to expose the reader to the various types of thermal spraying processes currently in use. There are four main categories of thermal spray processes as shown in Figure 12. This section will present the first three categories of thermal spray processes, since kinetic energy spray (cold spray) has been presented in full length in the previous section.

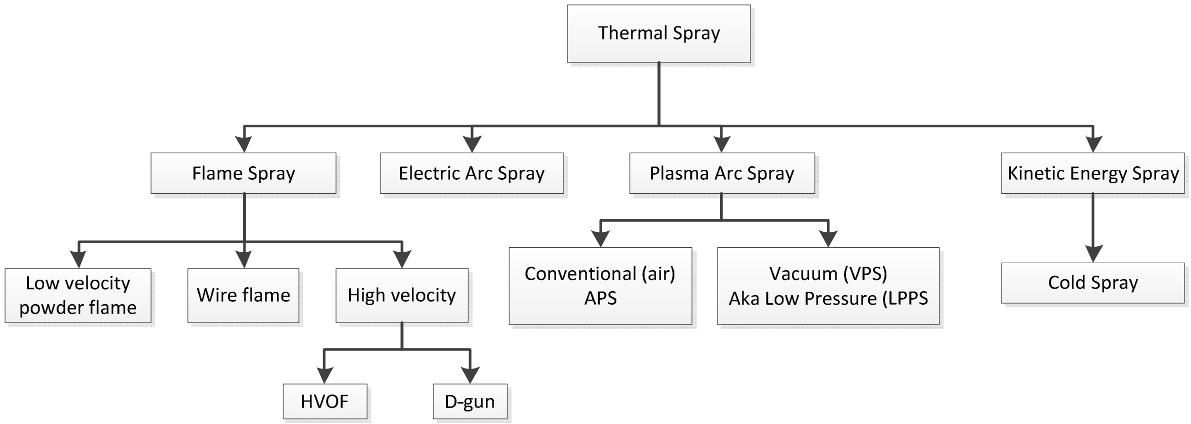

Figure 12. Thermal Spray Processes Flow Chart

Figure 13 presents a good representation of thermal spray process. Thermal spray is divided into four categories: Flame spray, electric arc spray, plasma arc spray and kinetic energy spray. Powder (can also be a wire or rod) is heated using a form or electricity or heat and is projected onto a substrate using either a process gas or atomization jets. In most cases, the heat will melt or partially melt the particles. (Except in CGDS) These molten or semi-molten particles are projected onto, and bond with, the substrate. Because of the high temperatures involved, oxides will form within the coating.

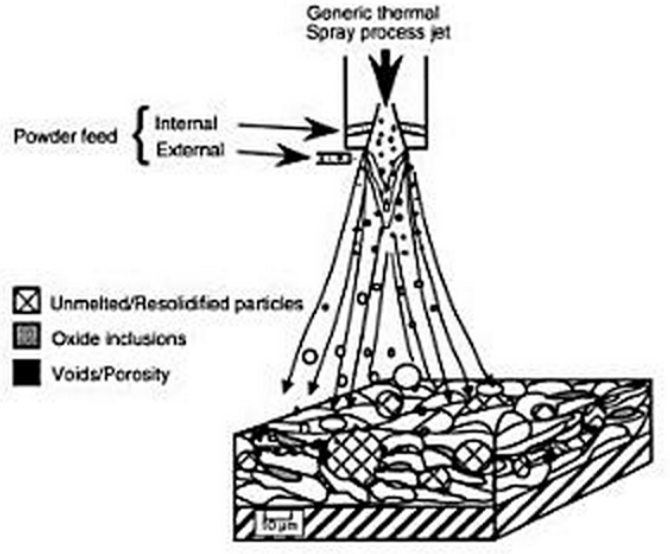

Figure 13. Schematic of a Typical Thermal Spray Powder Process [14]

2.2.1 Flame Spray

In most flame spray processes, less than 10% of the input energy is used to melt and carry the feedstock material [14]. The four flame spray processes presented (low velocity, wire flame, HVOF and D-Gun) work on similar principles. An oxy-fuel flame (oxygen combusting with a fuel such as hydrogen or propane) melts powder, wire or rod feedstock material. This molten material is then projected (using air in the case of wire flame or the combustion mixture in the case of powder flame) onto a substrate at low (low velocity spray) to high (HVOF) velocities. The substrate becomes very hot during the spray process. In low velocity, wire flame and HVOF, the process is continuous. In D-Gun, the process occurs in bursts where discrete quantities of powder are injected into a barrel. A small controlled explosion produces high velocities and temperature, propelling the powder out of the barrel onto the substrate.

2.2.2 Electric Arc Spray or Wire Arc

The wire arc spray is an efficient process – 100% of the energy input is used to melt the feedstock material [14]. A large current is fed through two consumable wires (feedstock material) whose tips are almost touching. The arc produced melts the tips. The molten material is propelled onto the substrate using a propellant gas, typically air.

2.2.3 Plasma Arc Spray

Plasma spray has the highest temperature of any process, reaching 15000^{o}C in some cases. A high power is required to accelerate and super-heat inert gas to a plasma state. The powder is injected into this stream and carried to the substrate as it is melted.

2.2.4 Summary of Thermal Spray Processes

Table 1 shows a comparison of the various thermal spray processes, including cold spray.

Table 1. Characteristic of Various Thermal Spray Processes [14] [15]

Spray type	Feed Type	Flame Temp (°C)	Particle Velocity (m/s)	Microstructural features	Machine Power (kW)	Applications
Powder-flame	Wire/ Powder	2200-3000	30-100	Relatively high porosity Oxidation	25-75	Reclamation; Corrosion protection
Wire flame	Wire	2800-6000	50-180	Medium density Thick	50-100	Reclamation; Wear coatings
HVOF	Powder	3000-3100	400-1000	High density Excellent adhesion Compressive stresses	160-270	Wear protection
Arc Spray	Wire	5500	240		4-6	
D-Gun	Powder	3900	910	Dense	160-270	
Plasma	Wire/ Powder	5000-25000	80-300	Porosity in ceramic deposits	30-80	Thermal barriers, insulators
Cold Spray	Powder	Room	400-1000	Dense Compressive stresses	5-70	Conductors; Reclamation; Cladding

2.3 Comparison between Thermal Spray Processes and CGDS

As Table 1 shows, the main differences between the other thermal spray processes and cold spray is the operating temperature of the sprays and the particle speed (exception: HVOF). Because cold spray does not melt the feedstock material, it is possible to maintain the initial powder metallurgy. To create very specific coatings (e.g. nano-sized grains or oxide-free Ti coatings) the only requirement is to have these features present in the feedstock powder. (The final coating will be harder due to mechanical deformation) There is no need to heat treat or make other modifications to the coating or the substrate after the deposition process.

2.4 Friction Stir Welding (FSW)

Friction stir welding is a new type of welding process invented at The Welding Instituted in 1991 [16] [17]. This process allows welding materials that were either difficult or impossible to join with a fusion welding technique. For instance, the 7075 aluminum alloy (AA), previously unweldable due to hot cracking and stress-corrosion [3], can now be joined with FSW. Furthermore, it is possible to join together two different types of metals. For example, studies have been performed on the successful joining of several combinations of aluminum alloys, Al-Steel, Al-Mg, Al-Cu and Steel-Ni plates [6].

The versatility of FSW brings forth new and unthinkable applications. For example, 7075 AA is used in aerospace for its high strength-to-weight ratio. Previously, fasteners such as rivets were used to join two plates together. Now, a simple welding procedure eliminates thousands of rivets, saving time and money (weight saving and aerodynamic efficiency saving for example). FSW is also used in many more applications including automotive, shipbuilding, nuclear and railway [18] even though the metallurgy of the welded joint is still not well understood [19].

2.4.1 Process Overview

A special tool consisting of a nib (or pin) protruding from a square shoulder is spun at several hundred RPMs [19]. The nib is forced at the weld joint until the friction creates enough heat to plasticize the metal plates. At this point the nib is inserted into the joint, until the shoulder rests on the top of the joint line (see Figure 14). The tool is then slowly advanced forward, continuously plasticizing the leading edge. The rotating action of the tool mixes the plasticized metals together in a swirling motion as the tool advances. High forces are applied on the tool and on the plates during the process to keep them from separating.

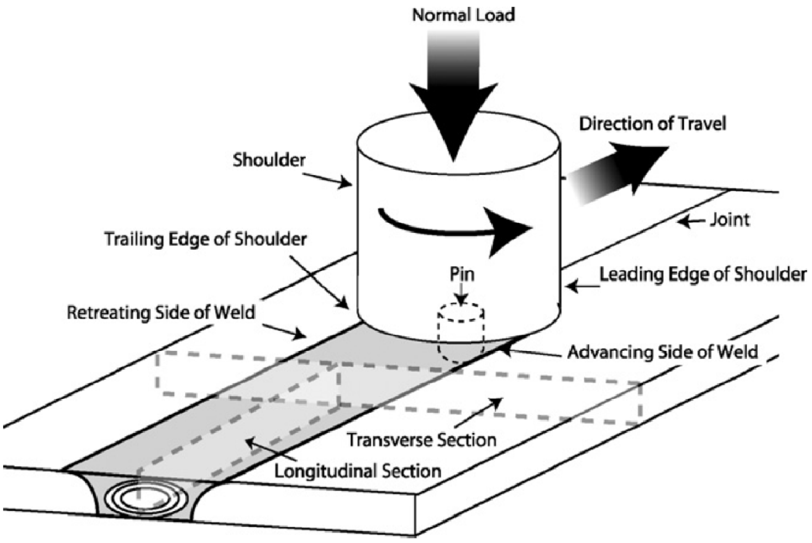

Figure 14: Illustration of a FSW Joint with Tool [20]

2.4.2 Details on the FSW Process

There are high forces involved in securing the plates during the welding process (in the order of several thousand Newtons [16]). This is essential since the plates must not move even though there are high frictional forces pushing the plates apart. Although the metal plates are not melted during the process, temperatures can reach close to 80% of the melting point [19] depending on the metal that is welded. For aluminum 7075 welds, maximum temperatures reach around 475°C which is 99.7% of solidus and 82.4% of the liquidus for this alloy [16][21][22].

A friction stir weld cross-section can be separated into 4 zones, as illustrated by Figure 15: the unaffected zone (zone A), the Heat Affected Zone (HAZ – Zone B), the thermo-mechanically affected zone (TMAZ – includes C and D) and the weld nugget (zone D). The HAZ will only suffer from heat transfer from the TMAZ. In the TMAZ, both heat and high plastic deformations are present. The weld nugget is the physical location where the tool had passed in the material. This is where to most severe stirring occurs.

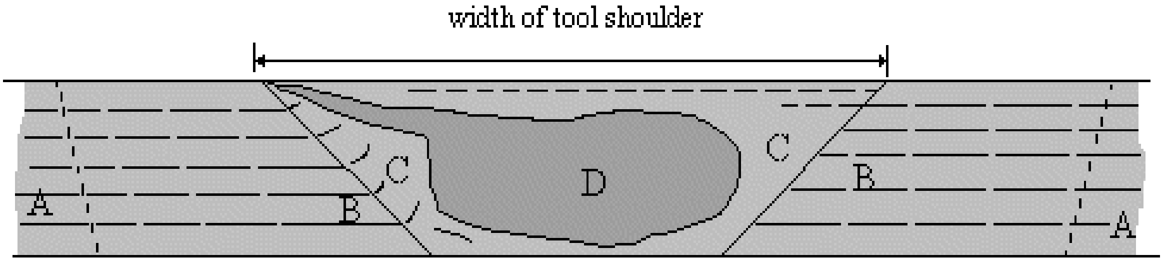

Figure 15: Illustration of a Transverse FSW zones. A: Unaffected Zone. B: Heat Affected Zone (HAZ). C: Thermo-Mechanically Affected Zone (TMAZ). D: Weld Nugget

Microstructural changes occur in the material during the process. The changes will be different depending on the region. In the weld nugget, the combination of high heat and high plastic deformation yield a fine equiaxed grain structure due to dynamic recrystalization [19]. In the TMAZ, this effect will be less pronounced due to reduced mixing leading to a partial recrystallization and severe plastic deformation. Since there is only heat transfer in the HAZ, there will be a grain coarsening [19].

2.4.3 FSW Advantages and Limitations

Friction stir welding presents many advantages [23]. First, the absence of melting results in less weld contamination, the ability to weld from any position, and welds with low distortion, residual stresses, shrinkage and porosity. There are no consumables, and because of this, no shielding gas or minimal edge preparation is required and the process is environmentally friendly (no fumes or spatter). The process is relatively simple, quiet, controllable, cost effective, and can join wrought cast products as well as different materials together.

FSW also has its disadvantages [23]. The weld speed is relatively low, and high clamping forces are required to keep the plates in place. Finally, the end of the weld joint will have a keyhole the size of the pin. This is because the pin must be removed from the joint after the weld.

2.5 Other Welding Processes

Welding is a highly developed field with many specialized and intricate welding techniques. Making a complete evaluation of all welding process is a tedious task and will not be completed here. The aim of this section is to briefly describe an overview of welding categories and expose the reader to the various welding processes available. A list of welding processes for each category will also be provided. In every case, the weld joint material is melted.

2.5.1 Arc Welding

The process of arc welding, similar to wire flame spray, is to create an arc between an electrode (consumable or not) and the material to be welded using either a DC or AC current. The welded region can be protected by an inert gas (shielding material) as required, and filler material can also be used in some cases. A list of arc welding processes is presented below.

Arc welding processes include atomic hydrogen welding, bare metal arc welding, carbon arc welding, flux cored arc welding, gas metal arc welding (GMAW) also known as (AKA) metal inert gas (MIG) welding, gas tungsten arc welding (GTAW) AKA tungsten inert gas (TIG) welding, plasma arc welding, shielded metal arc welding AKA stick welding and submerged arc welding [24][25].

2.5.2 Gas Welding

Gas welding consists of using a high temperature open flame created by the combustion of an oxidizer and a fuel. The most common gas welding process is oxy-fuel welding [25]. This process creates a flame temperature of approximately 3100^{o}C. Other types of gas welding processes are presented below. This
process leaves a coarser finish, but can be used to weld larges plates due to its high temperature. Gas welding processes include air acetylene welding, oxy-acetylene welding, oxygen/Propane welding, oxy-hydrogen welding and pressure gas welding [24][25].

2.5.3 Resistance Welding

Resistance welding generates heat by passing a current through the weld joint. Currents as high as 100,000 amperes are used in this process [25]. The most common resistance welding is spot welding widely used in robotic welding. A more complete list of resistance welding techniques is presented below.

Resistance Welding Processes include resistance spot welding, resistance seam welding, projection welding, flash welding, upset welding, and shot welding [24][25].

2.5.4 Energy Beam Welding

Energy beam welding is a relatively new process that uses a highly focused energy beam instead of an arc to produce local heat and melting to join the materials. The two most common processes involve either a laser or a focused electron beam. Two additional processes are presented in the list below.

Energy Beam Welding processes include laser beam welding, electron beam welding, electro-slag welding, laser-hybrid welding, and x-ray welding [24][25].

2.5.5 Solid State Welding

Solid state welding uses friction to generate heat. The heat generated is not sufficient to melt the material. Instead it reaches a plasticized state and is mixed with the other plate to be welded using high pressures. The most popular solid state welding technique is ultrasonic welding [25]. A variation of this process is explosion welding, where the two plates are pushed together under extremely high pressures. A full list of solid state welding techniques is presented below.

Solid-State Welding Processes include co-extrusion welding, cold pressure welding, diffusion welding, explosion welding, electromagnetic pulse welding, forge welding, hot pressure welding, hot isostatic pressure welding, roll welding, ultrasonic welding, induction welding, high frequency welding, exothermic welding, and friction welding which includes spin welding (friction stir welding) and linear friction welding [24][25].

2.5.6 Other Specialized Welding Techniques

There are other specialized welding techniques that do not fall under any of the previous categories. These techniques are highly specialized, and will not be discussed.

Other welding Processes include flow welding, percussion welding, thermite welding, electrogas welding and stud arc welding [24][25].

2.6 Al 7075

2.6.1 Bulk Al 7075 properties

Al 7075 is an alloy composed primarily of zinc, magnesium and copper. The composition of each element is shown in Table 2 below.

Table 2: Metallic Composition of Al 7075

Metal	Composition (%)
Aluminum	85.5 - 91.6
Zinc	5.1 – 6.1
Magnesium	2.1 – 2.9
Copper	1.2 – 2.0
Iron	0.5 max
Chromium	0.5 max
Manganese	0.5 max
Silicon	0.5 max
Titanium	0.5 max

The ternary phase diagram for this alloy (Figure 16) at the Al 7075 composition shows that the intermetallic formed is $Al_6Mg_{11}Zn_{11}$.

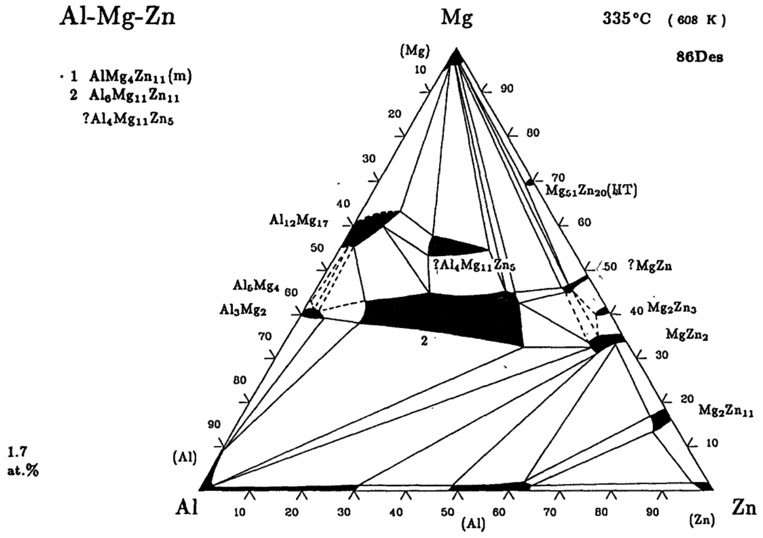

Figure 16. Al-Mg-Zn Ternary Phase Diagram at 335°C [26]

However, the strength of Al 7075 does not come from intermetallic compounds. All 7xxx series alloys are strengthened by a specific heat treatment process. This process consists of a series of steps outlined in the ASTM B918 standard [27] and presented in Table 3. Please note that there are two steps #1. This is because either a salt bath or an air furnace can be used for the solution heat treatment process.

The solution heat treatment dissolves the alloying elements into solid solution. The rapid quenching is induced to keep these elements dissolved in a supersaturated state before the proper temper can be applied [28]. The W51 temper represents a supersaturated alloy ready for natural ageing. Al 7075 is well known for its capability to age naturally at room temperature, in some cases doubling or tripling the yield strength over several decades [20][28]. The T651 temper shortens this ageing period to 24 hours.

Table 3. Recommended Heat Treatments for Bulk Al 7075 Alloy, as Outlined in ASTM B918 [27]

Step	Process	Medium	Temperature (°C)	Time (as a function of thickness t)
1	Solution heat treatment (temper –W51)	Salt bath	460-500	10-15 mins for t < 0.41mm 20-25 mins for 88.9 < t < 101.6mm (+15min per additional 12.7mm)
1	Solution heat treatment (temper –W51)	Air furnace	460-500	20-25 mins for t< 0.41mm 165-175 mins for 88.9 < t < 101.6mm (+30min per additional 12.7mm)
2	Quench	Water	38 start max 43 end max	As required
3	Precipitation heat treatment (temper -T651)	Not specified	121	24 hours
4	Cool	Not specified	Room	As required
-	Anneal (temper –O)	Not specified	407	2-3 hours

Al 7075 tempers will generally produce Guinier-Preston (GP) zones which strongly interact with dislocation motion, creating a high yield strength alloy [28]. GP zones occur in supersaturated solid solution heated at or above a certain critical temperature. (In this case this critical temperature is 121°C, the precipitation temperature.) GP zones are characteristic of aluminum alloys with copper as one of the alloying elements. They are characterized by small spherical precipitates that form in the material, including along grain boundaries. This will strongly act against intergranular dislocation motion. In the case of Al 7075, these precipitates can be any Cu-Mg-Al-Zn intermetallic such as $MgZn_2$ (most probably) or Mg_3Zn_3Al [28]. The exact composition of these precipitates depends on many factors including temperature. An example of GP zones is shown in Figure 17.

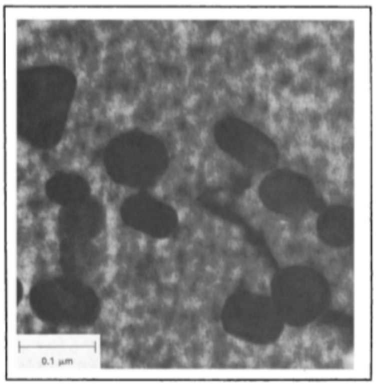

Figure 17. Transmission Electron Micrograph of 7075-W aged 25 years at Room Temperature. The Large Particles are $Al_{12}Mg_2Cr$ Dispersoid [28]

2.6.2 FSW Al 7075 Properties

This section aims to investigate the changes in mechanical properties of a FSW Al 7075 joint in comparison to an as-heat treated Al 7075 base material. This will help us understand why this part of the FSW joint corrodes preferentially.

The FSW process involves high heat and plastic deformation. As mentioned weld nugget temperatures in aluminum alloys can reach 475°C. This process leads to a reduction in yield strength. Mahoney reported a 45% reduction in yield strength, a 25% reduction in ultimate tensile strength and a 48% reduction in elongation in the HAZ zone for aluminum alloy 7075-T651 [28]. These losses in properties are linked to the process that strengthened the material in the first place: precipitates. Plastic deformation within the process as well as grain size changes must also be considered. Table 4 summarizes the important temperatures reached during the FSW process for every zone, as well as the heat treatment temperatures for each temper. It also lists observed precipitate size, dislocation density within the resulting FSW joint and grain size for all the FSW zones.

Table 4. Heat Treatment and FSW Temperatures for AA 7075 [27][29]. Arrows Indicate Impact on Zone Hardness. The "↑" Symbol Represents an Increase in Hardness, and the "↓" Symbol Represents a Decrease in Hardness. The Dash Sign ("-") Represents a Neutral Impact on Hardness

Process	T (°C)	MgZn$_2$ Precipitate Size (nm)	Dislocation Density	Grain Size	Resulting Hardness
Precipitation Heat Treatment (T651 temper)	121	N/A	N/A	N/A	N/A
Anneal (O temper)	407	N/A	N/A	N/A	N/A
Solution heat Treatment (W51 temper)	460 - 500	N/A	N/A	N/A	N/A
Effect on Hardness	N/A	High	Medium	Low	N/A
Weld Nugget	475 - 500	None (↓↓)	Low (↓)	Very small (↑)	Very low
TMAZ	450 - 475	Up to 70 (↓)	Very high (↑↑)	Medium (-)	Medium
HAZ	250 - 450	10 – 30 (-)	Average (-)	Large (↓)	Low
Parent material	< 100	10 – 20 (↑)	Average (-)	Medium (-)	High

The changes in properties are a function of both the change in precipitate size, dislocation density and grain size. Because the temperatures reached in the weld nugget are sufficiently high, the precipitates will dissolve, leaving only a solid solution.[1] The TMAZ and HAZ suffer from over ageing resulting in coarse precipitates throughout [21][23]. The parent material does not see sufficiently high temperatures to activate the ageing process – there will not be any change in microstructure or precipitate size in this part of the weld joint.

Grain size also plays a role in the hardness of the material. More grain boundaries indicate more dislocation obstacles, leading to an increase in elongation-to-failure rates and hardness. The grains within the weld nugget have been dynamically recrystallized. This is due to the nucleation of grains due to plastic deformation and high stress. (Grains boundaries are formed to absorb the deformation energy.) A higher heat results in smaller grains because there is more nucleation [30].
Figure 18 shows a hardness map illustrating the change in hardness with distance from the center of an Al 7075 FSW joint. In the weld nugget (center), the combined effect of a reduced number of precipitates, low dislocation density yet smaller grain size yields a low hardness. With an increasing distance towards the HAZ, the dislocation density increases, as well as precipitate count. Therefore

---

[1] This will be true for most parts of the weld nugget. However, it is possible that some precipitates remain within the weld nugget due to the complex nature of the process. These precipitates will be very coarse, ranging up to 100 µm in size [29]

the hardness increases (the effect of grain size does not seem to be a large contributing factor to the hardness of the material.) However, at the HAZ, the dislocation density falls significantly. The combined effect of smaller precipitate size (increased hardness), lower dislocation density (reduced hardness) and larger grains (reduced hardness) results in an overall hardness loss.

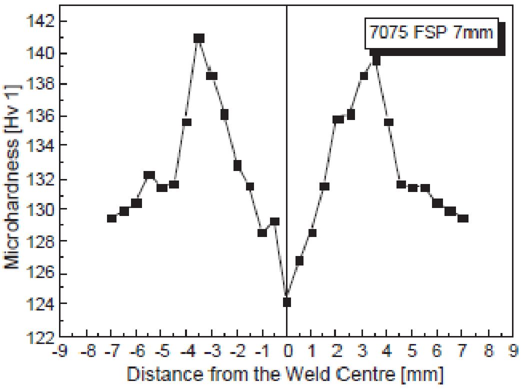

Figure 18. Micro-Hardness Profile Measured on the Cross Section of 7075 FSW Plate [23]

In summary, the loss in hardness is due in large part to a coarsening or dissolution of the precipitates through over-ageing within the weld nugget and HAZ [21][23]. Effect of dislocation density must be taken into account in the TMAZ while effect of grain size is an important factor in the HAZ.

2.7 Corrosion Basics Applied to Al 7075 and FSW Al 7075

Now that a good understanding of the properties of Al 7075 and FSW Al 7075 has been established, details on the corrosion principles and how they apply to FSW must be presented.

2.7.1 Corrosion Basics

Corrosion is defined as “a chemical or electrochemical reaction between a material, usually a metal, and its environment that produces a deterioration of the material and its properties” [31]. Corrosion occurs as a cell. There are 4 components to this corrosion cell:

1. An anode (loses material);
2. Ionic current (ions must be able to move between the anode and the cathode);
3. A cathode (builds material);
4. An electronic path (electrons must be able to move from the anode to the cathode).

With these 4 pillars in place, corrosion may occur. Many prevention techniques can be put in place to eliminate one of the 4 elements. Most commonly, the electronic or ionic path is blocked by means of insulation such as paint or metallic coatings.

The tendency of an element to corrode can be measured and classified in a list called the electromotive force series (EMF). This is a value noted by measuring the electrical potential created in a corrosion cell between the measured material and a standard hydrogen element. By measuring the voltage between the anode (metal) and the cathode (hydrogen), a reference chart can be built indicating each element's relative reaction to corrosion. A sample of the EMF chart is presented below in Table 5.

Table 5. EMF for Many Elements. Note Aluminum is -1.66, and Magnesium is -2.37 [31]

Electrode reaction	Standard potential at 25 °C (77 °F), V-SHE
$Au^{3+} + 3e^- \rightarrow Au$	1.50
$Pd^{2+} + 2e^- \rightarrow Pd$	0.987
$Hg^{2+} + 2e^- \rightarrow Hg$	0.854
$Ag^+ + e^- \rightarrow Ag$	0.800
$Hg_2^{2+} + e^- \rightarrow 2Hg$	0.789
$Cu^+ + e^- \rightarrow Cu$	0.521
$Cu^{2+} + 2e^- \rightarrow Cu$	0.337
$2H^+ + 2e^- \rightarrow H_2$	0.000 (Reference)
$Pb^{2+} + 2e^- \rightarrow Pb$	–0.126
$Sn + 2e^- \rightarrow Sn$	–0.136
$Ni^{2+} + 2e^- \rightarrow Ni$	–0.250
$Co^{2+} + 2e^- \rightarrow Co$	–0.277
$Tl^+ + 2e^- \rightarrow Tl$	–0.336
$In^{3+} + 3e^- \rightarrow In$	–0.342
$Cd^{2+} + 2e^- \rightarrow Cd$	–0.403
$Fe^{2+} + 2e^- \rightarrow Fe$	–0.440
$Ga^{3+} + 3e^- \rightarrow Ga$	–0.53
$Cr^{3+} + 3e^- \rightarrow Cr$	–0.74
$Cr^{2+} + 2e^- \rightarrow Cr$	–0.91
$Zn^{2+} + 2e^- \rightarrow Zn$	–0.763
$Mn^{2+} + 2e^- \rightarrow Mn$	–1.18
$Zr^{4+} + 4e^- \rightarrow Zr$	–1.53
$Ti^{2+} + 2e^- \rightarrow Ti$	–1.63
$Al^{3+} + 3e^- \rightarrow Al$	–1.66
$Hf^{4+} + 4e^- \rightarrow Hf$	–1.70
$U^{3+} + 3e^- \rightarrow U$	–1.80
$Be^{2+} + 2e^- \rightarrow Be$	–1.85
$Mg^{2+} + 2e^- \rightarrow Mg$	–2.37
$Na^+ + e^- \rightarrow Na$	–2.71
$Ca^{2+} + 2e^- \rightarrow Ca$	–2.87
$K^+ + e^- \rightarrow K$	–2.93
$Li^+ + e^- \rightarrow Li$	–3.05

PH is also an important part of the corrosion process as it will dictate how an element reacts to the environment. Pourbaix diagrams classify the reaction of the elements exposed to various combinations of potential-pH environments. The result is a map of corrosive, passive and immune regions, individualized for each element (see Figure 19 for a few Pourbaix diagrams). Immunity indicates that no chemical reaction will occur between the material and the environment. A passive reaction occurs when the corrosion product formed protects the material from further corrosion (e.g. aluminum oxide forming in aluminum). A corrosive region indicates the formation of ions in the material and progressive mass loss.

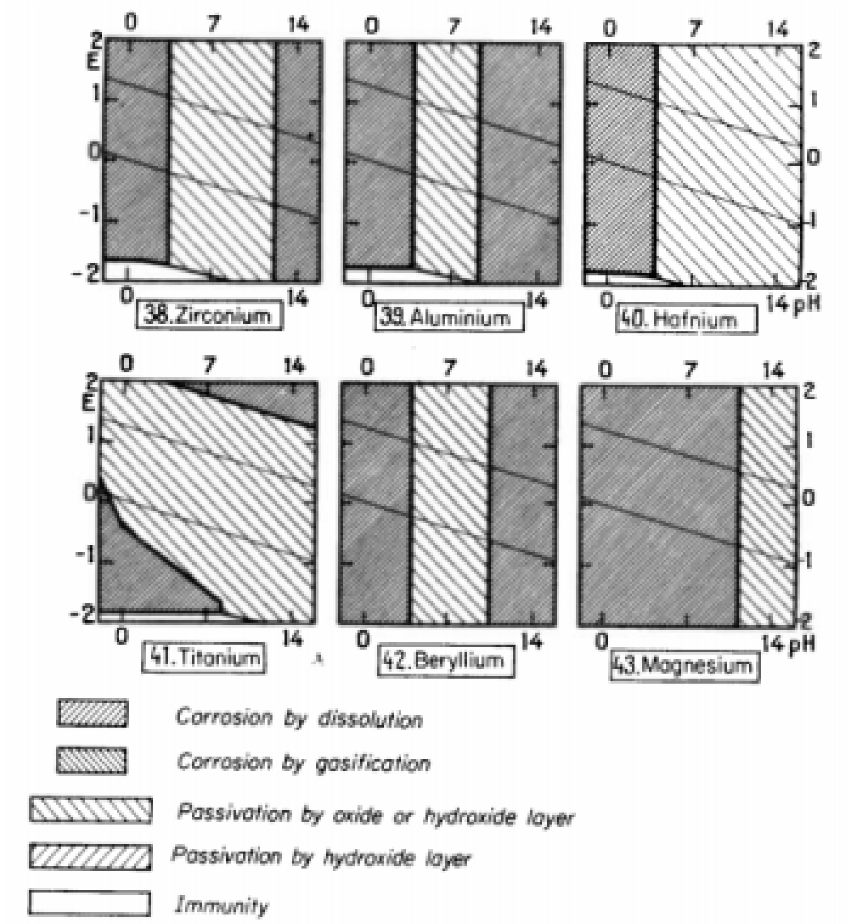

Figure 19. Pourbaix Diagrams of Zirconium, Aluminum, Hafnium, Titanium, Beryllium and Magnesium. X-axis is the pH Level, Y-axis is the Potential [32]

Pourbaix diagrams are intended for pure elements only. They do not represent well the corrosive map of alloys due to the complex interactions that can occur between elements in the alloys. These interactions change with temperature and alloying composition, making the creation of a Pourbaix diagram extremely difficult if not impossible. However, looking at the Pourbaix diagram of the major contributing element in the alloy can give us a good indication of the general corrosion performance for this alloy.

Correlating this chart with the one presented in Figure 20, it is possible to determine specific environments in which the element will corrode. This is very useful in determining applications for this element. For example, never use aluminum when sodium hydroxide is involved!

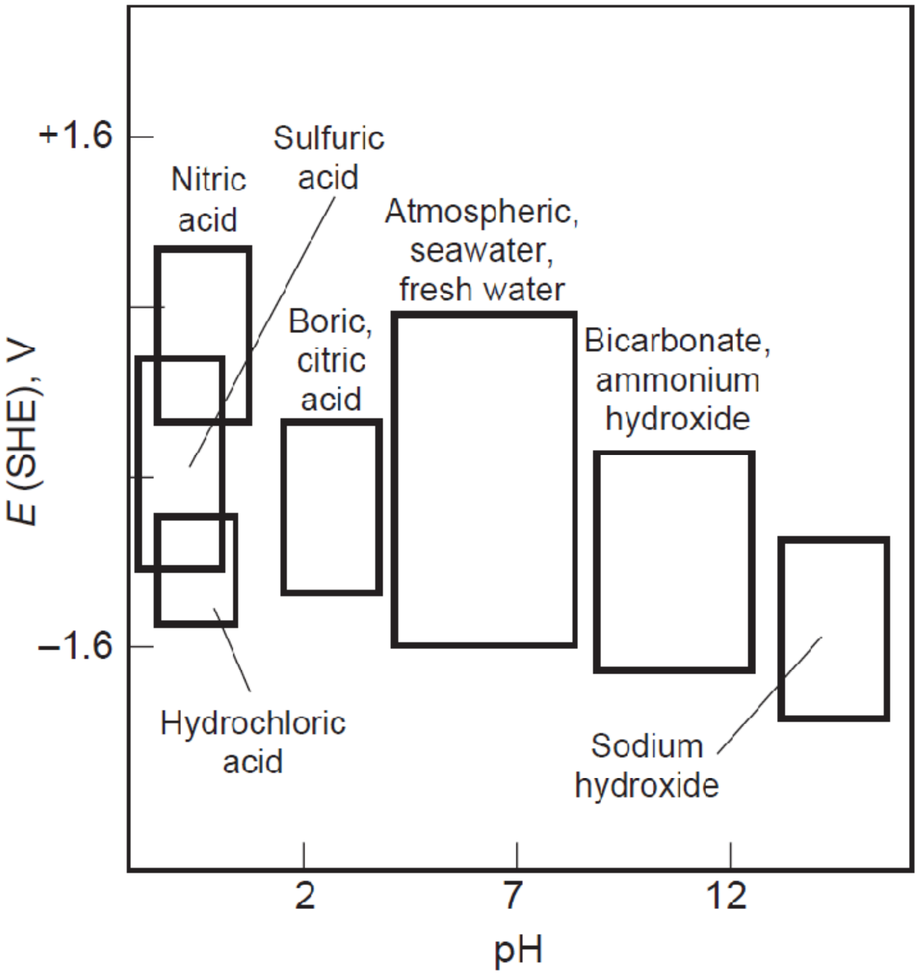

Figure 20: Potential-pH Diagram indicating the Range of certain Electrolytes [31]

2.7.2 Al 7075 Corrosion

There are many types of corrosion, but 7xxx series aluminum alloys are particularly sensitive to localized corrosion such as intergranular, exfoliation and stress corrosion cracking [22]. AA 7075 is also prone to pitting corrosion. A definition of each corrosion types is listed below:

- Intergranular corrosion: Corrosion at the grain boundaries propagates around the grains in a random fashion, eventually dislodging entire grains from the material.
- Exfoliation corrosion: Similar to intergranular corrosion, but the corrosion propagates in a direction parallel to the surface of the material. Material is removed in thin sheets.
- Stress Corrosion Cracking: Crack propagation under load enhanced by the effect of corrosion.
- Pitting corrosion: Surface corrosion characterized by localized, penetrating corrosion crevices (pits).

These corrosion modes occur because there is a significant potential between the magnesium-zinc precipitates and the aluminum matrix (0.71 Volts as shown in Table 5). This leads to the creation of a corrosion cell between the two with the addition of an electrolyte and electrical conductor such as water. As the precipitates are corroded away, the corrosion spreads along the weakened grain boundary, leading to intergranular, exfoliation and stress corrosion cracking corrosion types. In the case of pitting corrosion, the corrosion spreads vertically instead of along the grain boundaries, but the principles remain the same. Figure 21 shows an example of pitting corrosion in a FSW Al 7075 joint.

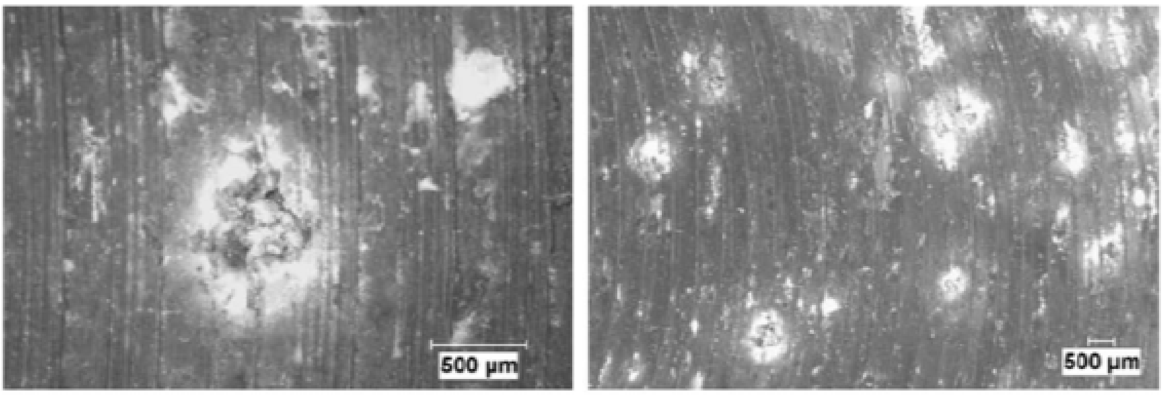

Figure 21: Surface of a FSW 7075 AA after 60 day Exposure to 3.5% NaCl Solution at Room Temperature [33]. FSW Al 7075 Corrosion

The question now becomes: why does a FSW joint corrode preferentially to a regular Al 7075 panel? There are several reasons affecting this, and a summary of the important factors is presented below:

- FSW joints have coarser precipitates due to over-ageing in the TMAZ and HAZ.
- The weld nugget suffers from precipitate dissolution in the metal, leading to a copper dilution in the intermetallic compound.
- The TMAZ suffers from grain realignment through mechanical processing. This leads to high angle grain boundaries [19].

The increase in corrosion susceptibility at the weld joints is due to the initiation of pitting corrosion at precipitate-free, copper depleted zones in the weld nugget and HAZ, followed by propagation through coarse precipitates at the grain boundaries leading to intergranular corrosion [21]. High angle grain boundaries are also more prone to corrosion [19].

2.8 Previous Research

This section aims to review possible solutions to the corrosion issue faced here and present literature relevant to the research carried out in this thesis.

2.8.1 Potential Solutions

There are a few possible solutions to this corrosion problem. If the part is small, then it is possible to re-heat treat the part to bring the joint back to its original properties. This would mean going through the lengthy T651 heat treatment process again. However, in aerospace applications, parts are likely to be very large, and an ageing heat treatment might not be an option. Since corrosion is only an issue at the FSW joint, the idea is to focus protection to this area in particular.

A literature review on this subject allows us to find potential solutions. Since 7xxx series alloys are subject to stress corrosion cracking, one potential solution aims to use a peening technique to induce a compressive residual stress on the plate surface. Peening techniques have been shown to mitigate the effects of stress corrosion cracking and enhancing the fatigue and SCC properties of aluminum alloys [32]. However they have proven to be worst in pitting corrosion than unpeened samples [34] as shown in Table 6.

Table 6: Pitting Corrosion of FSW AA 7075 Exposed to 3.5% NaCl Solution at Room Temperature [34]

Sample I.D.	General corrosion rate (mm/year)	Pits per 6.5 cm^2
Unpeened	0.017	5
Laser peened (3 layers)	0.020	1
Shot peened	0.022	1

Another solution is to use coatings. Micro-arc oxidation coatings have been used successfully to protect several FSW plates from material [35]. Micro-arc oxidation (MAO), like anodizing, is an electrochemical treatment made to thicken the oxide layer of materials such as aluminum, titanium and magnesium. MAO uses a high potential to create electrical discharge and plasma formation within the oxide. This leads to local melting and re-solidification of the layer leading to the formation of denser and harder oxides.

In this study, ceramic coatings were formed on 2xxx, 5xxx and 7xxx series friction stir weld plates (including the joint line) and tested for corrosion in a salt spray chamber. Results indicated severe corrosion in the uncoated plates, especially at the joint line (concurrent with literature presented in previous chapter) and no visible signs of corrosion on the coatings.

The Boeing Company has elected to use CGDS technology to produce a metallic layer on top of the FSW joint to protect it from the environment. The CGDS process is used because the formation of the coating is done at relatively low temperatures. Since Al 7075 is a heat-treated alloy, it is important to keep the plate temperature below a maximum threshold to maintain the heat treatment. CGDS is the only thermal spray process that can achieve this goal.

Three metallic powders were chosen for this purpose. The first is pure Al for its reputed corrosion protection capabilities. However, pure Al does not have good mechanical properties. It was elected to also test Al 5083 for this purpose – it is an alloy with a good combination of excellent corrosion resistance and strength. The final feedstock material to be used will be Al 7075, same as the parent material. This would be preferable since these FSW parts will eventually be submitted to surface coating techniques (e.g. painting) that will yield visual differences if the alloy employed is not the same. This could lead to potential problems with customers.

Creating an aluminum coating on top of the FSW joint would definitely eliminate its exposure to the environment, therefore eliminating two of the 4 pillars of corrosion (cathode and saline transport). However, since aluminum is susceptible to pitting corrosion, pits will eventually pierce through this protective coating, at which point the original FSW joint will be exposed. Penetration rates for pitting corrosion in aluminum obtainable in Table 6 show that the unpeened (as-performed) FSW joint has a general corrosion rate of about 17µm/year. This value is reliable because it was performed in a salt spray chamber which houses a similar environment to what these parts will operate in.

The Boeing Company requires a metallic coating of approximately 200 µm, or 0.2 mm. At the rate prescribed, it would therefore take 11.8 years for the coating to fail. This means that approximately every 10 years the part will need to be recoated. This value is for general corrosion value however and does not include pitting depth. A more frequent verification would therefore be needed.

Table 6 shows the effects of two peening techniques on general corrosion rates. Results do not seem promising, as the general corrosion rate seems to increase. This is because the corrosion rate is less uniform throughout the surface due to larger and deeper pits.

2.8.2 Coating Production

Aluminum coating production using cold gas dynamic spraying is not a new proposition. There are many published works demonstrating the possibility of this process and its ability to deposit aluminum coatings, while listing properties for the deposition process and the microstructure of the coating.

For instance, Van Steenkiste successfully deposited large Al powders (63-106 µm range) [36]. He concluded that the critical velocity for large powders was lower than anticipated since measured velocities were between 350 and 500 m/s. He also measured good coating properties including low thermal stresses and low porosities. This study shows that Al powder can be deposited easily in a wide range of powder sizes. Sieving Al powder is not necessary. An optical photograph of Van Steenkiste's coating is shown in Figure 22.

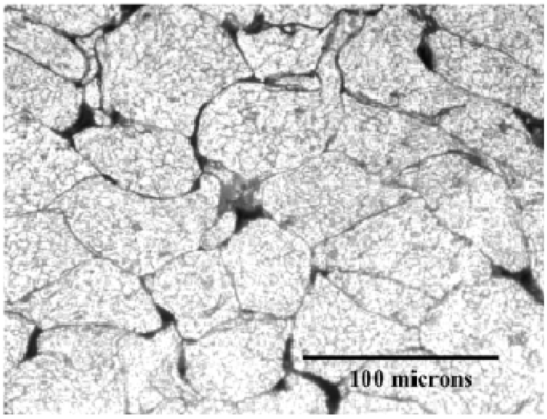

Figure 22. Optical Photograph of the Etch Surface of Al Coating Cross-Section Produced at an Air Propellant Gas Temperature of 315°C (600°F) [36]

Tao showed that dense Pure Al coatings can be formed. His study also showed that pure Al coatings show better corrosion resistance than bulk Al due to their non-connecting porosities which lower the electrochemical potential of the coating [37]. Figure 23 shows on of Tao's coatings.

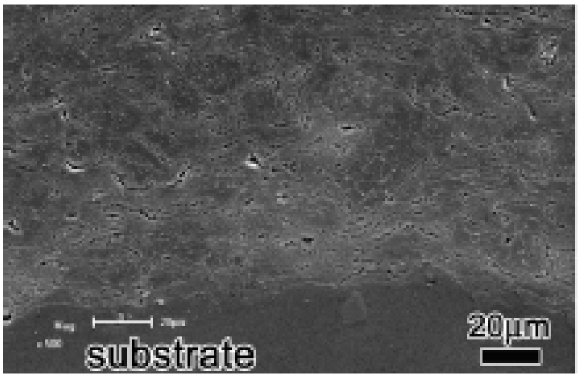

Figure 23. TEM Images of the Cold Sprayed Al Coating Showing Grain Refinement Occurring Close to a Good Bond of Particle/Particle Boundary [37]

A study performed by Ghelichi showed successful deposition of both pure Al and Al 7075 powders [38]. Al 7075 powders are harder, and therefore more difficult to deform than pure Al powder. The spray parameter for this particular alloy must therefore be higher in order to deposit a coating. However, the parameters used for both powder showed dense and uniform coatings (see Figure 24). Furthermore, Ghelichi was able to determine that compressive residual stresses are present in both coatings. These stresses are 50% higher in pure Al due to lower deposition stagnation temperature (which anneals the material).

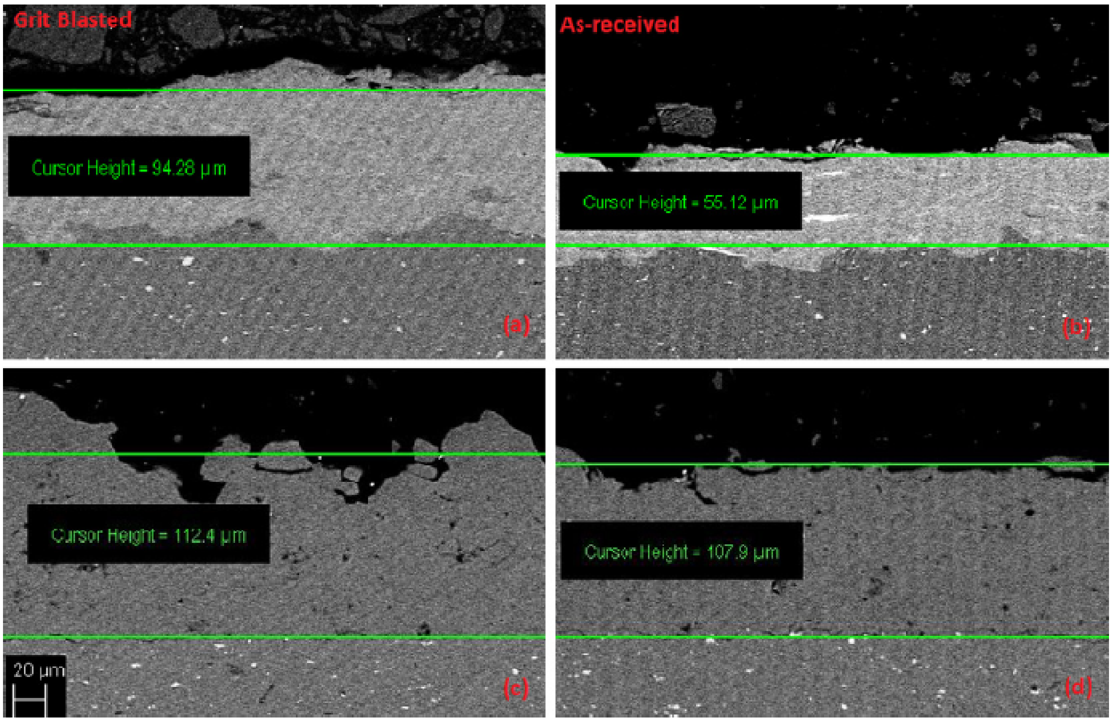

Figure 24. Cross-Section SEM Images of (a) the Grit-Blasted Specimen Coated with Al7075; (b) the As-Received Specimen Coated with Al7075; (c) the Grit-Blasted Specimen Coated with Pure Al; (d) the As-Received Specimen Coated with Pure Al (Magnification 500 X) [38]

Wang performed a study on the bonding mechanisms of cold gas dynamic spray. The pure Al coating deposited was dense with well deformed particles [39][32]. As discussed in section 2.1.5, he demonstrated that the main bonding mechanism was through mechanical anchoring. This high mechanical anchoring was partly due to the range in particle speed and size [39][32]. See Figure 25 for more details.

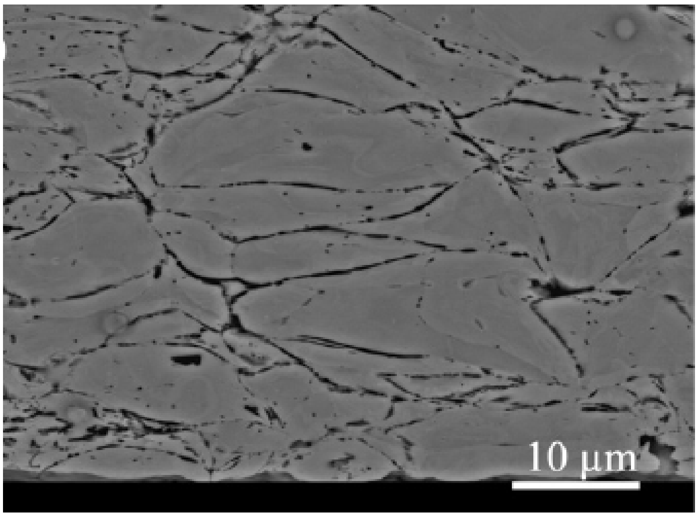

Figure 25. Backscatter SEM Micrograph of an Etched Pure Al Coating Cross Section [39]

Sova [40] used a micro-sized nozzle to deposit pure Al coatings. As shown in Figure 26, this nozzle is only around 20mm in total length. The powder used in this study was below 10 µm. This shows the ability of small powders to deposit while using very small nozzle (which translates to small exit particle velocities).

Figure 26. Micronozzle used in Sova's Experiments [40]

Finally, Spencer deposited Al, Al 6061 and Al 7075 coatings. He showed that the residual stress in coatings is mainly attributed to the peening effect of the powder particles impacting the deposited layer of particles [41].

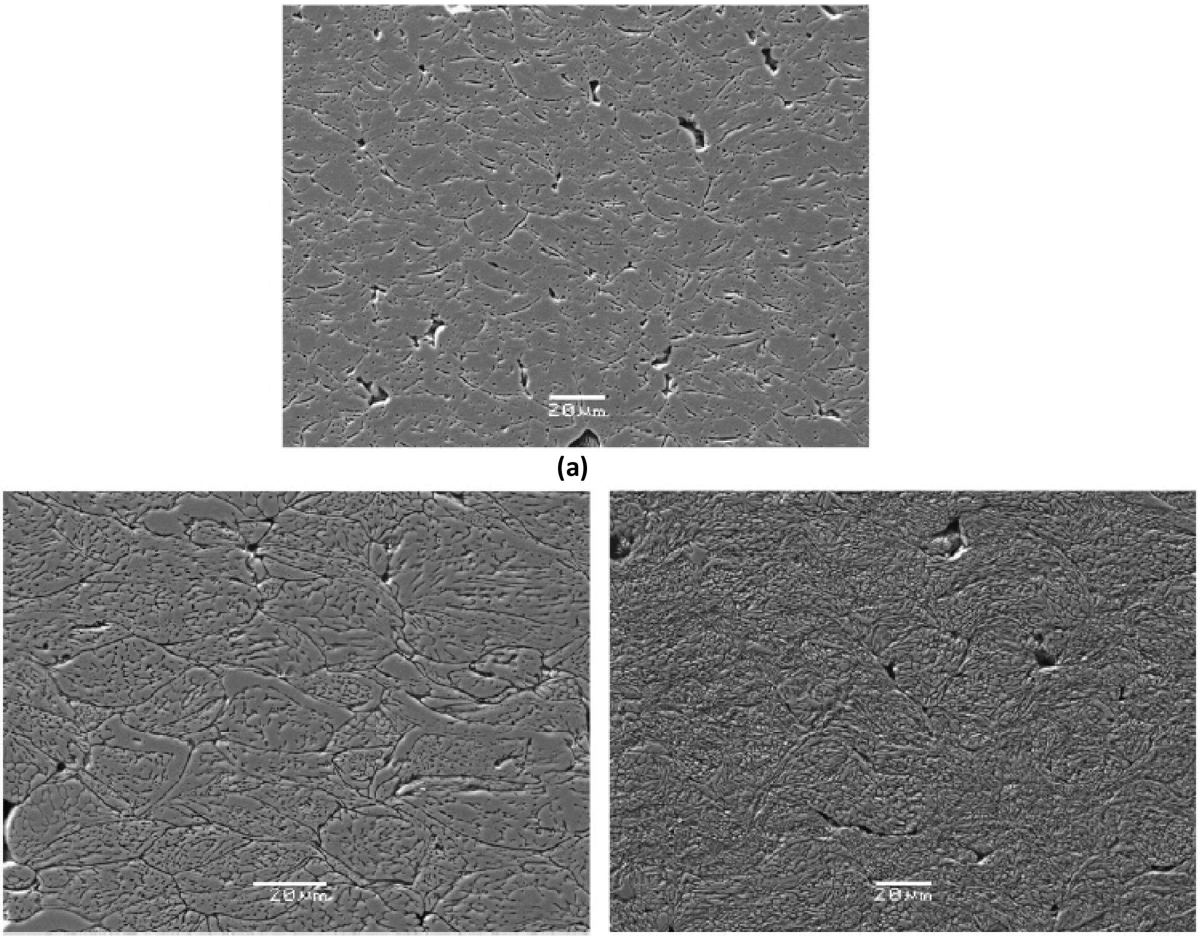

(a)

(b) **(c)**

Figure 27. Etched Metallographic Sections of the Al Coatings. Direction of the Spray Nozzle Travel is Normal to the Page. (A) KM Pure Al, He 132°C a) Pure Al (b) CGT 6061Al (c) CGT 7075Al [41]

Table 7 summarizes the important parameters from each of the listed references (where available). Figure 22, Figure 23 and Figure 24 show typical results from these studies.

Table 7. System and Coating Properties for Cold Spray Deposited Pure Al and Al 7075 from 3 Different Sources

Parameter	Van Steenkiste et. al [36]	Y. Tao et. al. [37]	R. Ghelichi et. al. [38]	Q. Wang et. Al. [39]	A. Sova et. Al [40]
Gas type	Air	Air	Nitrogen	Helium	Nitrogen
Powder Type	Pure Al	Pure Al	1 -Pure Al 2 - Al7075	CP Al	1 - Pure Al 2 - Al 7075
Powder Size (µm)	63-106	1-40	15-20	2-20	1 – 15 2 - 45
Powder morphology	Spherical	Spherical, elongated	N/A	Spherical	Spherical
Propellant gas Pressure (psi)	300	232	232	90	1 – 110 2 - 558
Propellant gas Temperature (^{o}C)	204-315	230	1 - 350 2 - 500	N/A	1 – 550 2 – 400
Standoff Distance (mm)	20	30	1 - 20 2 - 15	12	N/A
Nozzle Area Ratio	2.83	2.5	9.92	N/A, Innovati (Santa Barbara, CA) system	
Nozzle Length	80	90	120	N/A, Innovati (Santa Barbara, CA) system	
Substrate	Brass	AZ91D Mg Alloy	Al 5052	Al	ZE41A Mg alloy
Substrate preparation	"Roughened"	24 alumina grit blasting	"Grit blasting" and "As-is"	N/A	1200 SiC clean + ethanol rinse
Coating porosity (%)	1.75-4.51 See Figure 22	N/A See Figure 23	N/A See Figure 24	1.5	1 – 2 2– 1.5
Coating hardness (GPa)	0.380-0.513	N/A	1- ≈0.363 2 - ≈ 1.27	N/A	N/A

Generally, there is a dense uniform coating with low porosity values of 1.5 to 3.3%. The coating hardness is higher than bulk material due to mechanical stresses induced by the deposition process. High residual stresses remain in the coating after deposition. Higher stresses are seen in coating deposited a low stagnation temperature regardless of the powder used. This is because there is less annealing effect.

Several conclusions can be made from these studies. First, spray parameters indicate that pure Al powder requires less energy to deposit. This is due to its lower hardness which translates into a low critical velocity. However, stagnation temperature should be kept as high as possible to reduce residual stresses. Furthermore, sieving powder is not important since aluminum deposits in a large range of parameters. Peening effect is detrimental to coating quality (increased residual stresses), and so the amount of particles impacting the surface (per surface area) should be reduced.

As far as Al 7075 is concerned, deposition should be made at high stagnation pressure and temperature. The peening effect is not important for this alloy due to the coating's high hardness. Al 5083 was not mentioned in these studies. However, its properties resemble that of Al 7075 (as a solid solution). The Al 7075 recommendations will be used for Al 5083.

2.9 Corrosion Testing

In order to establish if the coatings are performing adequately for corrosion protection of Al 7075 FSW joints, corrosion tests must be selected adequately to produce all the potential corrosion types in Al 7075. In this case, the coatings will not be subject to high mechanical stresses – for this reason stress corrosion cracking will not be evaluated. This means that the final selection of tests should produce pitting, intergranular, and exfoliation corrosions in order to fully test the corrosion protection capabilities of these coatings.

Many tests are available to test corrosion susceptibility of heat treated aluminum alloys. (Heat treated aluminum alloys include 2xxx and 7xxx series alloys.) Table 8 lists the ASTM-recommended corrosion test standards for aluminum corrosion.

Table 8. Recommended Corrosion Test Standards for Aluminum and Aluminum Alloys Corrosion [42]

Corrosion Type	Test	Title
General	ASTM F110	Test Method for Sandwich Corrosion Test
	ASTM B680	Test Method for Seal Quality of Anodic Coatings on Aluminum by Acid Dissolution
Pitting	ASTM G44	Practice for Evaluating Stress Corrosion Cracking Resistance of Metals and Alloys in 3.5% Sodium Chloride Solution
	ASTM B117	Test Method of Salt Spray (Fog) Tests
	ASTM G50	Practice for Conducting Atmospheric Corrosion Tests on Metals
	ASTM G46	Standard Recommended Practice for Examination and Evaluation of Pitting Corrosion
	ISO 8993	Anodized Al and Al alloys – Rating System for Evaluation of Pitting Corrosion – Chart Method
	ISO 8994	Anodized Al & Al alloys – Rating System for the Evaluation of Pitting Corrosion – Grid Method
Intergranular	ASTM G85 Annexe 2, 3 or 4 [43]	Practice for Modified Salt Spray (Fog) Testing
	ASTM G110	Practice for Evaluating Intergranular Corrosion Resistance of Heat Treatable Aluminum Alloys by Immersion in Sodium Chloride and Hydrogen Peroxide Solution
Exfoliation	ASTM G34	Test Method for Exfoliation Corrosion Susceptibility in 2xxx and 7xxx Series Aluminum Alloys (EXCO Test)
	ASTM G112	Guide for Conducting Exfoliation Corrosion Tests in Aluminum Alloys
Stress Cracking	ISO 9591	Corrosion of Aluminum Alloys – Determination of Resistance to Stress Corrosion Cracking
	ASTM G139	Test Method for Determining Stress Corrosion Cracking Resistance of Heat-Treatable Aluminum Alloy Products Using Breaking Point Load Method

This is an exhaustive list of test. Each standard can be inspected and it can be determined whether or not the test is applicable for this purpose. (In this case Al 7075 corrosion tests are being performed.) Many tests can be eliminated because of time restriction (e.g. ASTM G50 atmospheric tests take several years) or for application purposes (ASTM B680 is for porous anodic coatings and ASTM F110 is for aircraft maintenance chemical compounds). There are reference standard such as ASTM G46, G47 and G112. There are also other standard which required specialized corrosion testing equipment – ASTM G139 is used a tensile setup under environmental testing, while ASTM G85 used a cycle of salt fog, dry air purge and soak only available from specialized environmental chambers.

The remaining tests cover all of the corrosion categories; ASTM B117 for pitting, ASTM G34 for exfoliation, ASTM G110 for intergranular corrosion. ASTM G47, G139 and G129 can be used for stress corrosion cracking, although there is more literature available on ASTM G129. However, as mentioned stress corrosion cracking will not be performed in this study.

Several papers have been published on corrosion resistance of either Al 7075 or FSW Al 7075 panels using these 3 tests. Rao showed that corrosion resistance of FSW aluminum alloys can be significantly increased in ASTM B117 tests [44] with micro-arc oxidation coatings [35]. A study of pitting corrosion for FSW AA2219 was also carried out by Surekha [45] using the same test. This author also used ASTM G110 [46] to analyze for intergranular corrosion. ASTM G110 was also used by Paglia [47] in Al 7075-T651 FSW panels showing significant intergranular corrosion in the weld nugget. Figure 28 shows typical results for an ASTM B117 test (pitting corrosion). Figure 29 shows typical results of an ASTM G110 test (intergranular corrosion).

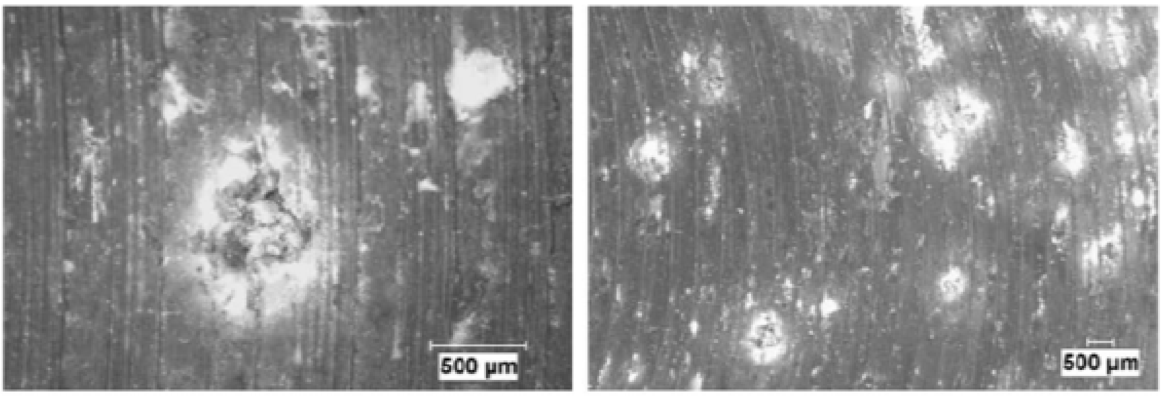

Figure 28: Surface of a FSW 7075 AA after 60 day Exposure to 3.5% NaCl Solution at Room Temperature [32]

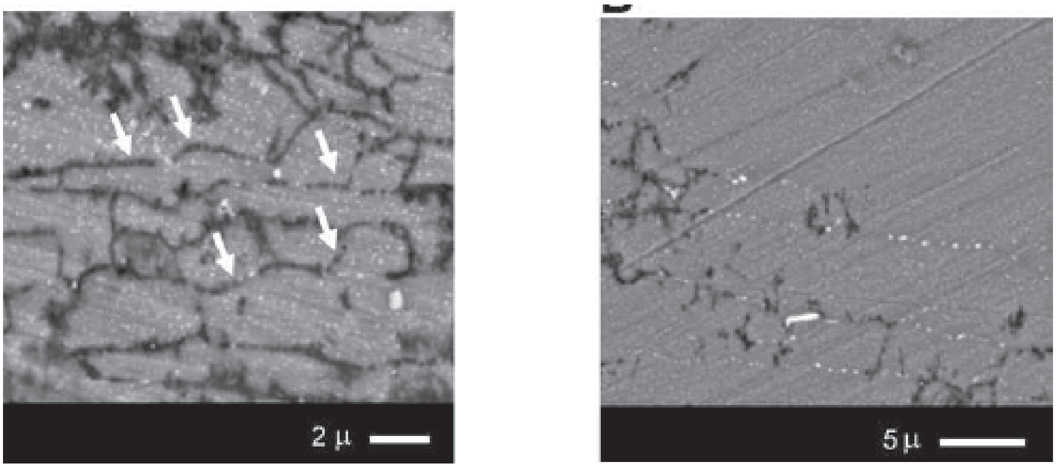

(a) (b)

Figure 29. (a) Initial Stage of Intergranular Corrosion on a Heat-Affected Zone of 7075-T651 FSW with the Attack of the Precipitate-Free Zones. Note the Residual Presence of Small "White" Grain Boundary Precipitates (Arrows) and the Attack of the Precipitate-Free Zone (Black). (b) Complete Attack and Dissolution of the Precipitate-Free Zone and the Grain Boundary Phases in the Plunge Area of a 7075-T651 FSW. The Corrosion Immersion tests Were Carried out According to the ASTM G110-92. SEM Images in BSE Mode [47]

Finally, Li [22] and Kang [48] used ASTM G34 to measure exfoliation corrosion of aluminum alloys. Li tested AA 7075 plates while Kang tested FSW AA 2024-T3. Figure 30 presents typical results for this EXCO (EXfolication COrrosion) test.

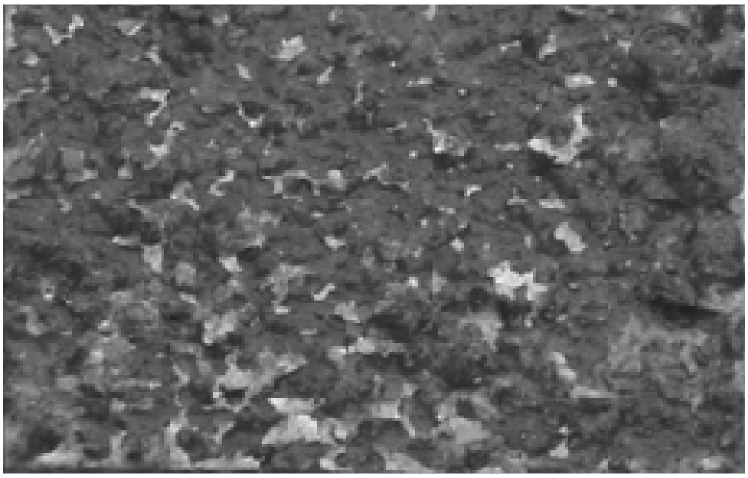

Figure 30. Corrosion Morphologies of 7075 Al Alloy with T6 Aging Treatments After 48 h of Immersion in EXCO Solution [22]

3 Research Objectives

Chapter 1 presented a list of general research objectives to be met during this research. This chapter aims to describe the tasks that will be performed in order to meet these objectives.

This thesis is divided into three main research objective categories. The first, presented in section 1, presents the main research objectives as described in the general research objectives. These deal with the direct research associated with the corrosion susceptibility and protection of Al 7075 joints.

The secondary research objectives were added later on to further our understanding of specific subjects. The first secondary research objective group was created to obtain a greater understanding of the mechanical properties of the coatings produced in order to complete the primary research objectives. The second secondary research objective group aims to increase comprehension in nozzle design and propose a new nozzle design for optimized powder deposition efficiency.

3.1 General (Primary) Research Objectives

The following sections present each primary research objective individually.

3.1.1 Identify the Causes of the Loss in Corrosion Resistance to Ensure that Producing a Metallic Coating is a Viable Solution

It is interesting to better understand the mechanics of corrosion in FSW Al 7075 plates and why there is preferential corrosion at the weld joint. Most of the theory behind this process has been presented in the previous chapter. This will be confirmed experimentally with FSW joints prepared for this purpose. The joints will be analyzed for microstructure and hardness to confirm the accuracy of the literature.

3.1.2 Determine the Feasibility of Spraying Metallic Particles onto Al 7075 by Testing Multiple System Parameters, then Modify the System Parameters to Optimize the Coating Produced

The goal of these two sections is to find system properties that will achieve the desired coating properties. This entails the selection of specific metallic powder for the use of this project. Then preliminary coatings of these powders will be produced on bulk Al 7075 plates. This is to ensure that coatings can be deposited on this material. Multiple system parameters will be tested.

After having determined that coatings can be produced, the spray variables will be fine-tuned in order to obtain the best compromise between coating density and high deposition efficiency. After this is done an “optimized” coating will have been optimized. This must be done for every metallic powder.

The Boeing Company has imposed a set of restrictions for the coating properties. A list of these restrictions is presented below:

- The final coating thickness must be 5 – 10 thou (125-250 µm) i.e. average thickness 7.5 thou (187.5 µm)
- There must be an invisible transition between the coating FSW joint and the rest of the plate. To achieve this, the surface roughness of the protective coating should be between 125µin and 250µin (3.2µm to 6.3 µm) which is as smooth as the sheet metal on which they are sprayed.
- The coating may be sprayed thick and machined down to the required thickness in order to obtain the required roughness.
- The coatings shall be produced with pure Al, Al 5083 and Al 7075 powders.
- The system used shall be the Centerline SST-P series system.
- A series of plates shall be sprayed with these three coatings and tested in ASTM B117. Results from this test will determine the superior coating for corrosion protection.

3.1.3 Spray Coatings of Various Aluminum Alloys onto Al 7075 and Test their Corrosion Resistance via Multiple Testing Standards and Measuring Methods

Once optimal system parameters for each powder are established they can be used to create coatings on FSW plates and test the resulting system in corrosion tests for improved performance. The tests will always be performed with a control sample (uncoated FSW sample) to properly compare the results.

3.1.4 Compare the Corrosion Resistance of the Various Protective Aluminum Alloy Coatings and Compare them with the As-FSW Panels' Corrosion Resistance

Once the corrosion tests have been completed, they can be analyzed. The results will be compared with literature values on the subject, and a comparison with expected results detailed in the literature review will also be carried out.

3.1.5 Perform Additional Tests to Deepen Understanding of the CGDS Process Applied on a FSW Joint

An interesting proposition occurs from the combination of FSW and CGDS. When the FSW occurs, the temperatures reach a significantly high percentage of the melting point. Should the CGDS process be used immediately after the FSW process, the substrate will still be very hot leading to changes in the coating. It is of interest to analyze the change in coating properties as the substrate temperature is increased. It will be important to have this understanding if this CGDS process is ever to be implemented after a FSW process.

3.2 Secondary Research Objectives #1 – Mechanical and External Variables

While the primary research objectives deal in large part with corrosion performance, there is a need to further and validate understanding of the mechanical properties of CGDS coatings. There is also little information available on the effect of external variables on the coating quality. External variables are not related to the system parameters but can affect the quality of the coating. They include but are not limited to nozzle clogging and thermal losses through the equipment holding the substrate material.

There are many aspects of mechanical properties that can be analyzed. In this case, focus will be placed on the fundamentals and analyze the following factors:

- Adhesion of the coating / substrate interface;
- Hardness;
- Tensile properties of CGDS coatings, as measured by subjecting multiple dogbone-shaped specimens to tension until failure.

The effect of the following external variables on the coating quality will also be inspected:

- Effect of substrate insulation on substrate temperature;
- Effect of nozzle clogging on deposition efficiency.

3.3 Secondary Research Objectives #2 – Nozzle Optimization

The second secondary objectives deal with nozzle optimization. As a secondary research project a study of nozzle optimization was undertaken and presents the following aspects:

- Nozzle design – in depth theory and new nozzle design
- Reducing current nozzle system clogging
- Quantitative performance measurements
    - Powder velocity measurements for quantitative comparison
    - Schlieren imaging for shockwave
    - Coating properties for various nozzles

4 Experimental Research Approach

The present chapter will discuss the experimental research approach used to achieve the previously outlined research objectives. More specifically, this section will describe the equipment used in producing and analyzing coatings.

4.1 Pre-Spray Grit Blasting and Glass Beading

Grit blasting occurs before performing the spray and is a substrate preparation technique. Several types of grit can be used – in this case 80 grit silicon oxide pellets are used. 20 grit copper slag pellets are also available for this purpose for harder substrates and rougher surface finishes. Figure 31(a) and (b) show the 80 grit and 20 grit blasting mediums respectively.

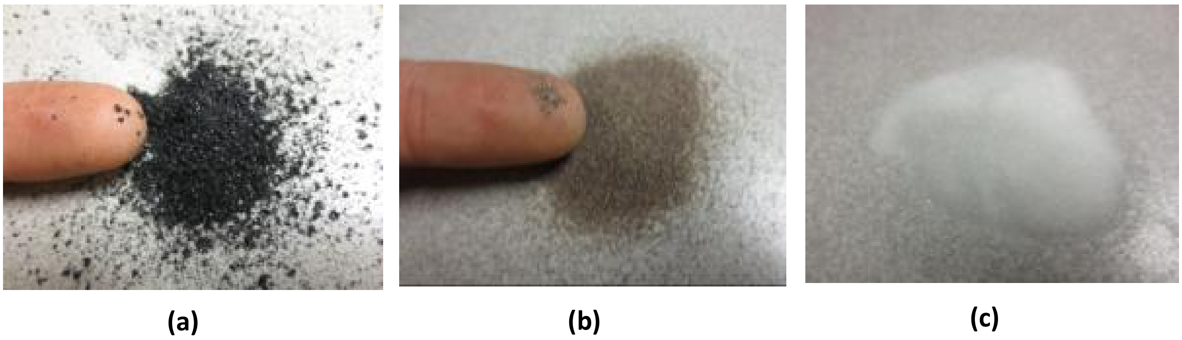
(a) (b) (c)

Figure 31. Blasting Medium. (a) 20 Grit Copper Slag, (b) 80 Grit Silicon Oxide, (c) Glass Beads

Finally, glass beads can also be used. This is mainly a post processing technique used to induce compressive stresses in the coating and create a more uniform surface finish. (Glass beads will create a smoother surface finish due to their extremely small size). Figure 31(c) shows the glass beading material.

Figure 32. Dedicated Grit Blasting Chamber.

These three blasting mediums are used in a dedicated grit blasting chamber (shown in Figure 32). Non-recycled material in loaded into a clean grit blasting gun. A pressure of 60 psi is used to propel the material onto the substrate. The angle of the gun nozzle to the substrate is 45 degrees for best results while minimizing particle embedment. Figure 33, Figure 34 and Figure 35, show typical surface finish results after preparing the surface with glass bead, 80-grit and 20-grit materials respectively. A coarser grit (20) will result in a rougher surface finish. Some 20-grit particles may also embed the surface affecting the adhesion strength of the coating.

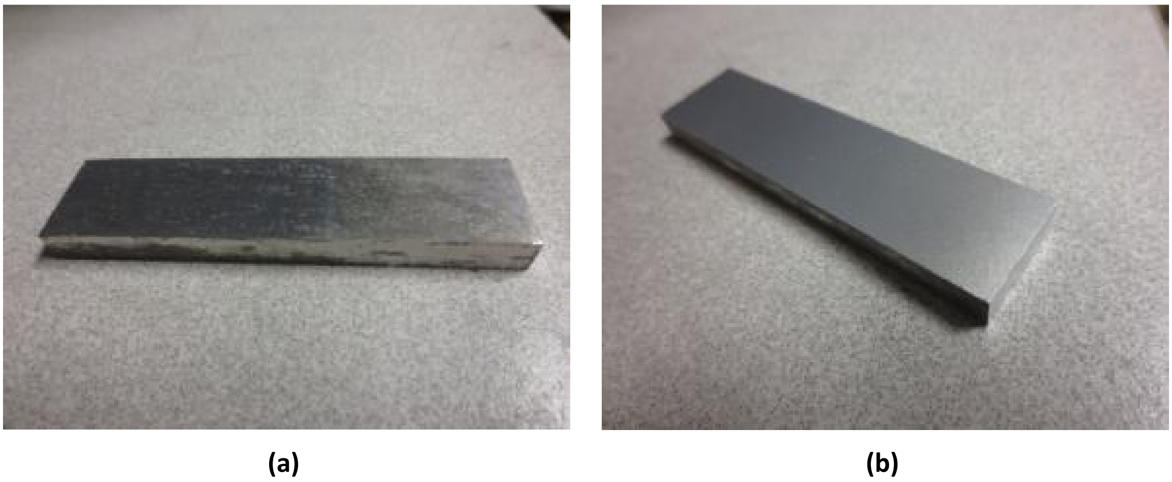

(a) (b)

Figure 33. Bulk Al 7075 Coupon (a) Before and (b) After Glass Beading Process

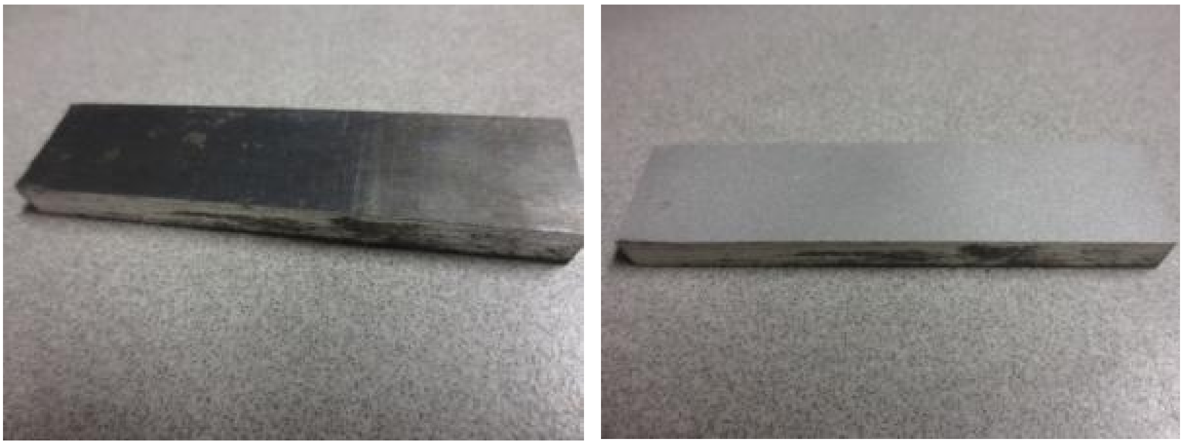
(a) (b)

Figure 34. Bulk Al 7075 Coupon (a) Before and (b) After an 80 Grit Silicon Oxide Sand Blasting Process

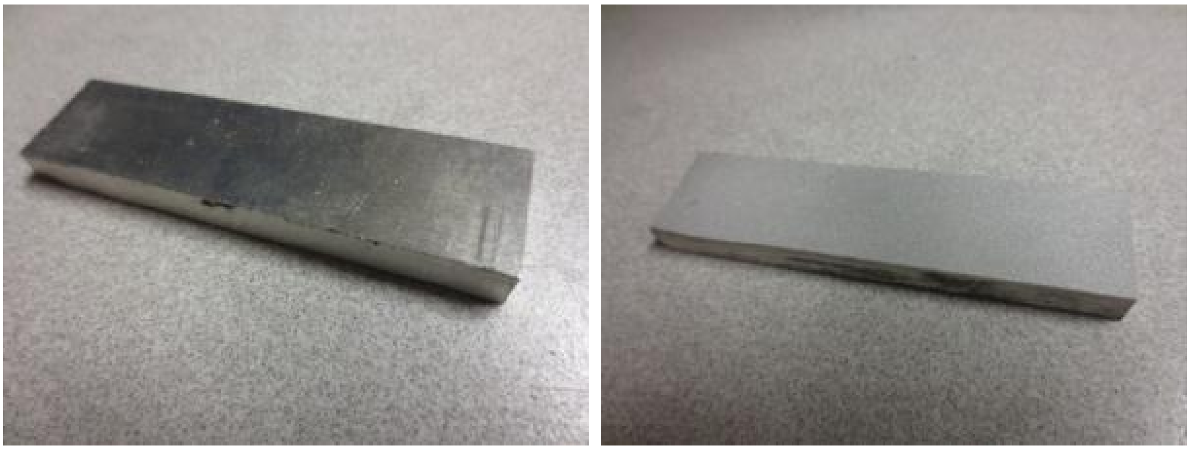
(a) (b)

Figure 35. Bulk Al 7075 Coupon (a) Before and (c) After a 20 Grit Copper Slag Grit Blasting Process

4.2 University of Ottawa Cold Spray Laboratory Facility – Cold Spray System

The cold spray system, as described schematically in Figure 2, is comprised of the propellant gas bottle pack, propellant gas pressure & temperature controller, the heater, the powder feeder, the feeder gas bottle, the de Laval nozzle assembly and the substrate. These components are shown below (from Figure 36 to Figure 43) and a ready-to-spray assembly is shown in Figure 44.

Figure 36. CGDS Equipment Overview

Figure 37. Open Cabinet Assembly. Right Half Contains the CGDS System Spray Booth

Figure 38. Propellant gas Bottle Pack. Consists of 11 Single Bottles. This Gas is Fed to the Pressure and Temperature Controller

Figure 39. Pressure and Temperature Controller Feed Propellant gas to the Heater

Figure 40. Propellant gas Heater. Within the Cabinet Assembly. Powder Feed Tube is Dangling Next to the Heater and Connects to the Nozzle Assembly Powder Inlet Tube

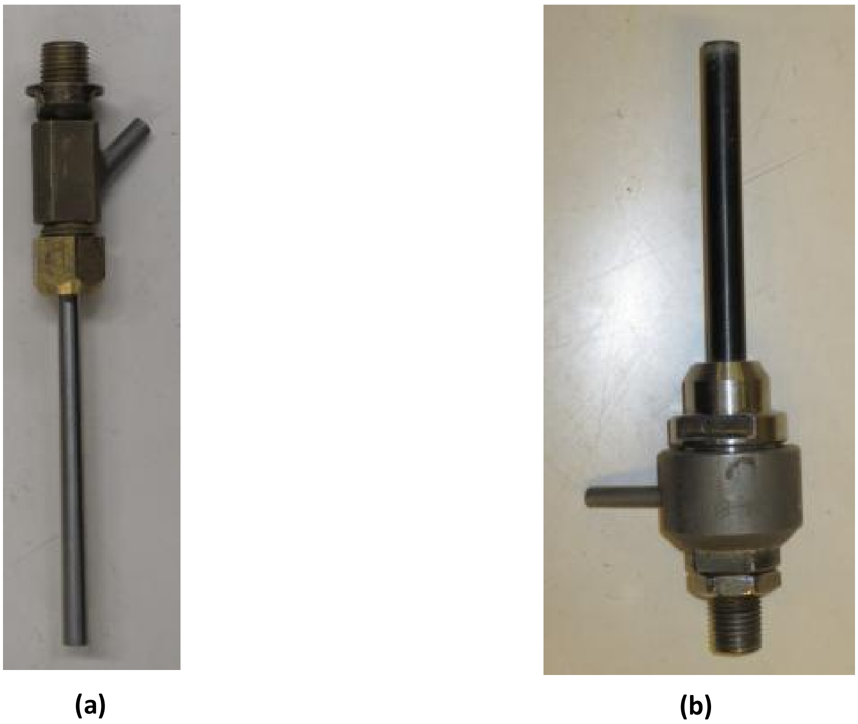

(a) (b)

Figure 41. Assembled de Laval Nozzle. These are screwed into the heater. (a) Stainless Steel Nozzle used for High Propellant Gas Temperatures (Above 350°C) and Hard Materials. Powder Feed Tube at an Angle (b) Polymer Nozzle used for Low Propellant gas Temperatures (Below 350°C) and for Low Hardness Materials. Powder Feed Tube is Horizontal, Bottom Left.

Figure 42. Feeder Gas Bottle. Gas From This Bottle is Fed into the Powder Feeder

(a) (b)

Figure 43. (a) Front View and (b) Side View of a Praxair Powder Feeder. Gas Line is Fed from the Res Line, Powder Exits at the bottom of the Feeder

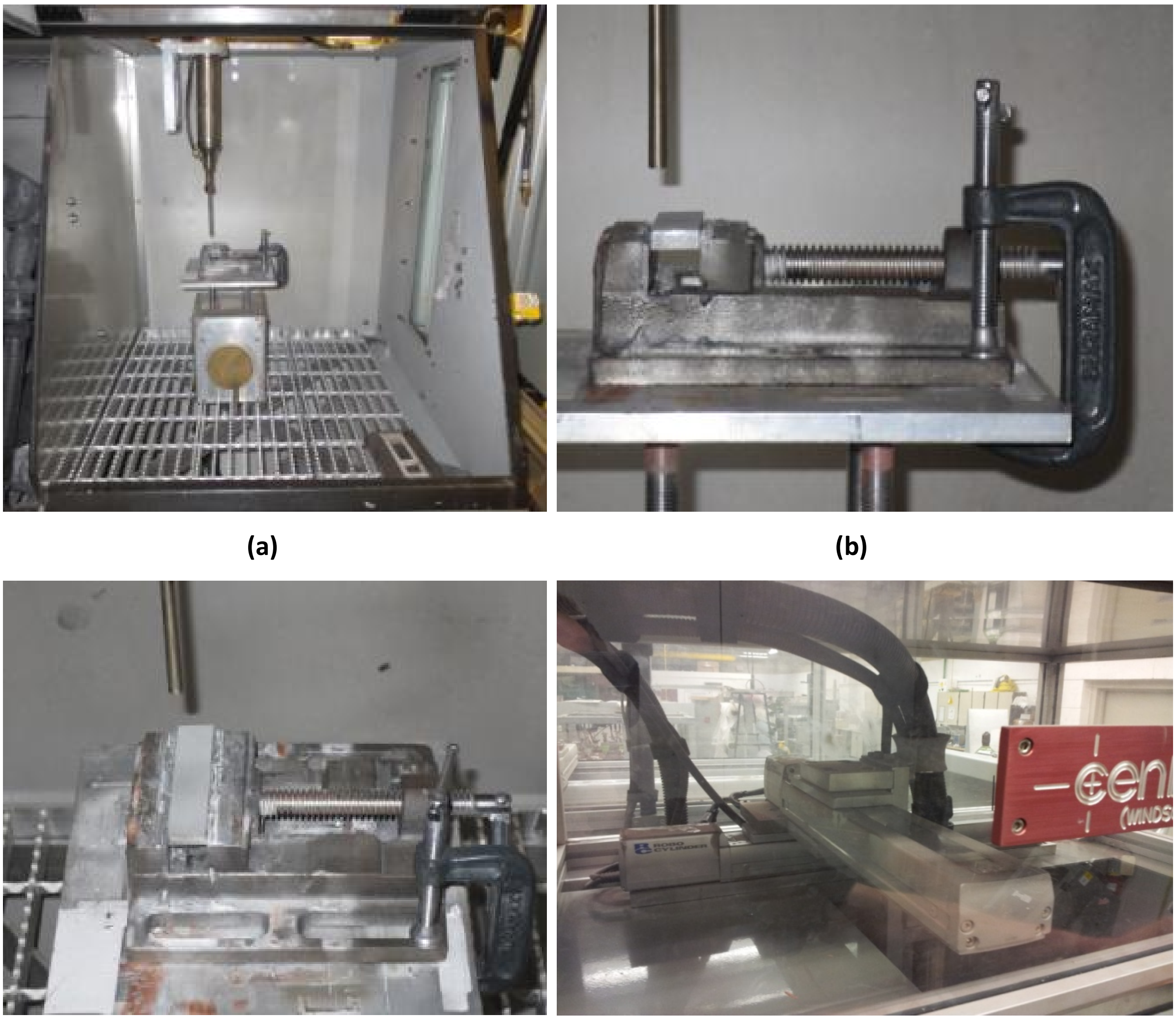

(a) (b)

(c) (d)

Figure 44. Substrate Setup, Ready to Spray. Substrate is Mounted onto a Vise Secured to a Jack with a C-Clamp. (a) General Layout, (b) Side Close-Up, (c) Top Close-Up (d) Programmable X-Y Robot on Top of Cabinet

4.3 University of Ottawa Cold Spray Laboratory Facility – Sample Processing

To be able to measure the coating's properties, sample cross sections must be easy to inspect optically. To do this, a cross section of a sprayed coating is cut, then mounted it inside a polymeric cylinder. Finally samples are polished for analysis. The cutting, mounting and polishing process are described in this section.

4.3.1 Cutting Process

Using a Struers Secotom-10 cutting machine, samples are cut once or many times to obtain a piece of coating and substrate that is less than approximately 19 x 15 x 7 mm (Sample must fit inside a 25.4mm diameter area). To perform the cuts correctly, the correct cutting wheel and cutting speed must be used to prevent equipment or coating damage. Figure 45 and Figure 46 present the cutting machine as well as an example of a coating after the cutting process.

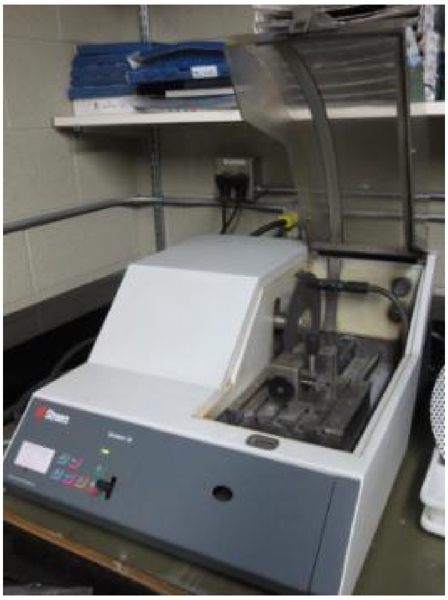

Figure 45. Struers Secotom-10 Cutting Machine

Figure 46. Typical Example of Sample After Cutting Process. Note the Aluminum Coating on Top (Pure Al) and the Saw Marks on the Cut Side (Facing Front). Sample is ¾" wide

4.3.2 Mounting Process

Once the sample is ready for mounting, there are two options. If the sample is temperature-sensitive, as in the case of carbon-fibre substrates or polymeric coatings, the sample will be cold-mounted. This involved surrounding the sample in a transparent epoxy and waiting for it to set. This process is called cold-mounting. However, in most cases, samples will be hot mounted. This involved placing the sample on the surface of a Struers LaboPress-3 mounting machine (See Figure 47). The sample is then surrounded with a polymeric powder, compressed and melted at the correct parameters. Once the polymer is set, the result is a small cylinder with the observable coating on one side. See Figure 48 below for more detail.

Figure 47. Struers LaboPress Mounting Machine

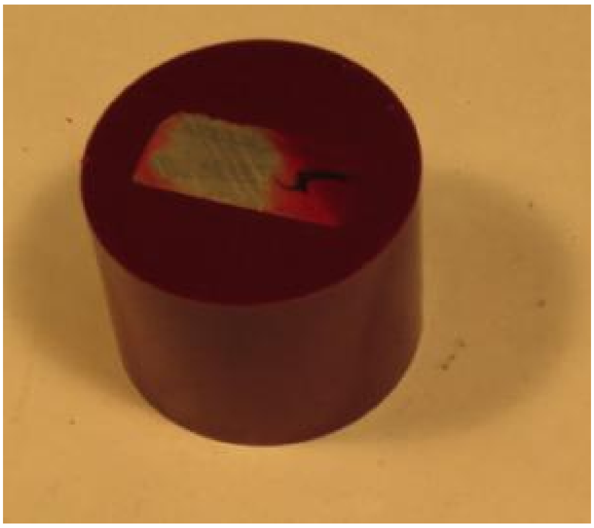

Figure 48. Example of a Typical Sample after the Mounting Procedure. Cut Side is Facing the Outside of the Mount - Coating is Visible on Top. Some Mounting Material has Flowed on Top of the Piece During the Mounting Procedure - This will be Removed During the First Polishing Step

4.3.3 Polishing Process

After mounting, the coating can be seen (unless very thin) but cannot be analyzed yet. This is because the surface is too rough for optical inspection. In order to get the required surface smoothness, the sample is polished in multiple steps with a Struers TegraPol-31 polishing machine. The polishing steps will depend on the coating material, but the goal is to use progressively finer polishing wheels (along with their polishing fluid) to reduce the surface roughness to an acceptable value of around 0.5 µm, the surface roughness of the finest polishing wheel. Figure 49 below illustrate the polishing steps for an Aluminum alloy. Figure 50 shows the Struers polishing machine.

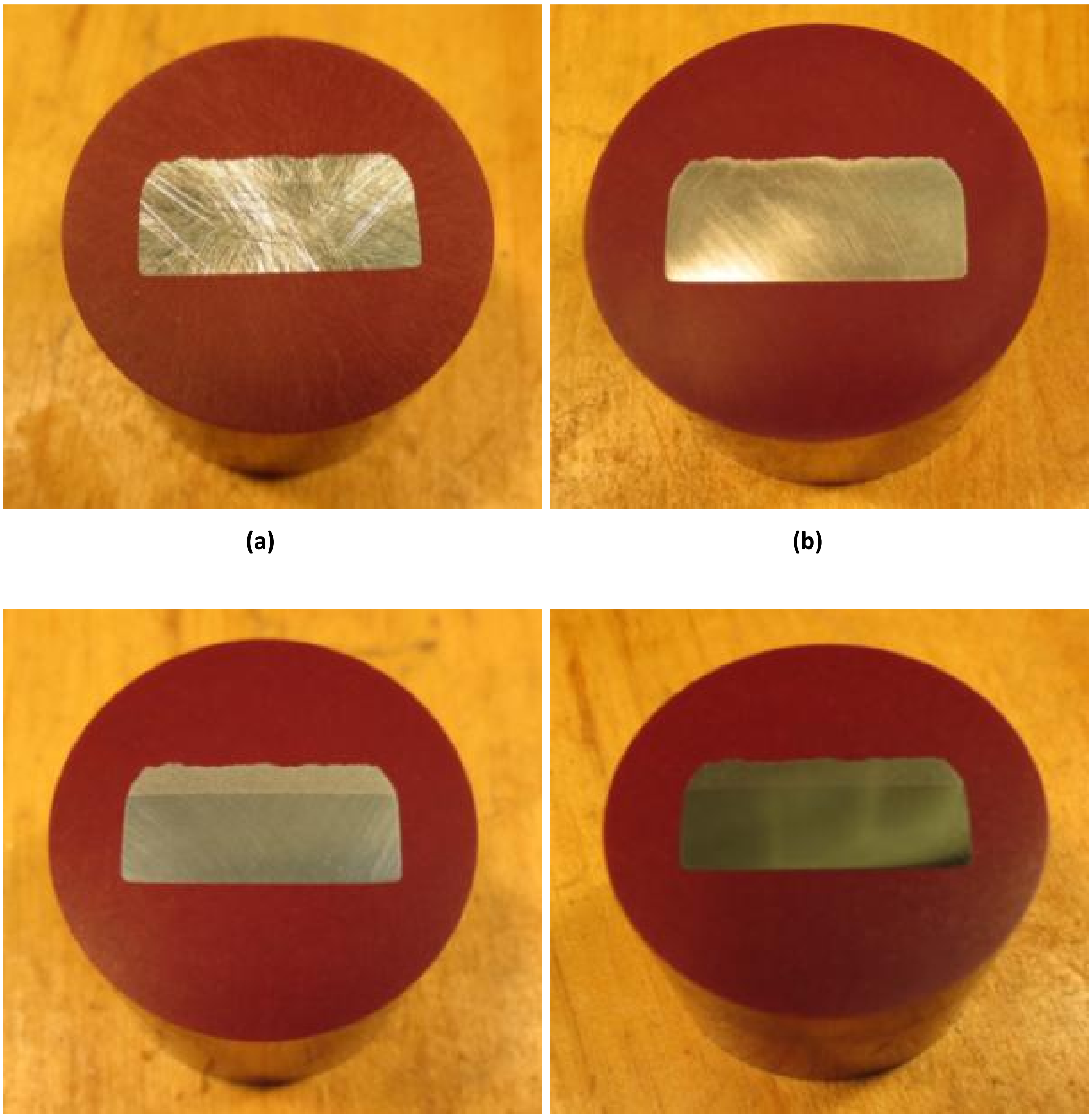

(a) (b)

(c) (d)

Figure 49. Aluminum Polishing Steps. (a) Piano 120 Grinding Wheel, Water. (b) Largo Grinding, 9µm Solution. (c)Mol Polishing, 3µm Solution. (d) Chem Polishing, 0.5µm Solution and Water

Figure 50. Struers Tegra-Pol Polishing Machine

4.4 University of Ottawa Cold Spray Laboratory Facility – Sample Analysis

Once the coating has been cut, mounted and polished, it can be analyzed objectively using analysis tools to determine its properties. Several analysis tools are used. A Vickers indenter machine is used to measure the coating hardness. An optical microscope (along with an image processing software as shown in Figure 51) allows us to measure the coating thickness and porosity. A scanning electron microscope (SEM) can also be used to take very precise optical imagery.

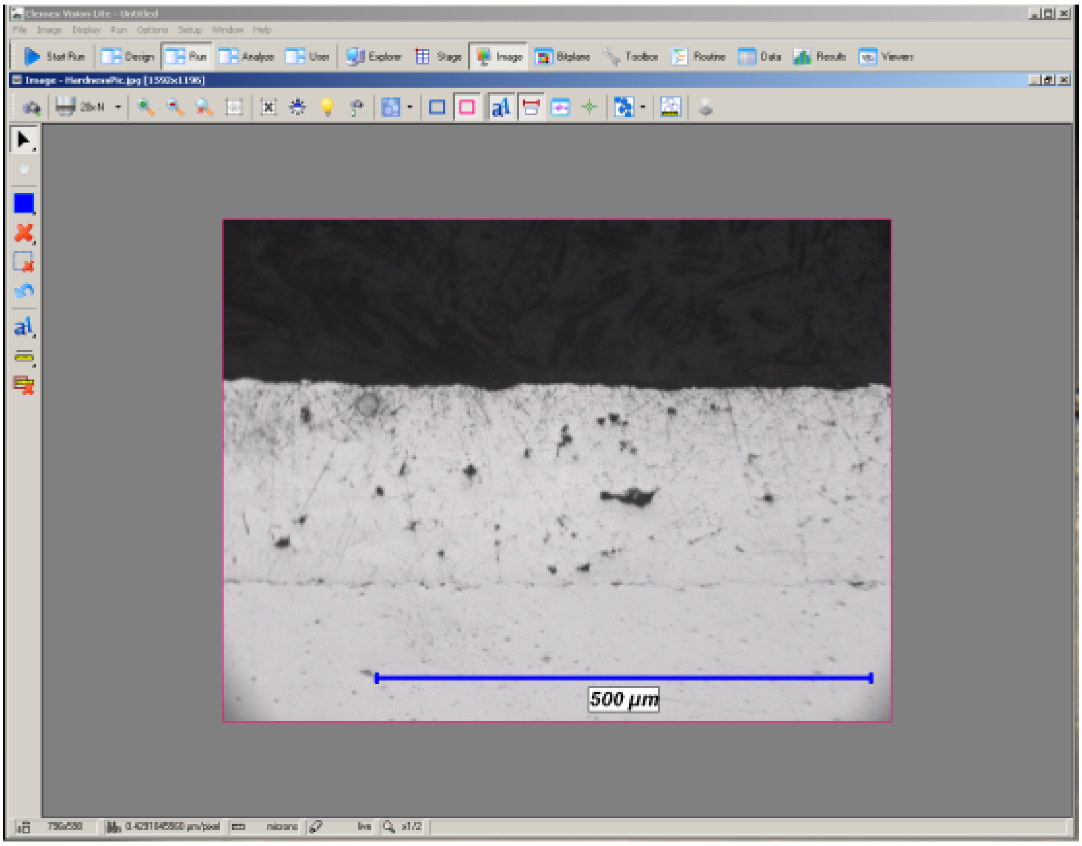

Figure 51. Clemex Vision Lite Image Analysis Software Screenshot

4.4.1 Hardness Testing

If particles are more deformed, the work hardening of the particle is increased, increasing the hardness of the coating. This can be either beneficial or detrimental depending on the desired outcome of the coating; however it is indicative of a better spray quality. Hardness can be measured in coatings as thin as 25 to 100 µm with the help of a Struers Duramin micro-hardness meter (see Figure 52). This is a machine that can be used once the coating has been cut, mounted and polished. It makes small diamond-shaped indentations in the coating using a constant weight. The larger the resulting indent, the softer the material. By measuring the size of the indent, a harness value can be calculated. Figure 53 shows an indent in a pure aluminum coating.

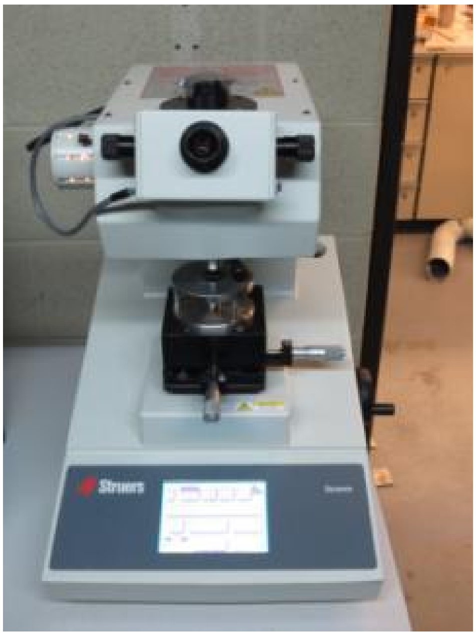

Figure 52. Struers Duramin Hardness Testing Machine

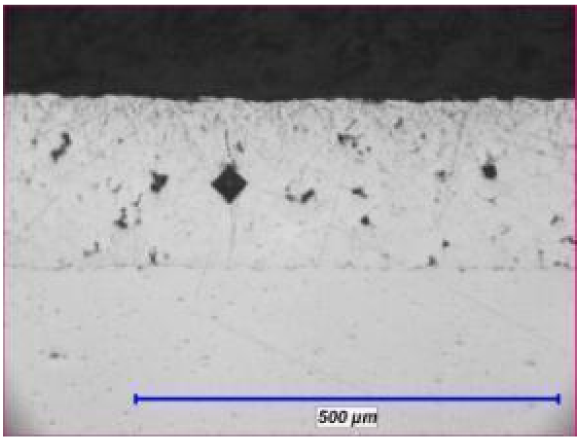

Figure 53. Example of a Vickers Microhardness Indent Performed on a Pure Aluminum Coating

4.4.2 Optical Microscopy Image Analysis

Any optical microscope can be used for qualitative analysis. However, for quantitative measurements, an optical image analysis software is used to process the images. The software used is Clemex Vision Lite. This software can perform many different image analysis functions. The ones used were thickness analysis and porosity calculations.

Thickness Evaluations: For the same porosity value and travel speed across the substrate, thickness is proportional to deposition efficiency. This is because a higher DE results in a thicker coating per pass. Comparing an increase in coating thickness is analogous to comparing an increase in DE. Thicknesses between 15 and 1000 µm can be measured with the optical microscope, using the Clemex Vision Lite tool to make measurements. Figure 54 shows a typical coating thickness measurement.

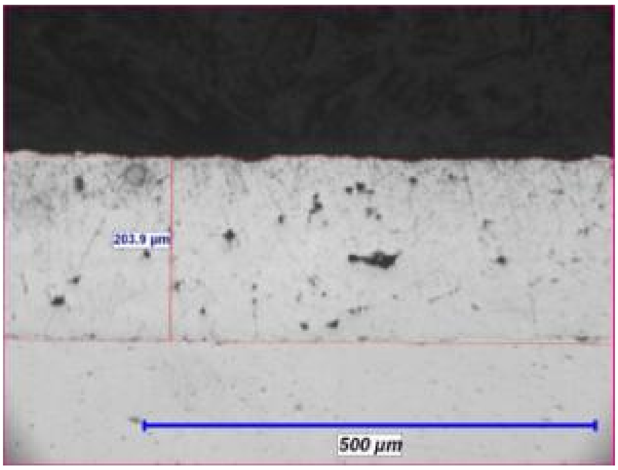

Figure 54. Example of a Thickness Measurement on a Pure Aluminum Coating Approximately 200 µm Thick

Porosity: In most cases, porosity is an indication of poor coating quality. Porosity occurs when particle do not deform enough to morph to a surface, leading to voids inside the coating. Porosity is detrimental to the coating in many ways, including to its strength and corrosion properties. Porosity is measured in terms ratio of voids to dense material. This is done with the help of the Clemex Vision Lite optical microscope analysis tool. Typical porosity values range from full dense (0%) to 10%. See Figure 55 and Figure 56 for different coating porosity examples.

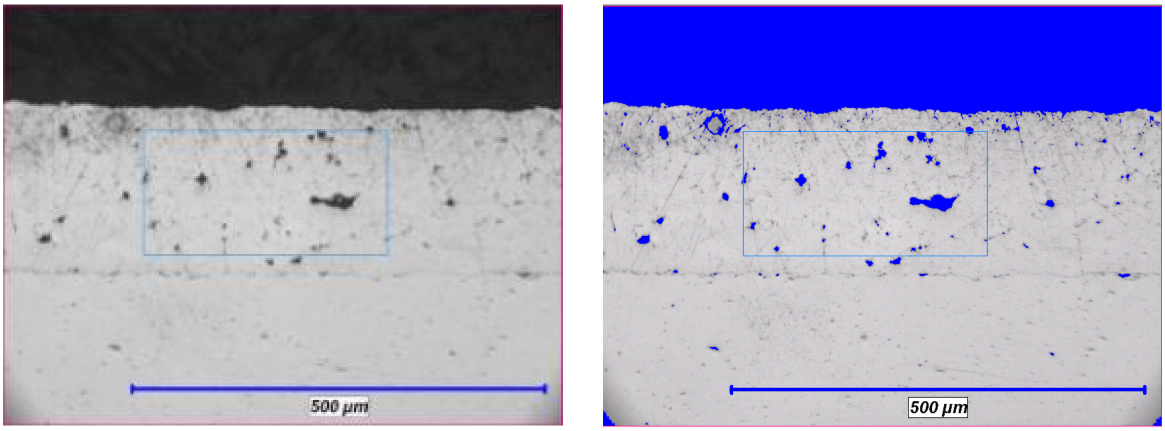

(a) (b)

Figure 55. Example of a Porosity Analysis. (a) Step 1 of the Analysis - Select Analysis Region (Square Region within Coating). (b) Modifying the Grayscale Factor to Select the Entire Dark Region Sections Consistent with Porosities. Porosity Output is Area Ratio of Grayscale Selection to Total. Total Porosity here is between 2 and 4%

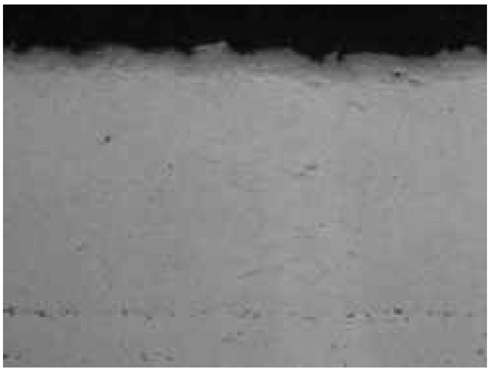

Figure 56. Example of a Fully Dense Al 7075 Coating, 100x, 590 μm Thickness

4.5 In-House Corrosion Testing

Two corrosion tests were performed in-house. They are the ASTM G34 and ASTM G110 corrosions. Both these tests were selected due to their simplicity and ease of testing. Unlike other tests that require environmental chambers to change environments (from humid, to wet, to dry) over multiple cycles, these two tests are immersion only. They only vary in the immersion solution and in thhe required testing time and solution temperature. A testing apparatus was designed and built for these two tests. (Figure 57 to Figure 59) It consists of a temperature-controlled test basin. The basin has a heated flexible pad glued underneath it. A thermometer passing through the lid (which prevents evaporation –see Figure 60) measures the temperature of the immersion fluid within the basin and relays this information to the control system. The control system adjusts the power delivered to the heated pad in order to maintain the desired immersion fluid temperature to within 2 degrees Centigrade.

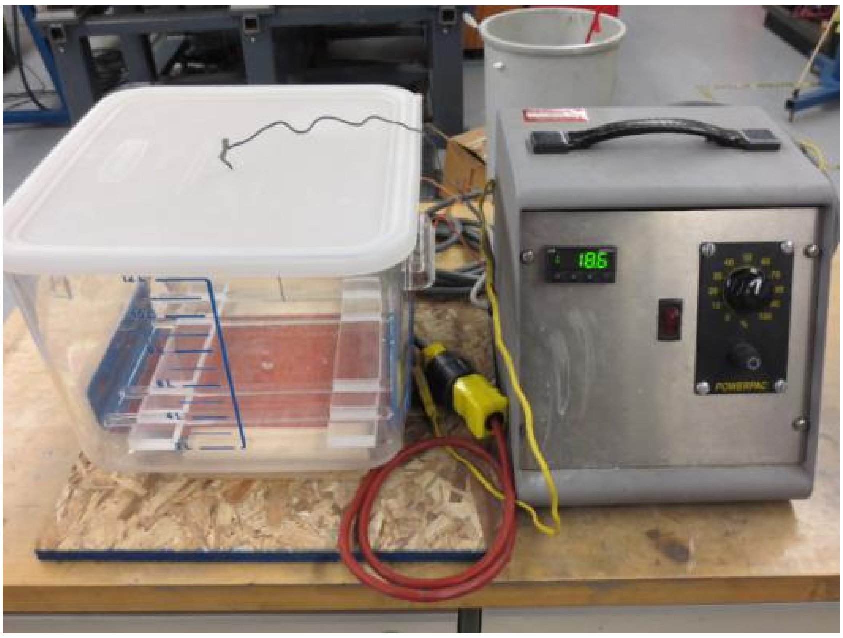

Figure 57. In-House Corrosion Test Apparatus, Showing Control System (Right) and Test Basin (Left)

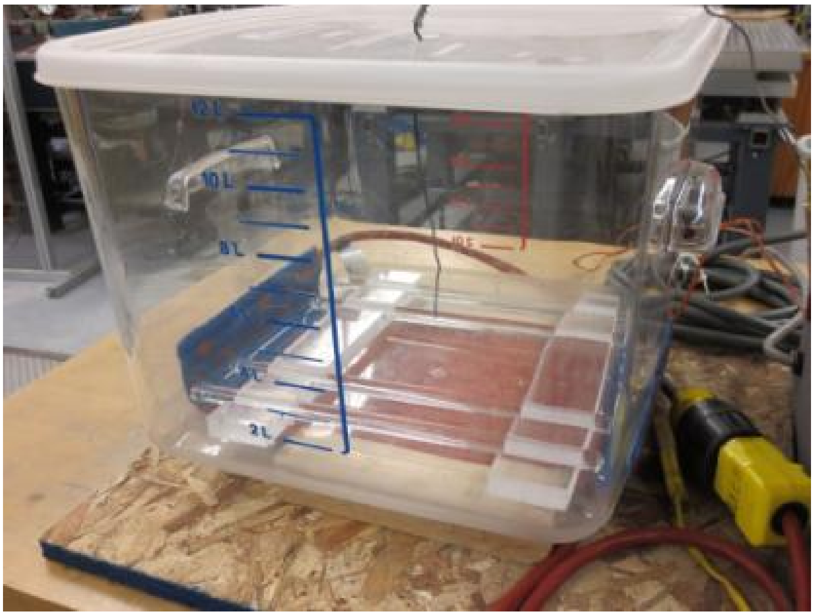

Figure 58. Corrosion Tests Apparatus Thermocouple Placement during Tests

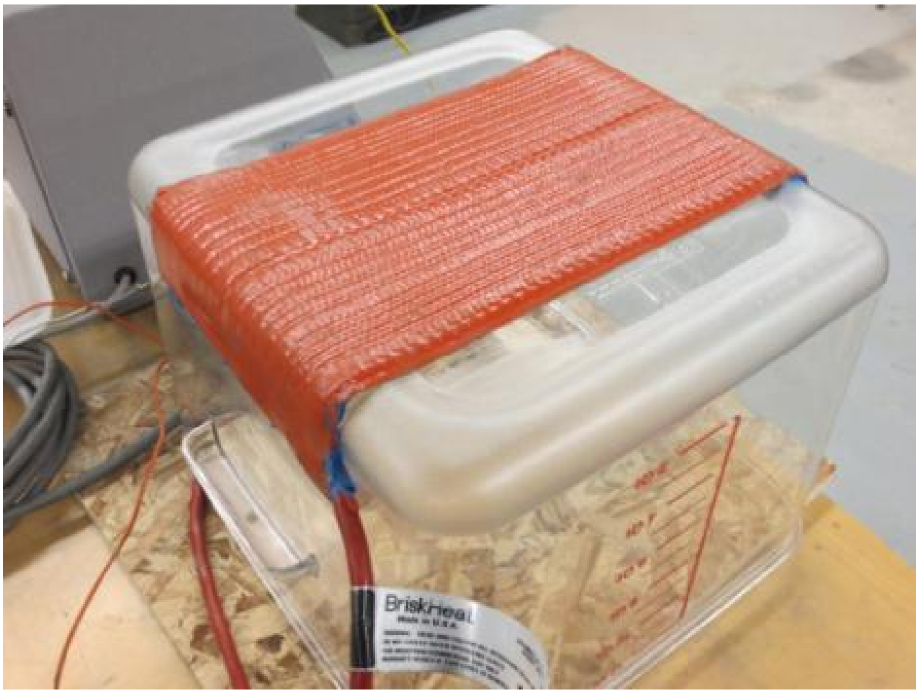

Figure 59. Corrosion Test Apparatus Glued Heated Pad

(a) (b)

Figure 60. Thermocouple and Lid Assembly. (a) Lid Showing Thermocouple Entry Hole. (b) Thermocouple Passing Through the Lid. Hole is Tight Enough to Hold the Thermocouple in Place

Inside the test basin, as shown in Figure 61 two notched acrylic pieces hold 4 glass rods. The test samples are placed on these glass rods. This minimizes the contact surface and allows the samples to rest horizontally with the test surface facing up.

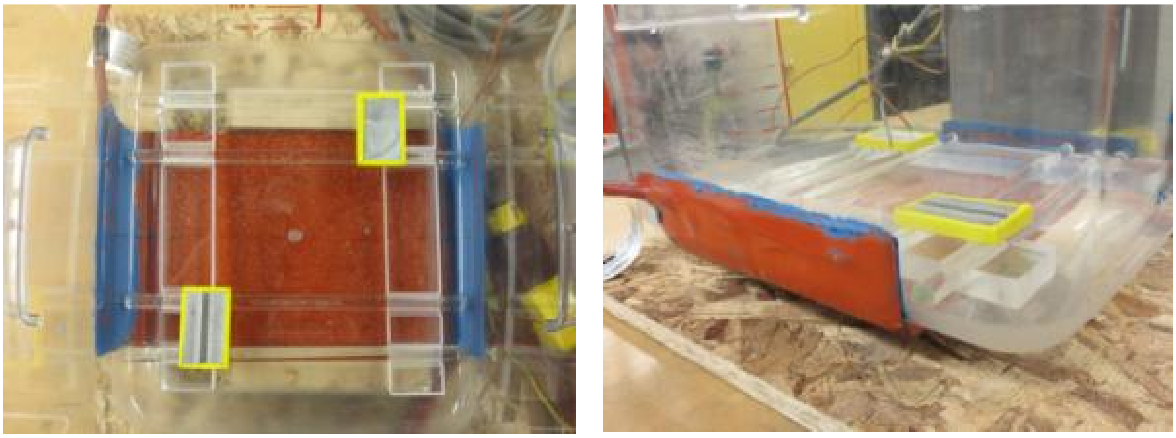

(a) (b)

Figure 61. Corrosion Test Basin Support System. Notched Acrylic Pieces Hold Glass Rods which Support the Samples. (a) Top View. (b) Side View

5 Feedstock Powder Characterization

To be able to make decisive conclusions about the coatings produced, there must be information on the powder used to create them. This section will provide information on the feedstock powder.

Since this project is commercially involved, only commercially available powders will be used. This ensures that once the project is adopted in the industry, the process can be replicated on a large scale with commercially available equipment and materials.

5.1 Al 7075

The metallurgical composition of Al 7075 is listed in Table 9.

Table 9: Metallic Composition of Al 7075

Metal	Composition (%)
Aluminum	85.5 - 91.6
Zinc	5.1 – 6.1
Magnesium	2.1 – 2.9
Copper	1.2 – 2.0
Iron	0.5 max
Chromium	0.5 max
Manganese	0.5 max
Silicon	0.5 max
Titanium	0.5 max

Please note that the powder produced is not heat treated. The alloying elements are present in solid solution in this powder. Therefore, without annealing, the powder properties are relatively low as shown in Table 10.

Table 10. Al 7075 Mechanical Properties Comparison for the O (Annealed, Solid Solution) and T651 Tempers [49]

Property	Al 7075 - O	Al 7075 – T651
Hardness (Vickers)	68	175
Ultimate tensile strength (MPa)	228	572
Elongation at break (%)	16-17	11
Shear strength (MPa)	159	331

The supplier used for this powder is Valimet (Stockton, CA 95206). They supply a 200-mesh gas atomized Al 7075 powder creating spherical powder morphology as showed in Figure 62.

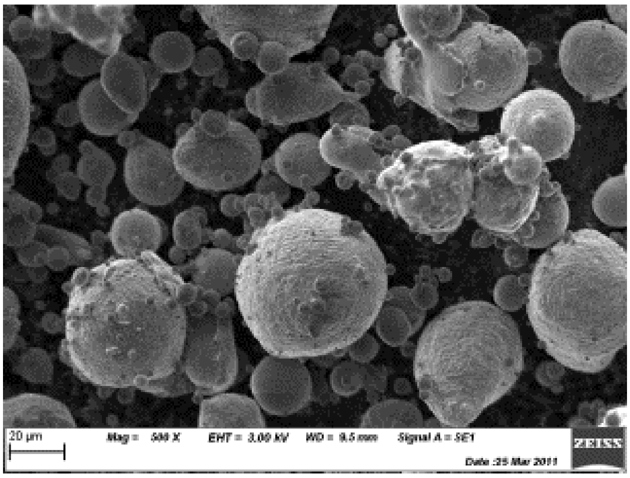

Figure 62. SEM Image of Valimet 200-Mesh Al 7075 Powder Showing a Spehrical Powder Morphology

As Figure 62 shows, this powder exhibits spherical particles, with a large percentage of them being in the 40 to 50 µm range. There are many small particles in the nanometre scale. To better quantify this analysis, a particle size distribution was carried out on this powder. The analysis was performed with a Microtrac S3500 laser diffraction particle size analysis machine. This machine shines a laser through a vial containing the powder in liquid suspension. An optical sensor records the amount of diffraction within the vial, and a particle size is calculated based on this value. Results are presented in Figure 63.

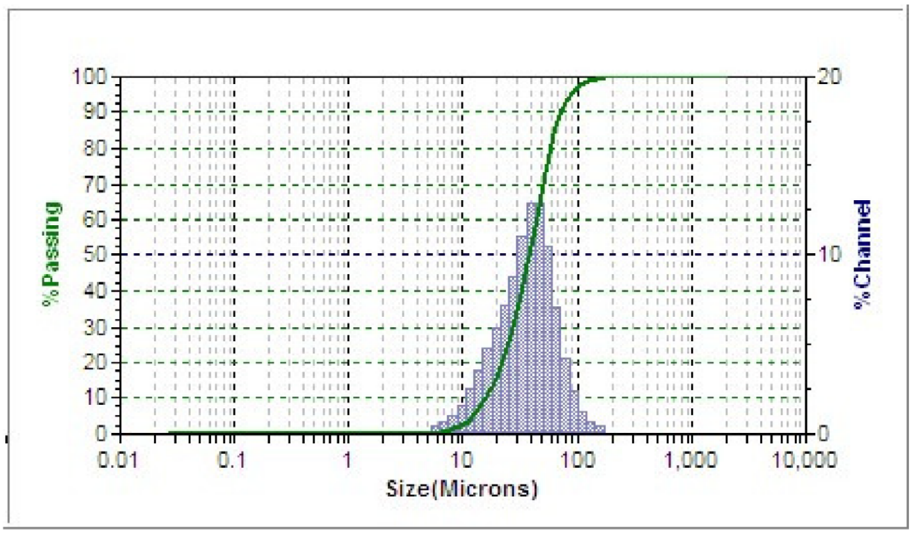

Figure 63. Al 7075 Particle Size Distribution Analysis Performed at the Geology Department of the University of Ottawa

The analysis shows a narrow particle size distribution between 10 and 100 µm. The peak average is 38 µm. A second analysis was performed (not shown) indicating an average particle size of 42 µm. The difference is due to a combination of sample batch and machine error.

5.2 Al 5083

The same analysis procedure was carried out for the Al 5083 powder. A typical composition for Al 5083 is shown in Table 11 below.

Table 11: Metallic Composition of Al 5083

Metal	Composition (%)
Aluminum	92.35-95.55
Chromium	0.05 - 0.25
Copper	0.1 max
Iron	0.4 max
Magnesium	4 - 4.9
Manganese	0.4 - 1
Remainder Each	0.05 max
Remainder Total	0.15 max
Silicon	0.4 max
Titanium	0.15 max
Zinc	0.25 max

This alloy's strength comes in solid solution. Therefore the powder is hard as compared to pure Al and even Al 7075 powders (87 Hv compared to 68 Hv for Al 7075-O). This powder has the same supplier as the Al 7075 powder (Valimet), and has the same 200-mesh size, gas atomized properties. An SEM image of the power is presented in Figure 64.

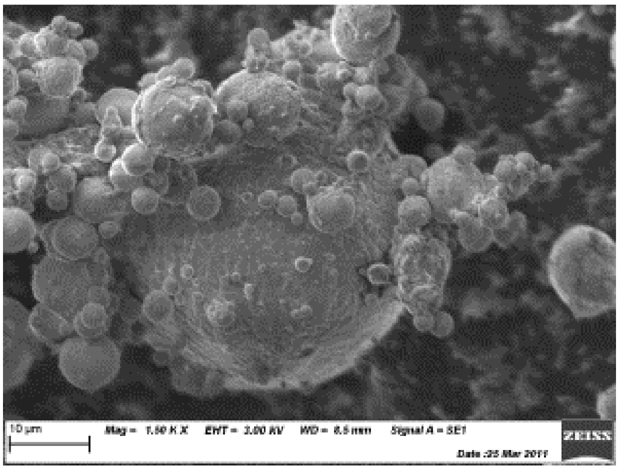

Figure 64. SEM Image of Valimet 200-Mesh Al 5083 Powder Showing a Spehrical Powder Morphology

In this case, there is a large distribution in particle size. This was confirmed with a particle size distribution analysis shown in Figure 65.

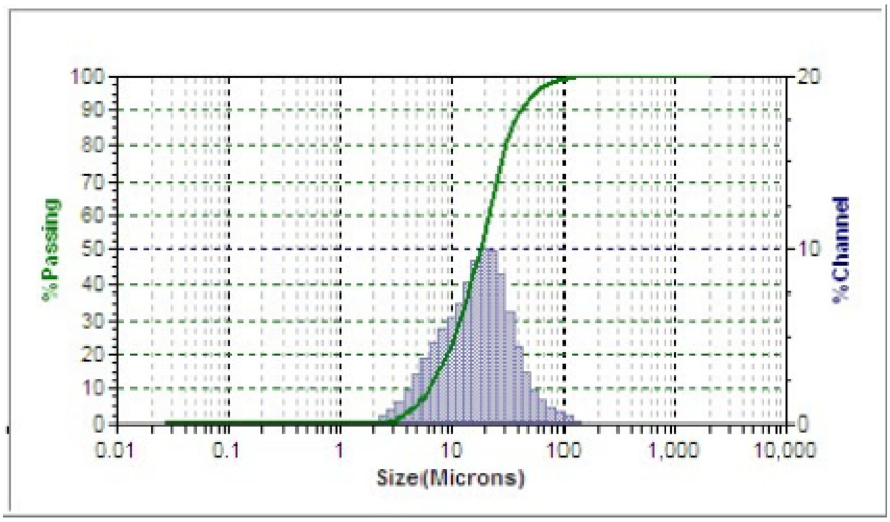

Figure 65. Al 5038 Particle Size Distribution Analysis Performed at the Geology Department of the University of Ottawa

The distribution is much wider than the previous powder. The peak average is 18 µm. A second analysis confirmed this value.

5.3 SST 5001 (Centerline Pure Al)

The last powder used to create metallic coatings is pure aluminum. The specific powder is Centerline power SST-5001. An SEM image of this powder is shown in Figure 66.

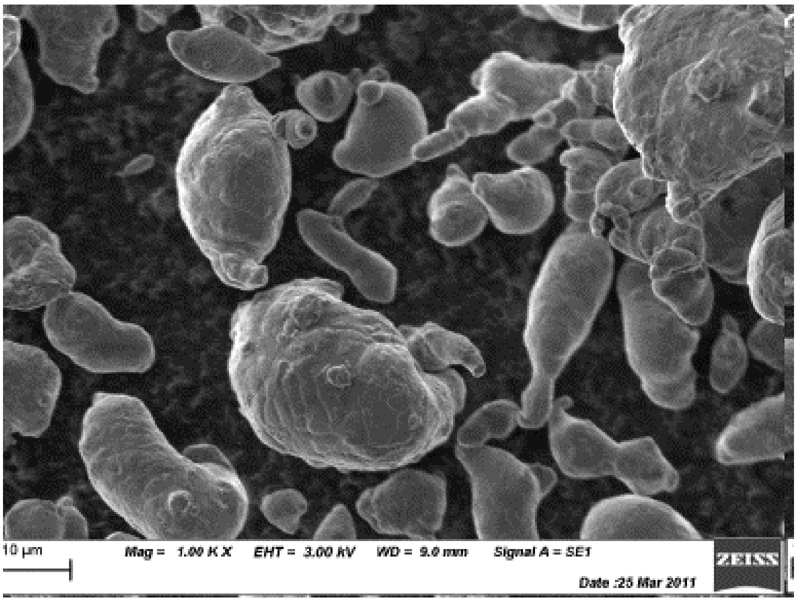

Figure 66. SEM Image of the Centerline SST-5001 Pure Aluminum Powder, Showing Elongated Powder Morphology

Although not explicitly stated by Centerline, the powder morphology indicates that this powder was water atomized. A particle size distribution for this powder is presented below. There is a relatively small distribution (Figure 67) similar to the one for Al 7075. However, the peak particle average is 25 µm.

Typically, for the same volume, particles with elongated shapes will have higher drag. This is due to higher skin drag due to higher surface area per unit volume. This is beneficial to particle speed and to overall coating. Therefore, out of two powders with the same average particle diameter, often the best performing powder will be the one with elongated morphology. However, since the goal of this study is to use commercially available powders, this effect was not investigated.

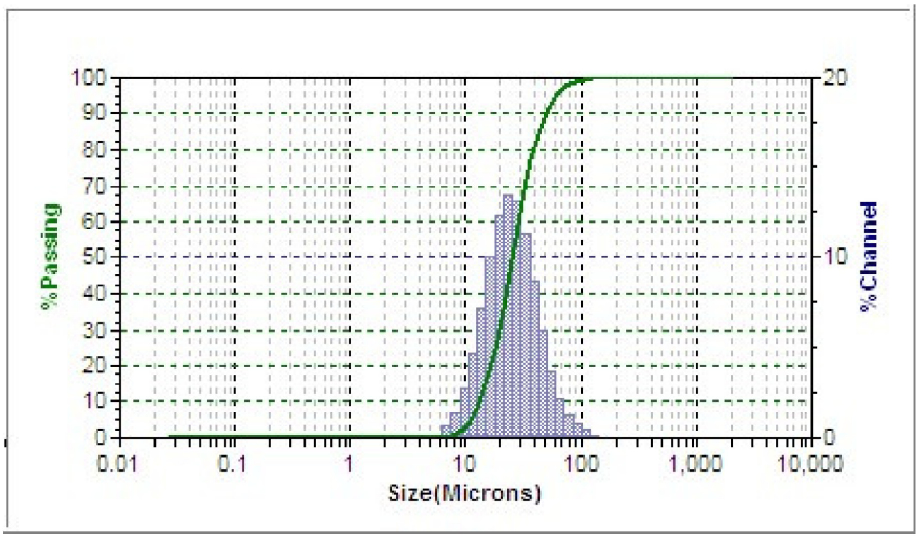

Figure 67. Pure Al Particle Size Distribution Analysis Performed at the Geology Department of the University of Ottawa

5.4 Summary

The powder information is summarized in Table 12.

Table 12. Summary of Important Information Concerning the Three Metallic Used to Create Coatings in this Study

Parameter	Al 7075	Al 5083	Pure Al
Supplier	Valimet	Valimet	Centerline
Product Code	Al 7075	Al 5083	SST-5001
Atomizing	Gas	Gas	Water
Powder Morphology	Spherical	Spherical	Odd-shape, elongated
Peak Average Size (µm)	38-42	18	25

6 Primary Research Objective: FSW Corrosion Protection

This section covers, as described in chapter 3, the primary research objectives. Each subsection presents one or two of the research objectives, the process generated to accomplish them and the results from the experiments.

The work to be completed was divided into four sections: Phases 1.1, 1.2, 2 and 3. They are schematically illustrated in Figure 68. Phase 1.1 is an evaluation phase, which includes testing FSW joints, performing preliminary process feasibility and a preliminary study of the effect of the spray process parameters on commercially available ¾” Al 7075 bars cut into 3” coupons. It also includes an analysis of FSW joint microstructure. Phase 1.2 involves testing the feasibility of spraying optimized coatings on FSW joints and verifying that the coating properties remained unchanged. Phase 2 involves the qualification of the optimized coating against metrics of corrosion, adhesion, etc.

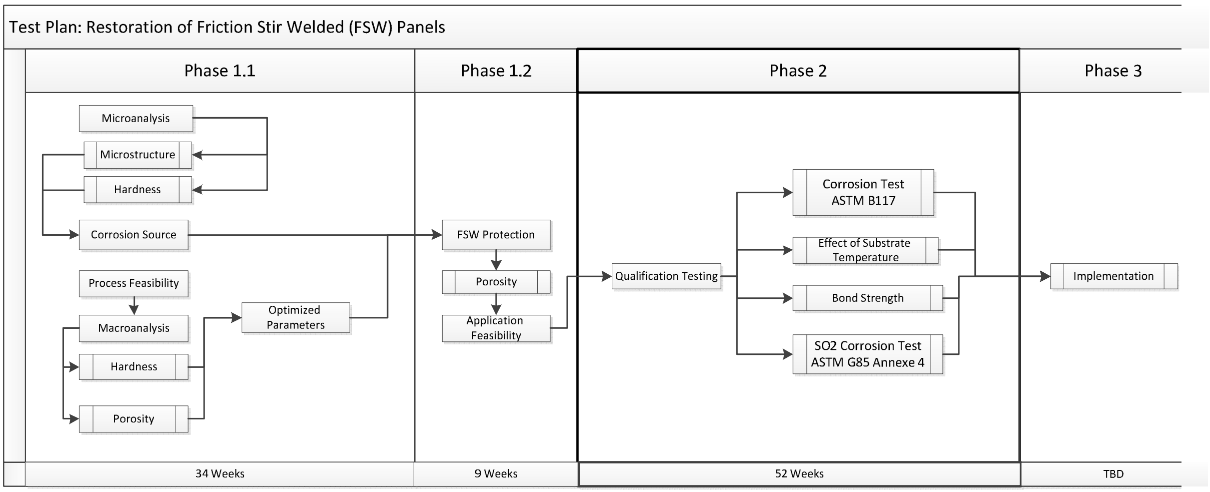

Figure 68. Overall Project Test Plan

6.1 Phase 1.1: Process Feasibility and Parameter Optimization

This phase will determine the most suitable parameters that should be used to achieve the best aluminum and aluminum alloy coatings possible. The spray parameters that will be studied are: gas pressure, gas temperature, standoff distance and nozzle travelling speed (or traverse speed). At the end of this phase, the best spray parameters will be identified based on coating porosity and thickness (i.e. deposition efficiency). An investigation on the weld joint will be performed. This will confirm the corrosion properties of the received plates to be as presented in the literature review.

6.1.1 Confirm Theory for Reduction in Corrosion Performance

As described in section 2, there is preferential corrosion at the weld joint because pitting occurs preferentially at precipitate-free, copper depleted zones in the weld nugget and HAZ. This leads to a propagation of the corrosion through the coarse precipitates at the grain boundaries (i.e. intergranular corrosion). High angle grain boundaries as observed in the TMAZ are also more prone to corrosion. Finally, a reduction in hardness due to precipitate coarsening (even though grain size reduction occurs through dynamic recrystalization) leads to preferential stress corrosion cracking. To confirm these statements the FSW joints will be inspected.

For the use of testing corrosion protection methods, The Boeing Company provided us with simulated FSW joints. These joints do not joint two plates but are rather performed on a single thick plate – the tool is inserted into the plate (without reaching the bottom) and the tool is advanced forward to create a simulated weld joint. There were 6 sample joints per plate, with a weld joint of 10mm and a spacing of 5mm between joint extremities. Figure 69 shows the plates as-FSW and after a grinding process (using an abrasive grinding tool to blend the as-FSW joints). A total of 5 plates of each type were received.

(a) (b)

Figure 69. FSW Plates (a) As-FSW Plate Showing the 6 Weld Joint Lines. (b) Grinded Plate Showing a Blended Surface

Transverse cross sections of the as-FSW joints were analyzed for microstructure and hardness. Etched cross-sections (Figure 70 and Figure 71) revealed a fine equiaxed grain structure within the weld nugget. (Annotated cross-sections are shown in Figure 72 and Figure 73 outlining the FSW regions that are seen in the optical microscope photographs.) Using a large magnification it is possible to establish that the recrystalized grains are approximately one order of magnitude smaller than the parent material which exhibits large and elongated grains typical of hot rolled plates. The shape of the weld nugget is clearly distinguishable - the width of the shoulder where the nugget increases in size near the top of the substrate is noticeable. The TMAZ (at the weld nugget / HAZ interface) also shows signs of plastic deformation through grain reorientation, a clear sign of residual stresses and mechanical hardening.

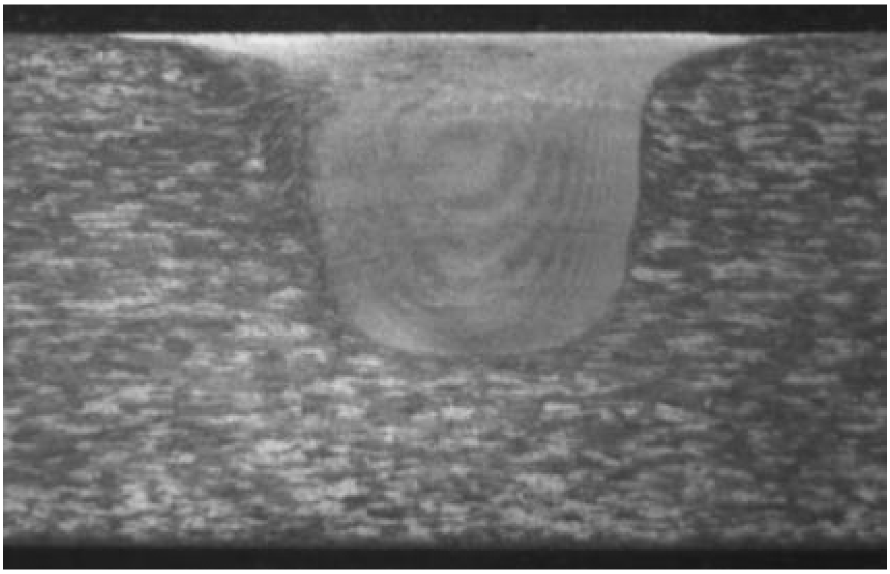

Figure 70: Etched FSW Al 7075 Cross Section, General View. Another Friction Stir Weld Joint Begins Almost Immediately Off The Edge of this Picture

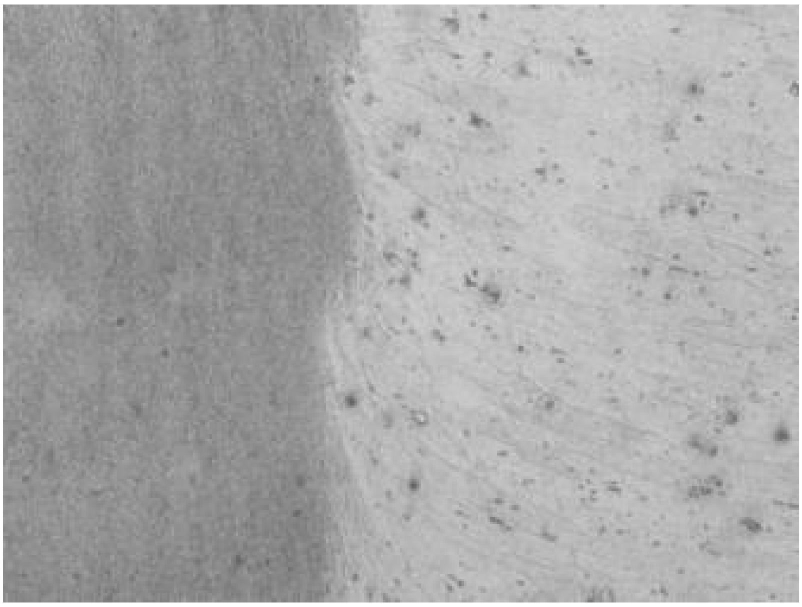

Figure 71: Close-Up view of an Etched FSW Al 7075 Showing Transition from TMAZ (Center) to Nugget (Left). Notice the Grain Plastic Deformation at the Interface and the Large Difference in Grain Size

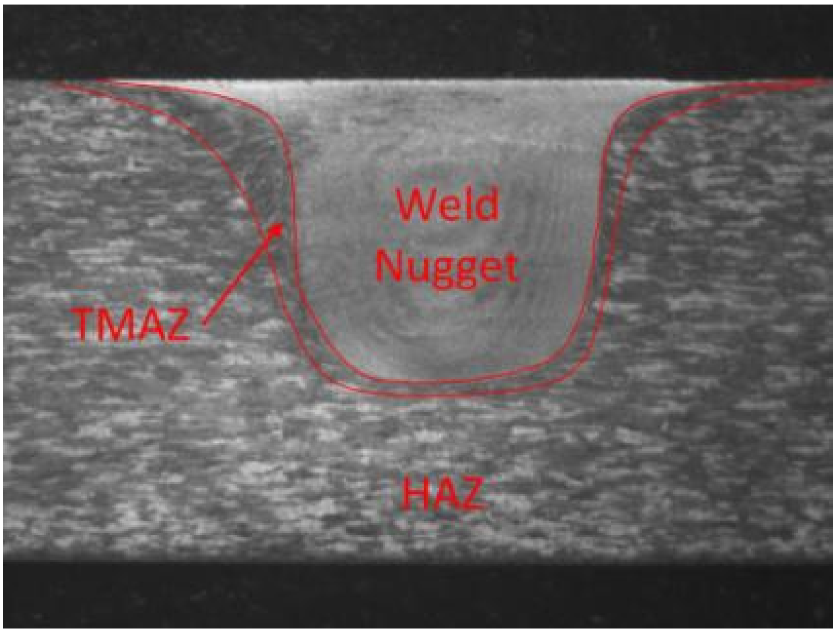

Figure 72: Figure 70 with Annotations

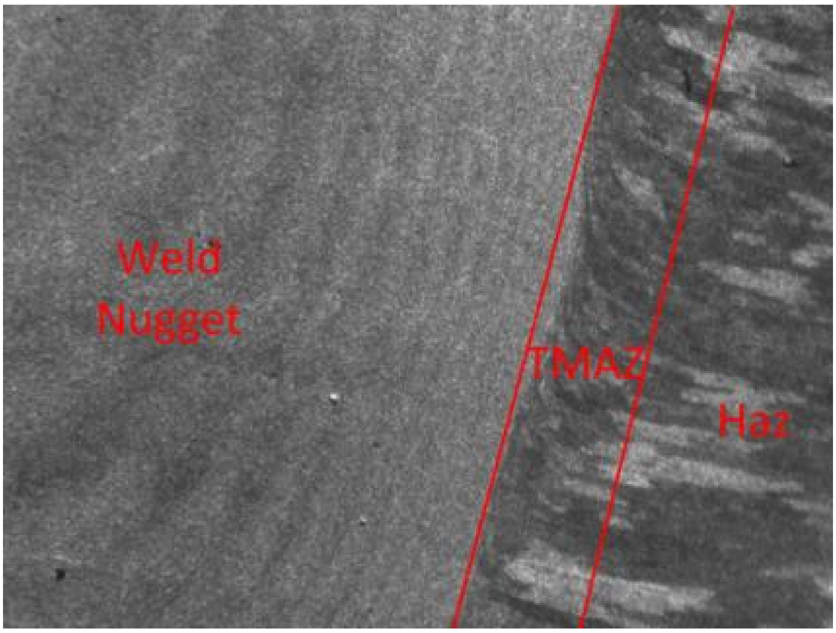

Figure 73: Close-Up Annotated View of an Etched FSW Al 7075 Showing Transition from HAZ to TMAZ to Weld Nugget. Notice the Grain Plastic Deformation at the Interface and the Large Difference in Grain Size

The grains within the nugget are approximately one order of magnitude than the unaffected material grain size. Theory presented in section 2.6 also indicates that the hardness will decrease compared to the unaffected material zone. To verify this a hardness mapping consisting of approximately 500 hardness measurements at 500 µm intervals in a 38 x 13 matrix was performed, centered on the center of the weld joint. Appendix A shows a table listing all the hardness values. Figure 74 shows the left and right halves of the physical hardness mapping performed over the entire FSW zone. Each dot represents one hardness test.

Each hardness measurement was noted and plotted in a Mathematica Contour Plot. The result is presented in Figure 75. The location of the weld nugget (120-130 HV), of the TMAZ (140 HV) and of the HAZ (160 HV) are clearly delimited. These zones overlay very well to the zones as illustrated in the previous two figures. The parent material has a hardness of 180 HV. By comparison, a pure aluminum substrate has a hardness of approximately 15-20 HV.

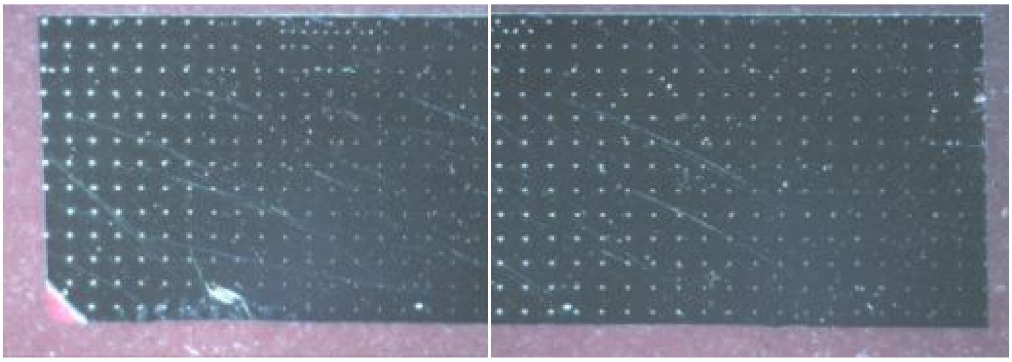

Figure 74: Picture from a FSW Hardness Matrix Test. Each Dot Represents 1 Hardness Indent. Indents are 500 Microns Apart

Figure 75: Transverse Hardness Plot of an Al 7075 Friction Stir Welded Panel Resulting from a Hardness Matrix Test

This hardness plots confirms literature review finding on this subject. As shown in Figure 18 and shown again in Figure 76 below, Al 7075 hardness was noted as HV 124 at the weld center, with a maximum HV 140 at the edge of the TMAZ. However, there is a discrepancy in the results with regards to the HAZ. Literature data indicates that the hardness should be lower as shown in Figure 76. Theoretically this would be due to grain coarsening and slight precipitate coarsening occurring without the competing effect of work hardening as seen in the TMAZ and weld nugget resulting in a general loss in hardness. In this case (Figure 75) the hardness seems to progressively increase to a value of 160 HV.

This means that the HAZ was less affected than in standard FSW joints. Since the only difference between the HAZ and the unaffected material is the heat transfer through the plate, then the HAZ must have received less heat, resulting in a less prominent hardness loss (through grain coarsening and precipitate coarsening). This can be explained by the fact that creating a joint in a single plate requires little clamping. Less clamping reduces the stress on the joint, and therefore the friction within the joint. Less friction will produce less heat. This is a reasonable theory, however it was not further investigated.

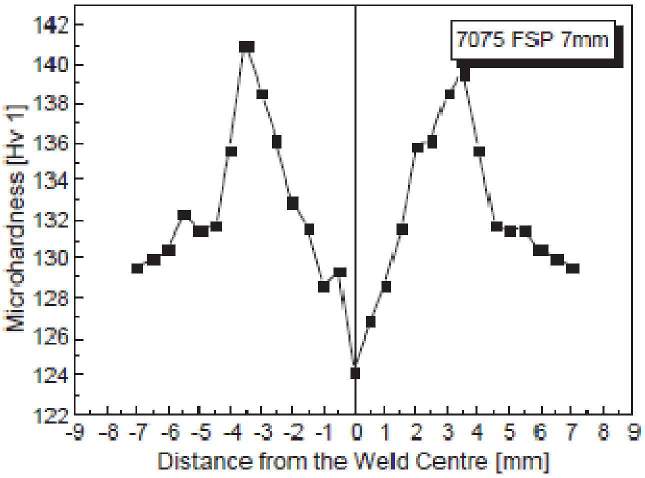

Figure 76. Micro-Hardness Profile Measured on the Cross Section of the 7075 FSP plates [23]

Overall, the sample presents a fine, equiaxed grain structure and a mostly corresponding hardness profile corresponding with typical FSW joints. These results corroborate well with the literature review [6][16][21][23][34]. The results from this hardness study indicate that the sample FSW joints received from The Boeing Company will have corrosion properties sufficiently close to real FSW joints to be used in corrosion studies interchangeably.

3 real FSW joints were also analyzed. These joints consisted of one 10mm thick Al 2024, one 4mm thick Al 6061 and one 2 mm thick Al 7075 FSW joint. The samples were subjected to a matrix of hardness indentations of between 89 (thinner Al 7075 FSW) and 171 (thicker Al 2024 FSW) points. The minimum distance between the indents was 500 µm. The indent results were compiled in a Mathematica contour plot and are shown in Figure 77 to Figure 79.

Figure 77. 10 mm Al 2024 FSW Hardness Mathematica Contour Plot. (171 Indents) Scale Indicates Vickers Hardness. Weld Regions are Represented by the Following Hardness Ranges: Weld Nugget from 110-130 Hv, TMAZ 140 Hv and HAZ 150-160 Hv

Figure 78. 4 mm Al 6061 FSW Hardness Mathematica Contour Plot. (110 Indents) Scale Indicates Vickers Hardness. Weld Regions are Represented by the Following Hardness Ranges: Weld Nugget 85-90 Hv, TMAZ 80 Hv, HAZ 70-75 HV

Figure 79. 2mm Al 7075 FSW Hardness Mathematica Contour Plot. (89 Indents) Scale Indicates Vickers Hardness. Weld Regions are Represented by the Following Hardness Ranges: Weld nugget 120 – 140 Hv, TMAZ 150-160 Hv and HAZ 170-200 Hv

In both the Al 2024 and Al 6061 FSW plates, the weld joint is discernable, going through the entire depth of the plate. The Al 2024 joint behaves similarly to a typical Al 7075 joint showing hardness loss towards the center of the joint. The Al 6061 joint is the opposite, getting harder towards the center. This can be due to the fact that in the case of Al 6061, the increase in hardness due to dynamic recrystalization and strain hardening more than compensates for the loss of hardness through annealing. This is a probable explanation since the strength of heat treated Al 6061 is not significant when compared with that of Al 2024 or Al 7075. No studies on the corrosion behaviour of FSW Al6061 or Al2024 joints have been investigated. However, 2xxx series alloys are heat treated similarly to 7xxx series alloys – a similar corrosion performance is expected. 6061 alloys have very little alloying elements (1% Mg, 0.6% Si and other trace elements) – no change in corrosion performance is expected in this alloy.

In the case of the Al 7075 FSW, the weld joint is not easily recognizable, although a region of lower hardness can be seen. This could be due to thin material, resulting in less clamping force and energy required to join the material, resulting in a non-uniform joint and lower hardness loss. Furthermore, the FSW Al 7075 plates had two joints close to each other. This explains why the hardness stays low on the right side – the other weld joint's HAZ is visible.

Generally, there is the same hardness loss and profile as the first hardness plot performed. Therefore the FSW plates used in the corrosion tests should behave similarly in corrosion than regular FSW plates and can be used comparatively in these experiments.

6.1.2 Coating Optimization

The goal of this section is to obtain the final spray parameters (independent for each powder) which will produce dense coatings of the correct thickness (as outlines in chapter 3) on bulk Al 7075 substrate. If the deposition parameters for the powders are totally unknown, a large amount of tests must be run to find optimal parameters since there are so many variables in the cold spray process. These variables are the following:

1. Orifice shape
2. Nozzle shape
3. Powder feeder wheel type
4. Travel speed
5. Feeder gas flow rate
6. Standoff distance
7. Propellant gas pressure
8. Propellant gas temperature
9. Powder feeder wheel RPM

By varying these parameters, the coating's properties can be changed. After testing a host of variable combinations, one set can be found that will produce the thickness coating with the lowest porosity. The properties used to produce this coating will be called the optimized properties and are valid only for that specific powder-substrate combination. It may be possible to find a combination of parameters that produce a better result. However this is less of a concern once parameters are found that produce the desired coating properties.

There are parameters that cannot be changed with the current equipment. These are nozzle and orifice shape. Furthermore, the powder feeder wheel type is not important for coating optimization because it is only important for high travel speed spraying. In the same way (for aluminum and aluminum alloys), travel speed only affects the coating thickness. Traverse speed will be set to a low, constant value (between 5 and 40 mm/s depending on the powder) for all investigative sprays and use a more typical 120-hole wheel. To determine the feeder gas flow rate, first a standard 10 SCFH (standard cubic feet per hour) will be set and modified as required. In the same fashion, the standoff distance will be set as 15mm, a common value utilized in cold spray.

The only parameters left to optimize are propellant gas pressure, propellant gas temperature and powder feeder wheel RPM. By experience, the most important parameters identified are first the propellant gas pressure and temperature, followed by the powder feeder wheel RPM. To start the optimization process, the RPM will be fixed to a low setting to avoid clogging the system. A matrix of pressure and temperature sprays will be sprayed and the best pressure / temperature combination will be found. Once the best parameters has been found for a specific wheel RPM, the powder flow rate will be increased (i.e. increase the wheel RPM) until the coating quality is compromised. Once this is done the feeder gas flow rate or the standoff distance can be increased. Figure 80 presents a flowchart of the optimization order as described in the few previous paragraphs.

Based on the literature review, the pressure and temperature range required for the deposition of the aluminum powders are close to the maximum parameters the system can supply. (This is 250 psi / 500°C for Al 7075 / Al 5083, and 250 psi / 350 °C for the pure Al powder. Pure Al must be deposited with a polymer orifice to reduce clogging which limits the stagnation temperature to 350°C) Instead of performing a large optimization study, a confirmatory study (based on the literature review properties) was performed to ensure that the Centerline system was performing similarly to the systems used in the literature review papers. For this reason, only 4 coatings were produced as outlined in Figure 81 (Tests 17 to 20 - Results are shown in Table 14) The test plan also shows the sprays that need to be performed to obtain the final travel speed once the optimized parameters are found.

Every time a coating is deposited it undergoes a visual inspection. This inspection is to verify the adherence of the coating and will be a pass or fail test. If the coating passes the first test it will then be cut, mounted and polished for microstructure examination. The polished pieces will be processed using the optical microscope and image processing software; from this an average value of porosity and thickness will be found. Results are presented in Table 13.

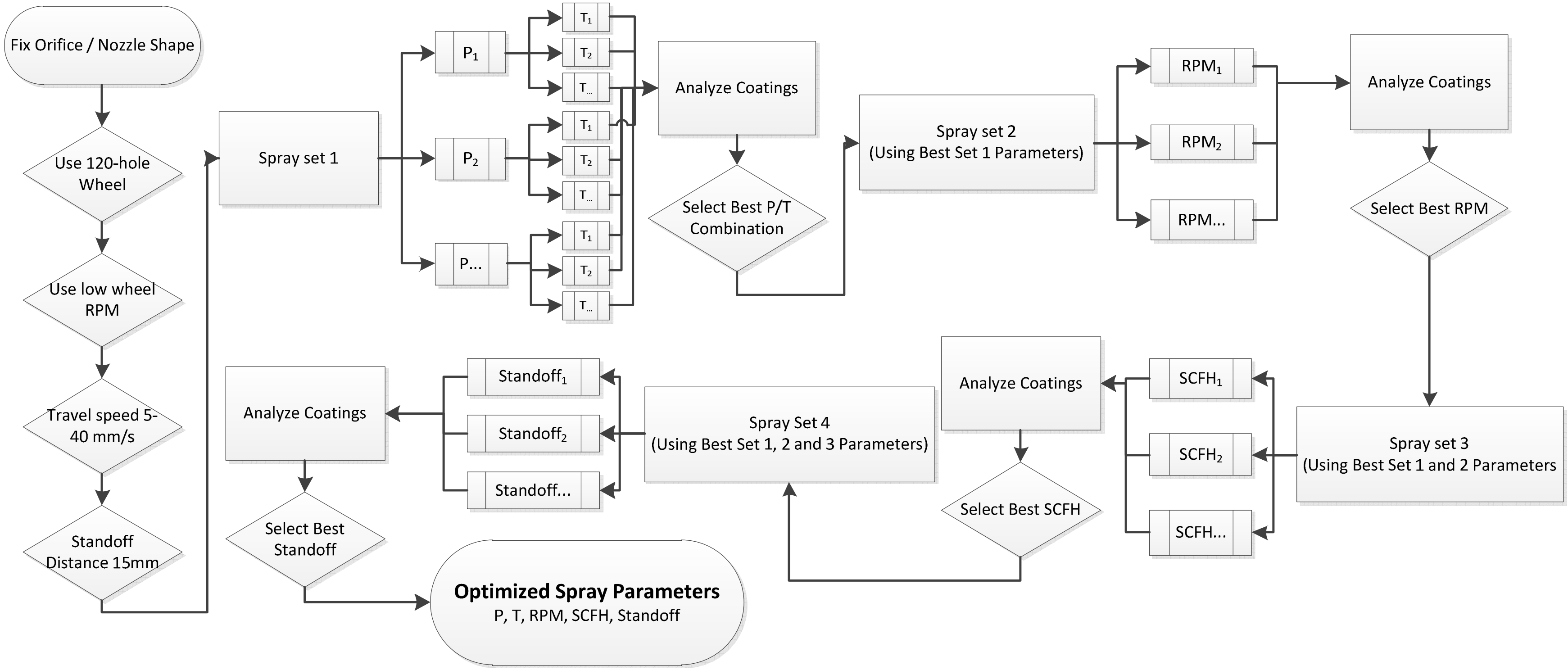

Figure 80: Spray Parameters Optimization, Full Algorithm

Table 13. Optimization Tests #17-20 (Al 5083 on Al 7075) Summary. Showing parameters that were modified. Other parameters can be found in Table 14

Test #	Pressure (psi)	Temperature (°C)	Porosity	Thickness (μm)
17	200	400	< 1%	19 ± 4
18	250	400	< 1%	48 ± 13
19	200	500	< 1%	41 ± 8
20	250	500	< 1%	113 ± 13

As can be seen, the optimized parameters are for test #20 i.e. 250psi and 500°C since the porosity has remained constant for an increasing coating thickness. Table 14 presents the final optimal parameters for all three powders. Parameters for pure Al and Al 7075 have been obtained from a parameter database for the Centerline system compiled by the University of Ottawa Cold Spray Laboratory.

Table 14. Optimized Spray Parameters for Al 7075, Al 5083 and Pure Al Powders on Al 7075 Substrate

Property	Al 7075	Al 5083	Pure Al
Gas Nature	Nitrogen	Nitrogen	Nitrogen
Nozzle Material	Stainless Steel	Stainless Steel	Polymer
Throat diameter (mm)	2	2	2
Nozzle Exit Diameter (mm)	6.3	6.3	6.3
Nozzle Length (mm)	120	120	120
Propellant gas Pressure (psi)	250	250	250
Propellant gas Temperature (°C)	500	500	350
Powder Feeder Wheel Type (# holes)	120	120	320
Powder feeder RPM	3	3	14
Propellant gas Flow Rate (SCFH)	10	10	25
Standoff distance (mm)	15	15	15

These optimized parameters give us the thickness coating with lowest porosity for a specific traverse speed. This speed can be modified to adjust the coating thickness with no detriment to the coating quality. In order to find the traverse speed required for the coating thickness to fall within the specified range, several coatings can be created using the optimized parameters but varying the travel speed. A test plan for these tests is shown in Figure 81. The samples were analyzed for thickness and the results were plotted. From these graphs the optimal travel speeds for each powder can be determined in order to obtain a coating thickness of 125 – 250 μm. Results are presented in Figure 82 to Figure 85.

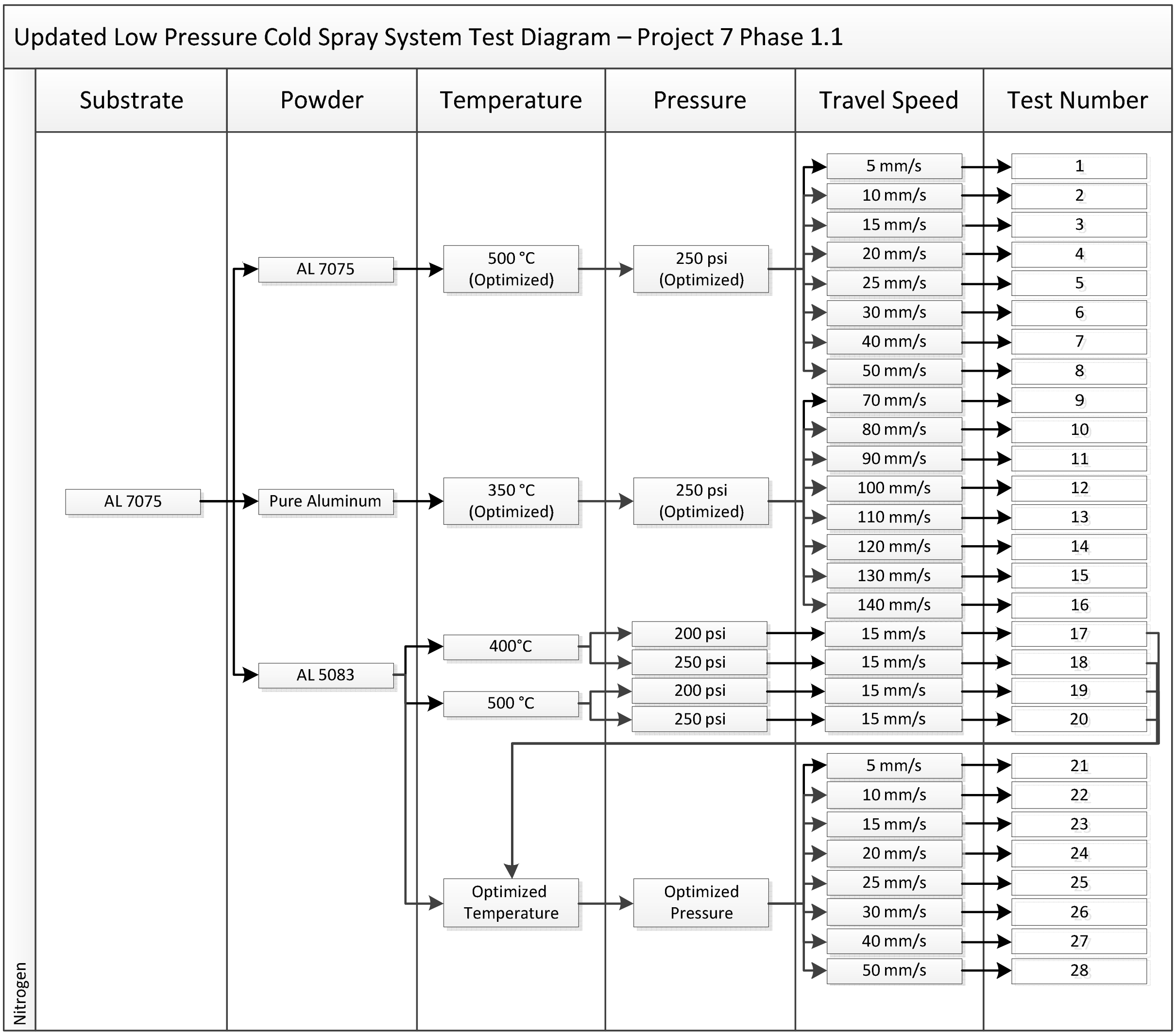

Figure 81 Project Phase 1.1 Traverse Speed and Al 5083 Parameters Optimization. All Coatings Adhered

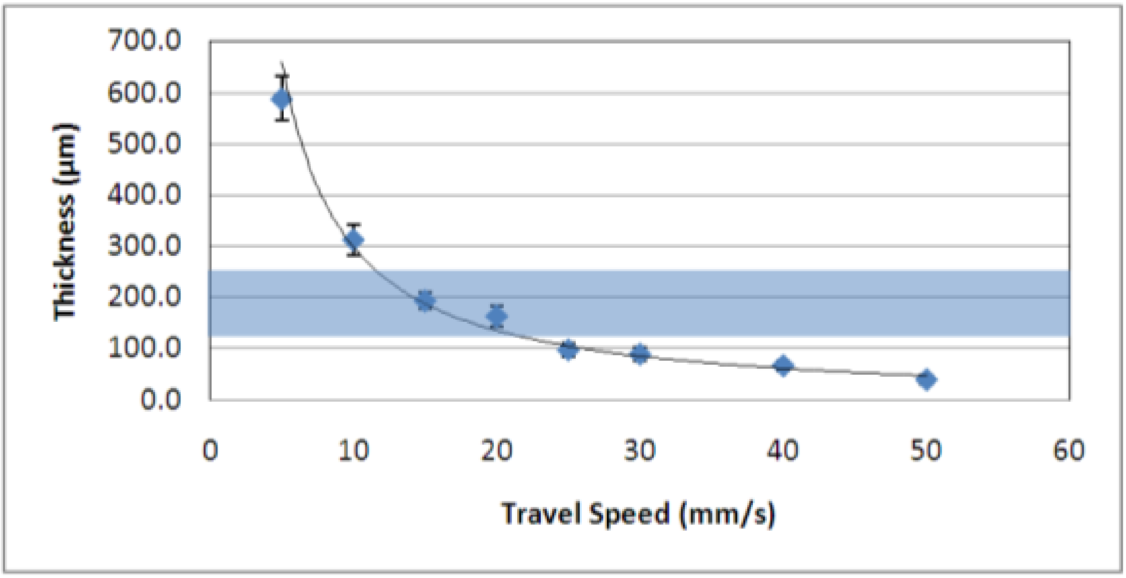

Figure 82. Traverse Speed Optimization for Al 7075 Powder on Al 7075 Substrate. Band Highlights Allowable Coating Thickness Range

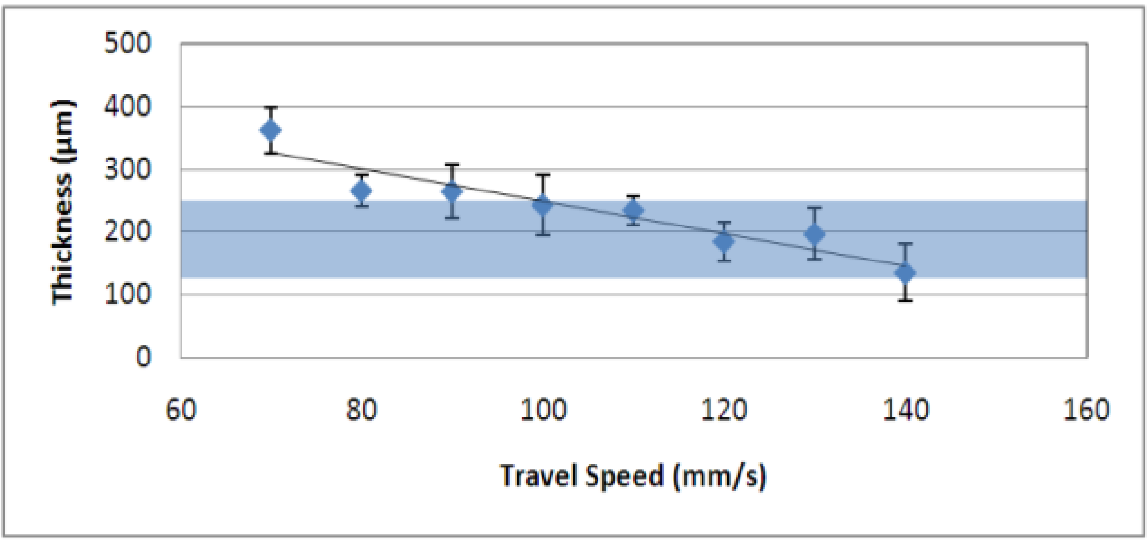

Figure 83. Traverse Speed Optimization for Pure Al Powder on Al 7075 Substrate, 120-Hole Wheel. Band Highlights Allowable Coating Thickness Range

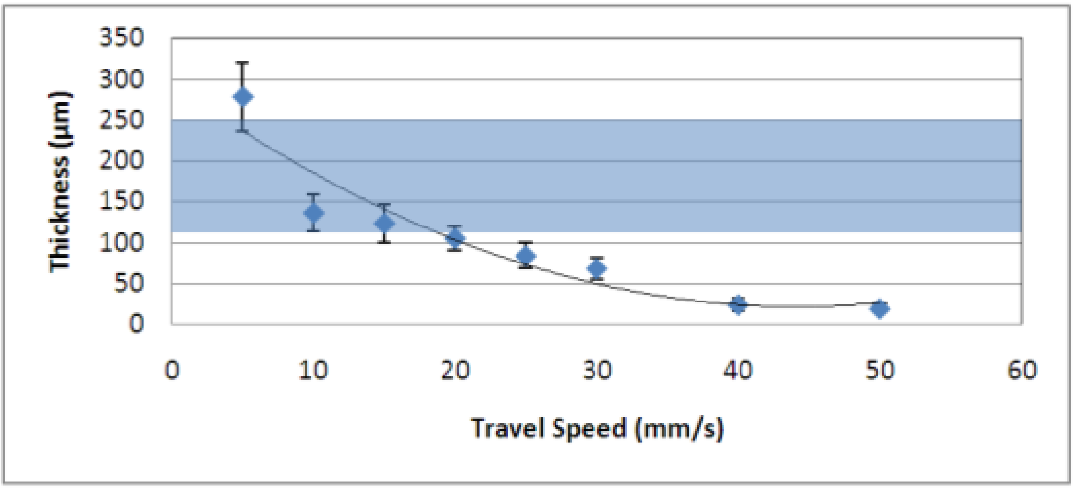

Figure 84. Traverse Speed Optimization for Al 5083 Powder on Al 7075 Substrate. Band Highlights Allowable Coating Thickness Range

The previous tests were performed with the same powder feeding wheel (120 hole). A different powder wheel containing 320 was tried for the pure Al powder. This yields a more continuous powder flow which allows spraying at higher travel speeds (above 120 mm/s). This new wheel will be used uniquely for the pure Aluminum because it is the only metal which requires speeds at which the inconsistency of the old feeding wheel can be noticed.

New parameters needed to be optimized for this new powder wheel. First of all, the wheel RPM had to be modified to take into account the new hole size. An RPM optimization series was sprayed to determine the optimal RPM at which to spray to obtain maximal deposition efficiency but keep the porosity consistent. Pure aluminum was sprayed on Al 7075 substrates at the same parameters of 250 psi, 350^{o}C, 15mm standoff and a 40mm/s traverse speed. The results are presented below in Table 15.

Table 15. Pure Aluminum RPM Optimization for New Powder Feeder Wheel

Powder RPM	Thickness (µm)	Porosity (%)
12	963 ± 72	2.2 ± 0.6
13	1080 ± 62	1.9 ± 0.3
14	1299 ± 87	1.4 ± 0.7
15	1443 ± 64	3.1 ± 0.5
16	Too thick to measure by optical microscopy	3.3 ± 1.0
17	Thicker than #16	3.7 ± 0.6

Notice that the thickness increases for every increase in RPM. However, the porosity increases suddenly at 15 RPM, from 1.4% at 14 RPM to 3.1% at 15 RPM. For this reason, it was chosen to spray at 14 RPM with the 320-hole wheel because it offered the thickest coating (hence, better deposition efficiency) for the lowest porosity.

Because the spray parameters for pure Aluminum changed, a new travel speed optimization was performed with the new 320-hole wheel. Using the same parameters used on the last travel speed optimization for pure aluminum, but using a 14 RPM powder wheel rotation velocity, a new travel speed optimization curve can be generated. This curve is presented in Figure 85 below.

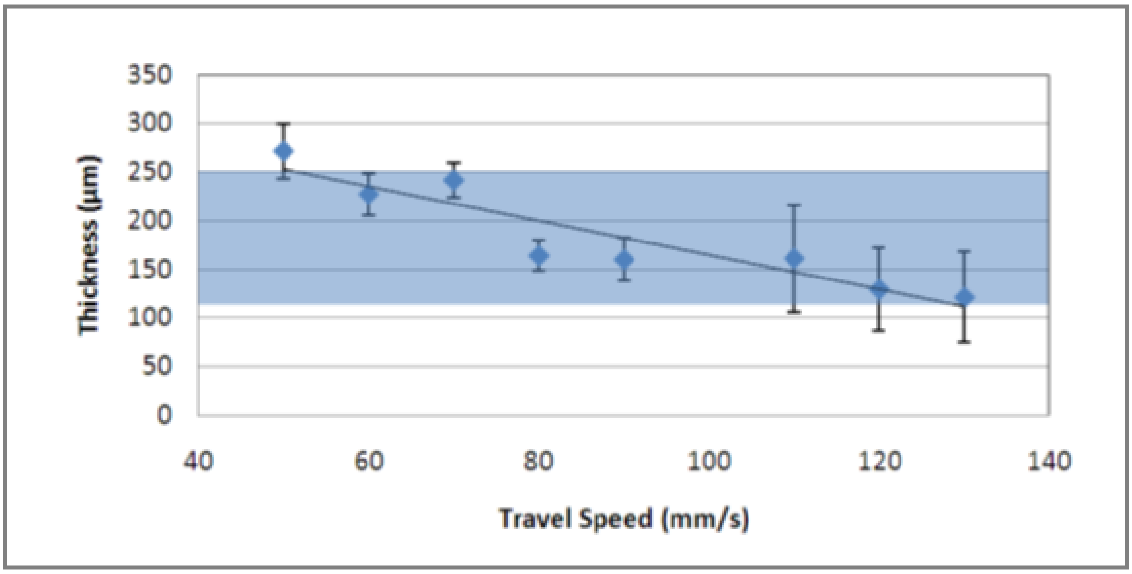

Figure 85. Traverse Speed Optimization for Pure Aluminum Powder on Al 7075 Substrate, 320-Hole Wheel. Band Highlights Optimal Coating Range

Table 16. Optimized Parameter Summary For Al 7075 Substrate Travel Speed and Powder Feeding for a 5-10 thou Coating (125-250 μm). Please Consult Table 14 for Full Parameter List

Powder	Wheel Type (# holes)	Feeder RPM	Feeder Gas Flow Rate (SCFH)	Traverse Speed (mm/s)
Pure Al	320	14	25	85
Al 5083	120	3	10	7
Al 7075	120	3	10	15

6.2 Phase 1.2 – FSW Plate Feasibility and Coating

This project was initially intended for one corrosion test, the ASTM B117. The finalized spraying parameters were tested on FSW test plates. The results proved satisfactory, and all the plates for this corrosion test were sprayed at once.

The FSW plates were sprayed with the optimized parameters. Plates labelled as “X” were as-FSW, “Y” plates were grinded. Table 17 presents a summary of the powders that were sprayed on each plate. Figure 86 presents the Al 5083 powder sprayed on the “Y” plate and the same for Figure 87 on the “X” plate. Al 5083 is the softest aluminum alloy that can be deposited at 500^{o}C stagnation temperature. High-temperature softening produces deposition of the powder within the walls of the orifice and the nozzle components of the system. This effect is called “clogging” and prevents the deposition from occurring indefinitely. Because of this the Al 5083 coatings had to be performed over multiple days to allow orifice and nozzle cleaning time. (The nozzle and orifice can be cleaned by soaking in a 10-25% NaOH solution for 12-24 hours.) Clogging would occur after 7-10 minutes for Al 5083, while 20 minutes of spray time was required to cover the entire plate. Therefore, 2 to 3 sprays were required to cover one plate. The “Y” plate was coated in 3 separate trials, while only 2 were required to spray the “X” plate. Small bumps can be noticed in these coatings from the overlap that was created to ensure a full coating.

Table 17. Plate Identification

Plate Number	Cold Spray Metallic Coating
X3	Pure Aluminum
Y3	Pure Aluminum
X4	Al 7075
Y4	Al 7075
X5	Al 5083
Y5	Al 5083

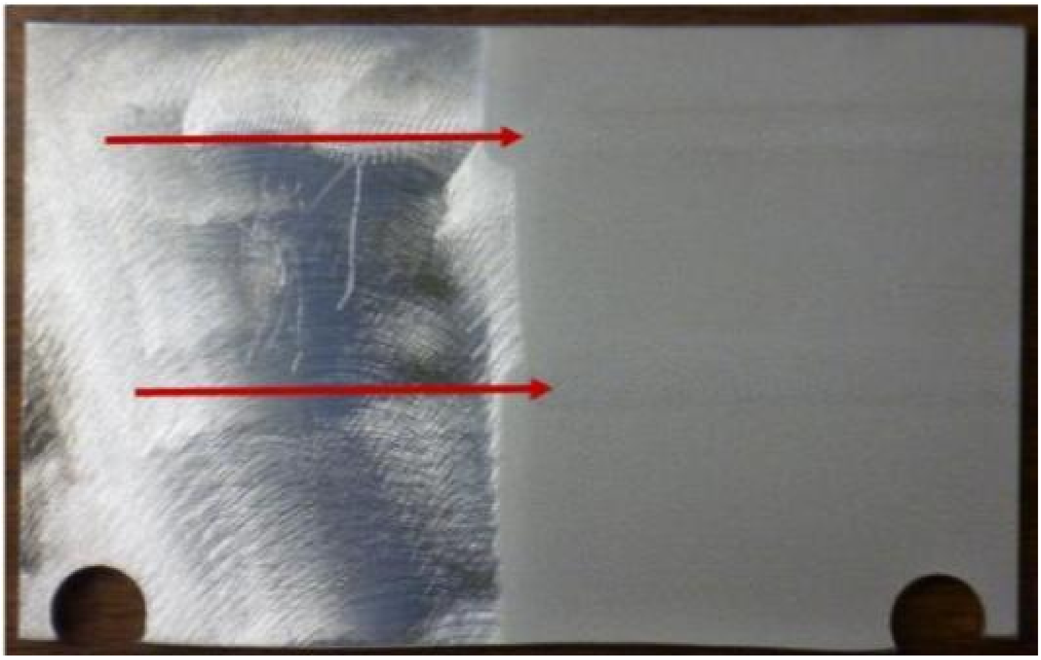

Figure 86: Plate Y5 – Al 5083 Plate Done in 3 Sprays (2 Overlaps Shown by Arrows)

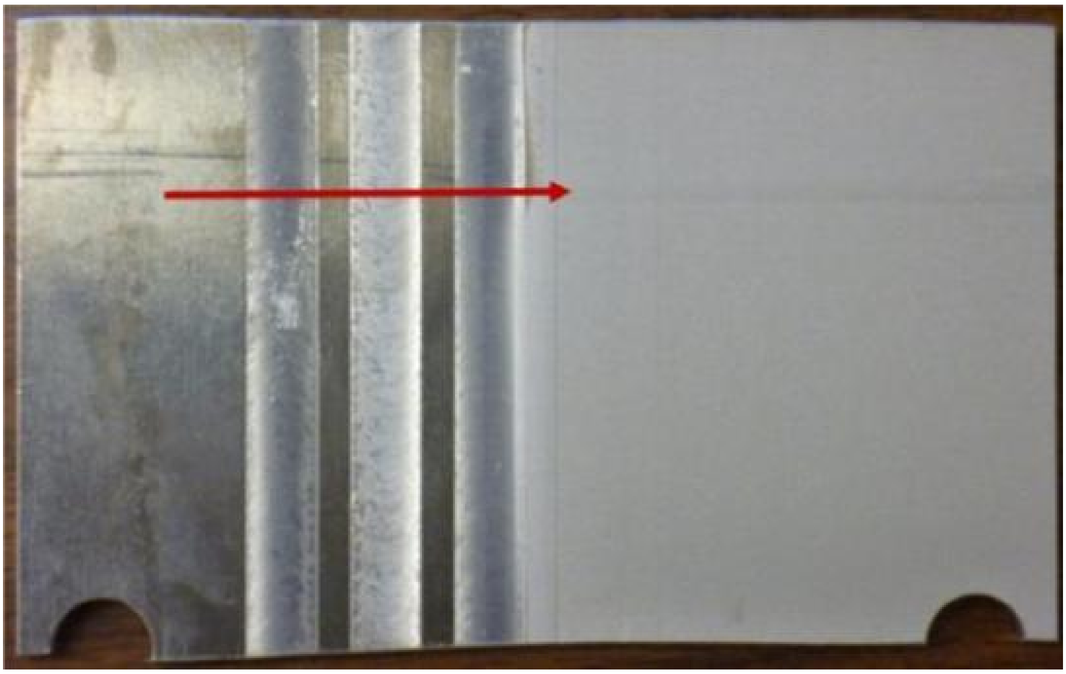

Figure 87. Plate X5 – Al 5083 Plate Done in 2 Sprays (1 Overlap Shown by Arrow)

6.3 Phase 2: Corrosion Testing

The first corrosion test was the ASTM B117 standard salt spray fog test. To confirm results from these tests, two other corrosion tests were performed. These were the ASTM G34 and ASTM G110 corrosion tests.

6.3.1 ASTM B117 Salt Spray Fog Test

ASTM B117 [44] is an industry standard used to measure general and pitting corrosion types. A salt fog is created in a chamber using a 5% NaCl solution (6.5 to 7.2 pH) atomized at 35°C. The test can be run for as long as required in order to create a noticeable difference between the control group and the experiment. For aluminum alloys the trend is to test for a continuous 1000 to 2000 hours.

As shown in the last section, half of the surface area of each FSW plate was covered with a 200 µm CGDS aluminum coating (to cover 3 of the 6 weld joints). The entire plate was then coated with a hexavalent chromium conversion coat Type I, class 1A in accordance with military standard MIL-C-5541D [50] which involves immersion and cleaning in several corrosive baths. hThis layer improves the corrosion performance of the plates, and improves paint adhesion. A mask was applied to the edges and back of the plate to prevent corrosion from penetrating at the coating/substrate interface.

Once this preparation process had taken place, the plates were subjected to 2000 hours of continuous testing. Photographs were taken at 0, 672 and 2000 hours. All coatings performed better than the exposed FSW side. However, Al 7075 was only marginally better, while Al 5083 performed very well. The best coating performance was visually determined to be pure aluminum, which had no visible signs of corrosion after 2000 hours of exposure. Figure 88, Figure 89 and Figure 90 below show photographs of results for each of the three metallic coatings. Note the preferential corrosion occurring at the friction stir weld joints.

0 hours (As-is) | 672 hours (As-is) | 2000 hours (As-is) | 2000 hours (Grinded)

Figure 88. Corrosion Results for Al 7075 at 0, 672 and 2000 hours

0 hours (As-is) | 672 hours (As-is) | 2000 hours (As-is) | 2000 hours (Grinded)

Figure 89. Corrosion Results for Al 5083 at 0, 672 and 2000 hours

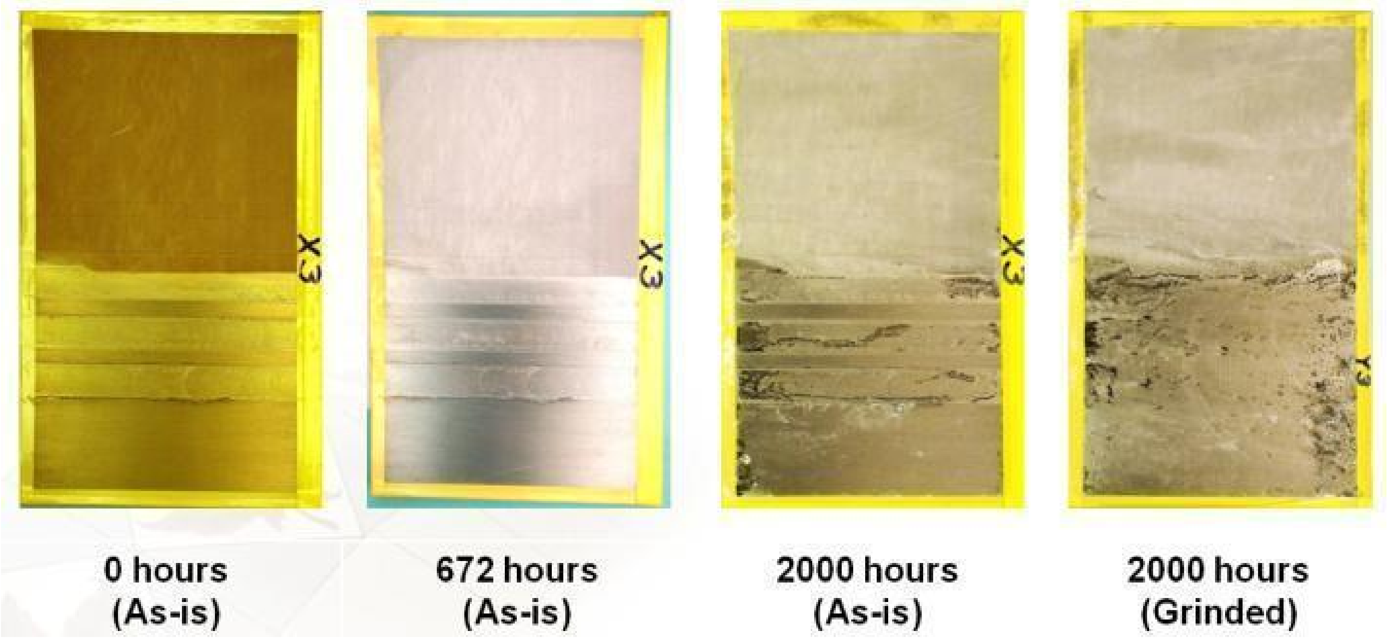

Figure 90. Corrosion Results for Pure Al at 0, 672 and 2000 hours

Good adhesion of the conversion coating at 0 hours was observed. The chromate in the conversion coating was subsequently leached out before the 672 hour mark as shown by the aluminum-color of the plate, preventing the plates from corroding prematurely before this point. There is preferential corrosion occurring in the exposed plates' weld joint at 2000 hours. Large pitting regions (identified by the black-coloured corrosion in the weld region of the 2000 hour tests) in and around the FSW joint regions are present in both as-is and grinded plates. This is concurrent with the corrosion theory presented earlier.

Comparing the coatings' performance, small pit marks – dark concentrate spots – are seen in the Al 7075 coating, while minor surface corrosion (slightly darker surfaces) appears in the Al 5083. No corrosion is seen in the pure Al coating after 2000 hours. White corrosion products are present on the edge of some of the test plates – this is due to mask failure leading to a small concentration cell and preferential corrosion which is not representative of the coating performance. In summary, depositing a coating will be beneficial to corrosion protection. Al 7075 will only have a slightly better performance than the as-FSW material, while Al 5083 presents a significant improvement. A pure Al coating is best for corrosion protection in the ASTM B117 test, showing no signs of corrosion after 2000 hours.

6.3.2 ASTM G34 Standard EXCO Test

The ASTM G34 standard [51] is used to measure exfoliation corrosion in 7xxx series alloys. The test consists of immersing test plates in a 4.0 M NaCl, 0.5 M KNO_3 and 0.1 M HNO_3 solution maintained at 25 ± 3^oC for a recommended period of 48 hours. All samples are sections of the larger FSW plates used in the ASTM B117 test and have exposed areas of either 25 x 55 mm or 23 x 67 mm. A total of 24 samples were cut from remaining available FSW plates. Half were used for ASTM G34, and the remaining half was used for the ASTM G110. There were an equal number of as-FSW and grinded samples (6 each per test). At least one sample of each surface finish type was used in each of the 4 coating categories i.e. bare and with the 3 metallic coatings. A summary is presented in Table 18.

Table 18. ASTM G34 Plate Information

Coating	Surface type		
	#1	#2	#3
None (bare)	Grinded	As-FSW	Grinded
Al 7075	Grinded	Grinded	As-FSW
Al 5083	Grinded	As-FSW	Grinded
Pure Al	As-FSW	Grinded	As-FSW

A mask is applied on the edges and back of the plate to prevent the corrosion from penetrating the coating-substrate interface. This mask is 3M electrical tape. Figure 91 shows an example of sample prior to the corrosion test. Figure 92 to Figure 95 show each sample after a 50 hour exposure time.

(a) (b)

Figure 91. ASTM G34 and ASTM G110 Test Coupons (a) Front and (b) Back. Grinded Coupon on Left Side, As-FSW Coupon on Right Side

(a) (b) (c)

Figure 92. ASTM G34 As-FSW Samples (a) Ground Substrate (b) As-Received Substrate (c) Ground Substrate

(a) (b) (c)

Figure 93. ASTM G34 Al 7075 Samples (a) Ground Substrate (b) Ground Substrate (c) As-Received Substrate

(a) (b) (c)

Figure 94. ASTM G34 Al 5083 Samples (a) Ground Substrate (b) As-Received Substrate (c) Ground Substrate

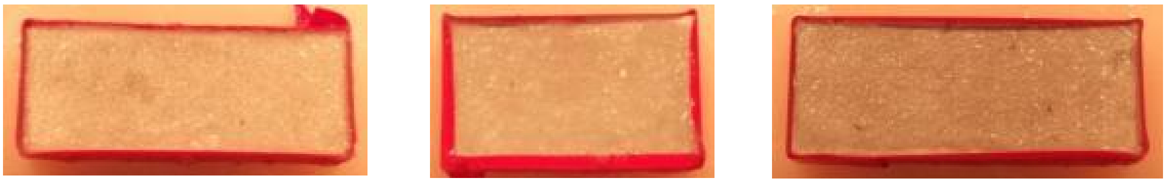

(a) (b) (c)

Figure 95. ASTM G34 Pure Aluminum Samples (a) As-Received Substrate (b) Ground Substrate (c) As--Received Substrate

As can be seen, pure aluminum fared best, with only a few noticeable pits on some samples. Al 5083 fared very well, with pits covering the surfaces of most of the samples. When analyzing Al 7075 corrosion, it can be seen that the as-is samples performed better than the AL 7075 samples. The coatings have noticeably peeled off of the AL 7075 samples. This can be attributed to small particle grain boundary size resulting in more grain boundary corrosion and therefore more intergranular corrosion [10]. Although the test results indicate that pure Al and Al 5083 perform similarly, the pure Al outperformed the Al 5083 coatings. There was no exfoliation on either end, however the pits present in Al 5083 were more frequent and deeper than those present in the pure Al.

The ASTM G34 tests correlates very well with the results from the ASTM B117. The ratings detail the extent of corrosion as specified by reference photography in the standard. An "NC" rating signifies "No Corrosion". A "P" rating signifies that pitting was present in the sample. Finally, "EA", "EB", "EC", and "ED" ratings signify there was exfoliation corrosion damage, with "EA" being the lightest, least corroded, and "ED" being the worst corrosion damage. A summary is presented in Table 19.

Table 19. Results from the ASTM G34 Corrosion Test for As-FSW Plate, and FSW Plate Coated with Al 7075, Al 5083 and Pure Al Powders

Samples	1	2	3	Coating Rating
As-is	EA	EC, P	EB	EC, P
Al 7075	ED, P	EC, P	ED, P	ED, P
Al 5083	P	P	P	P
Pure Al	P	NC, P	P	P

These results correlate with the ASTM B117 tests, which indicate the same order of performance for all three metallic coatings i.e. Pure Al, closely followed by Al 5083, and Al 7075 far behind.

6.3.3 ASTM G110 Intergranular Corrosion Test

The ASTM G110 corrosion test [46] consists of immersing cleaned samples (prepared and masked in a similar fashion as the ASTM G34 test) in a solution containing a specific concentration of nitric acid (HNO_3) and hydrofluoric acid (HF). The solution temperature must be maintained at 30 ± 3°C for a recommended testing time of 6 to 24 hours.

Samples were immersed for a period of 24 hours, after which they were cleaned, visually inspected, mounted and analyzed. Results are presented in Figure 96 to Figure 99.

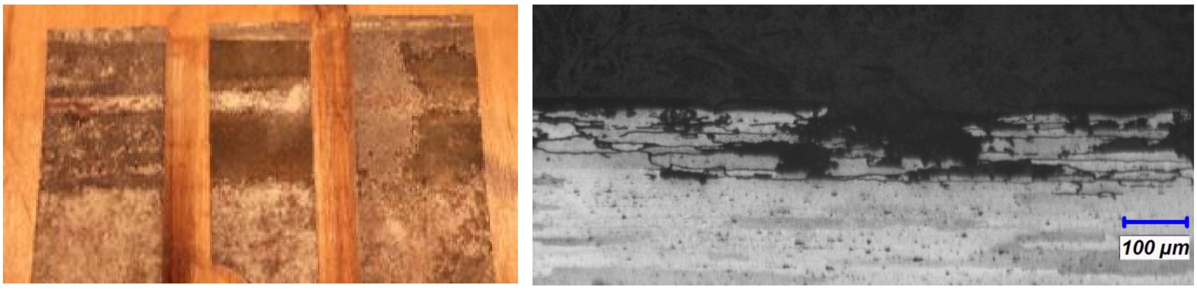

(a) (b)

Figure 96. As-FSW plates. (a) Visual inspection After Cleaning (b) Optical Microscope Image (100x) of an Etched Cross Section

(a) (b)

Figure 97. Al 7075 Coated FSW plates. (a) Visual inspection After Cleaning (b) Optical Microscope Image (100x, Dark-Field Mode) of an Etched Cross Section

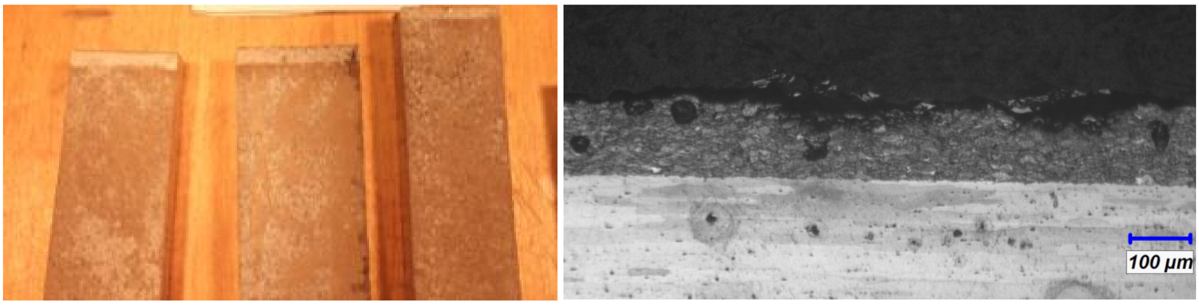

(a) (b)

Figure 98. Al 5083 Coated FSW plates. (a) Visual inspection After Cleaning (b) Optical Microscope Image (100x) of an Etched Cross Section

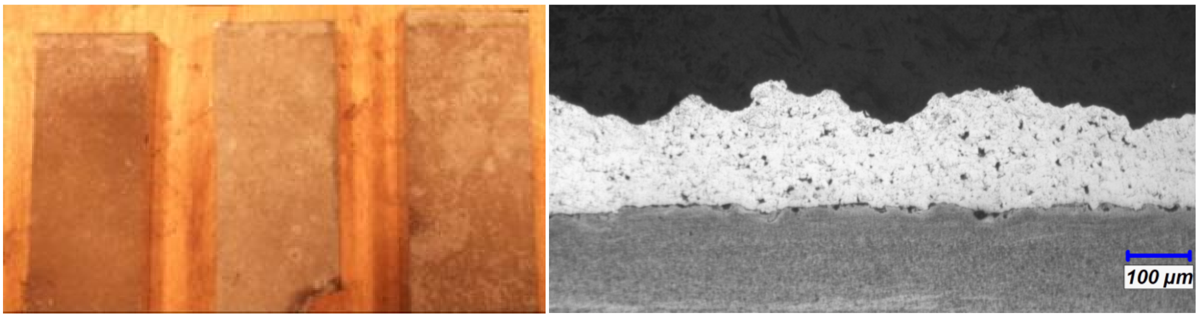

(a) (b)

Figure 99. Pure Al Coated FSW plates. (a) Visual Inspection After Cleaning (b) Optical Microscope Image (100x) of an Etched Cross Section

It appears from the visual inspection alone that the Al 7075 coating performs similarly to the as-FSW plates. Grinding the plate seems to reduce the localized corrosion in the bare samples. Furthermore, pits are present in the Al 5083 coating, while the pure Al coating seems intact. These inspections are confirmed in the optical images, noting vast regions of intergranular corrosion and material loss in both the as-received and Al 7075 coated plates. (Deeper penetrations are noted for the as-FSW plates.) The Al 5083 coatings showed some intergranular corrosion, while no corrosion was present in the pure Al.

The optical analysis shows the depth of the corrosion. The corrosion in the FSW is deeper and more extensive than in any of the coated samples. In both Al 7075 and Al 5083, the corrosion did not penetrate the coating and the depth of corrosion is similar. However, since Al 7075 presents more corrosion sites than the Al 5083 alloy, it is still slightly less preferable. There is no optical sign of corrosion in any pure Al coatings.

These results match those from the corrosion tests performed previously. The ASTM B117, ASTM G34 and ASTM G110 test all confirm that the best coating for corrosion protection is pure Al, closely followed by Al 5083. An Al 7075 coating is better than a bare Al 7075 FSW substrate, but only by a small margin.

6.3.4 Corrosion Testing Summary

The results for all three corrosion tests are summarized in Table 20.

Table 20. Coating Corrosion Test Performance Summary

Coating	Corrosion test – relative performance (test rating if available)		
	ASTM B117	ASTM G34	ASTM G110
Pure Al	1	1 (P)	1
Al 5083	2	2 (P)	2
Al 7075	3	4 (ED, P)	3
None	4	3 (ED, P)	4

All three tests agree in the relative corrosion performance. Pure aluminum outperformed the other sets, followed closely by Al 5083. Far behind is Al 7075, followed closely by the parent material.

6.4 Phase 2: Additional Primary Objective Research

6.4.1 Adhesion tests

Adhesion tests are performed using the ASTM C633-01 standard. This standard consists of creating a coating on a one inch diameter rod substrate (a “bond plug” – see Figure 100) and co-radially gluing an identical rod on this coating with the help of high-strength glue. The assembly can then be pulled in a universal testing machine. The coating will separate from its original substrate at a certain tensile force. A value of adhesion strength be calculated knowing the bond plug surface area.

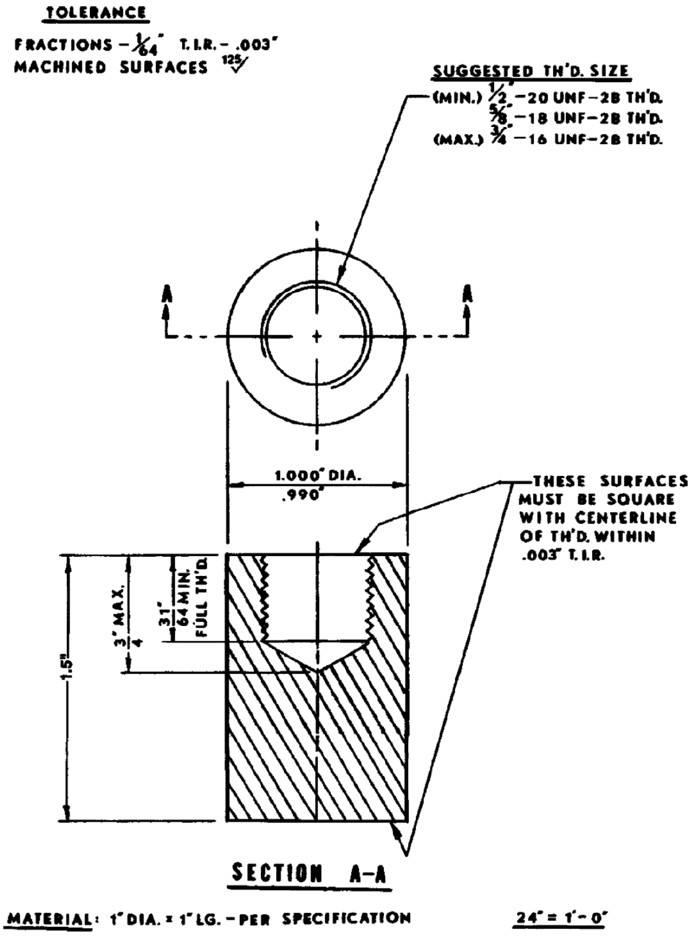

Figure 100. ASTM C-633 Substrate and Loading Fixture [52]

The glue used is called FM-1000 (Couch Sales LLC, Hilton Head, SC 29926) It is a film adhesive wafer pre-cut to the correct size that must be cured in an oven at 190°C for 2 hours under slight pressure and very slowly cooled to room temperature. A picture of the setup used to mount the glue is shown in Figure 101. Figure 102 shows a bond plug before coating while Figure 103 shows a tensile specimen ready for testing. Figure 104 shows the preparation and execution (in diagram form) of the standard.

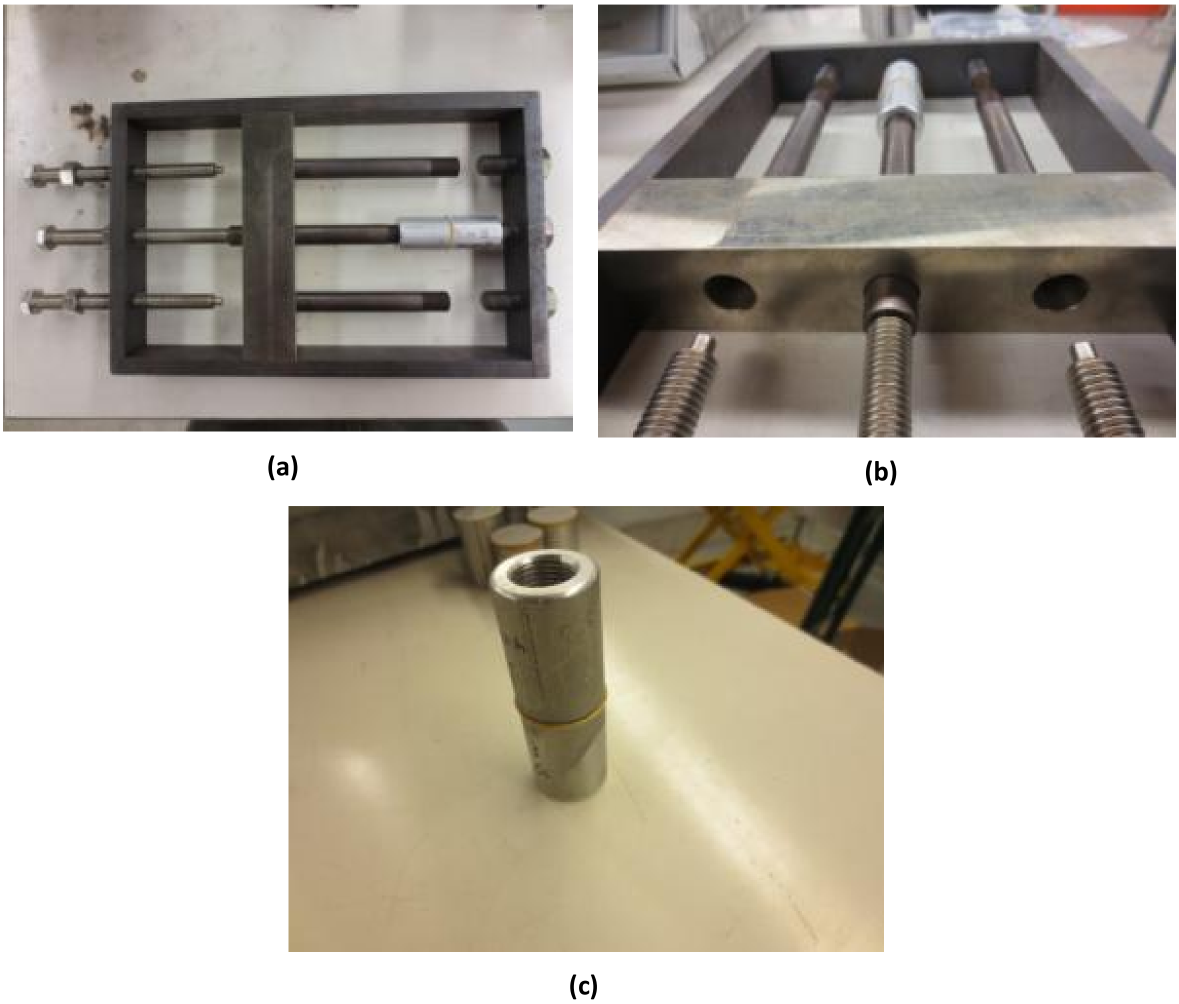

(a)

(b)

(c)

Figure 101. Bond Plug Glue Mounting Setup. (a) Fixture Top View (b) Fixture Side View (c) Sample After Glue Mounting, Ready to Pull

Figure 102. Virgin Bond Plug

Figure 103. Tensile Specimen Mounted in a Universal Testing Machine, Ready for Testing

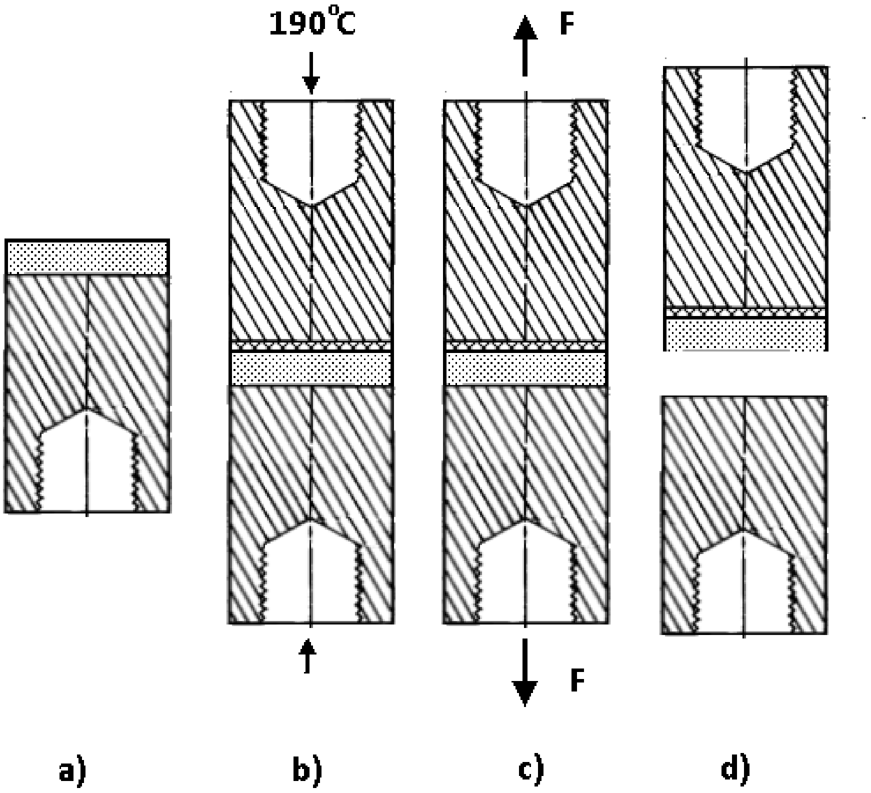

Figure 104. Preparation and Execution of a Tensile Test ASTM C-633. a) Coating is Produced on a Bond Plug b) Second Bond Plug is Glued onto the First c) The Assembly is Installed and Pulled in an Instron Machine Until d) the Coating is Removed from its Original Substrate

Initially, 3 to 5 bond plugs for each powder were sprayed, glued and pulled. Values for bond strength were obtained. However, later on during the project, the validity of these tests was put into question. Mainly, the surface preparation technique was found to be inconsistent and the spray pattern was determined to be non-optimal.

The surface preparation technique used previously was surface roughening using the mechanical engineering department's machine shop's grit machine. This is done to provide better adhesion. This machine uses 20 grit copper slag pellets and is used for multiple purposes such as cleaning rusty parts and removing dirt and oil. Since the grit is recycled, concerns were raised over the repeatability of the machine and whether or not recycled rust or oil contaminants would affect the surface preparation. It was noticed in the past that adhesion was sometimes poor in coatings. For this reason, a new grit blasting machine with dedicated spraying orifices was acquired. The surface preparation techniques was set to use 80 grit aluminum oxide grit at shop air (50-80 psi) using a 45 degree angle respective with the surface of the substrate. The grit is used only once and discarded to prevent any contamination.

The second issue involving bond plug testing was the spray pattern used during coating deposition. As shown in Figure 105, the first pattern consisted of performing one continuous line for all bond plugs (only 2 shown in the image, but the process can be extended to all 5 bond plugs) while the new process coats one bond plug at a time. The new spray pattern increases the heat concentration on the surface of the bond plug, leading to better adhesion of the particles.

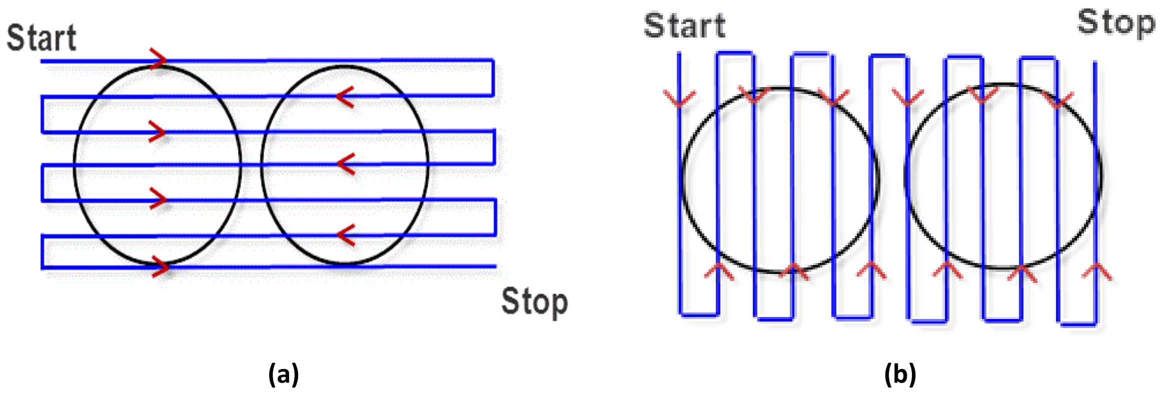

(a) (b)

Figure 105. Spray Patterns (a) 1 (b) 2

The test performed with the old grit blasting technique and spray pattern were labelled “shop”. “In-house” sets were performed with the new grit blasting method. The final results are shown in Table 21 and Figure 106.

Table 21. Bond Plug Results for Project 7

Powder	Bong Plug Set	Spray Pattern Used	Grit Blasting Technique Used	Bond Plug Quantity	Pressure (MPa)	Pressure (psi)	% Increase
Pure Al	1	1	Shop	5	16 ± 5	2340 ± 706	70%
	2	1	In-house	4	18 ± 2	2615 ± 300	
	3	2	In-house	5	28 ± 4	3982 ± 620	
Al 7075	4	1	Shop	5	47 ± 18	6828 ± 2661	45%
	5	2	In-house	5	68 ± 19	9896 ± 2777	
Al 5083	6	1	Shop	3	25 ± 8	3680 ± 1154	130%
	7	2	In-house	4	58 ± 17	8450 ± 2525	

Sets 1 and 2 show that the surface preparation technique did not have a large impact on the bond strength. However, this might not always be the case due to the inconsistencies of the machine shop grit blasting unit.

The spray parameters presented in section 6.1.2 creates a 200 µm coating. Because the ASTM C-633 standard requires at least 320 µm after machining, the coating is layered 3 times to form one thick 600 µm “multi-pass” coating. Literature on the matter [53] suggests that adhesion strength values from triple-pass coatings are 35% lower than their single-pass counterparts.

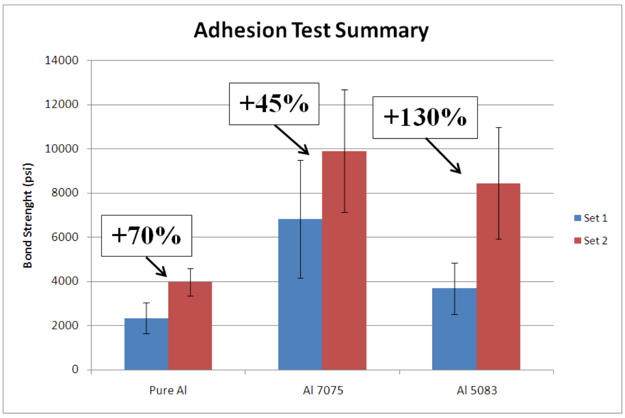

Figure 106. Bond Plug Result Chart

Pure aluminum results are 70% higher with the new set. It can be observed that the Al 7075 is less affected by temperature than the other alloys, and that the Al 5083 is greatly sensitive to temperature. Although the specific mechanisms have not been inspected, it is suspected that this is due to the powders initial softness and ability to deform under higher temperatures.

It was noticed that the powder injection point inside the orifice was the key location for clogging. (There is some powder deposition inside the wall of the nozzle, but this is insignificant compared to the orifice clogging). After 12-15 minutes on average, this area would completely clog, halting the spray. The clogging is progressive and affects proportionately (in a negative fashion) the deposition efficiency of the process. This is most likely due to a reduced powder flow rate due to the constriction caused by the clogging.

When the system is nearly fully clogged, or when the coating was insufficiently thick due to the lowered deposition efficiency resulting from the clog, the orifice and nozzle would be changed and deposition would resume. Since every AA 7075 bond plug takes approximately 3.5 minutes to spray, the orifice and nozzle assembly was changed after 3 bond plugs.

Interestingly, the bond strength decreases as the clogging in the nozzle increases. For a fresh orifice, the bond strength is high, breaking glue in both cases. A reduction in bond strength then occurs (with almost identical values in both cases) for the second bond plug for each nozzle / orifice combination.

6.4.2 Substrate Temperature Test

This section was instigated to analyze the effect of initial substrate temperature on the coating properties. As shown in the literature review, the temperature inside a FSW joint can reach up to 475^{o}C. If the deposition process occurs immediately after the FSW operation, the initial substrate temperature will be significantly higher than room temperature (the initial substrate temperature used until this point). In order to measure the effect of substrate temperature on coating properties, a test plan was created. It is presented in Figure 107 below. The goal of this test plan is to deposit a coating as per the optimal parameters found and observe the change in coating properties as the substrate temperature changes.

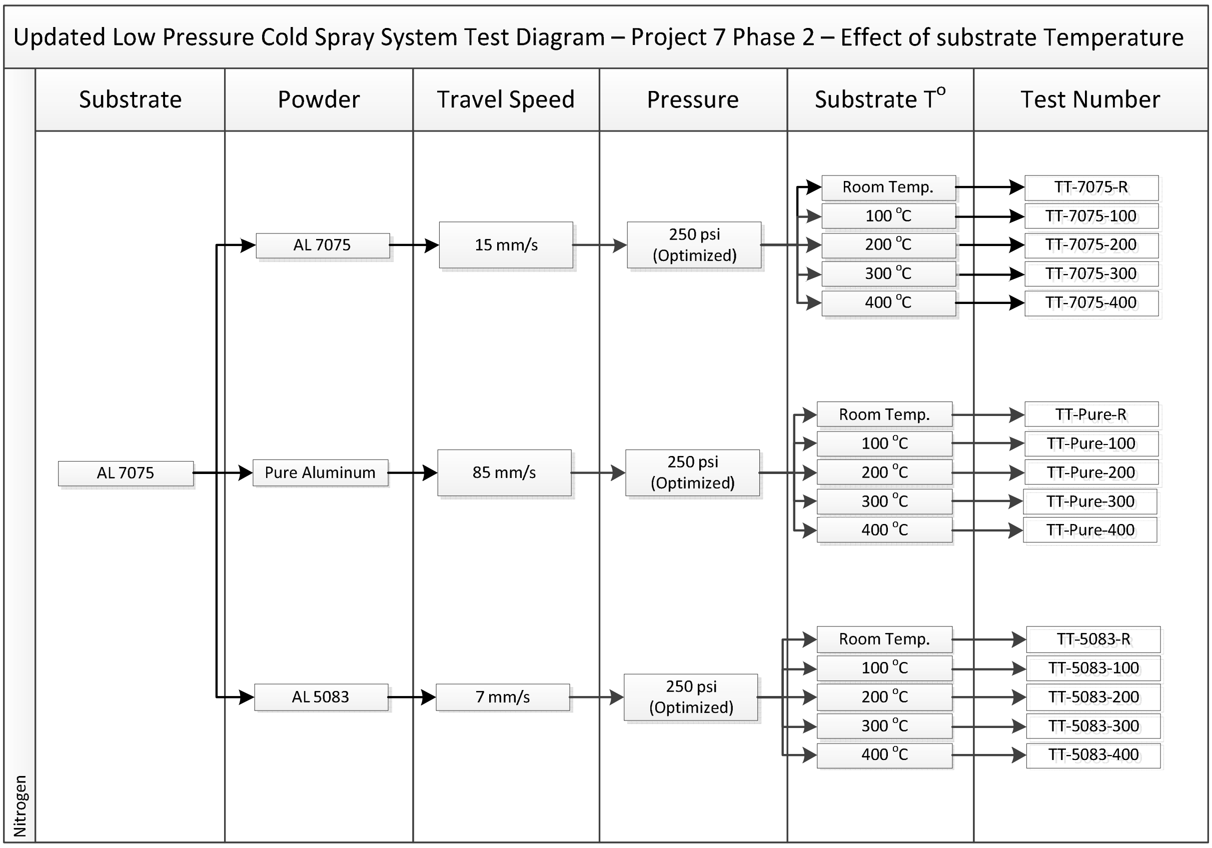

Figure 107. Initial New Test Plan for Measuring the Effect of Substrate Temperature on Deposition Efficiency

To measure the substrate temperature, a T-type thermocouple is inserted in a hole placed at a 0.5mm parallel distance from the top of the substrate where the coating is deposited. The thermocouple is placed at the center of the coupon. This thermocouple is connected to a LabView station that will measure temperature in 0.25 second interval. A temperature plot for each test is generated.

To modify the substrate temperature, a small coupon heater assembly was built. This assembly consists of an aluminum base, supporting a small 120V, 150 W, 2” x 8” heater. The heater is separated from the base, which allows insulation to be inserted in this gap to protect the base from the high heat and increase the temperature of the top surface. To protect the heater from the coating process, a piece of 4130 steel was bent and placed on top of the heater. This protects it from any overspray. To hold the coupon on this assembly, a simple paper clip is used where no coating is produced. A few pictures of the heater assembly are presented in Figure 108 to Figure 112.

Figure 108. Side View of the Heater Assembly, Showing the Heater underneath the Steel Barrier

Figure 109. General View of the Heater Assembly

Figure 110. Side View of the Temperature Test Coupon with Thermocouple Entry Hole (Substrate is on Top Surface)

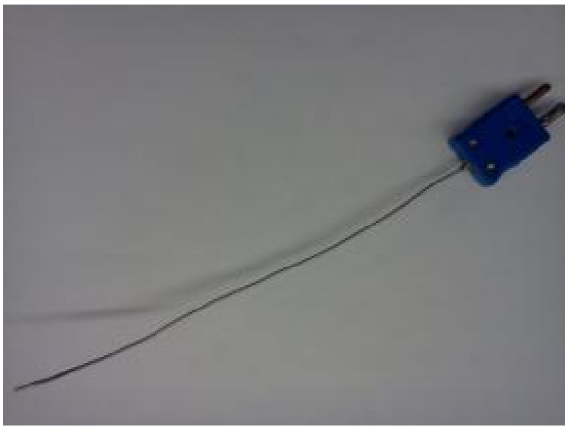

Figure 111. T-Type Thermocouple

Figure 112. Heater Assembly with Substrate and Thermocouple Attached with a Paper Clip

An initial heater test was performed to measure the substrate temperature against time. This test was performed with a blank substrate, just like indicated in the previous figures. The heater was turned on at full power (i.e. plugging it into a wall electrical socket) and the temperature increase over time was measured. The result is presented in Figure 113.

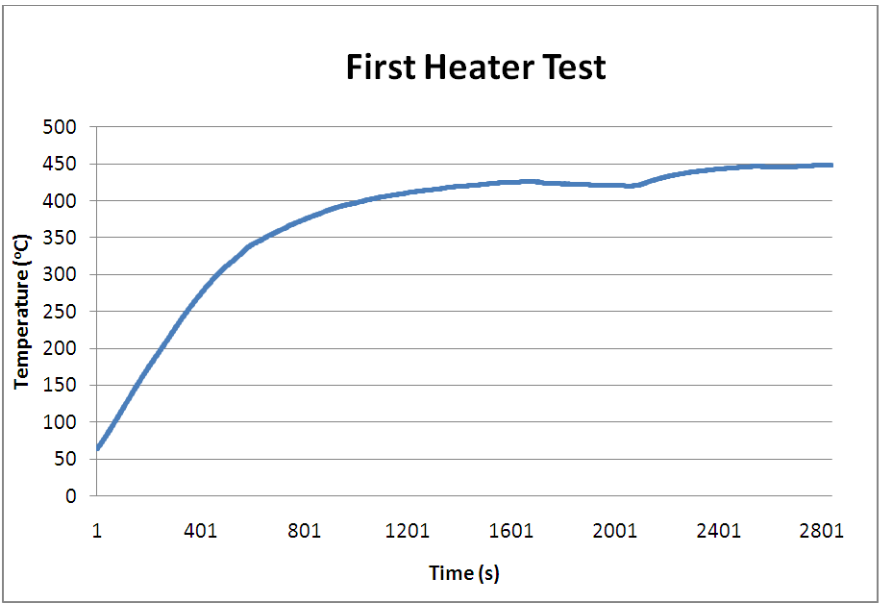

Figure 113. First Heater Test to Measure Substrate Temperature against Time

The heater can easily reach a temperature of 425°C. This confirms that the test plan can proceed. To be able to reach 450°C, however, the exhaust system used by the Centerline system to filter the air within the spray cabinet needs to be turned off. This is the phenomena that can be observed near the 2001st second. Once the exhaust system is turned off and there is no more air circulation cooling the substrate, the temperature increased from around 410°C to 450°C.

The substrate temperature tests were performed and analyzed. Figure 114 shows typical results of the temperature plot during the coating production. Both examples show a propellant gas warm-up time of 50 seconds. This warm-up period occurs near the substrate allowing some turbulent off-gas to flow over the substrate during this period. The substrate temperature will either rise (if initially at a low temperature e.g. 100°C) or fall (if initially at a high temperature e.g. 300°C) At this point the coating process occurs, and the substrate temperature will rise incrementally (each pass above the thermocouple can be seen in small temperature cycles) to peak at approximately the same temperature, around 300°C.

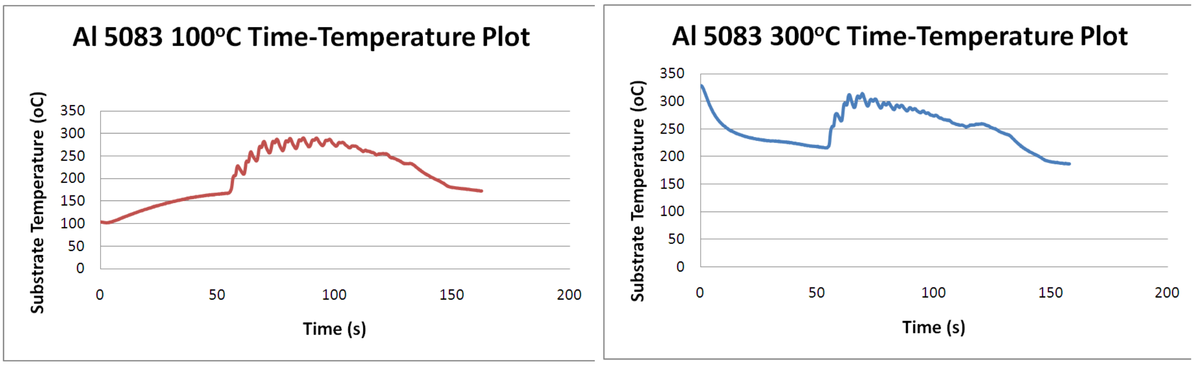

Figure 114. Al 5083 Substrate Temperature Curve Plots (100 and 300°C) Showing a Plot of Substrate Temperature over Time during the Deposition Process

The temperature plots indicate that the peak temperature is very similar. This leads to question why there is such a difference in coating thickness if there is seemingly almost no difference in peak temperature observed during the spray process. The process total heat is slightly higher when starting at higher substrate temperature i.e. even though the substrate cools down near the surface, the heat stored in the substrate quickly reheats the sample during spray time. (At 100°C, the average temperature seen by the substrate is 252°C. At 300, because the gas flow initially cools the substrate, the average temperature is 265°C, only slightly higher than at 100°C) This is shown in Figure 115. The starting temperature is also higher. Further tests are required to understand this phenomenon better.

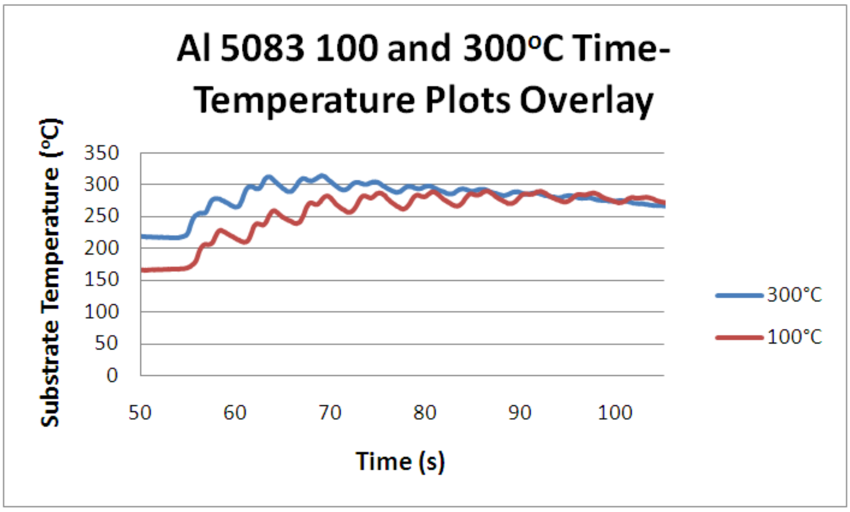

Figure 115. Combined Al 5083 Substrate Temperature Curve Plots Showing Higher Heat at 300°C

The results from the substrate temperature test for pure aluminum can be seen in Table 22. An increase in thickness, with a constant porosity value, was observed. Figure 116 shows that the increase in coating thickness is proportional to the substrate temperature. This will be important to recall once spray parameters are established for deposition shortly after the FSW process.

Table 22. Pure Aluminum Coating Thickness with Increase in Substrate Temperature

Substrate Temperature (°C)	Thick (μm)	Increase (%)	Porosity (%)
25	200 ± 16	0	2.4 ± 0.8
100	238 ± 18	19	2.7 ± 1.1
200	265 ± 19	33	2.4 ± 0.9
300	300 ± 30	50	2.3 ± 1.0
400	354 ± 18	77	1.9 ± 1.8

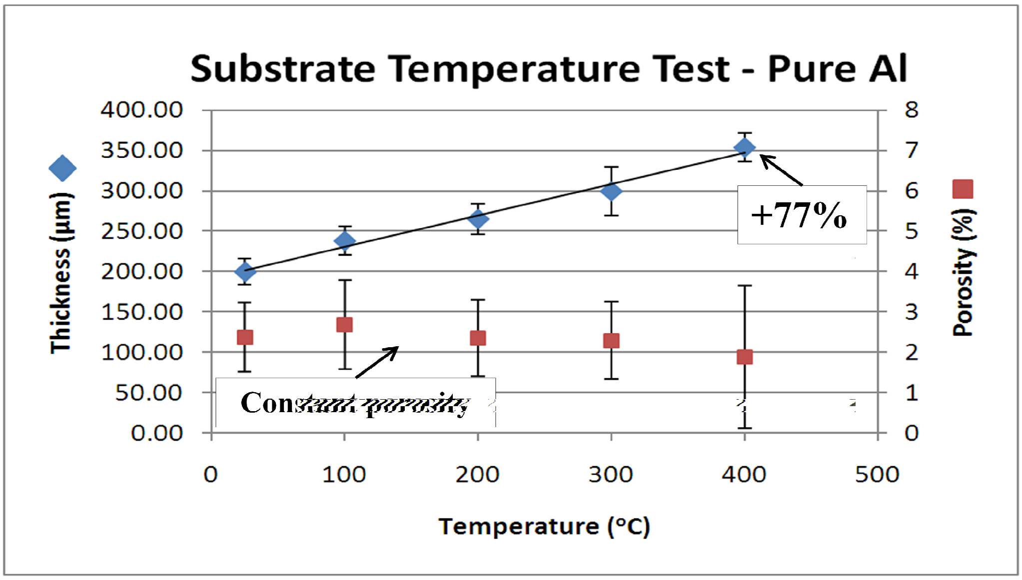

Figure 116. Pure Al Substrate Temperature Test Graph Showing Coating Thickness as a Function of Substrate Temperature

Al 5083 values are presented in Table 23. Once again, an improvement in coating thickness with substrate temperature is noted. However, there is a sudden jump in porosity between 100°C and 200°C. This discrepancy in porosity is likely due to nozzle clogging, which can affect the coating quality.

Table 23. Al 5083 Coating Thickness with Increase in Substrate Temperature

Temp (°C)	Thick (µm)	Increase (%)	Porosity (%)
25	174 ± 10	0	1.1 ± 0.5
100	163 ± 19	-6	0.4 ± 0.4
200	194 ± 22	12	3.8 ± 1.6
300	241 ± 26	39	3.4 ± 1.3
400	293 ± 20	69	4 ± 1.7

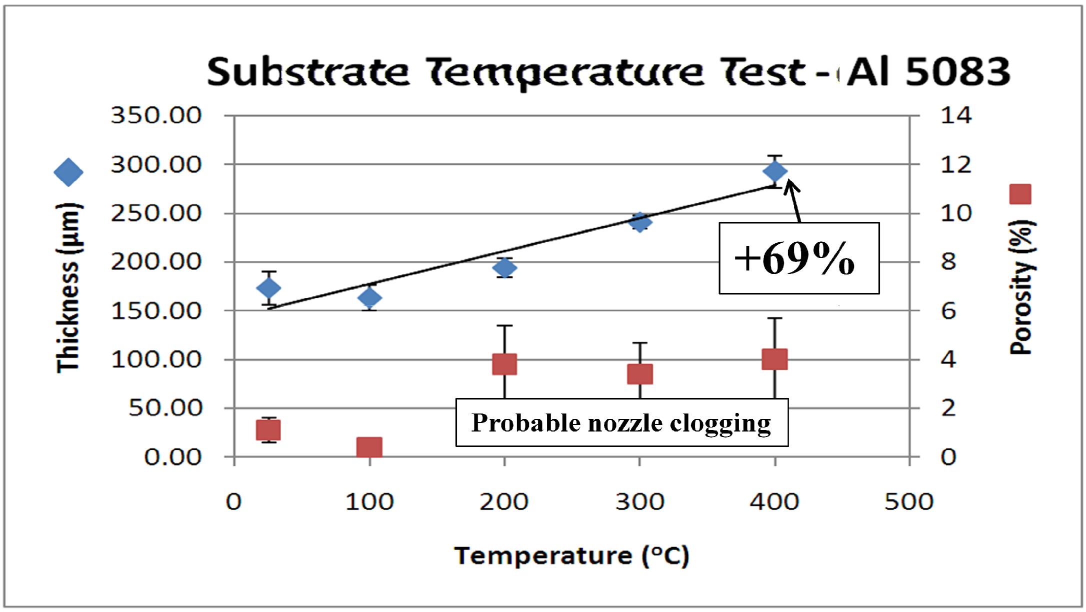

Figure 117. Al 5083 Substrate Temperature Test Graph Showing Coating Thickness as a Function of Substrate Temperature

To validate the results obtained, a clean orifice was used to produce a coating on a 400°C substrate temperature. The new coating was completed and analyzed. The resulting thickness was 224 ± 23µm and the porosity was 1.6 ± 0.7%. These results indicated that the porosity does not increase significantly with substrate temperature. This also points to the fact that the previous results where porosity increased drastically can be attributed to orifice clogging. The thickness increase between room temperature and 400°C is 30%. A new study was performed for the porous results. The new results are presented in Table 24 and show a more conservative 30% increase.

Table 24. New Al 5083 Coating Thickness with Increase in Substrate Temperature

Temp (°C)	Thick (µm)	Increase (%)	Porosity (%)
25	174 ± 10	0	1.1 ± 0.5
100	163 ± 12	-6	0.4 ± 0.4
200	176 ± 13	2	0.5 ± 0.5
300	195 ± 14	12	0.2 ± 0.1
400	224 ± 29	29	1.6 ± 0.7

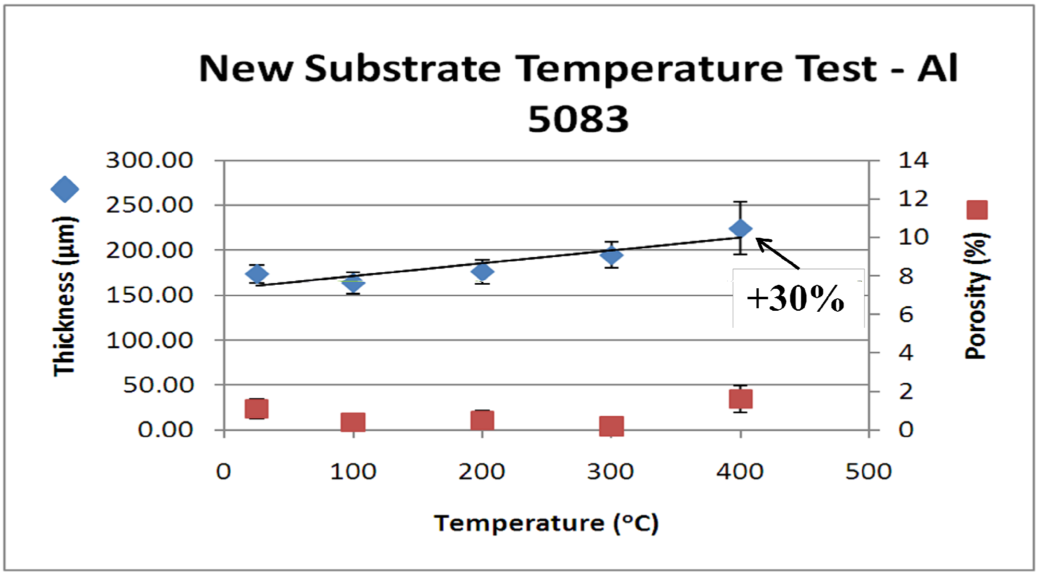

Figure 118. New Al 5083 Substrate Temperature Test Results Showing Increase in Coating Thickness with Increase in Substrate Temperature up to a 30% Increase at 400°C

Below are the results for Al 7075 (Table 25). It appears that this alloy is not affected by the substrate temperature. Figure 119 shows a decrease in coating thickness, but this is likely due to progressive nozzle clogging. There is no change in porosity as the coatings are always fully dense.

Table 25. Al 7075 Coating Thickness with Increase in Substrate Temperature

Temp (°C)	Thick (µm)	Increase (%)	Porosity (%)
25	191 ± 17	0	Fully dense
100	179 ± 13	-6	Fully dense
200	177 ± 10	-7	Fully dense
300	166 ± 7	-13	Fully dense
400	171 ± 17	-10	Fully dense

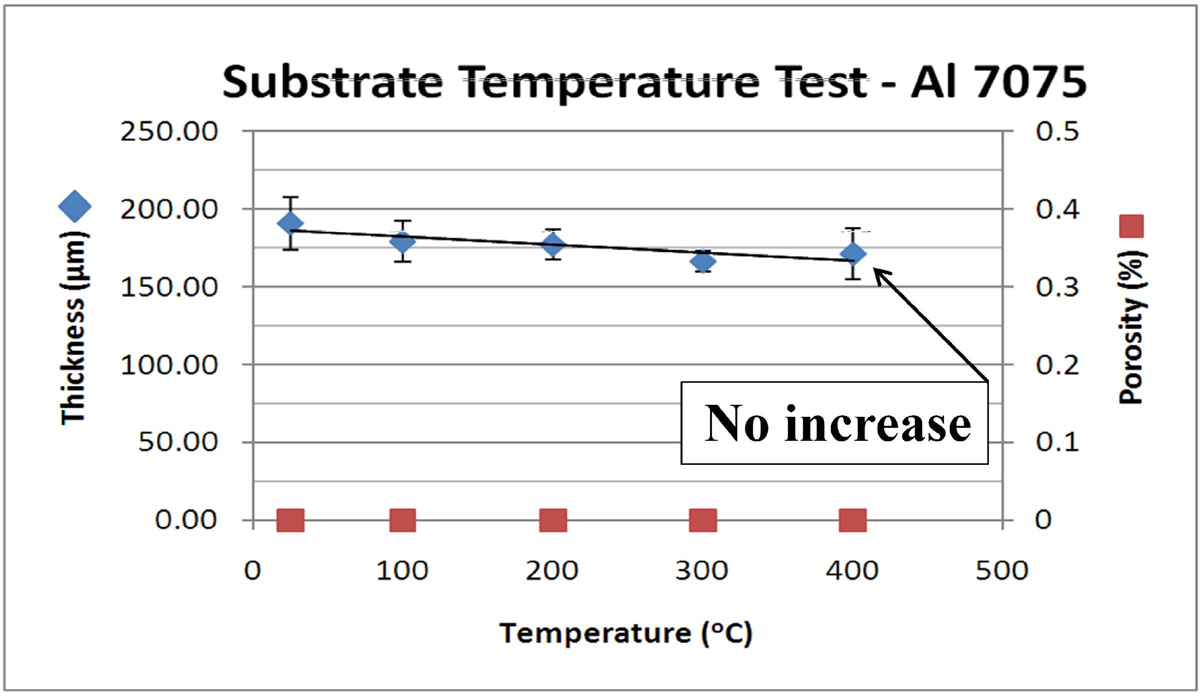

Figure 119. Coating Thickness as a Function of Substrate Temperature

In general, there was no observed impact of substrate temperature on coating properties for the Al 7075 coatings. Pure Al and Al 5038 are dependent on substrate temperature, showing a 77 and 30% increase in coating thickness. Table 26 presents a summary of the substrate temperature tests.

Table 26. Summary of Substrate Temperature Test Results

	Pure Al	Al 5083	Al 7075
Thickness at 25°C or Room (µm)	200	174	190
Thickness at 400°C (µm)	354	224	167
Increase in thickness from 25 to 400°C (%)	77	30	0 (slight clogging)

Therefore, to spray directly after the FSW process, the travel speed will have to be increased slightly. The increase in travel speed will depend on the actual temperature recorded during the spray.

6.4.3 Wipe test

Wipe tests are single-pass lines sprayed onto a polished substrate with optimal parameters but at very high travel speed. This prevents particle build-up (to form a coating) allowing for single-particle analysis. Wipe tests are useful for analyzing particle/substrate interactions in order to determine bonding mechanisms and other features of interest.

Wipe tests were performed on an Al 7075 substrate, polished for better particle observation. The goal is this test is to determine the mechanism leading to increased coating thickness. The optimized parameters from the first phase of this project were used to deposit these coatings. Each powder wipe tests were performed at 3 different substrate temperatures concurrent with Table 27. This was done to compare the impact of substrate temperature on bonding mechanisms and attempt to explain why coating thickness increases with substrate temperature.

Table 27.Wipe Test Summary

Test #	Powder	Pressure (Psi)	Temperature (^{o}C)	Powder Feeder Wheel RPM	Substrate Temperature (^{o}C)
Pure-Room	Pure Al	250	350	14	25
Pure-200	Pure Al	250	350	7	200
Pure-400	Pure Al	250	350	4	400
5083-Room	Al 5083	250	500	3	25
5083-200	Al 5083	250	500	1	200
5083-400	Al 5083	250	500	1	400
7075-Room	Al 7075	250	500	1	25
7075-200	Al 7075	250	500	1	200
7075-400	Al 7075	250	500	1	400

Traverse speed was the maximum robot traverse speed, 500 mm/s. This speed, along with a reduced powder flow rate was sufficient to leave individual particle deposition on the substrate.

6.4.3.1 Pure Al Wipe Tests

Because the Centerline SST-5001 powder does not have a spherical morphology, making visual conclusions on powder deformation cannot be done accurately. However, conclusions on substrate deformation and jetting can be done. In the case of pure Al, the mechanisms that lead to higher deposition efficiency cannot be observed with a wipe test. There was no observable jetting at any higher temperature. Substrate deformation due to particle impact remained constant throughout the temperature test range. This is shown in Figure 120, showing no increase of particle deformation or substrate deformation with increase in substrate temperature.

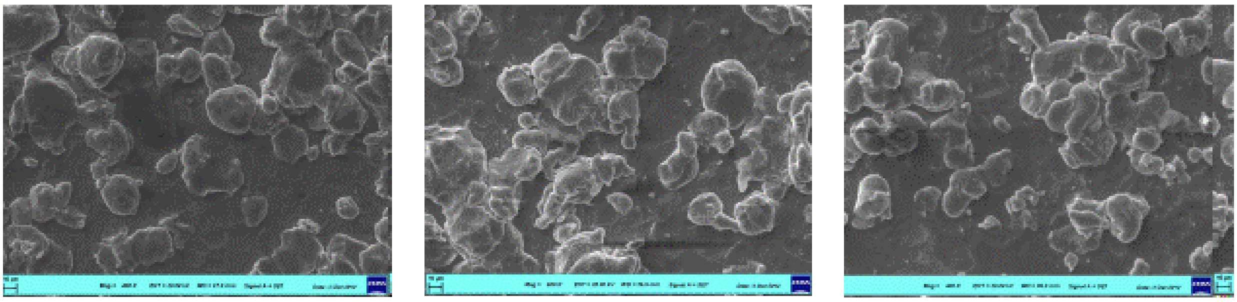

(a) (b) (c)

Figure 120. Constant Substrate Deformation for Pure Al (Centerline SST-A5001) Powder at (a) Room Temperature, (b) 200°C and (c) 400°C

6.4.3.2 Al 5083 Wipe Tests

Al 5083 coatings are about 60% of the hardness of bulk Al 7075. As the Al 7075 gets progressively hotter, there is deeper substrate indentation due to substrate softening and annealing (see Figure 121). There is also a larger deposition for the 400°C test. However, phenomenon such as jetting or metallurgical bonding to the substrate or between particles was not observed.

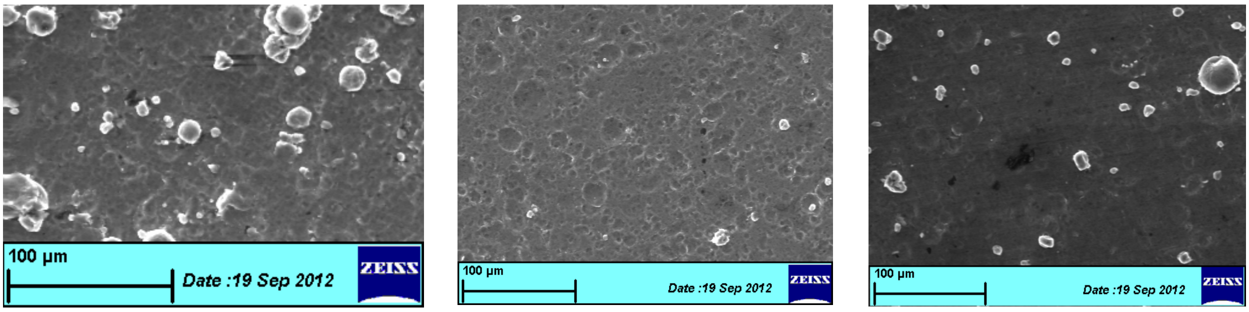

(a) (b) (c)

Figure 121. Slight Increase in Substrate Deformation for Al 5083 Powder at (a) Room Temperature, (b) 200°C and (c) 400°C.

6.4.3.3 Al 7075 Wipe Tests

As the substrate temperature gets progressively hotter, deeper substrate deformations occurs (Figure 122). This is similar to the Al 5083 results but in a more prominent fashion. Substrate jetting seems to initiate at the 200°C test (Figure 123). The powder does not seem to adhere to the jetted substrate. It has generally the same amount of deformation, which correlates with the fact that the incoming powder temperature is consistent throughout the test.

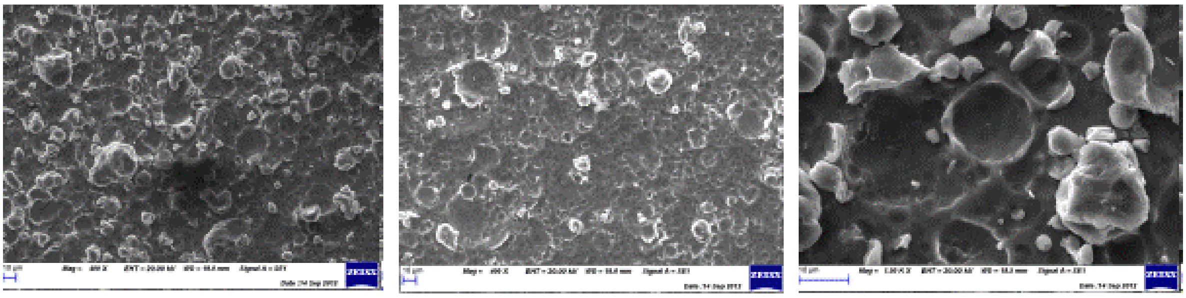
(a) (b) (c)

Figure 122. Increase in Substrate Deformation for Al 7075 Powder Wipe Tests at (a) Room Temperature, (b) 200°C and (c) 400°C. The Images Also Show Consistent Particle Deformation.

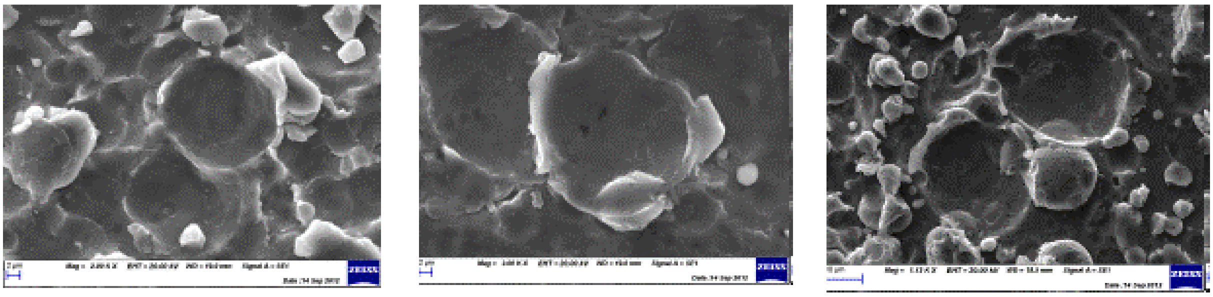
(a) (b) (c)

Figure 123. Substrate Jetting for Al 7075 Powder Wipe Tests at (a) Room Temperature (Non-Existent – Showing Substrate Deformation), (b) 200°C and (c) 400°C.

6.4.3.4 Wipe Test Analysis and Summary

These wipe tests were done to identify the underlying causes explaining the increase in deposition efficiency for pure Al and Al 5083 powders. However, the wipe tests did not provide a definite answer as to the mechanisms behind this phenomenon. It is clear however that an increase in substrate temperature does have an impact on the coatings and that each powder responds differently to this change in temperature. In every case, no significant increase in powder deformation was noted, which concurs well with the fact that the powder does not receive any additional heat before impacting the substrate. There is also typically an increase in substrate deformation with an increasing substrate temperature – this is probably due to the combined effects of precipitate dissolution and general high-temperature softening. The prominence of this effect will be dependent on the particle hardness – the harder the impacting particle, the greater the effect. This is why pure Al showed almost no increase in substrate deformation with increasing temperatures, while Al 5083 showed some increase and Al 7075 showed large increases.

The increase in deposition efficiency could be due to heat transfer through the coating. The first layer of particle is deposited as per usual (with only minor effects of substrate temperature on initial deposition as demonstrated in the sections above), and then gets heated by the substrate. This has two beneficial effects on the next layer of impacting particle. First, a softer layer will be more prone to mechanical anchoring (bonding) since deformation is easier. Secondly, the hotter surface will be more prone to metallurgical bonding. Assuming a constant input of kinetic energy from the particle which correlates to a constant temperature rise due to local adiabatic sheer instability, then a higher substrate temperature increases the chances of local particle melting, and metallurgical bonding.

6.5 Problems Encountered During Coating Production

Several spray problems have been encountered during this project. They have been organized in this section for organizational purposes and presented in chronological order.

6.5.1 Pure Aluminum Coatings Decrease in Performance

There had been a decrease to the quality of the pure Aluminum coatings after coating deposition had started. It was noticed that the pure aluminum coatings were slightly porous where the coatings obtained a few months ago were fully dense. It was concluded that this was due to the polishing technique used. The initial coatings cross sections were polished with inadequate polishing plates. These plates would smear the material instead of removing it. This would fill in the porosities and make the coating appear fully dense.

6.5.2 Decrease in Coating Thickness

At one point, coaitng thickness (i.e. deposition efficiency) dropped significantly for the two aluminum alloy (AA) powders - by close to 50%. Even though the deposition efficiency was reduced, the coatings produced were still fully dense. This was believed to be due to a feeding issue, preventing the regular powder flow from occurring and letting less powder make it to the nozzle. Troubleshooting led to several dead ends including air filtration issues, powder ageing, temperature gauge malfunction, and nozzle dimensional change. In the end, there were two issues identified that affected the results.

The first issue that was significantly contributing to deposition efficiency reduction was the powder storage environment. If the powder is left in an environment that is too humid (the laboratory is routinely above 60% relative humidity) then the deposition efficiency drops dramatically. Hence, for the same spraying parameters, thinner coatings than usual are observed. To solve this issue, all powders were moved to a powder storage cabinet in a small storage room. The storage cabinet, a fire-resistant locker, was fitted with a radiator and thermostat that maintains the conditions inside the locker to approximately 25% RH and 30^{o}C. Furthermore a dehumidifier was installed inside the small storage room which maintains the humidity inside this room to approximately 45% RH at room temperature (21-25^{o}C).

The second and most significant issue that was identified was orifice damage. Previously there was only one orifice to spray a variety of metal powders. One powder that was particularly destructive, Al 2024, altered the dimensions of the brass orifice significantly enough to reduce the deposition efficiency of the spray for this particular orifice.

It was noticed that all the sprays following the Al 2024 sprays had significantly lower deposition efficiency, yet maintained almost-to-fully dense porosity levels. (Note that other parameters, such as bond strength, were not measured). It therefore became important to measure the wear on the orifices, but most importantly to ensure that the orifices were clean.

This led us to purchase multiple new brass orifices, each of which were marked and to be used for only one specific type of powder e.g. aluminum alloys. Because the AA powders clog the orifice this orifice had to be cleaned often. Recurring NaOH baths lead to progressive orifice damage, eroding the material, therefore increasing the throat area inside the orifice over time. The extent of this damage is measured by noting the maximum temperature that can be achieved with the orifice. A lower maximum temperature (i.e. below $500^{o}C$) indicated that the throat diameter has increased. This increase in throat area leads to an increase in gas flow rate. In order to reach the same temperatures, the heater power must be increased. If the throat diameter becomes too big, the gas heater will not be able to compensate for the increased flow rate and the orifice will have to be replaced.

Another possible cause to the thickness reduction could be particle size. As the powder was procured approximately one year ago, the source container is nearly empty and the powder used is the one at the bottom. Over this year, the smaller particles could have separated to the bottom, leading the current powder to have a smaller particle distribution than before. New powder has been ordered.

To ensure that the deposition efficiency is as good as previously measured, the powder must have been inside the powder cabinet for at least 24 hours or dried at $60^{o}C$ for 30 minutes to 1 hour. If Al 5083 is sprayed, the designated Al 5083 orifice must have been cleaned in a sodium hydroxide bath for 24 hours beforehand. All other preparation steps and spraying parameters have remained the same.

6.5.3 New Deposition Efficiency Problems

A gradual reduction in deposition efficiency was noticed over a period of a few months. Analyzing over several powder / nozzle combinations and in different systems, the conclusion was that the heater was defective and needed to be replaced. This was due to gradual clogging of the heater from improper powder ejection procedures after spray, leading to clogging and a reduction of spray pressure and flow rate. A new heater was ordered and the old heater was replaced. A new procedure to avoid clogging the new heater was put in place. This procedure involves setting a specific order to shut down the equipment after the deposition process to completely empty the powder tube before the propellant gas flow is stopped. If powder still flows in the orifice after the propellant gas flow is stopped, powder could be forced to travel upstream to the gas heater, melting and collecting around the heater's heating coils.

6.5.4 New Problems since New Heater Installation

Once the new heater had been installed and tested exhaustively, a qualitative difference when spraying Al 7075 was noticed. Specifically, there is poor adhesion when starting the spray, and that the initial first pass would peel off and stick to the rest of the coating, leaving a large surface defect on the start of the coating. (See Figure 124 and Figure 125 showing initial coating peeling)

Initially the culprit was through to be the surface preparation method. Both the machine shop's grit blast and the Cold Spray Laboratory grit blast unit were used prepare the surface of test samples. This produced similar results, indicating that the new Cold Spray Lab grit blast was working properly. Tests were then run to test the edge effect. Edge effects occur when the deposition area overlaps the edge of the samples and potentially causes disturbances in the coatings. Sprays were started in the center of the substrate as shown in Figure 125. This still had the same effect, meaning that edge effects were not a factor.

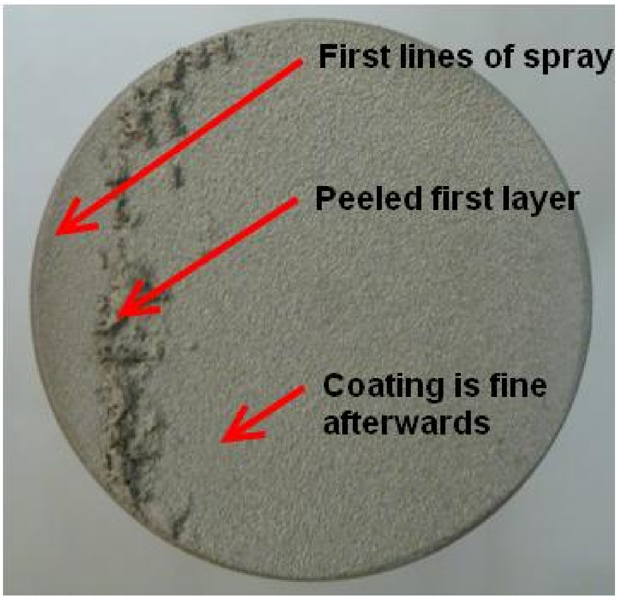

Figure 124.Initial Surface Defect when Spraying AA 7075

Figure 125. AA 7075 Spray Started on the Substrate to Eliminate Potential Edge Effects

The last theory regarded the heater. The previous heater was replaced because it could not reach the correct stagnation temperature. This was because the heater was progressively constricted from powder ingress clogging the multiple small cross sections of tubing. Therefore, there was less flow rate. The increased flow rate could yield higher particle velocities. This could cause increased internal stresses yielding to poorer adhesion. Several temperature trials were run to remove this effect. The first was to do a full spray without feeding powder, creating a very hot substrate. This worked well, however results obtained using this technique are not comparable to previous results because of the significantly different initial substrate temperature. A second spray test was performed where only the first line of coating was preheated. Even in this condition the spray was successful. Therefore, the previous results are still valid and comparable to this technique because the increase in heat addition is very small and contained only within the first line of spray.

6.5.5 Problems Summary

This concludes the major issues encountered with the system. A summary is presented below in Table 28.

Table 28. Issues Encountered Summary, with Source of the Issues and Solution

Problem	Source	Solution
Decrease in Al coating quality	Polishing procedure	• Change polishing procedure
Decrease in deposition efficiency	• Power humidity • Orifice damage • Powder age	• Heat / dry powder cabinet, • Assign new orifice for individual powders, • Order new powder
Decrease in deposition efficiency	Heater clogging	• Replace heater • New spraying procedure
Al 7075 coating peeling	Increased flow rate in the new heater leads to higher particle velocities and coating stress leading to de-bonding at low substrate temperatures.	• Preheat first line of spray

7 Secondary Research Project #1: In-Depth Analysis

This first secondary research project is a collection of experiments that were performed to gain a better understanding of the FSW process and how it affects the CGDS coatings (and how the CGDS coatings affect the FSW properties). These tests are mostly mechanical in nature, and include coating hardness, CGDS tensile properties, and other tests (new Al 7075 powder qualification, effect of insulation on substrate temperature, and effect of nozzle clogging on deposition efficiency).

7.1.1 Coating Hardness

Coating hardness was performed to verify the hardness of the final optimized coating, of the substrate it was created on and to measure this difference with various substrate temperature tests. The substrate temperature tests at room temperature and 400°C were tested. Results are presented in Table 29. Spray parameters are shown in Table 14 on p.90.

Table 29. Substrate Temperature Test Hardness Testing. Bulk Al 7075-T651 Hardness is 180-190 Hv

Powder	Temperature Test (°C)	Area	Weight	Average HV	Min HV	Max HV
Al 7075	25	Coating	HV0.1	149 ± 5	137	154
		Substrate	HV0.3	172 ± 3	169	176
	400	Coating	HV0.1	138 ± 6	128	145
		Substrate	HV0.3	101 ± 2	100	105
Al 5083	25	Coating	HV0.1	125 ± 8	112	137
		Substrate	HV0.3	175 ± 5	170	181
	400	Coating	HV0.1	92 ± 12	73	110
		Substrate	HV0.3	102 ± 1	101	104
Pure Al	25	Coating	HV0.05	53 ± 9	32	62
		Substrate	HV0.3	191 ± 2	189	194
	400	Coating	HV0.05	52 ± 6	40	64
		Substrate	HV0.3	112 ± 2	109	114

For all tests, the Al 7075 substrate hardness drops from 180-190 HV at room temperature tests to a low 100-110 HV at the 400°C test, which represents 41.5 ± 0.2% of hardness loss. This trend correlates well with bulk Al 7075 theory presented in the literature. The loss of harness is due to the coarsening of precipitates at high temperatures.

The Al 7075 coating suffers very little softening between tests (from 149 to 138 Hv). This is counterintuitive when comparing with the substrate. However Al 7075 is not heat treated – it is in solid solution. Therefore, there are no grain precipitates to coarsen. At high temperatures, annealing will take place, removing some stresses – and therefore reducing the hardness – within the coating.

The aluminum 5083 coating sees a 26% reduction in hardness, from 125 to 91 Hv. This is because the strength of this alloy is in solid solution. High temperatures (above 65°C [54]) will weaken this alloy. Annealing effects also take place.

The pure aluminum coating hardness does not change with an increase in substrate temperature. This is plausible since pure aluminum is not strengthened by any means including heat treatment or solid solution. Therefore its coating hardness should only be a factor of strain hardening.

7.1.2 Tensile Properties (Dogbone Samples)

It was decided to measure the tensile properties of a pure CGDS coating. To do so, dogbone samples have been machined from thick coatings produced with pure aluminum powder. The samples were machined and tested conforming to the ASTM E8 standard [55].

The substrates used for the dogbone samples are 19 x 110 x 6.35mm sand blasted Al 6061 substrates. (80 grit aluminum oxide grit at 45°, approx. 70 psi used). A 2 to 4 mm pure Al coating is deposited on this substrate. The coating then goes through a series of machining steps. These consist of first facing the coating flat, then milling out the shape of the dogbone in the coating (see Figure 126). The faced coating is then glued onto a block to secure it in place and the substrate is machined off the coating. The glue is dissolved leaving the proper dogbone dimensions in the cold spray coating. Once the dogbone samples are produced (Figure 127 shows a sample ready for testing), they are tested in tension, and their properties (yield strength and elongation to failure) are determined. The ASTM E8 standard used for the shape of the dogbone did not indicate a pulling speed. A pulling speed equivalent to the one used in the ASTM C633 standard (bond plug adhesion test) was used.

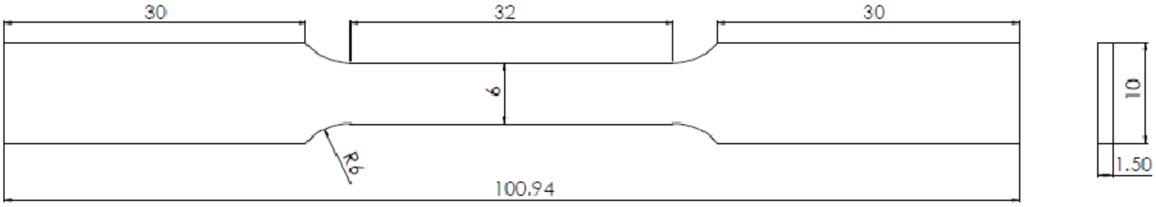

Figure 126. Dogbone Shape Used in the Cold Spray Tensile Tests as Presented in the ASTM E8 Standard [55]. Dimensions are in Millimetres

(a) **(b)**

Figure 127. Machined Dogbone Sample (a) Front View (b) Side View

In total, 22 dogbone samples were created and machined. As described in Table 30, each set of 3 or 4 had different production steps. This was done in order to make various comparisons. Set one is the control group. Set 2 was created to measure the effect of annealing when compared to the control group. The annealing procedure involved putting the samples in the oven at 350°C for 2 hours, removing from the oven and air cooling until room temperature. In some cases the samples were prepared in the "width-wise" direction, while other samples were prepared in the "length-wise" direction. This indicates that the direction of load in the tensile test was performed perpendicularly to the spray direction ("width-wise" – consult Figure 128) or parallel to the spray direction ("length-wise" – consult Figure 129).

Table 30. Dogbone Production Procedure. Comparisons Between Sets 1 and 4, Sets 1 & 2 and Set 2 & 3 are Possible

Set	# Dogbones	Process 1	Process 2	Process 3
1	4	Spray – width-wise	Machine	N/A
2	4	Spray – width-wise	Machine	Anneal
3	4	Spray – width-wise	Anneal	Machine
4	4	Spray – length-wise	Machine	N/A
5	3	Spray – length-wise	Machine	Anneal

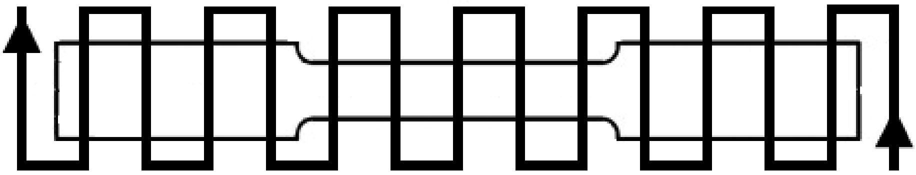

Figure 128. Nozzle Path during "Width-Wise" Spraying, Superposed on Final Dogbone Shape

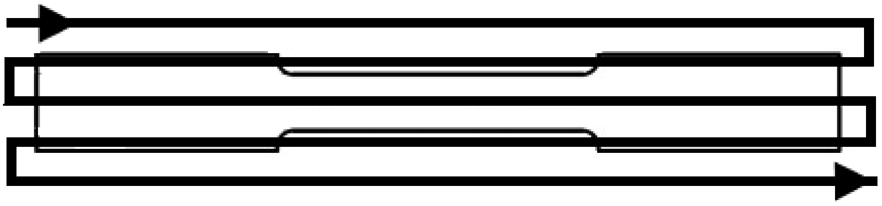

Figure 129. Nozzle Path in "Length-Wise" Spraying, Superposed on Final Dogbone Shape

Set 3 was done due to a discussion involving residual stress. It was suggested that annealing before machining will incur less residual stresses in the samples during the machining (samples are softer during machining, therefore easier to machine incurring less stress overall), and therefore less stress in the final coating. Set 4 will be compared with set 1’s results to compare the difference between spraying length-wise and spraying width-wise. Set 5 is compared with set 4 to discern a difference in annealing in the length-wise sprayed samples.

The results from this study are summarized in Table 31. A complete list of individual results is presented in Appendix B. Typical brittle and ductile stress-strain curves are shown in Figure 130. These results have been observed in all as-machined and annealed samples respectively.

Table 31. Spray Summary, Organized by Set, Showing UTS and % Elongation for all 5 Dogbone Sets

Set	# / Set	Spray	Then	Then	UTS	% Elongation
1	4	Width	Machine	N/A	66 ± 1	0.6 ± 0.1
2	4	Width	Machine	Anneal	76 ± 22	1.4 ± 0.7
3	4	Width	Anneal	Machine	83 ± 11	1.2 ± 0.3
4	4	Length	Machine	N/A	85 ± 15	0.7 ± 0.1
5	3	Length	Machine	Anneal	84 ± 3	2.8 ± 0.1

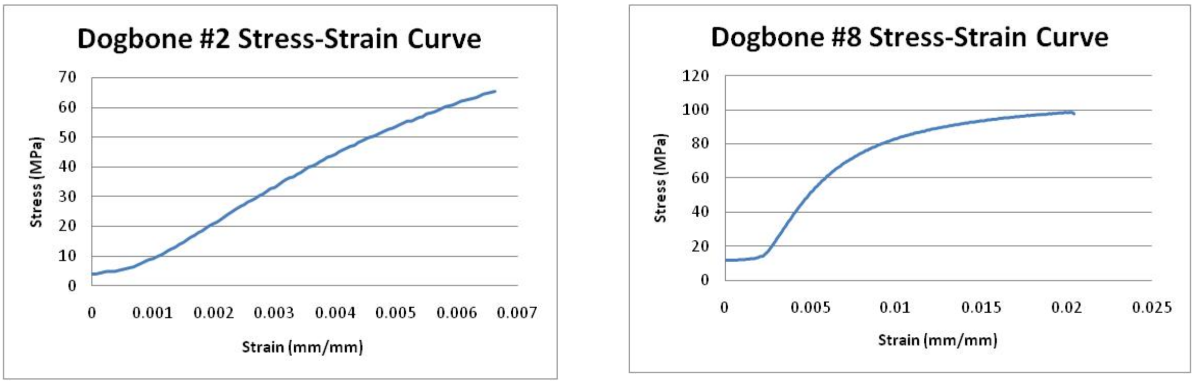

(a) **(b)**

Figure 130. Dogbone Stress-Strain Curves Showing (a) Brittle Fracture in Dogbone #3 and (b) Ductile Fracture in Dogbone #6

These results were generally expected, since similar results were obtained with copper samples. The study pinpointed the UTS of as-is copper cold sprayed dogbone coatings to approximately 25 MPa (3.625 ksi) and the elongation to failure to 0.1% [53]. There is little standard deviation in set 1 and set 5 samples. The results also indicate that length-wise spraying produced UTS values 50% higher than width-wise spraying and that annealing has no effect on the UTS of length-wise spraying. To try to explain these results the fracture surface from sets 1, 2 and 5 were analyzed in the SEM for signs of metallurgical bonding. Results are shown in the Figure 131 to Figure 134.

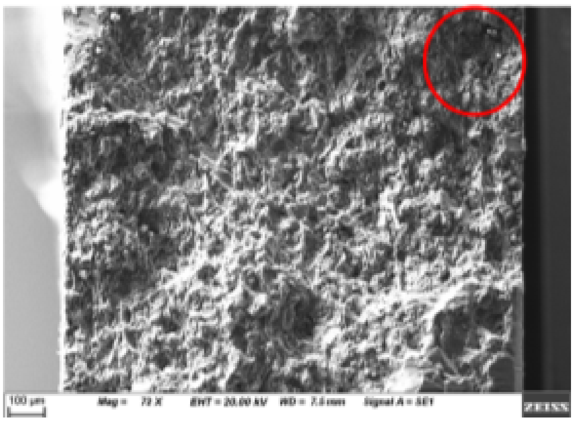

Figure 131. Set 1 Dogbone Fracture Profile Overview with Circled Metallurgical Bonding Area

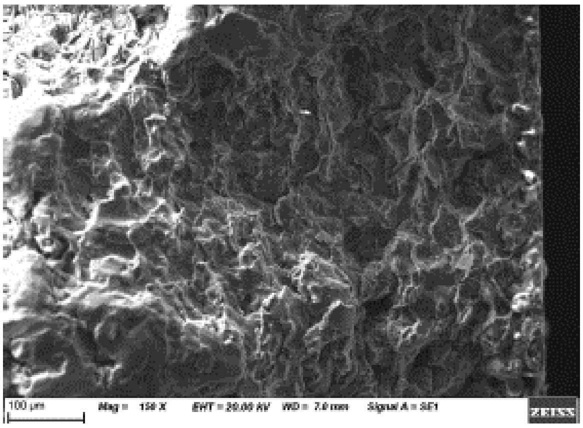

Figure 132. Metallurgical Bonding Section Enhancement in Set 1 Dogbone

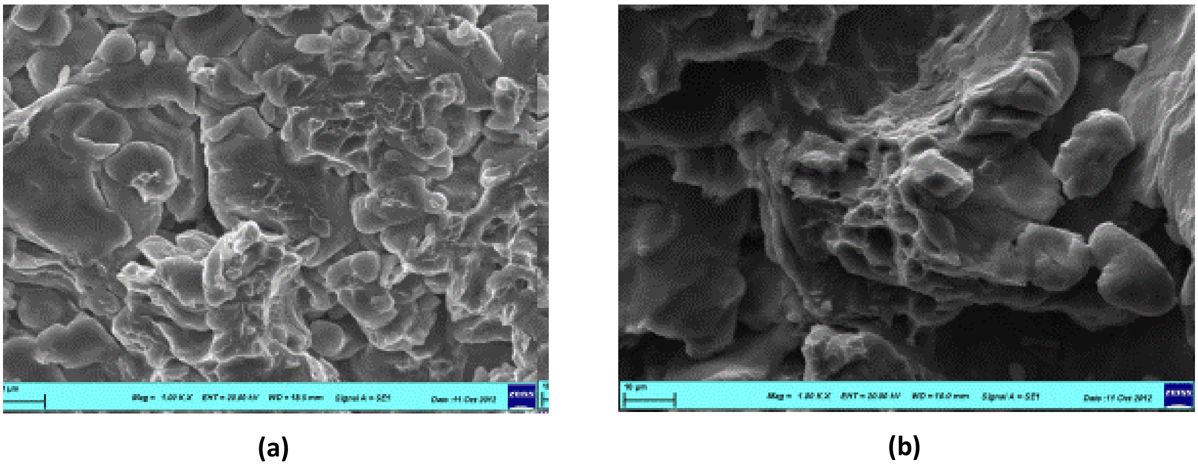

Figure 133. Metallurgical Bonding in Set 2 Annealed Dogbone Samples (a) Dogbone 4 and (b) Dogbone 6

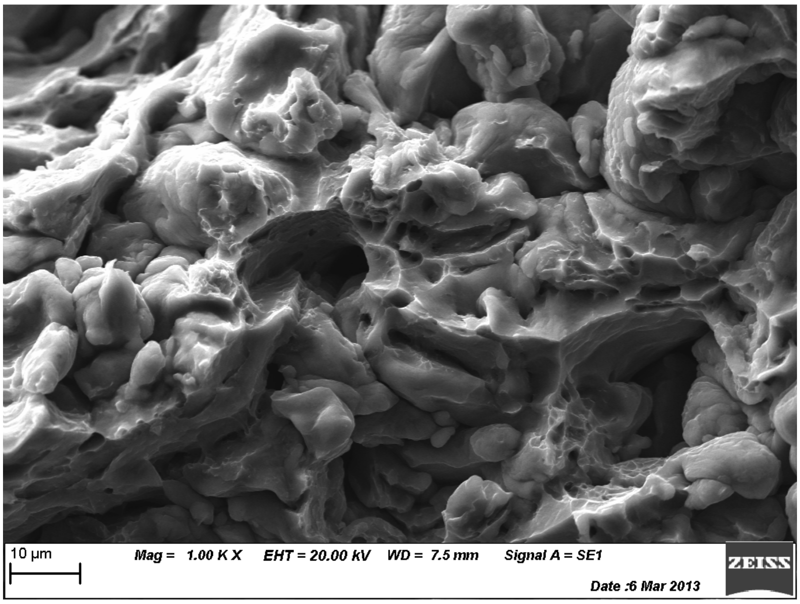

Figure 134. SEM Image of Dogbone 17 - Length-Wise Spray and Annealed Sample (Set 5) Showing Significant Signs of Metallurgical Bonding

As shown in Table 32, annealed samples showed increased elongation to failure. This can be attributed to an increase in metallurgical bonding since little metallurgical bonding is seen in samples that were not annealed (set 1) and high metallurgical bonding in annealed samples (set 2). This is also plausible since metallurgical bonds behave similarly to bulk material i.e. ductile fracture, as compared to a more typical brittle cold spray failure. Therefore, it is reasonable to assume that as the relative metallurgical bonding increases, the elongation to failure will increase. Also, a length-wise orientation produces more metallurgical bonding at the fracture surface.

Table 32. : Correlation between Dogbone Metallurgical Bonding and UTS & Elongation to Failure

Dogbone # (set #)	Temper	UTS (MPa)	Elongation to Failure (%)	Metallurgical bonding total area
1 (1)	As-is	66	0.8	Very low
6 (2)	Annealed	99	2.0	High
17 (5)	Annealed	87	2.8	Very high

Discerning features other than metallurgical bonding in SEM images is more difficult. In one of the length-wise samples, a macroscopic evaluation lead to the discovery of discernable passes across the failure profile (see Figure 135). The length between discernable peaks/valleys formed in the profile was approximately the spray increment of 1mm. The angle of these discrepancies was approximately 51 degrees, which is exactly the angle that would be formed by a 6.3mm nozzle creating single-pass 3.9mm coating (which is this case). This finding indicates that the interface between passes behaves differently than the line itself.

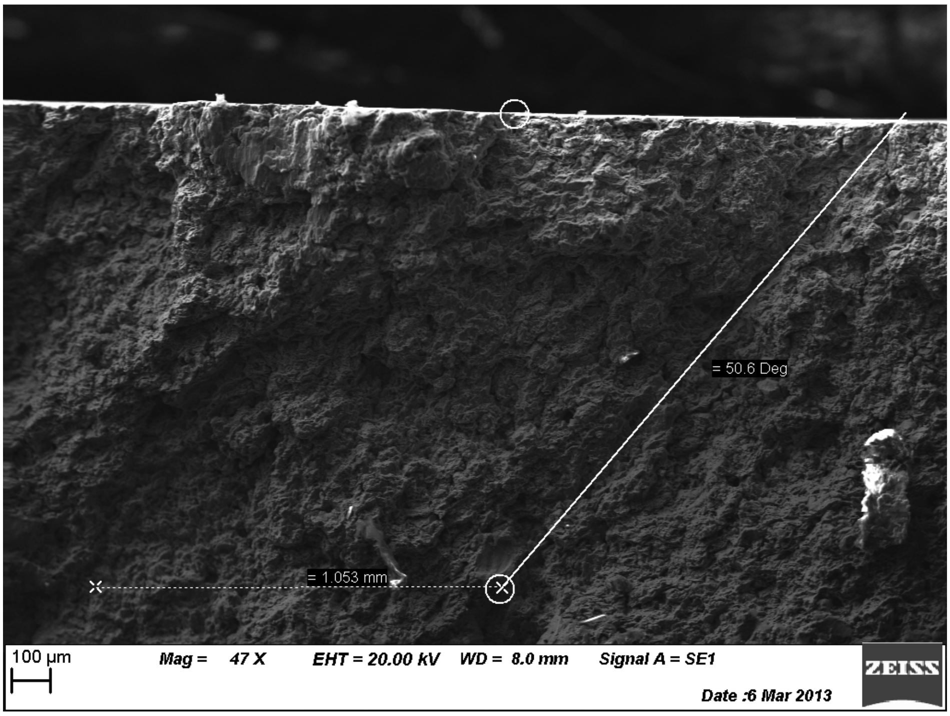

Figure 135.SEM Image of a Set 5 Dogbone (Sprayed Length-Wise and Annealed) Showing Signs of Passes Across the Failure Profile

To try to discern more features of these pass interfaces, dogbone samples were cut, mounted and polished. They were then etched in a few solutions for various periods of time until a suitable etch/etching time combination was found. The final combination was selected based on its ability to adequately reveal particle interfaces. The etching preparation selected was to immerse the sample for 10-15 seconds in a solution of 10g of NaOH in 90 mL of water at 70^{o}C. The results of this etching process and inspection are presented in Figure 136 to Figure 137. However, no discernable features can be made. Particle deformation seems consistent and significant.

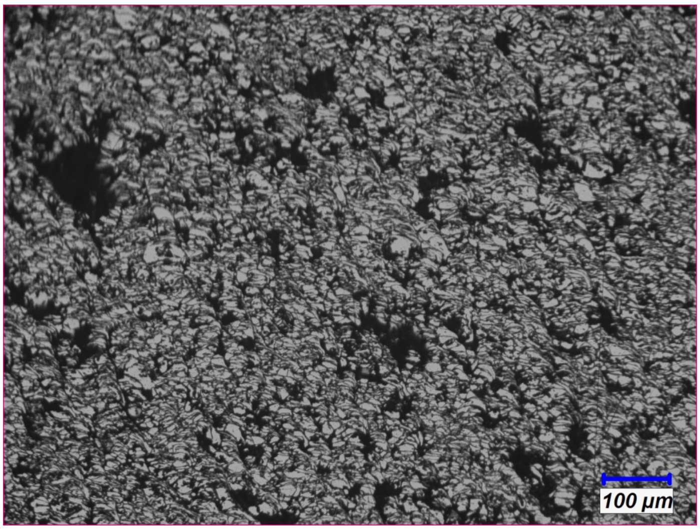

Figure 136. Tensile Sample #9 (Set 1: Width-Wise Un-Annealed Sample) after Etching

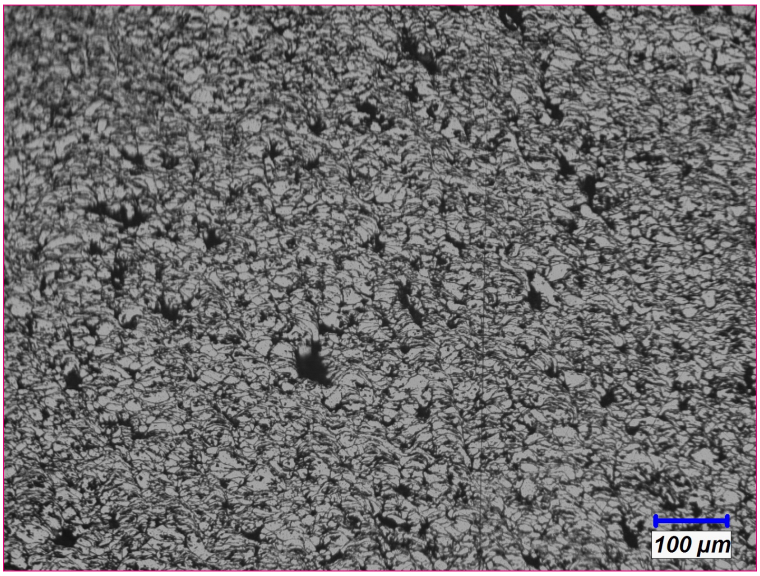

Figure 137. Tensile Sample #7 (Set2: Width-Wise, Annealed) after Etching

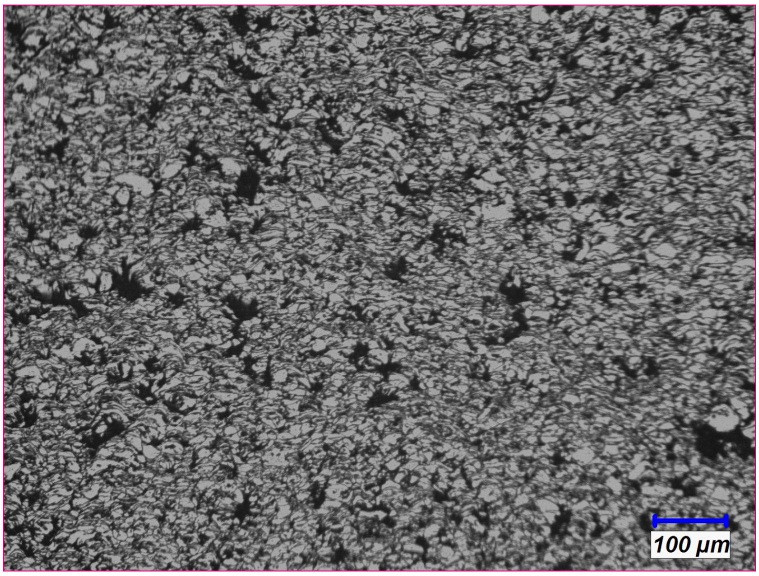

Figure 138. Tensile Sample #13 (Set 4: Length-Wise, Un-Annealed) after Etching

There seems to be no crystallographic difference between the length-wise and width-wise samples. Considering that the only factor between the two orientations seems to be the concentration of metallurgical bonding regions, a theory has been postulated to explain the difference in UTS. The increase in strength between spraying length-wise as compared to width-wise is most likely due to better particle bonding within spray lines. A spray line is a linear “fibre” formed by a continuous deposition from the nozzle as shown in Figure 139.

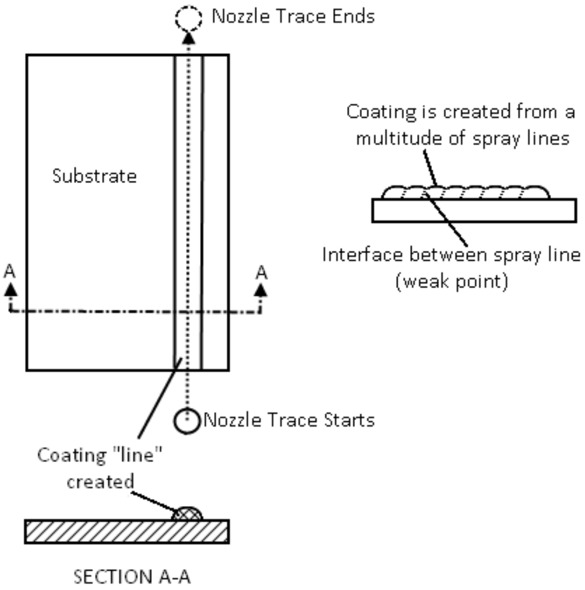

Figure 139. Illustration of Spray Lines Showing the Weak Points in the Coating

There is more metallurgical bonding within these fibres due to the concentrated heat generated by the nozzle gas, coupled with gas shielding from the bow shock generated at the substrate. (This could reduce the oxide formation resulting in better particle bond). These lines are superimposed (by multiple nozzle passes) to form coatings. However the interface strength between the fibres is not as strong because the previous fibres have had time to cool down. This means the layer have a full oxide coating, and are less prone to deformation and mechanical anchoring from impacting particles. To summarize, there is high bonding and cohesion within spray lines (therefore a higher strength and ductility), and little cohesion between spray lines.

When performing tensile tests in the width-wise direction, the fibres are perpendicular to the spray direction. The weak point will be the interface between the lines, and a brittle failure will occur. Annealing the sample will create metallurgical bonding between the spray lines, increasing the UTS and the elongation to failure.

When performing tensile tests in the length-wise direction, the fibres are aligned with the direction of tension. The UTS and elongation will be higher since even without annealing since stronger bonds are present. Annealing will have little effect for this reason.

To reiterate, the failure mechanism for the width-wise and length-wise samples is therefore different. For the width-wise samples, the weakest point is between the lines of spray. The failure is therefore of cohesion between passes. During annealing metallurgical bonds form between particles, which strengthen the interfacial bond between passes. For the length-wise samples the failure is due to crack initiation, most probably at an already present void (porosity). A defect needs to be started in order for crack propagation to occur. Since the void is most likely initiated at the same stress value, then the length-wise samples will not benefit from annealing and metallurgical bonding.

For the time being, it is uncertain whether or not the large standard deviation in samples is due to the nature of the process, or to the many sources of error in the process. These may include different spray days, powder batch, humidity and size, machining technique used, machinist performing the job (attention to detail), etc. To eliminate these external factors mentioned, additional tensile samples will be produced. These samples will be smaller (Figure 140), and created out of a single plate coated at once as shown in Figure 141. This will eliminate the variability with the spray conditions and the spray parameters. It will also eliminate the machining uncertainty. A spray and test layout (has established to spray, machine and test these small dogbone samples. Once the results from these new tests are obtained, the coating tensile theory will be finalized.

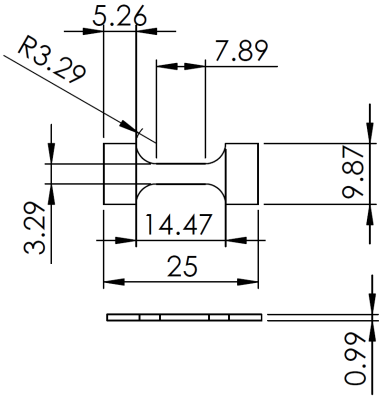

Figure 140. Tensile Specimen Dimensions. Values are in Millimetres

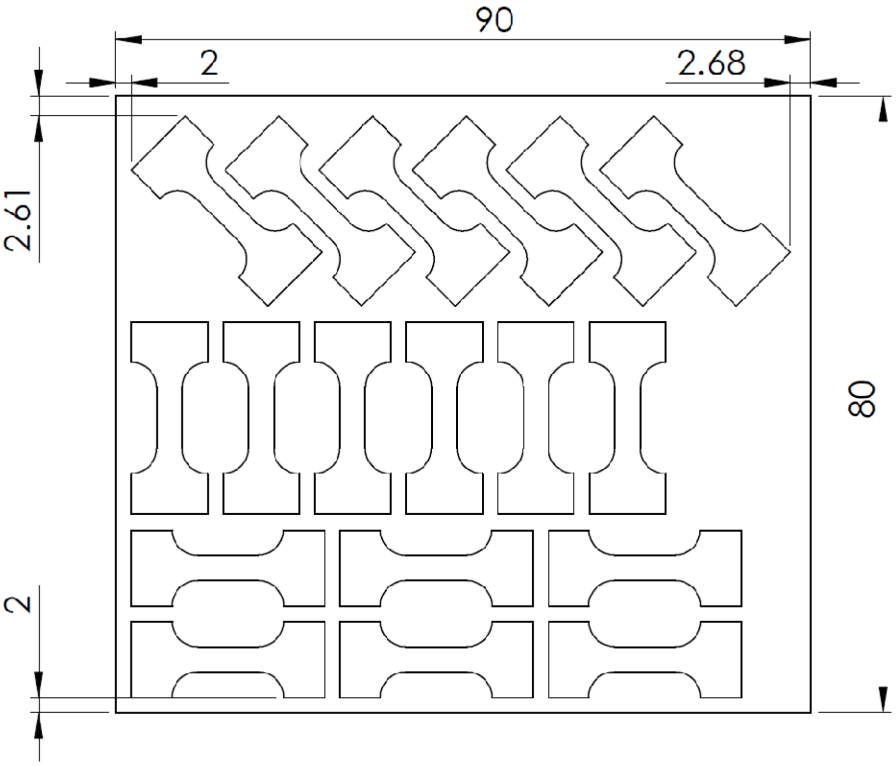

Figure 141. New Tensile Specimen Plate Layout. Dimensions are in Millimetres

7.1.3 Other Projects

7.1.3.1 Centerline 7075 Powder Qualification

This section described the work that was undertaken to optimize and characterize a new Al 7075 powder, the Centerline SST-5007 powder.

Once the powder was received it was analyzed in the SEM. The particle shape is spherical, with a qualitatively smaller particle average than the currently used Valimet-sourced powder. The Valimet powder's average particle diameter is 22 µm while nearly all the observable SST-A5007 particles are below 20 µm. A visual comparison of both powders is presented in Figure 142. All other factors constant, this should decrease the time before orifice clogging since smaller particles of similar hardness deposit more easily.

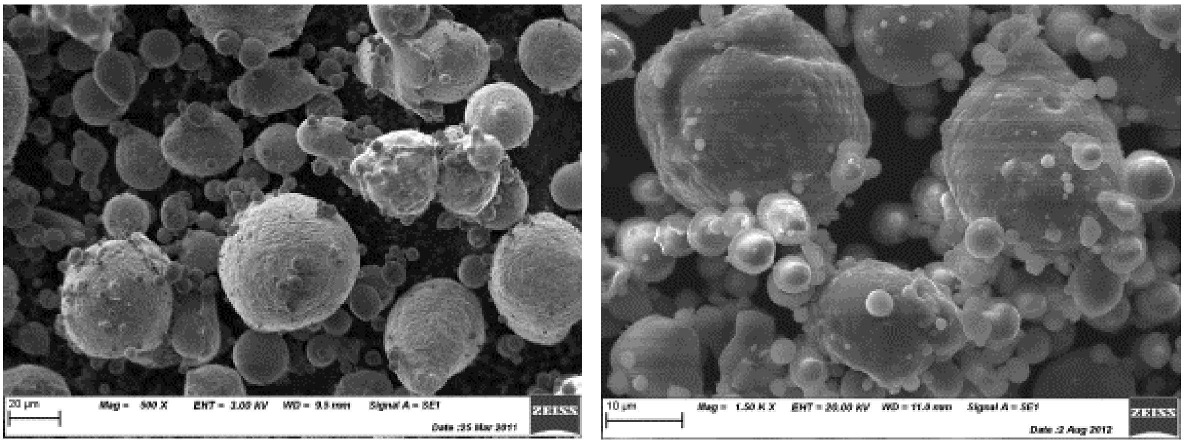

(a) **(b)**

Figure 142. Al 7075 Powder Sourced from (a) Valimet and (b) Centerline

Preliminary sprays have been conducted to optimize the deposition efficiency of the powder. A list of sprays performed is presented in Table 33 below. The clogging time for the Centerline powder is the same, at approx. 15 minutes.

Table 33. Centerline Al 7075 Powder Spray Optimization Results. Only Variable Parameters are Shown

#	Pressure (psi)	Temperature (°C)	120-Hole Wheel RPM	Thickness (µm)	Porosity (%)
1	250	500	3	68 ± 9	0.8 ± 0.7
2	250	500	6	178 ± 7	0.8 ± 0.3
3	250	400	3	22 ± 7	Too thin
4	200	500	3	179 ± 29	1.2 ± 0.8

Table 33 shows that spray #4 has a similar thickness and porosity for a lower powder flow rate (RPM). Therefore these parameters are optimal. However, a higher pressure such as spray #1 should be beneficial as it is for the Valimet powder. (Using the Valimet powder with the #1 spray parameters yielded a fully dense coating with a thickness of 588 ± 43 µm.)

To confirm these uncharacteristic results, the sprays presented were redone, resulting in the data shown in Table 34. Some potential factors were identified that influenced the spray quality. The first was the influence of clogging. The second is the influence of a progressively hotter vice (substrate holder) as more coatings are sprayed in the same period. This effect occurs when multiple coatings are deposited subsequently. The first sample will be held by a room temperature vice. During the spray, off-gas and conduction through the sample will heat up the vice. The next sample will then get heated by this warm vice, increasing its initial substrate temperature. In most cases, as shown in section 6.4.2, this was shown to improve the coating quality and deposition efficiency. Therefore, spraying an identical coating 2 or 3 times in a row will yield different results.

Both these factors (clogging, vice temperature) are influenced by the spray time. To eliminate these factors the coating order was reversed. Two additional sprays were also performed afterwards as shown in Table 34. Spray #5 tests the impact of the clogging factor by spraying the same parameters as test #1 at the end when the nozzle is more clogged. Spray #6, consisting of an insulated substrate, provides data on the impact of vice temperature on coating quality. Results are shown in Table 35.

Table 34. Parameters and Order for the Centerline SST A5007 Sprays Performed this Month

Previous Order	Test #	Pressure (psi)	Temperature (°C)	Wheel RPM	Wood Insulation?
4	1	200	500	3	No
3	2	250	400	3	No
2	3	250	500	6	No
1	4	250	500	3	No
N/A	5	200	500	3	No
NA	6	200	500	3	Yes

Table 35. Centerline SST-A5007 Spray Results as Compared to the Previous Month's Results (if Applicable)

Test #	P (Psi)	Temp (°C)	Wheel RPM	Previous Results		New Results		
				T (μm)	Por. (%)	T (μm)	Por. (%)	Powder Feeder Pressure (kPa)
1	200	500	3	179 ± 29	1.2 ± 0.8	541 ± 30	0.5 ± 0.3	-17
2	250	400	3	22 ± 6.5	Too thin	430 ± 42	0.2 ± 0.2	-8
3	250	500	6	178 ± 6.7	0.8 ± 0.3	618 ± 24	0.8 ± 0.3	+4
4	250	500	3	67.5 ± 8.7	0.8 ± 0.7	417 ± 29	6.4 ± 1.3	+15
5	200	500	-	-	-	410 ± 26	1.9 ± 0.3	+6
6	200	500	-	-	-	322 ± 26	1.5 ± 0.5	+6

Comparatively, the results are similar to the first ones obtained. The optimal coating is still at 200 psi and 500°C. The increase in coating thickness between the two trials can be attributed to a powder feeding issue. A comparison of optimal coatings for both powder sources is presented in Table 36. Results indicate that the coatings are comparable, with the Valimet powder slightly superior in coating thickness and lack of porosity.

Table 36. Optimal Coating Comparison for Valimet and Centerline AA 7075 Powders

Al 7075 Source	P (psi)	Temp (°C)	T (μm)	Por. (%)
Valimet 200 mesh	250	500	588 ± 43	Fully dense
Centerline SST 5007	200	500	540 ± 30	0.5 ± 0.3

The coating quality is greatly affected by the powder feeder pressure as noted in Table 35. (As the powder feeder pressure increases, the porosity increase) An increased pressure indicates a restriction in the powder feed line, most likely caused by a clog in the orifice/nozzle assembly. The pressure drop between sprays 4 and 5 indicates that a portion of the clog was dislodged.

There is also a large impact of substrate insulation that must be taken into account, as a 21% reduction in thickness between sprays 5 and 6 was measured (no increase in powder feeder pressure means a relatively constant coating quality).

To confirm the quality of the Centerline Al 7075 coatings, adhesion tests were performed. A set of 5 adhesion test samples (Table 37) were sprayed, glued and pulled. This was done according to ASTM C633 as previously described. As per the other tensile specimens performed in this project, 3 layers of a 200 µm coating were created on the bond plug.

The results are presented in the Table 38 and compared with the Valimet 7075 powder.

Table 37. Adhesion Test Results for Centerline Al 707 Powder

#	Pressure (MPa)	Failure Type
1	26	Adhesive
2	74	Adhesive
3	20	Adhesive
4	16	Adhesive
5	10	Adhesive
Total	18 ± 7	Adhesive

Table 38. Comparison Between Valimet and Centerline Al 7075 Powders

Powder	# Samples	Bond Strength (MPa)	Bond Strength (Psi)
Valimet Al 7075	5	68 ± 19	9860 ± 2755
Centerline Al 7075	4	18 ± 7	2610 ± 1015

The bond strength difference is most likely due to the difference in spraying pressure. The centerline powder is sprayed at 200 psi, while the Valimet powder is sprayed at 250 psi.

In conclusion, the Centerline 7075 powder can be used since it deposits well and at lower energy requirements than the Valimet Al 7075. However, the bond strength applications are limited since the lower spray parameters result in bond strengths of about only 2600 psi.

8 Secondary Research Project #2: System Optimization

An issue arises when trying to take a look at the efficiency of the deposition process. Although powders can be deposited well, the process is long because the deposition efficiency for this powder is very low, an estimated 5-50% depending on the powder used. In the case of Al 7075, the deposition efficiency was calculated at between 4-6%.

The second secondary research project is a separate project aiming to increase the efficiency of the nozzle assembly in order to increase the deposition efficiency of process.

8.1 Introduction

There are many aspects to this project. First the current system must be well understood. Chapter 8.2 will present the current equipment that is used, how the aforementioned performance of the system will be evaluated and the current issues that have been highlighted with the system that will be worked upon in this study. Secondly, the current Centerline equipment's lacks in performance (if present) must be quantified. This will be done by comparing the current equipment with student designs using baselines for efficiency presented in Chapter 8.3.

Chapter 8.4 will present theoretical design work done to improve the student designs. Once this is done, the design in chapter 8.5 can be validated using verification tests using various techniques (laser velocity measurement and Schlieren imaging).

The final aspect to this project revolves around design for manufacturing. The optimal design must be found that will allow for the easiest manufacturing possible while providing a nozzle that is geometrically precise and that incorporates all the most important design factors. This will be done in Chapter 8.6. Chapter 8.7 will present the steps that can be taken to measure the performance of the new nozzle in comparison with the current equipment.

8.2 Centerline System Description and Performance

8.2.1 Current Equipment

The cold spray system was presented in section 4.2, showing the general location of the nozzle assembly within the cold spray process. A more detailed analysis of nozzle assembly will be presented in this section.

The de Laval nozzle consists here of two main components. There are also a few auxiliary components that hold these two pieces together. The first main piece is the orifice – a brass piece at the center of which there is a converging cross section. The second part is the nozzle, a stainless steel tube with diverging cross section. Combined together, the orifice and nozzle form a converging-diverging cross section, which forms the basis of supersonic-velocity spraying. Auxiliary pieces include a collet and two nuts. One nut holds the nozzle to the orifice, while another one fixes this assembly to the rest of the system. See Figure 143 to Figure 146 below for details. This allows the cold spray process to work by accelerating particle at supersonic velocities before impacting a substrate and forming a metallic coating.

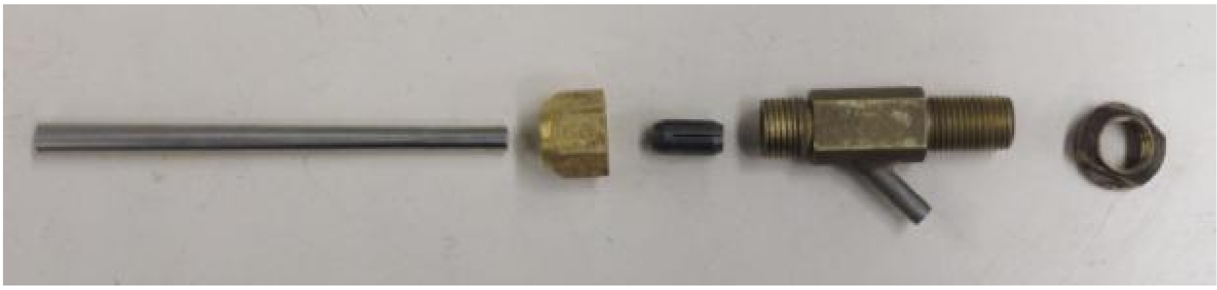

Figure 143. Disassembled de Laval Metal Nozzle Showing, From Left to Right, Stainless Steel Nozzle, Tightening Nut, Tightening Collet, Brass Orifice and Heater Nut

Figure 144. Assembled de Laval Metal Nozzle Assembly

Figure 145. Disassembled de Laval Plastic Nozzle Showing, From Left to Right, Plastic Nozzle, Quick-Connect Cap, Spring, Orifice and Heater Nut

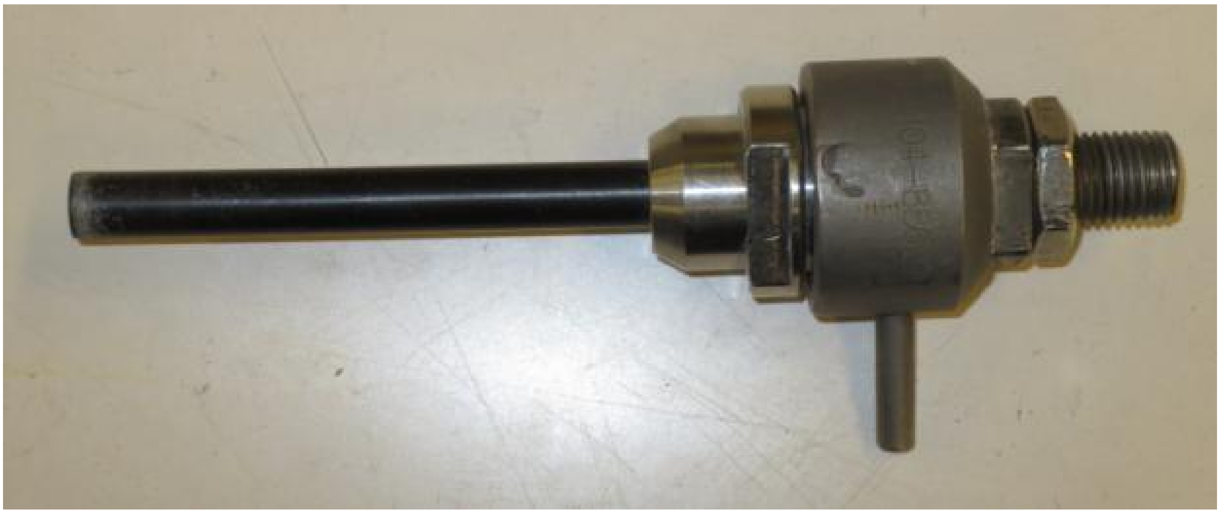

Figure 146. Assembled de Laval Plastic Nozzle Assembly

8.2.2 Determining System Performance

Even though an optimized coating may be produced for a specific equipment set, the equipment performance itself might be improved to increase the performance of the system in general. The main factor that determines the system's performance is its ability to obtain high deposition efficiencies for a powder. The deposition efficiency is defined as the mass ratio of powder deposited on the substrate to powder fed through the system during the spray. High deposition efficiencies means less gas and operator time use, which translates to more parts per hour and a lower cost per part in a commercial setting.

There are several factors that impact deposition efficiency. Pressure and temperature of the gas flow are very important, since a higher temperature will soften the particle and allow it to better adhere to the substrate. (A good analogy for this is the concept of throwing a slush ball (softened particle) on a wall (substrate) instead of an ice ball.) Propellant gas pressure is also important because a higher pressure will created a greater force for the particles to deposit onto the substrate. These two parameters are system dependant, and can only be adjusted up to the maximum system parameters possible, 250 psi and 500^{o}C (or 500 psi / 500^{o}C for the new Centerline SST-EP system). Without changing the entire system, the upper limit of these parameters cannot be increased.

Another very important factor impacting deposition efficiency is particle velocity. A higher particle velocity creates a higher particle momentum, and more impact force when colliding with the substrate. Particle velocity is a key factor in mechanical bonding to the substrate. Particle velocity is governed by many factors, including propellant stagnation properties (pressure, temperature) as well as nozzle shape.

There are also secondary performance factors that can be measured during the spray which can be used to quantify the quality and overall performance of the spray system, which include clog time, propellant gas flow rate, and powder flow rate as described below:

- **Clog time**: Clog time is the spray time (while powder is flowing) required before the nozzle must be cleaned or replaced. Typically the nozzle will clog gradually, resulting in a loss of performance over time. With experience, a time can be selected after which the coating produced is not satisfactory anymore (generally this is because the DE is too low). This time constitutes the clog time.

- **Propellant gas flow rate**: Main gas flow is important in determining the cost of a coating. Furthermore, producing the same coating with less gas indicates a more efficient nozzle. A comparative gas flow rate can be analyzed based on the size of the throat (the choke point). Throat area and gas flow are linearly dependant.
- **Powder flow rate**: In the same fashion as gas flow, a lower powder flow rate is indicative of a less expensive coating (powder cost) and a more efficient nozzle.

8.2.3 System Performance Issues

The cause of the low deposition efficiency can be due to the system itself. A higher pressure and temperature would certainly help increase the deposition efficiency. However, the goal is to keep the same system and still increase the deposition efficiency. The nozzle assembly shape shows some problems with the current design. Gas dynamics principles can be used to show that the current cross section is not adequately designed. In all of the nozzles, the design exit Mach number of the nozzle is too large. This means that the flow is accelerated too much. This will cause a shockwave that will slow down the powder. Furthermore, the plastic nozzle is manufactured in steps, meaning 3 different drill sizes are used to create the diverging cross section, as shown in Figure 147. These rapid increments in cross section can create shockwaves and turbulence which can slow down the flow and reduce the powder particle’s final velocity.

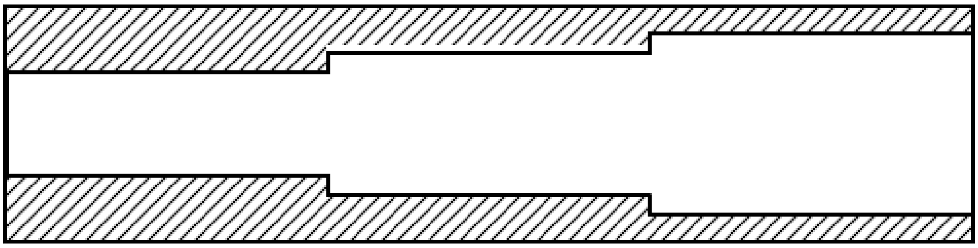

Figure 147. Diverging Cross Section of the Plastic Nozzle

With a properly designed cross-section, the nozzle could perform better, thereby increasing the efficiency of the process.

Another problem observed with the Centerline equipment is the clogging factor. Within a certain period of time – ranging between 0.5 and 45 minutes depending on the metallic powder being sprayed – the orifice / nozzle assembly gets clogged with powder. In the orifice, the clogging occurs at the powder injection point in the diverging section. The nozzle gets slowly coated with the powder in its interior walls. Because the spray loses some of its performance as the orifice or nozzle clogs (through a reduction of pressure and particle velocity), an effort to reduce this clogging factor as much as possible must be made.

8.2.4 Work to be Completed in this Project

The goal is to increase the efficiency of the Centerline SST-P series system by increasing the particle velocity of Al 7075 powder when compared with the current equipment. The design parameters will focus on optimizing the geometry of the de Laval nozzle at 500^{o}C and 250 psi propellant gas pressure and temperature for an average powder diameter of 22 µm. Al 7075 will be used because this aluminum alloy is difficult to spray due to its hardness.

8.3 Baseline Nozzle Performance

This section will detail how the comparison study will measure performance and will list the performance of 3 nozzles that will be used as a basis for comparing the new nozzle design. These 3 nozzles are the Centerline nozzle, the PR nozzle and the JM nozzle. The metrics of performance have been decided, and performance measurements have been completed for the Centerline nozzle. However, they have not been completed with the two other nozzles.

8.3.1 How to Measure Increase in Performance

Deposition efficiency is a very important factor to the overall performance of the system. However, it is hard to measure directly because the mass of powder used in the coating deposited is very small compared to the mass of the powder in the feeder used to feed the powder. Weighing the mass of powder sprayed can be very difficult to measure accurately.

Instead of using deposition efficiency directly, other complimentary measurements taken from the coating and the system after the spray can be made. These include porosity, thickness, hardness, clog time, gas flow rate and powder flow rate. Porosity, thickness and hardness will be the main factors analyzed during this study as they are the easiest and fastest way to measure the performance of a coating. Clog time will also be measured for all nozzles but due to its qualitative nature cannot be used accurately. Finally, gas and powder flow rates can also be used in the case that two or more nozzles perform equally in the three main factors. As a confirmation factor, the powder velocity can be measured with a Tecnar Cold Spray Meter.

The following sections will present the three different nozzles used as a basis for comparing the new nozzle design. Please note that the PR and JM nozzles have been optimized to spray MCrAlY and not Al 7075. Although the cross section is better suited for particle acceleration, it can be further optimized for aluminum powders of a certain size distribution such as the design intended to be presented here. In this case, these two nozzles serve to show that even a nozzle properly designed, although not for the right material, can still perform better than the Centerline nozzle.

8.3.2 Baseline: Centerline Nozzles

The Centerline nozzles consist, as previously stated and shown, of 5 pieces; the orifice and nozzle, a collet, a cap and a nut. Once assembled, the orifice and nozzle form a continuous internal cross section in the shape of a de Laval nozzle. A main focus in this nozzle design was ease of assembly and part life.

Before starting this study, an Al 7075 coating had already been optimized for the stainless steel nozzle. The parameters are presented in Table 39 below:

Table 39: Centerline Nozzle Optimized Spray Parameters (120-hole wheel) and coating results for Al 7075 deposition using the Stainless Steel Nozzle

Parameters		Centerline Nozzle
System parameters	P (psi)	250
	T (^{o}C)	500
	RPM	3
	SCFH	10
	Standoff (mm)	15
	Traverse Speed (mm/s)	5
Coating properties	Coating Thickness (µm)	588 ± 43
	Porosity	Fully dense
	Hardness	149 ± 5
Other Properties	Clog time	≈15 minutes

The parameters were also optimized for pure Al for Centerline's plastic nozzle. They are presented in Table 40.

Table 40: Centerline Nozzle Optimized Spray Parameters (320-hole wheel) and coating results for pure Al deposition using the Plastic Nozzle

Parameters		Centerline Nozzle
System parameters	P (psi)	250
	T (^{o}C)	350
	RPM	14
	SCFH	25
	Standoff (mm)	15
	Traverse Speed (mm/s)	70
Coating properties	Coating Thickness (µm)	240 ± 18
	Porosity	2.3 ± 1.0
	Hardness	53 ± 9
Other Properties	Clog time	Does not clog

8.3.3 PR Nozzle

This nozzle was designed to improve the bond coats of high-performing coating systems for high heat and work environments such as turbine blades. These coating systems would consist of a single-crystal super alloy as a substrate, a bond coat and then a ceramic top coat. The bond coat is the most important part of the coating system because a failure in the bond coat results in spallation of the top coat which protects the part from the high heat. Over time, an oxide layer form between the bond and top coats, this eventually leads to stress gradients and flaking of the top coat.

The goal of this early cold spray study was to optimize the cold spray properties of MCrAlY coatings (the preferred bond coat material) to reduce impurities, porosity, and improve the life of the coatings. A nozzle was designed to this effect and is shown in Figure 148 to Figure 150.

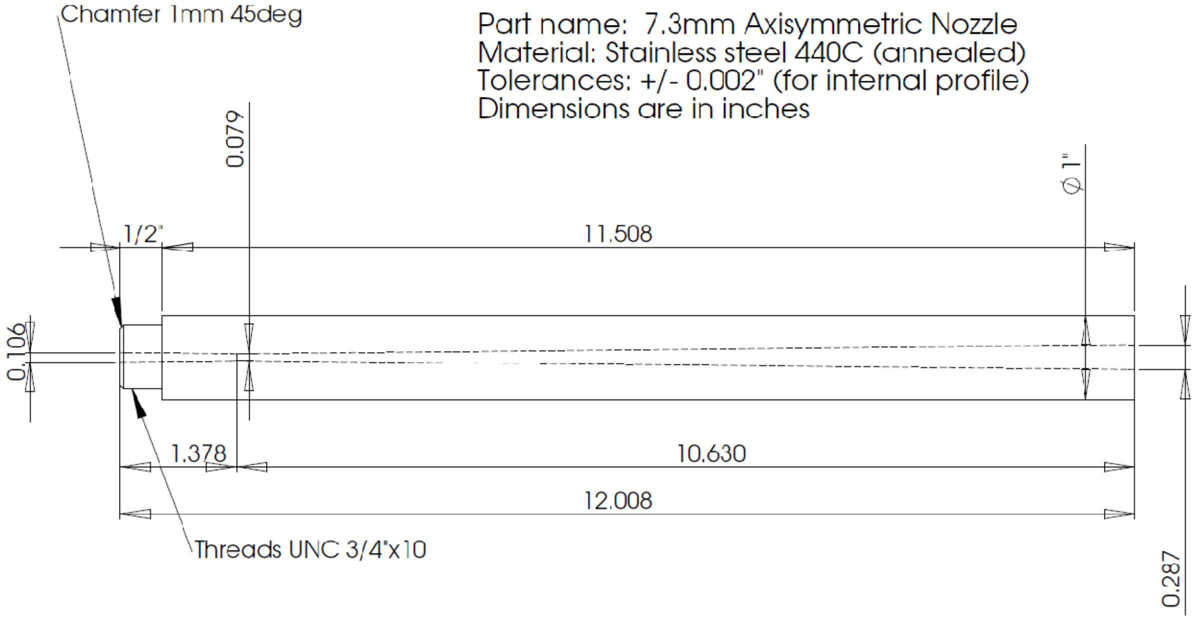

Figure 148. PR Nozzle Technical Drawing

Figure 149. PR Nozzle. Propellant gas Inlet on the Left. Powder Injection on the Top.

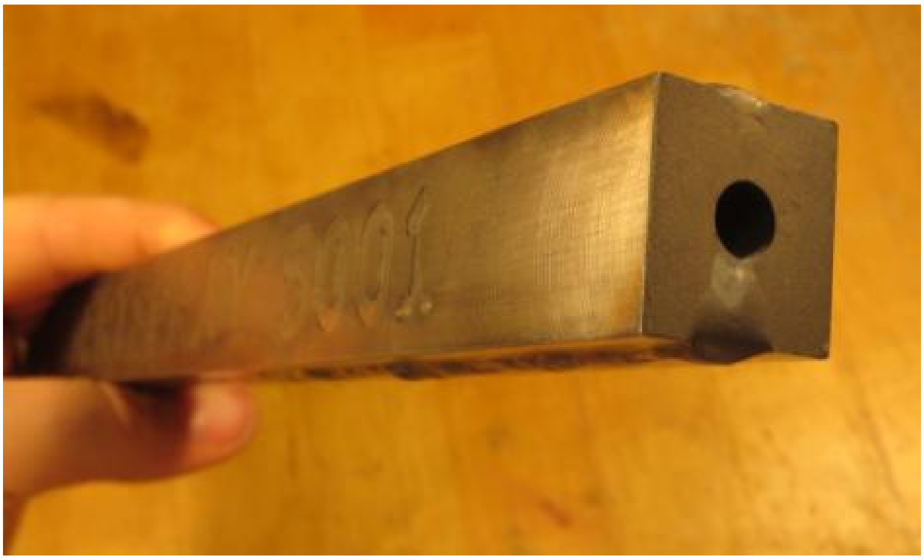

Figure 150. PR Nozzle, View of the Exit Area

The nozzle was machined with two identical halves welded together. A powder injection point was drilled in afterward. There are a few advantages to this manufacturing technique. The first is that it is easy to do. The shape can be machined in a CNC mill, and then welded together. The second advantage is that it can be opened and cleaned if there is ever a clog. However, a major disadvantage is that the shape can be deformed during welding, and the two shapes might not be aligned up during the welding procedure.

8.3.4 JM Nozzle

The JM nozzle is the result of a master's thesis of design and simulation for optimizing CoNiCrAlY powders. The result in the nozzle depicted in here. It is machine and built similarly to the PR nozzle, but its internal cross section is slightly different. See Figure 151 to Figure 154.

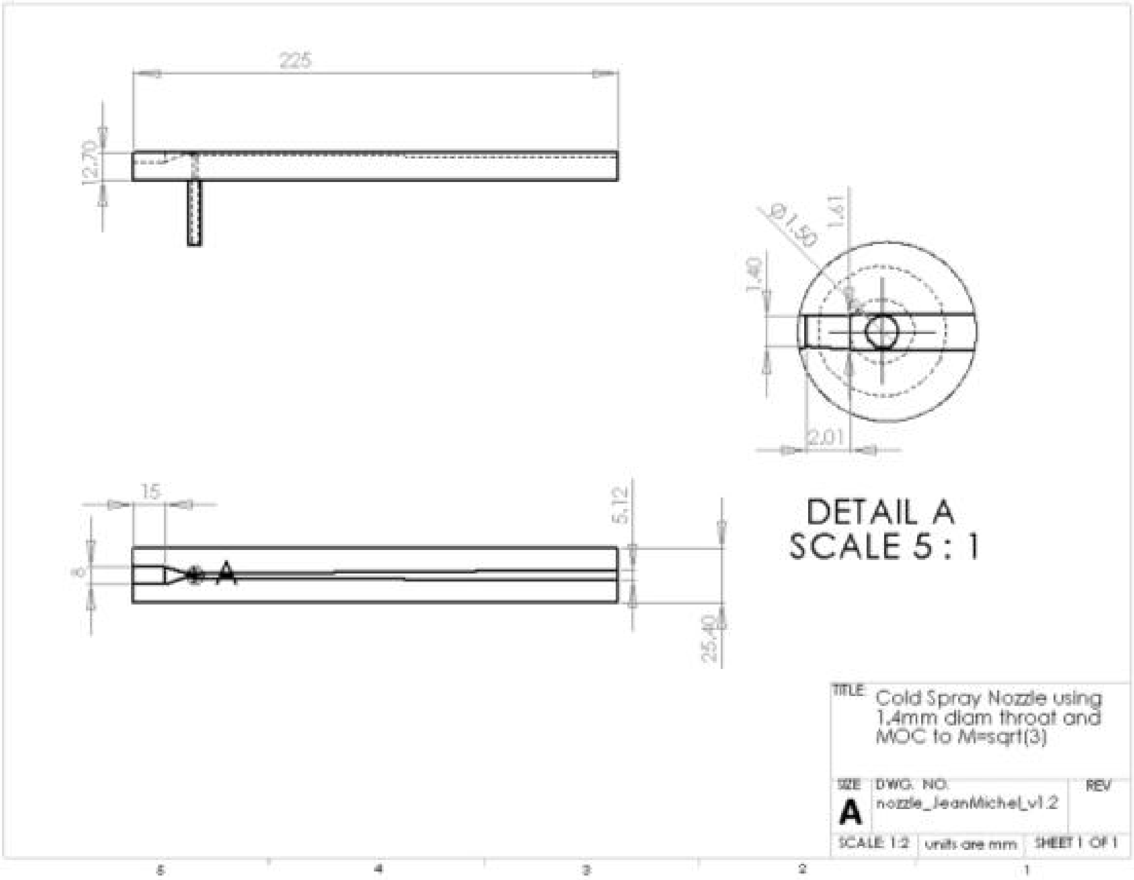

Figure 151. JM Nozzle Technical Drawing (Powder Injection Half Shown Here)

Figure 152. JM Nozzle General Side View. Propellant gas Inlet on Left, Powder Injection on Top.

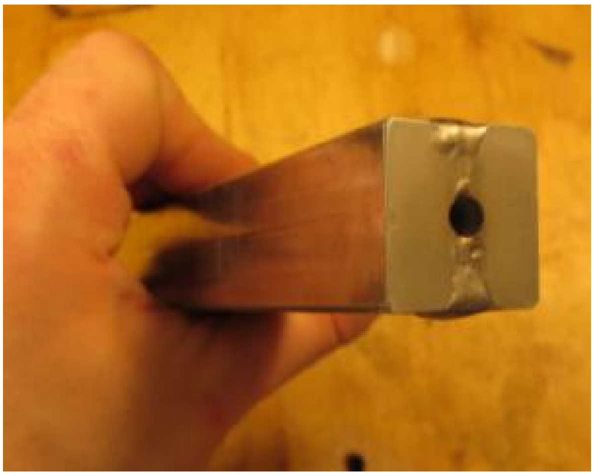

Figure 153. JM Nozzle, Exit Area View.

Figure 154. Side-by-Side Comparison of the PR (Top) and JM (Bottom) Nozzles

8.4 Design Theory

8.4.1 Reducing Orifice Clogging

The theory of nozzle clogging requires its own analysis. An attempt was made here to understand how and why the nozzle clogs and how to improve on it in the next design. However, only the preliminary steps were undertaken here to understand this phenomena.

The current equipment has a few clogging areas. Depending on the powder used, this will affect which area clogs first. The first area is by coating the interior surface of the nozzle. As the powder exits the orifice, its sticks to the inside portion of the nozzle. As this unwanted coating builds, the pressure will increase until the powder stops flowing. There are two ways to prevent this. The first method is to increase the hardness of the nozzle. This will make the particles bounce off the walls instead of adhering. In the same vein, it is also possible to reduce the surface roughness of the walls to prevent the same thing from happening.

A second clogging mechanism occurs at the powder injection point. This is at the point where the powder injection tube meets the main tube where the propellant gas is flowing (within the brass orifice). At this point there is powder build-up until the entire injection tube cross section is clogged. The phenomenon behind this mechanism is still unknown.

There are several current theories of why clogging occurs. Rapid diameter changes could be to blame by inducing pressure drops and fluid stagnation, leading to increases heat concentration, powder softening and eventual adhesion to the walls. Obviously, powder flow rate is very important. Shockwaves inside the nozzle could also lead to clogging.

In summary, with the current understanding of the clogging process, the new nozzle should have very smooth and hard internal walls, have very gradual area changes and have no shockwaves within the nozzle.

8.4.2 Shape Optimization

8.4.2.1 JM Thesis

The most optimized nozzle is the JM nozzle. This nozzle was part of a master's thesis research [56] and was designed to provide the maximum acceleration possible for a specific CoNiCrAlY powder and specific propellant gas, stagnation pressure and stagnation temperature. However, hand calculations can only go so far, and simulations had to be performed in order to complete the shape of the diverging part. This involved making demanding simulations that required about 2-3 weeks each. Simulations will not be completed in this study.

The typical drag force equation can be written as:

$$F_D = \frac{1}{2}\rho V^2 C_D A \tag{8}$$

Where F_D is the drag force, ρ the flow density, V the flow velocity, C_D the shape's drag coefficient and A the shape's cross sectional area. There are two modifications that must be made. First, since powder is travelling at a certain speed inside the nozzle, the velocity here must be the velocity difference between the flow and the particle:

$$F_D = \frac{1}{2}\rho\left(MC - V_p\right)^2 C_D A \tag{9}$$

V_P is the particle velocity and M the Mach number. Note that this equation will not be applicable when the particle velocity is higher than the flow velocity, since the drag force should be negative. Finally, the fact that the flow density and speed of sound are at the current flow Mach number must also be taken into account. To obtain a usable format a conversion into stagnation values must take place. This can be done using standard gas dynamics equations (see equation (4) on page 10 and (11) below).

$$\frac{\rho_o}{\rho} = \left(1 + \frac{(k-1)}{2}M^2\right)^{\frac{1}{k-1}} \tag{10}$$

$$F_d = \frac{1}{2}\frac{\rho_o}{(1 + \frac{k-1}{2}M^2)^{\frac{1}{k-1}}}\left(M\sqrt{kR\frac{T_o}{1 + \frac{k-1}{2}M^2}} - V_p\right)^2 C_d A \tag{11}$$

ρ_o is the stagnation density, T_o the stagnation temperature, k the gas constant, R the universal gas constant.

Solving for multiple particle velocities yields the required gas Mach number for optimal drag speed. In subsonic flows a sphere drag coefficient would be 0.47. However in supersonic flows this values changes drastically. For this study the drag coefficient will be considered constant and equal to 1 because literature on the subject is inconclusive and yields values between 0.8 and 1.3 [56].

8.4.2.2 Basic Shape Calculations

Instead of performing simulations an optimal shape can be found simply by incremental calculations. In order to do start this process, the plot of drag force equation as a function of Mach number and particle speed will be plotted. Figure 155 has the details.

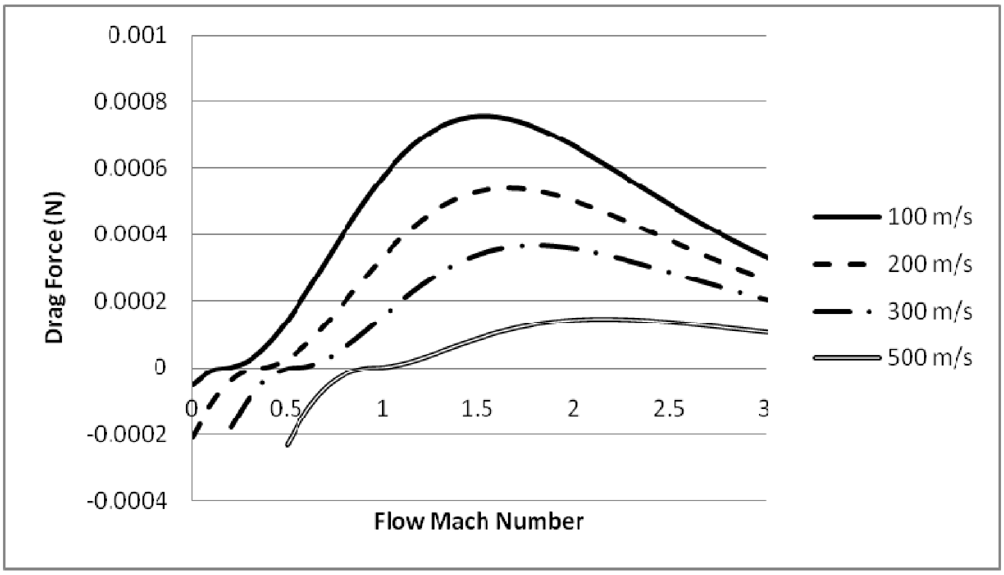

Figure 155. Drag Force Experienced by a 22 µm Al 7075 Powder Particle as a Function of Mach Number and Particle Velocity

Let us observe the 100m/s curve (blue) in this graph. Initially, the flow Mach number is 0, while the particle velocity is 100 m/s. This means that the particle is traveling faster than the flow, and is therefore slowed down by it; the drag force is negative. The drag force will be negative until the flow speed reaches the particle speed, at which point it will be 0. The drag force then increases until a peak value, then decreases. This phenomenon is characteristic of supersonic flows, where the density decreases as the velocity increase. There is therefore a balance between speed and density which results in a peak drag force value.

To find this maximum value, the drag force equation must be derived by M and set equal to zero. This will yield the local max/min values for the function. There are two solutions to this derivation:

$$V_1 = M\sqrt{\frac{kRT_o}{1+\frac{k-1}{2}M^2}} \tag{12}$$

$$V_2 = M\sqrt{\frac{2kRT_o}{1+\frac{k-1}{2}M^2}}\left(1-\frac{2}{M^2}\right) \tag{13}$$

V_1 represents simply the flow velocity, and is therefore the function minimum (where the drag force is equal to zero. Therefore the maximum of the function is V_2 and is equal to:

$$V_2 = M\sqrt{\frac{2kRT_o}{1+\frac{k-1}{2}M^2}}\left(1-\frac{2}{M^2}\right) = MC\left(1-\frac{2}{M^2}\right) \tag{14}$$

This equation dictates how to find the optimal particle velocity for a particular Mach number in order to obtain the highest drag force. However, the optimal Mach number for a particular particle velocity is desired. M can be isolated in a quartic equation that will have two negative and two positive roots. The two positive roots are:

$$M_{1,2} = \sqrt{\frac{{V_p}^2 + 4kRT_o \pm \sqrt{{V_p}^2\left(8k^2RT_o + {V_p}^2\right)}}{2kRT_o - k{V_p}^2 + {V_p}^2}} \tag{15}$$

However, Figure 155 shows that as the particle velocity increases, the Mach number must also increase. The real solution here is M_1,

$$M = \sqrt{\frac{{V_p}^2 + 4kRT_o + \sqrt{{V_p}^2\left(8k^2RT_o + {V_p}^2\right)}}{2kRT_o - k{V_p}^2 + {V_p}^2}} \tag{16}$$

The shape of the nozzle will be based off incremental calculation. The powder will be injected at a theoretical particle velocity of 0 m/s. The optimal Mach number will be calculated and an equivalent nozzle cross section will be calculated. The particle will then be accelerated at this value for a discrete distance. The final speed of the particle will be calculated after this distance, and the process will be repeated. The calculation steps are presented below;

1. Inject powder at V_p = 0 m/s.
2. Calculate ideal Mach number for maximum drag force. (Equation (16))
3. Calculate ideal cross section based on Mach number. (Equation (17))
4. Calculate drag force. (Equation (11)
5. Calculate final particle speed based on discrete distance, constant drag force and particle velocity. (Equation (22) below)
6. Repeat steps 2 to 6 as many times as required.

The ideal cross section calculation will be based on generic gas dynamics equation. The drag force will be calculated as shown previously.

$$\frac{A}{A^*} = \frac{1}{M}\left[\left(\frac{2}{k+1}\right)\left(1 + \frac{(k-1)}{2}M\right)\right]^{k+1/2(k-1)} \tag{17}$$

The final particle speed is based on the following cinematic acceleration:

$${V_2}^2 = {V_1}^2 + 2a(x_2 - x_1) \tag{18}$$

$$V_2 = \sqrt{{V_1}^2 + 2a\Delta x} \tag{19}$$

V_o is the initial particle velocity (i.e. powder velocity in the previous increment), while a is the particle acceleration, and Δx is the discrete distance. To find the acceleration, Newton's second law can be used:

$$F = F_d = m_p a \tag{20}$$

$$a = \frac{F_d}{m_p} = \frac{F_d}{{}^4\!/_3\,\pi r^3 \rho_b} \tag{21}$$

m_p is the powder mass, r is the particle radius and ρ_b is the material bulk density. Therefore the final particle velocity becomes:

$$V = \sqrt{{V_o}^2 + \frac{2F_d\Delta x}{m_p}} = \sqrt{{V_o}^2 + \frac{3F_d\Delta x}{2\pi r^3 \rho_b}} \tag{22}$$

Preliminary calculation can now begin. Using the methodology presented preliminary calculations can be made using a basic step of 0.01mm. A quick reduction of the step size down to 0.001mm (see Table 41) leads to a converged solution.

Table 41. Discrete Distance Convergence for Powder Velocity Calculations

Increment (mm)	V_p after 0.1mm (m/s)	V_p after 1mm (m/s)
0.1	94.829	235.99
0.01	87.35	232.184
0.001	**86.8008**	**231.8548**
0.0001	86.75079	231.8231

The same procedure was performed for a nozzle length of 1 to 100 mm and 100 mm and on. A step increment of 0.01 and 0.1mm respectively were selected.

The resulting nozzle geometry is shown in Figure 156, along with the final powder velocity in Figure 157.

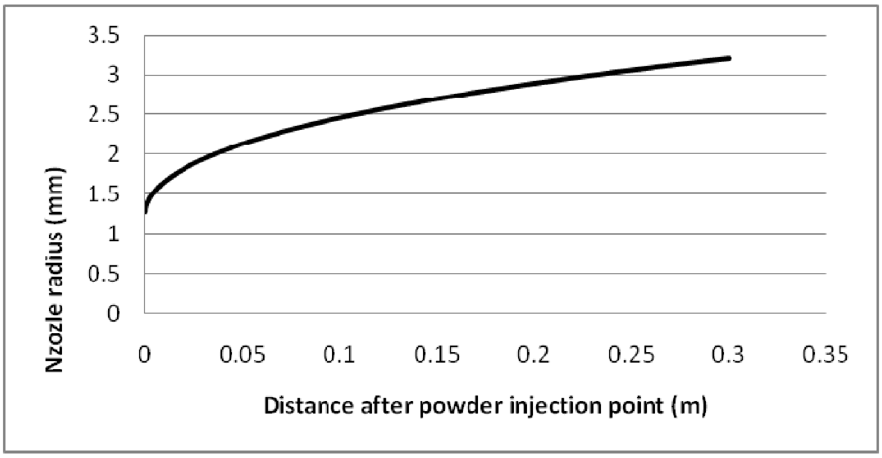

Figure 156. Initial Nozzle Geometry, Friction Not Considered

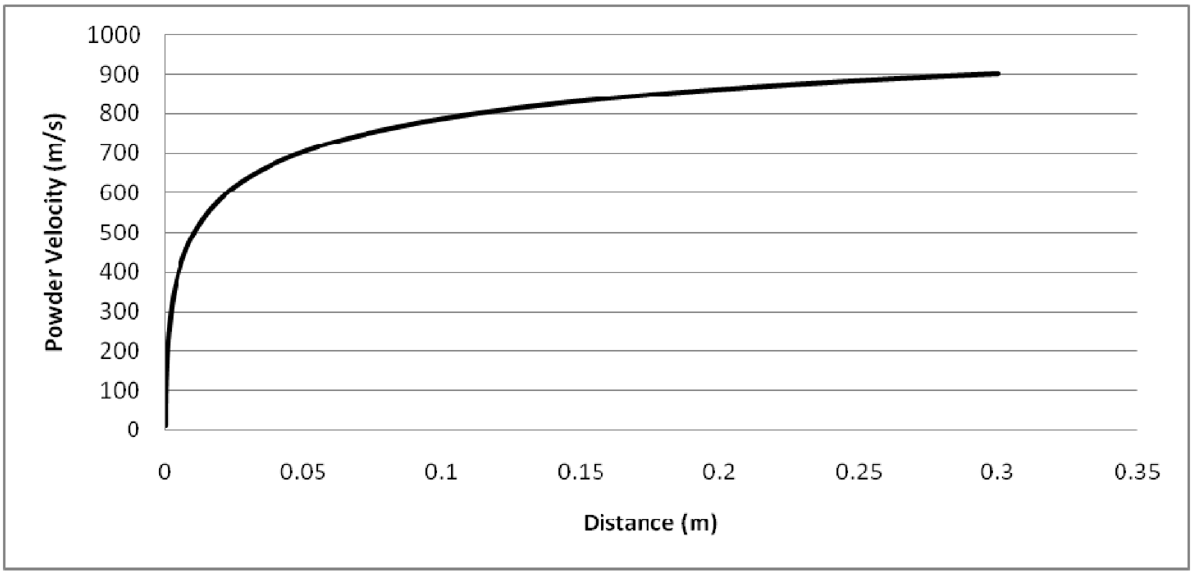

Figure 157. Powder Velocity for Initial Nozzle Geometry, Friction Not Considered

The optimal nozzle length is hard to determine. However, after 120mm, the powder velocity reaches a theoretical 809m/s, 90% of the speed at 300mm. This value seems acceptable. The current equipment's nozzle length is in fact 120mm.

However, this nozzle analysis does not consider friction. To consider friction, the Fanno flow law for supersonic friction losses must be included:

$$\frac{dM^2}{M^2} = \left(\frac{kM^2}{1 - M^2}\right)\left(1 + \frac{k-1}{2}M^2\right)\frac{4f}{D_h}dx \tag{23}$$

Where *f* is the fanning factor, D_h is the hydraulic diameter, *x* is the distance travelled by the flow. A common occurrence would be to integrate this from M to 1 to find the length required to choke the flow, L^*:

$$\int_{L^*}^{0} \frac{4f}{D_h}dx = \int_{M}^{1} \frac{1 - M^2}{(M^2)^2\left(1 + \frac{k-1}{2}M^2\right)}dM^2 \tag{24}$$

This leads to the well-known equation

$$\frac{4fL^*}{D_h} = \left(\frac{1 - M^2}{kM^2}\right) + \frac{k+1}{2k}ln\left[\frac{M^2}{\left(\frac{2}{k+1}\right)\left(1 + \frac{k-1}{2}M^2\right)}\right] \tag{25}$$

However there are discrete increments, from M1 to M2 and from X1 to X2:

$$\int_{x_1}^{x_2} \frac{4f}{D_h}dx = \int_{M_1}^{M_2} \frac{1 - M^2}{(M^2)^2\left(1 + \frac{k-1}{2}M^2\right)}dM^2$$

$$\frac{4f\Delta x}{D_h} = \left(\frac{1 - \left({}^{M_1}/_{M_2}\right)^2}{k{M_1}^2}\right) + \frac{k+1}{2k}ln\left[\frac{{M_1}^2}{{M_2}^2} \cdot \frac{(k-1){M_2}^2 + 2}{(k-1){M_1}^2 + 2}\right] \tag{26}$$

f, the fanning factor, can be represented for turbulent flows by the Colebrook equation:

$$\frac{1}{\sqrt{f}} = -4.0log_{10}\left(\frac{{}^{\epsilon}/_{D}}{3.7} + \frac{1.256}{Re\sqrt{f}}\right) \tag{27}$$

${}^{\epsilon}/_{d}$ is the ratio of pipe internal wall roughness over diameter. Re is the Reynolds number represented by the standard equation:

$$Re = \frac{\rho V D}{\mu} \tag{28}$$

Substituting the density term by equation (10) and the velocity component by its respective gas dynamics equation (see equation (4)) yields:

$$Re = \frac{\rho_o D}{\mu\left(1 + \frac{(k-1)}{2} M^2\right)^{\frac{1}{k-1}}} M \sqrt{\frac{kRT_o}{1 + \frac{k-1}{2} M^2}} \tag{29}$$

The viscosity of the fluid must be found using approximations for temperature. The Sutherland equation for ideal gases can be used which states that

$$\mu = \lambda \frac{T^{3/2}}{T + C}, \qquad 0 < T < 555\ K \tag{30}$$

Where λ is the Sutherland gas constant and C is Sutherland's constant. Both these constants are gas dependants, as stated in Table 42.

Table 42. Sutherland's and Sutherland Gas Constants (C and λ Respectively) for Various Ideal Gases

Gas	**Formula**	**C [K]**	**λ[μPa s K$^{-1/2}$]**
Air	-	120	1.512041288
Ammonia	NH_3	370	1.297443379
Carbon dioxide	CO_2	240	1.572085931
Carbon monoxide	CO	118	1.428193225
Helium	He	79.4	1.484381490
Hydrogen	H_2	72	0.636236562
Nitrogen	N_2	111	1.406732195
Oxygen	O_2	127	1.693411300
Sulphur dioxide	SO_2	416	1.768466086

Substituting this equation into the current Reynolds equation, and substituting equation (4) again, yields:

$$Re = \frac{\rho_o D^* \sqrt{\frac{A}{A^*}} M \sqrt{kR}}{\lambda \left(1 + \frac{(k-1)}{2} M^2\right)^{\frac{1}{k-1}}} \left(1 + \frac{\left(1 + \frac{k-1}{2} M^2\right) C}{T_o}\right) \tag{31}$$

The nozzle can now be modelled with these equations. Several modeling scenarios have been made and are presented below:

8.4.2.3 Scenario 1: Cross Section Increase

This scenario is very similar to what was presented before. The cross section at each discrete increment will be modified to give the Mach number that will yield maximum drag force on the particle. However, at the same time the flow is being slowed down by friction. Theoretically this scenario should give the highest particle velocity since drag force is being maximized. (Therefore the speed will be the same as the previous non-frictious study.)

To create this solution the following steps have been followed:

1. Inject powder at $V_p = 0$ m/s.
2. Calculate ideal Mach number for maximum drag force. (Equation (16))
3. Calculate drag force (equation (11)),
4. Calculate the Reynolds number (equation (31))
5. Calculate the Fanning factor (equation (27)).
6. Calculate Mach number as a result of the friction losses (equation (26)).
7. Follow equation (17) to find the new nozzle dimensions at this point.
8. Calculate the final powder particle speed (equation (22)) after the discrete interval.
9. Repeat steps 2 to 8 for the new speed at interval x+1.

The flow is being slowed down by friction creating pressure losses. Since the Mach number for the same cross section is lower, this means that the area ratios have changed. For this reason a new area ratio must be calculated, after which the nozzle's cross section can be adjusted to fit the ideal Mach number calculated in step 2.

$$D_2 = D_1 \sqrt{\left(\frac{A}{A^*}\right)^{-1}_{friction\_losses\_2}} \sqrt{\left(\frac{A}{A^*}\right)_{ideal\_2}} \quad \textbf{(32)}$$

These calculations yield the results presented in Figure 158 and Figure 159.

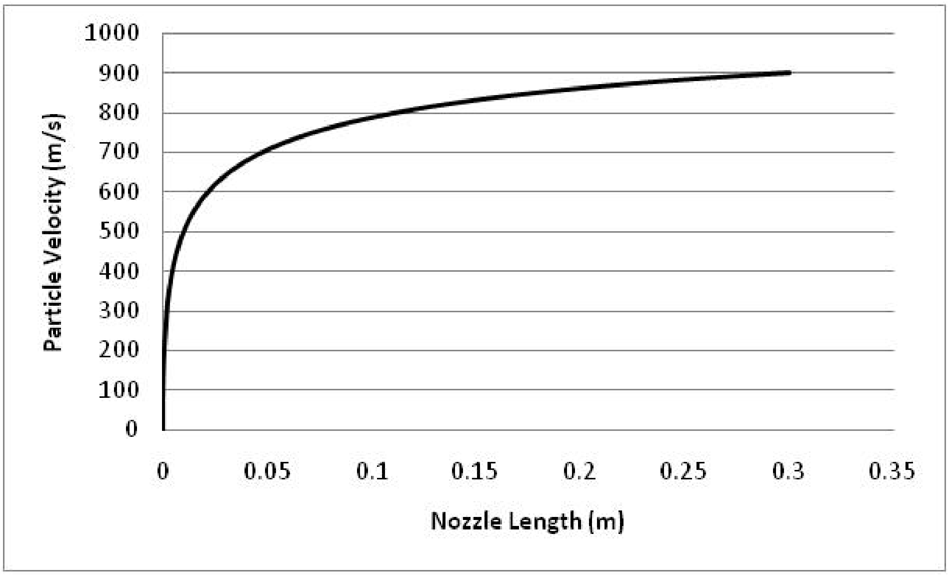

Figure 158. Powder Velocity for Optimized Drag Force, Friction Model Included. Is Identical to Non-Frictious Model

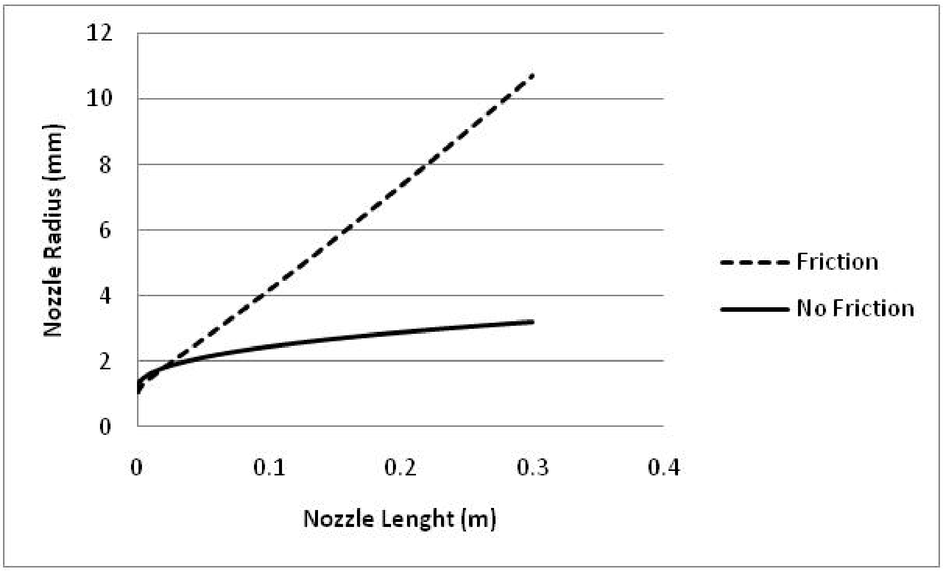

Figure 159. Nozzle Geometry for Optimized Drag Force, Friction Model Included

The particle velocity remains unchanged. This is reasonable since the cross section is optimized to maintain the same drag force, hence the same Mach number, resulting in the same particle velocity. However, to compensate for the friction losses, the cross section must be increased considerably, in a linear fashion. This will make it much easier to machine.

8.4.2.4 Scenario 2: Constant Cross Section

The second potential scenario is to have a constant cross section, but start at a higher Mach number. With friction the Mach number will eventually decrease. The exit Mach number can be set as the design Mach number. This scenario is particularly interesting because machining for this nozzle would be very easy, with a simple constant bore in the nozzle. However, because the flow will be initially overexpanded at the start of the nozzle, there is a possibility of obtaining shockwaves within the nozzle.

To create this solution the following steps were followed:

1. Inject powder at a certain Mach number. (V_p = 0 m/s) This Mach number must be higher than the design Mach number.
2. Calculate drag force with equation (11).
3. Calculate Reynolds number with equation (31)

4. Calculate fanning factor (by trial and error[2]) with equation (27).
5. Calculate new Mach number (by trial and error[2]) for a certain discrete interval using equation (26).
6. Repeat steps 2 to 5 for each discrete internal.

The scenario was performed multiple times, adjusting the start Mach number until the design Mach number was reached for a nozzle length of 120mm. The particle speed is presented in Figure 160.

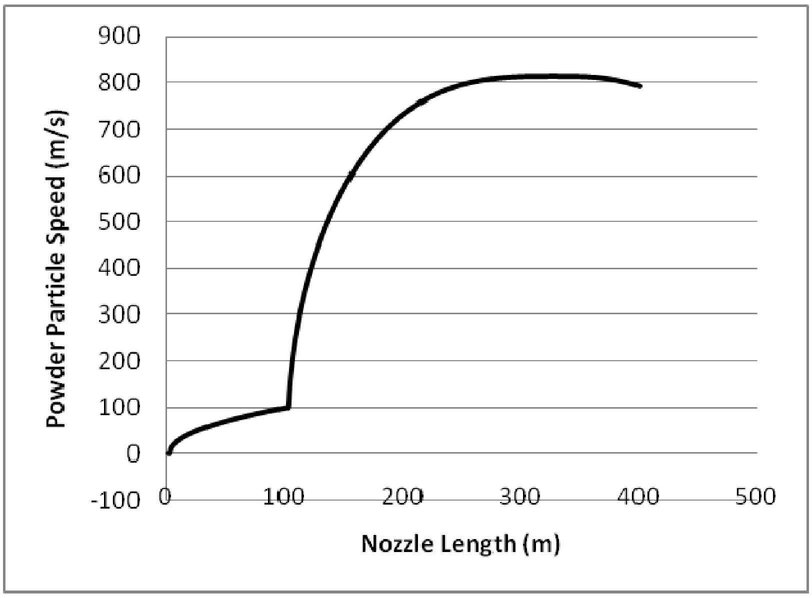

Figure 160. Constant Cross Section Friction Model Nozzle Design (Scenario 2) Particle Speed as a Function of Nozzle Length

The decrease in particle speed is due to the decrease in flow velocity below the particle velocity. This leads to a negative drag force, slowing the particle. The nozzle length should therefore be kept below 200mm.

---

[2] The trial and error process can be quickened with the Excel Goal Seek function.

8.4.2.5 Modeling Previously Designed Nozzles

Finally, the velocity of the particles exiting the nozzles can also be modeled. In this case the following steps were followed:

1. Nozzle geometry (i.e. diameter) is determined for all discrete locations
2. Inject powder at $V_p = 0$ m/s
3. Calculate the initial area ratio with the initial throat area and the current diameter.
4. Use this value to find the current Mach number (equation (17) – trial and error required)
5. Find the resulting drag force with equation (11).
6. Find the Reynolds number with equation (31).
7. Find the fanning factor with equation (27) by trial and error.
8. Find the new Mach number considering friction with equation (26).
9. Find the throat diameter of this configuration (Mach number considering friction with current diameter).
10. Increase distance by discrete increment.
11. Calculate the new powder velocity.
12. Calculate new area ratio using new throat diameter calculated in step 9 and the current diameter.
13. Repeat steps 3 to 12 for the length of the nozzle.

These steps can be performed for both nozzle designs currently in stock from Centerline. Doing this yields the results presented in Figure 161 and Figure 162 presented below.

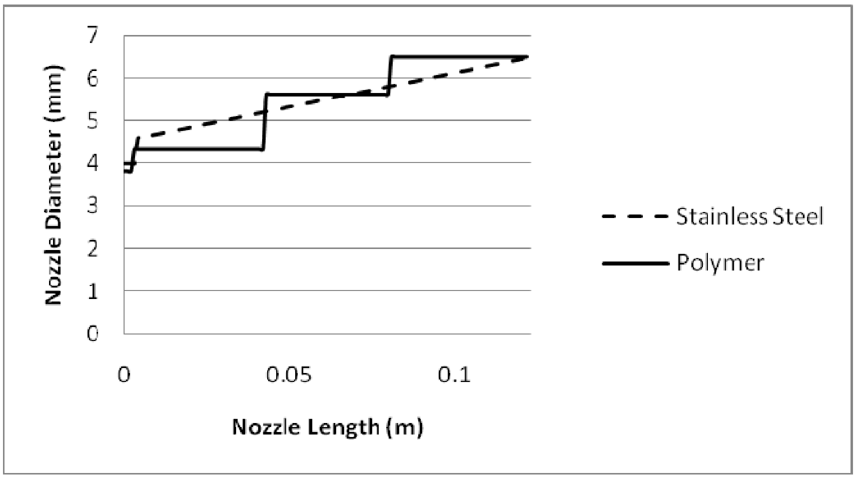

Figure 161. Centerline SST-P Stainless Steel and Polymer Nozzle Design Shape

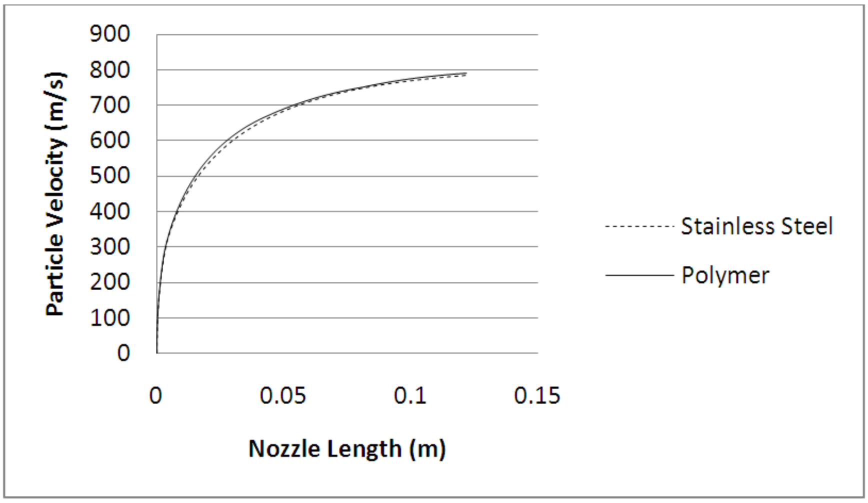

Figure 162. Centerline SST-P Stainless Steel and Polymer Nozzle Design Particle Velocities

Even though the nozzle shape is largely different, by design the final powder particle speed does not seem to change very much. Even compared with the optimal design at 120mm, the final particle velocity does not vary very much.

8.4.2.6 Nozzle Theoretical Design Summary

The summary of the 4 nozzles analyzed is presented in Table 43.

Table 43. Summary of Nozzle Designs. All Nozzles have a Throat of 2mm and a Length of 120mm

Nozzle	Initial Mach	Final Mach	Exit Diameter (mm)	Powder Exit Velocity (m/s)
Optimal Mach	1.41	3.08	9.10	810
Constant Cross Section	4.40	2.58	7.8	766
Centerline S/S	2.85	2.17	6.3	792
Centerline Polymer	2.94	2.17	6.3	785

These numbers seem to indicate that the nozzle shape for the Centerline equipment is adequate to reach 97-98% of the maximum powder velocity that can be reached for the same nozzle length with the best designed nozzle. However, there are many real-life conditions that have not been taken into account in this study. This includes internal wall true surface roughness and most importantly shockwaves and flow irregularities which may be induced in the Centerline nozzles. Furthermore, the design takes into account a single particle being uniformly accelerated. With a group of several thousand particles passing through per second, the drag will be significantly reduced. Finally, as the particles hit themselves within the nozzle, their speed will fall.

8.5 Theory Calculation Verification

In order to confirm the theory developed here, real-life measurements should be taken. There are many techniques that can be used to do this. The first involves making on-the-spot particle exit velocities using the Tecnar Cold Spray Meter. The second involves making a transparent replicate of the nozzles to be analyzed and create Schlieren imaging of the Schlieren internal and external sections. The coatings can also be observed for improvements. Coating improvements include porosity reduction or thickness increase.

8.5.1 Velocity Measurements

Velocity measurements have been performed for the Centerline nozzle. The velocity of the Al 7075 particles sprayed under optimal coating properties was 445 ± 146 m/s. There was insufficient time to measure the particle velocity of the other 2 student designed nozzles.

8.5.2 Schlieren Measurements

It was decided that before building the nozzle as specified, an attempt would be made to make a Schlieren video or picture of inside the nozzle i.e. at the orifice and shortly after. This is done to confirm predictions of shockwaves in the nozzle depending on the nozzle geometry and to better optimize the shape of the nozzle through experimental means.

On top of changing the material to a transparent one, the material should also be able to obtain good quality Schlieren images.

Schlieren imaging is a science in itself. As Hubert Schardin noted, "the basic principle of the Schlieren technique is the combination of the optical projection of an object with an indication of its light deflection." [57] It works by partially blocking out the shadows created by the deflection of light due to density gradients. The concept is illustrated in Figure 163 (basic operation of a Schlieren system) and Figure 164 which shows the layout type available for testing.

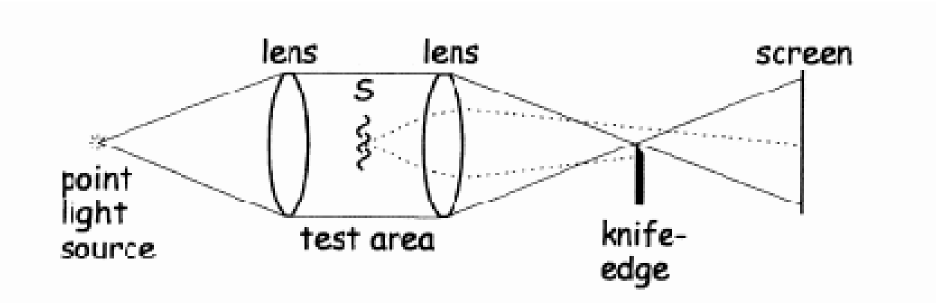

Figure 163. Diagram of a Simple Schlieren System with a Point Light Source [57]

Basically, as light enter a medium it is slowed down proportionately to the material's refractive index. The refractive index is the ratio of the speed of light in vacuum (c_o) over the speed of light in the material (c).

$$n = \frac{c_o}{c} \tag{33}$$

It is constant for a solid such as glass or acrylic, but can change for a gas such as air. The refractive index for air and other gases is dictated by a simple linear relationship between the refractive index and the gas density:

$$n - 1 = k\rho \quad (34)$$

The Gladstone-Dale coefficient, k, is about 0.23 cm^3/g for air at standard condition, given visible illumination. For other gases, it may vary from 0.1 to 1.5. However, n for air is 1.000292 and so a large change in air density causes only a small difference in refractive index. This means very sensitive optics are required in order to observe density differences. (For instance, the refractive index in water is 3 orders of magnitude higher, so less sensitive optics can be used.)

The type of system used: The Z-Type 2-Mirror Schlieren System (AKA z-type Herschellian system). This is the most popular Schlieren method because it eliminates many of the problems of other Schlieren methods such as coma. Astigmatism cannot be corrected for in any systems.

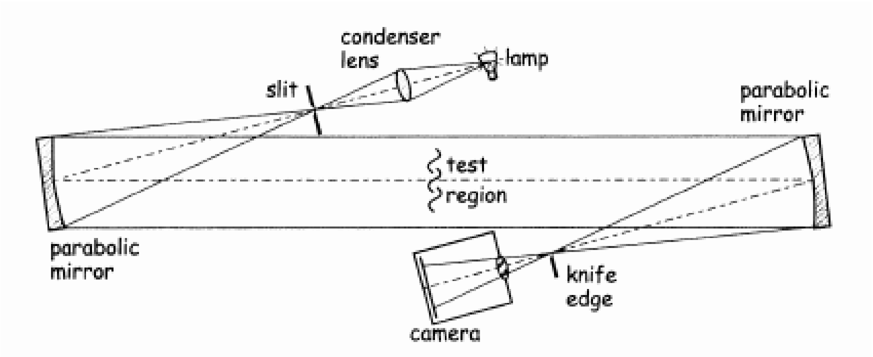

Figure 164. Z-Type Schlieren Arrangement as Available [57]

Several iterations were performed with the Nozzle. At 250psi and room temperature, both Nitrogen and Helium gases were sprayed using either infinite or a 15mm standoff distance. High definition videos were taken. Still shots from these videos are presented from Figure 165 to Figure 168.

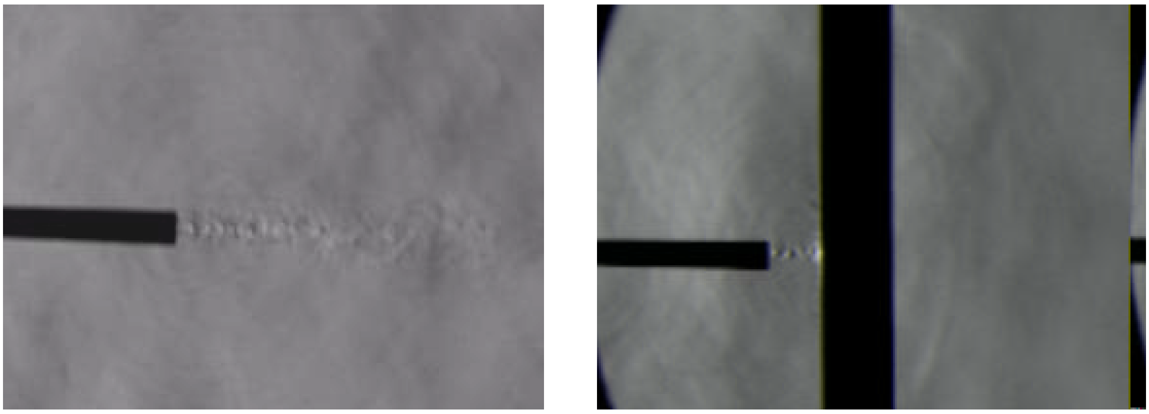

(a) (b)

Figure 165. Schlieren Frame of High Definition Video, for Stainless Steel Nozzle, Nitrogen Gas (a) Without Substrate and (b) With Substrate

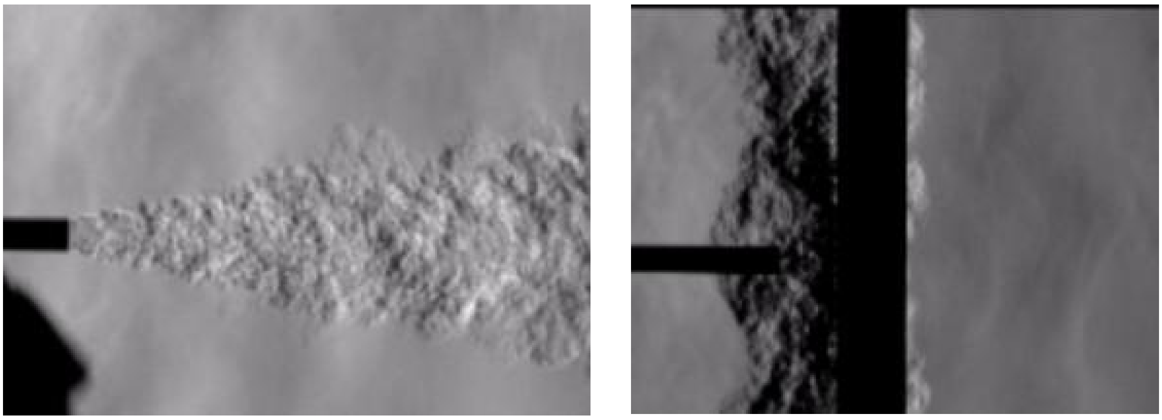

(a) (b)

Figure 166. Schlieren Frame of High Definition Video, for Stainless Steel Nozzle, Helium Gas (a) Without Substrate and (b) With Substrate

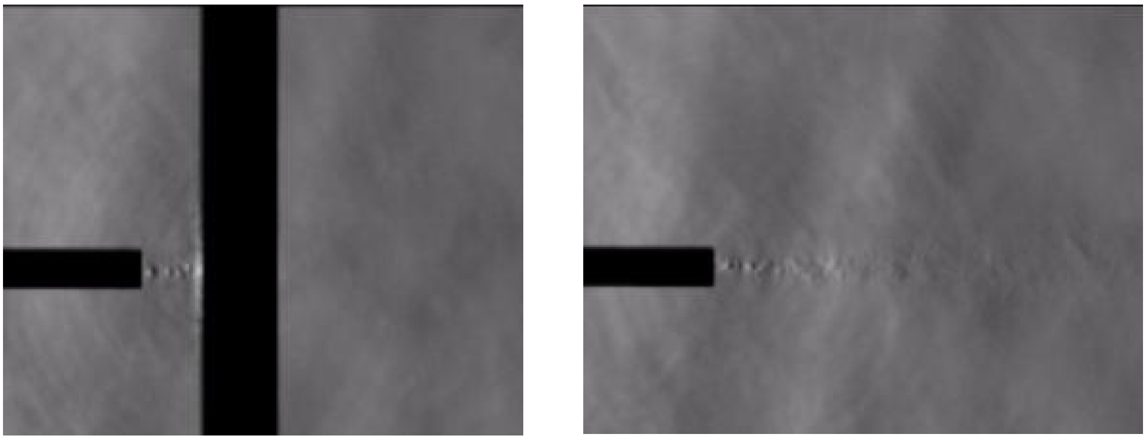

(a) (b)

Figure 167. Frame of High Definition Schlieren Video. Polymer Nozzle, Nitrogen (a) Without Substrate and (b) With Substrate

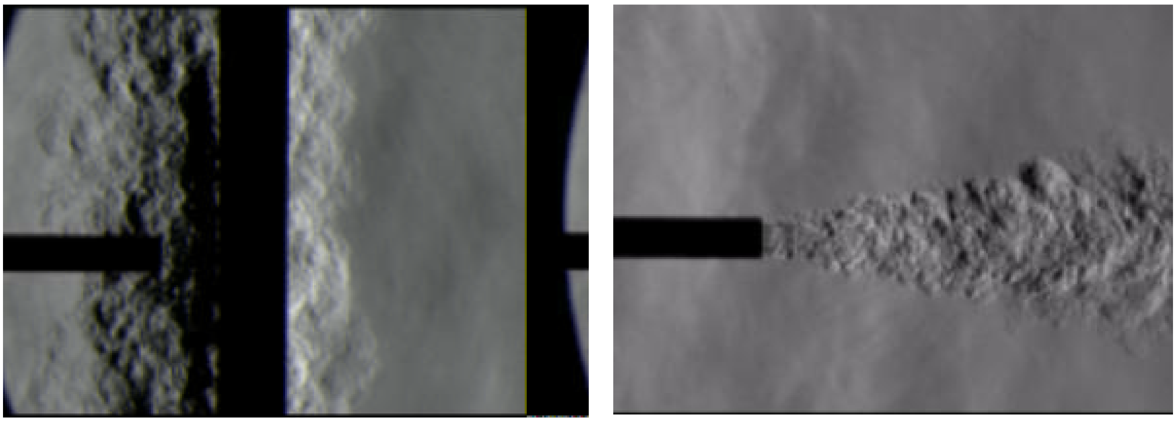

(a) (b)

Figure 168. Schlieren Frame of High Definition Video, for Polymer Nozzle, Helium, Gas (a) Without Substrate and (b) With Substrate

No conclusions can be made with this setup. There seem to be diamond shocks in the nitrogen tests, indicating some underexpansion. However, the resolution of the system is not high enough to be able to make definitive conclusions. The tests performed with Helium gas are inconclusive as well due to the large density gradient between helium and nitrogen. The system cannot pick up density gradients within the nozzle plume since the density difference between nitrogen and helium is so much greater.

Several things can be done to alleviate these problems. To spray nitrogen, a higher-definition system must be used. For Helium, a higher resolution must also be used. In addition, the spray must be performed in a Helium environment. These modifications were not completed.

The next step in nozzle Schlieren observation is to analyze what is going on inside the nozzle. However, perfectly replicating the nozzle cross section to avoid any differences in boundary layers will lead to round cross sections. Because Schlieren systems rely on light diffraction to work, a special technique must be used to avoid light diffraction through the curved walls. The called "refractive index matching" and has been very well described by Tavoularis [58]:

> In view of the preceding discussion, serious image distortion may occur when light propagates in non-homogeneous materials or encounters interfaces between different materials. A common situation in experimental fluid mechanics is the use of transparent walls or windows, made of glass or plastics, for viewing a contained gas or liquid flow. In some cases, models and internal sections of the apparatus are also made of transparent solids to allow optical access. When fluids are viewed through curved walls, their images get particularly distorted. In some cases, this may result in entire flow regions becoming invisible or multiple images of the same region appearing simultaneously. These distortions can be reduced by use of walls as thin as possible and avoidance of curved sections. Corrections for the refraction of laser beams and other collimated light beams through curved walls are also available [59][60]; such corrections are difficult to apply to broad images.
>
> An effective method to reduce or eliminate optical distortion is to match the refractive indices of the contained fluid and the transparent wall. As shown in Table 5.3, the refractive indices of air and water are appreciably smaller than those of glass and other transparent wall materials, so there is no possibility of matching the refractive index of these fluids. The same applies to all gas flows. On the other hand, a number of liquids and solutions are available with refractive indices in the same range as those of common wall materials. Thus it is possible to precisely match the refractive indices of glass and acrylic materials by either mixing different liquids, for example glycerol and water or various natural and mineral oils (e.g., silicon oil, xylene, naphtha, turpentine) or by dissolving various salts (e.g., ammonium thiocyanate at near-saturation concentrations) in water or other solvents [61]. This procedure is by no means routine, as most liquids with a relatively large refractive index happen to be flammable, volatile, toxic, corrosive, foul smelling, unsafe, or a combination of

> any of these. Besides a careful consideration of potentially hazardous effects of the selected liquid on the experimenter and destructive effects on the apparatus and the laboratory, consideration must be given to their clarity, density, viscosity, sensitivity to temperature, environmental impact, and price. Because the refractive index of materials is sensitive to many factors, it may also be necessary to conduct on—site measurements of the refractive index of both the wall material and the liquid. This can be achieved with the use of a refractometer.
>
> Even when a contained liquid is matched optically with the surrounding walls, optical distortion will be inevitable if light propagating through air encounters a curved wall (e.g., a circular tube) before it enters the liquid. In such cases, it is advisable to create by immersing the viewing section into a rectangular viewing tank, filled with the same liquid, but still and not communicating with the liquid inside the test section. In the latter case, one must take care to eliminate possible temperature differences between the still and flowing liquids. If such differences persist, they may introduce optical distortion that is due to refractive-index variations; in addition, temperature-related density variations may generate convection currents, which could cause flow distortions, especially in very low-Reynolds-number flows.
>
> When dealing with two-phase or variable-density flows, one encounters differences in refractive index not only between fluids and surrounding walls, but also within the fluid itself. In most cases, these differences are impossible to eliminate, and one has to work within the limitation of the adopted visual or optical technique. Under certain conditions, however, one can match refractive indices by selecting specific materials. For example, dense solid suspensions in liquids have been simulated by use of liquid-particle combinations consisting of chemicals carefully mixed such as to match their refractive indices as well as having a desired density ratio, including unity.

In short, it would be extremely difficult to perform Schlieren measurements for a curve nozzle. The only possible way would be to make a very thin-walled glass or acrylic nozzle because refractive index matching would not work between a gas and a solid wall (see Table 44). However this solution is not practical. At this point performing Schlieren of the de Laval section is not feasible.

Table 44. Refractive Index for Common Solids, Liquids and Gases. Organized in Ascending Order. Showing that Gases Refractive Indexes are Very Small Compared to Typical Solids [59][61]

State	Name	n
Gas	Air	1.00029
Gas	He	1.00036
Gas	CO_2	1.00045
Gas	H_2	1.00013
Liquid	Water	1.333
Liquid	Ethyl Alcohol	1.361
Solid	Fused quartz	1.46
Solid	Pyrex glass	1.47
Liquid	Turpentine	1.472
Liquid	Benzene	1.501
Solid	Plexiglas	1.51
Solid	Crown glass	1.52
Solid	Flint glass (min)	1.57
Solid	Lexan	1.58
Solid	Polystyrene	1.59
Solid	Sapphire	1.77
Solid	Flint glass (max)	1.89
Solid	Zircon	1.92
Solid	Diamond	2.42

Another potential, less preferable solution is to create square cross-section nozzle. This would allow using flat material and the use of gases in the study at the cost of a somewhat unrepresentative result. This task was not performed.

8.6 Design for Manufacturing

There are two internal shapes that can be produced. The first is the optimal design with diverging section. The second is the straight cross section. The nozzle assembly that will be machined is essentially the entire converging-diverging section. For many reasons, it makes sense to divide this long assembly into two more manageable parts: the first is the orifice, which contains the converging part and a section of the diverging cross section. The second section is the nozzle, which houses the powder injection point and either a straight cross section or a diverging cross section.

As mentioned, there are many reasons why the assembly should be split into these two parts. The first is that it allows using a material that is easier to machine in the orifice that perhaps would not be able to resist multiple baths of cleaning solution. It also prevents us from having to manufacture the orifice out of a very hard material to prevent clogging within the nozzle.

The second advantage is machinability. Although theoretically feasible to manufacture this entire section out of one piece, there are many extraneous steps involved in making a casting mould and ensuring proper surface finish. However, by separating the two, the orifice can be machined on a lathe with any soft material because there is no powder flow in this area. This means that the angle of convergence within the orifice can be quite large because there is no need to accelerate powder particles at this point. For this reason, a drill bit can easily machine the internal cone required. As for the nozzle, the cross section can be formed from a rod. The internal cross section is either straight – which means that drilling and reaming are very easy – or a diverging cross section, allowing for a more complex drilling and tapered reaming. In either case, it is much easier than trying to machine the entire shape out of a block.

Another advantage to separating the two pieces is that even with all the efforts to prevent nozzle clogging, eventually clogging within the nozzle will occur. When this occurs, a cleaning process must be undertaken to remove the build-up of particle within the nozzle walls. With time, this process can damage the surface of the nozzle, and eventually the nozzle will have to be discarded. By isolating the cleaning to the nozzle only, the orifice is protected from cleaning damage.

8.6.1 Design Requirements

Here is a list of the design requirements for this project:

1. The nozzle and orifice internal cross section must meet as precisely as possible, paying special attention to the change in cross section in the interface and the offset, both of which must be as small as possible.
2. During operation, the interface must not shift or separate
3. The internal section after the powder injection should be made of the hardest material while conserving a surface finish that’s as smooth as possible. A balance must be found between hardness and ease of machining.

4. Nozzle external diameter should be as small as possible to allow for a more expensive material to be purchased.
5. The method used to connect the two pieces together should be as quick as possible using the least amount of tools possible.

8.6.2 Suggest Potential Solutions

There are many problems in designing “quick connect” fittings for a nozzle assembly such as this. Mainly, the thermal expansion of the materials between room and 500^{o}C (system maximum temperature) is an issue. Several quick-connect-type solutions were considered and are enumerated below:

- **Latches** would be easy to connect the nozzle to the orifice. It is even possible to find latches small enough. A great feature is that the nozzle can be adjusted correctly just before being tightened. However, latches loosen under thermal expansion.
- **Snap fits**’ speed would be great, however precision of snap fits would be critical, and because of thermal expansion once again location accuracy is compromised. (There would always be gap between the nozzle and the orifice)
- **Screw fit**s seem like a good compromise between speed and accuracy. The nozzle is set in place with locating pin that enter the orifice and properly situate it. Then a secondary piece would screw into the orifice, pinning the nozzle in place. There are two questions that need answering with this design. First, how is the nozzle aligned? This can be done with alignment pins. Secondly, can it be insured that the nozzle will not loosen when the temperature is increases? This issue can be avoided with the use of a jam nut (a secondary nut to jam the other one in place) This would prevent much of the thermal expansion and prevent bolts from loosening under thermal expansion.

8.6.3 Nozzle Shape Design

The recommendations from the last section are:

1. Divide the nozzle and orifice into two parts: the orifice and the nozzle

2. Assemble the two components together using tightening screws. Pins will guide the nozzle into the orifice.

Based on these two recommendations, and the internal shape of the nozzle as determined previously, a design was made for this nozzle assembly. A general view is shown in Figure 169.

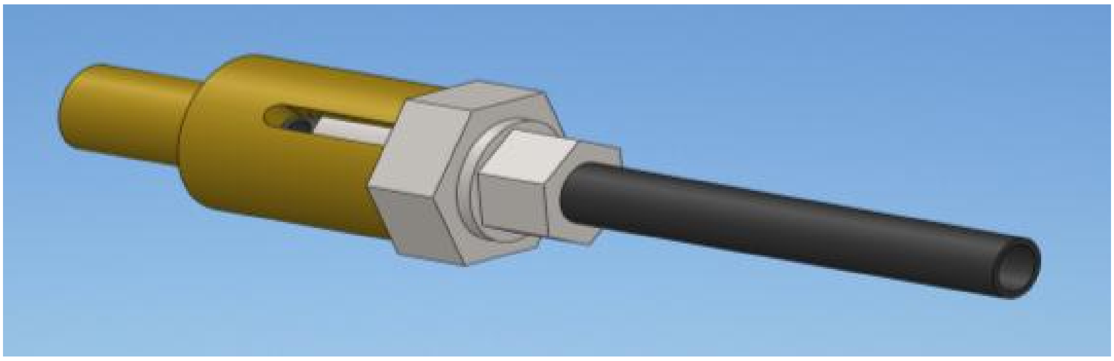

Figure 169. Constant and Ideal Cross Section Nozzle, General View

The nozzle has 4 distinct parts. The first is the brass orifice, which houses a converging-diverging section. Brass was chosen due to its easy availability and easy machinability. Since this piece will not be in contact with powder, then the wear resistance of the material does not matter. The second part is the nozzle, which perfectly continues the diverging cross section in the brass piece. To ensure a perfect alignment, two alignment pins are used. Finally, to keep the nozzle in place, first a large steel piece is screwed in the brass orifice, pressing the nozzle against the bottom of the orifice. A lock nut is then thread on top of this piece to keep the assembly steady during thermal cycling. The cross section of the "constant cross section" nozzle is shown in Figure 170 below.

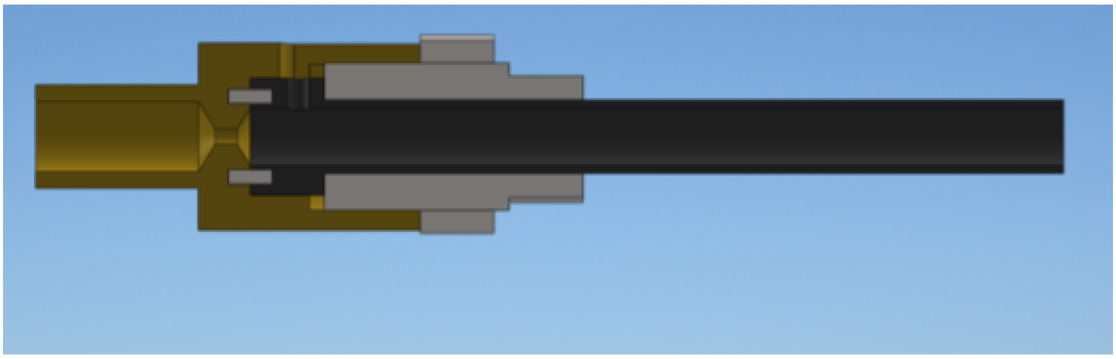

Figure 170. Constant Cross Section Nozzle, Section View. Notice the Constant Internal Cross Section within the Nozzle

The design for the "ideal cross section" nozzle is identical, except that the dimensions for the internal cross section of the converging-diverging orifice and the nozzle have been modified to accommodate the ideal expansion cross section. A cross section of this nozzle is shown in Figure 171.

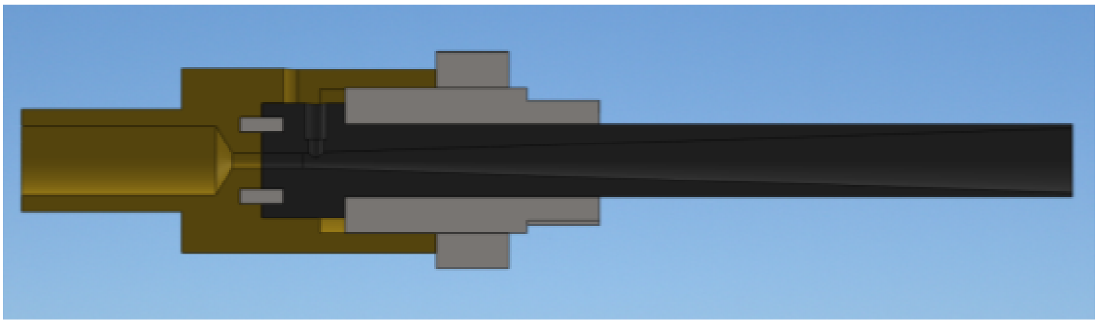

Figure 171. Ideal Cross Section Nozzle, Section View. Notice the Diverging Cross Section within the Nozzle

8.6.4 Manufacturing Techniques

There are many manufacturing techniques that can be utilized to make this nozzle. Specifically, some very precise details must be chosen to narrow the choice of manufacturing and finishing techniques.

Furthermore, multiple design techniques must be used to account for the lifetime utilization of the product. Should this product eventually clog, this product must be cleaned easily. For this reason, this product must be designed for easy manufacturing, assembly, disassembly and service. The part geometry might have to be adjusted to facilitate these areas.

A proper material must be selected to offer the proper surface finish and hardness. It also needs to have a melting point that is high enough so that it does not become soft below 550°C. This part should also be corrosion resistant as, should clogging occur, various cleaning solutions including NaOH (sodium hydroxide) for aluminum and aluminum alloys and a Nitric Acid (HNO_3) solution for copper deposits will be used. However, if the material can completely prevent clogging, then the corrosion resistance can be ignored. The material cannot be ferro-magnetic or magnetized, as some sprayed powders are. The appearance of the material is irrelevant, but the internal surface finish must be extremely good.

There are many manufacturing techniques available. These include casting, forming and shaping, machining, joining, finishing, micro fabrication, nanofabrication and polymer-processing processes [62]. Many of these processes can be discarded for lack of simplicity. (Mainly because these processes would be too expensive for the amount of parts produced.) These include any form of casting, forming & shaping and micro-and nano-fabrication. What is left is machining, joining, finishing and polymer-processing processes. These processes can be completed within the department's machine shop.

Machining techniques available are turning (on a lathe), boring, drilling, milling, planning, grinding and advanced machining techniques such as computer-numerically controlled machining (CNC) and wire electro-discharge machining (EDM) [62]. Wire EDM is only possible with conductive materials but is very effective at removing straight sections of materials up to 6" or 150mm.

Joining techniques include welding, brazing, soldering and mechanical bonding [62]. However these methods are imprecise and should not be used.

Finishing techniques include deburring, honing, lapping, reaming, coating and plating [62]. These surface finishes offer the possibility to reduce the surface roughness of the internal cross section and creating a hard surface finish once the main machining technique has been completed.

Finally, potential polymer-processing processes include extrusion and injection moulding for thermoplastics, and compression moulding, pultrusion and vacuum-bag forming for thermosets [62]. For this application, the most likely process to be used will be injection moulding for a thermoplastic or vacuum-bag forming for a thermoset. This is due to the processes' simplicity and applicability to the shape at hand.

Based on the processes available, the only available solution for a metallic nozzle is machining. A material must be found for both the orifice and the nozzle. The orifice can be machined out of any material because it will not see any powder flow. Historically, orifices were made of brass for its higher melting point, ease of machining and good sealing properties. For the nozzle, however, the hardest material possible must be used while still being able to machine the part. The surface finish must also be as good as possible.

Several materials were considered. First, several hard materials such as tungsten carbide (WC), titanium carbide (TiC), boron carbide (BC), cubic boron nitride (CBN) and diamond coating. These materials all have hardness values above 2000 Hv. Martensitic steel was considered since regular steel can be machined easily, and then quenched to produce hard martensitic steel. However, this material was deemed too soft to be a suitable nozzle material with hardness range between 400 and 700 Hv. Superalloys present interesting properties, but only at high temperatures [63]. Ceramics would also be interesting; however machining is next to impossible since ceramics are very hard and electrically insulating. Finally, a high temperature thermoset could be used, but a mould would have to be created.

Looking at the list of material, it is obvious that a harder material will be harder to machine. Instead of obtaining a very high hardness material and machining it, another approach could be to machine a softer material and coat the internal walls with a high-hardness material, thus reducing the cost of machining while maintaining a high hardness as observed by the traveling particles within the nozzle. Some potential coatings / treatments include:

- Case hardening (surface hardening) which includes boronizing and nitridizing.
- Electroplating

- Diamond-like coating (DLC) using freestanding diamond films (deposited using CVD, plasma-assisted vapour depositing and ion beam)
- Hardcoat anodizing of aluminum

DLC coatings would be very difficult to perform inside a nozzle cross section. The other three processes would be feasible, yielding a similar final roughness i.e. the roughness of the initial part. To determine a superior process these processes must be analyzed quantitavely. An enumeration of process final hardnesses is shown in Table 45.

Table 45. Process Hardnesses. Roughness for All Processes is Similar

Process	Material	Hardness
Case Hardening - Boronizing	Plain carbon steel	1600 - 2800
Electroplating – Hard chromium plating	Carbon steel	950-1000
Hardcoat anodizing	Aluminum	1500-1650

Boronizing produces the same surface roughness as the material and has higher hardness than any of the other processes by a large margin. It should therefore be used as the hardening process.

Before this process is performed, the surface roughness must be extremely low. There are many techniques available for machining and polishing. These include polishing of internal areas (such as ultrasonic machining, superfinishing, chemical-mechanical polishing, electropolishing, magnetic Field polishing and buffing), chemical milling, electrochemical machining (ECM), wire EDM (Electrical-discharge machining), electrical discharge grinding (EDG) and water-Jet machining and abrasive jet machining.

Most of these processes are not available in the machine shop. In most cases, it would be possible to have this process done by a sub-contractor at a significant cost. Therefore, the machine shop equipment will be used. In this case, simple reaming will provide an adequately smooth surface. Should this technique prove insufficient, other potential means will be inspected.

Like Centerline, it would be possible to create a plastic nozzle. The plastic used in Centerline's plastic nozzle is most likely PBI, or polybenzimidazole. It is a high temperature thermoplastic with service temperature of up to 350-400°C. The advantage of using this polymer is its extremely low coefficient of friction, which prevents any clogging from occurring. However, because PBI can only operate at a maximum of 350°C and is relatively soft, only soft powders that do not require high temperatures such as pure Al can be deposited with this nozzle. The manufacturing technique for this nozzle can be machining,

8.6.5 Summary of Manufacturing Details

There are 5 components to the nozzle assembly. The brass orifice, machined with a lathe and drill press, does not need any polishing or finishing step. (The orifice converging and diverging angles are 118°, the same angle as standard drill bits.) The nozzle, made of plain carbon steel and either straight- or tapered-reamered, is then polished or buffed (inside section) for minimal internal surface roughness. The nozzle then goes through a boronizing process (one type of case hardening) to create extremely hard internal walls.

There are also aligning pegs (OEM) press-fitted into the nozzle that serve to align the nozzle and the orifice. Two nuts, made out of any available material, are used to secure the nozzle to the orifice. The first nut secures the nozzle to the orifice, and the second nut locks the first nut in place.

8.7 Test to confirm improvement

Once the nozzles have been manufactured, they will be tested against the Centerline system's nozzles and the other two nozzles for performance comparison. Performance metrics will include clog time (if applicable), deposition efficiency, porosity, powder velocity. Wipe tests can also be performed to analyze the particle deformation.

9 Conclusions

This endeavour was part of a series of projects performed for The Boeing Company. In this particular case, there were several objectives. The first one was to attempt to see if a cold gas dynamic spray coating could be created on top of an Al 7075 FSW plate. If this was possible, the second objective was to optimize the deposition properties. Finally, once the coatings were optimized, the corrosion behaviour of the cold spray coatings was to be observed and compared to an uncoated Al 7075 panel.

Al 7075 FSW are notorious for corrosion problems at the weld joint, and the idea brought forward by The Boeing Company was that creating a metallic layer would protect the joint from premature corrosion. The original requirements were to create a 125 to 250 µm coating with pure Al, Al 7075 and Al 5083 powders on a FSW joint and test their relative performance. The best performing coating would then be selected.

In order to achieve this goal, optimal deposition properties were found for each of the three powders. Once these parameters were found, the nozzle travel speed was modified until the correct coating thickness was obtained. FSW plates were supplied by The Boeing Company and coated with each of the three metallic coatings. They were subjected to standard corrosion tests, ASTM B117, for 2000 hours. Results indicated that pure Al was the best coating, followed closely by Al 5083 and Al 7075 last. Two other corrosion tests, ASTM G34 and ASTM G110, were performed to confirm these results. Both confirmed that pure Al was the best coating to use for corrosion protection.

Adhesion tests were performed to ensure that the coating adhesion surpassed the minimum standard of 2500 psi (17.2 MPa). This was true in every case, with Al 7075 values at 68 ± 19 MPa, Al 5083 values at 58 ± 17 MPa and Pure Al values at 28 ± 4 MPa. The difference in adhesion strength is due to a combination of impacting particle velocity and particle hardness.

Because the coatings were intended to be deposited immediately after the FSW equipment (which can create temperature of around 475^{o}C within the plates), substrate temperature tests were performed, varying the substrate temperature of the coupon on which the coating was deposited and measuring the effect on the coating. The results showed no change in coating porosity, yet an increase in coating thickness (therefore an increase in deposition efficiency). Pure Al showed the highest, with 77% increase between a room temperature substrate and a 400°C substrate. Al 5083 showed a more conservative increase with 30%. The thickness in Al 7075 samples showed no sign of substrate temperature dependence. This is due to the variability in the change of each powder's softness with a change in temperature, leading to a more or less prominent dependence on substrate temperature.

To better understand this phenomenon, wipe tests were performed at multiple substrate temperatures. The results indicated that the initial powder layer is not affected by this temperature, but the increase is thickness is most likely due to heat transfer through the subsequent particle layers. Coating hardness was measured for the Room and 400°C tests, noting a reduction in substrate hardness for Pure Al and Al 5083, and none for Al 7075.

Velocity measurements performed indicate a good correlation between particle diameter and speed. (since densities are relatively similar) They show as well that the particle shape (whether spherical or odd) had a great impact on the drag coefficient and the final speed of the particles.

Tensile specimens were sprayed, machined and pulled, indicating a vast difference between width-wise and length-wise sprayed samples, leading to the theory of cold spray "fibres". SEM analysis revealed indications of discontinuities at pass interfaces, hinting at confirming this theory. SEM analysis also revealed that elongation to failure was proportional to the amount of metallurgical bonding in the specimen. Microscopic analysis of etched cross sections did not reveal significant information.

New 7075 powder was optimized and analyzed. The new Centerline SST-5007 powder can be used instead of the Valimet powder as long as low bond strengths are acceptable. (The bond strength average, 18 MPa, falls slightly above the Boeing minimum standard of 17.2 MPa. However there is a large 7 MPa standard deviation)

New nozzle designs were made. Gas dynamics theory (1-D isentropic flow) coupled with friction theory seems to indicate that the Centerline nozzles accelerate the particles to 98% of the maximum theoretical speed (considering max drag force) for a particular nozzle length. However, the model does not include overexpansion corrections, shockwaves within the nozzles or true roughness values integration. A few new nozzles were designed. These include “max drag force”, “constant cross section” and “custom” nozzles. Each design includes theoretical work and design for manufacturing up to parts drawings and assemblies. The maximum drag force nozzle has a cross section that should always propel the particle at the maximum drag force possible for the current particle speed. The “constant cross section” design starts off at high Mach number, and through friction this speed is slowed down to the design Mach number at the nozzle exit. The custom analysis was made to input certain nozzle geometries e.g. the Centerline model to compare it to the other designs. Schlieren images were taken of the exiting gas from the Centerline nozzle but did not reveal significant details due to the lack of focus in the system. It was determined that internal cross section Schlieren was not feasible with this setup.

10 Future Work

All Boeing requirements associated with this thesis have been entirely fulfilled. Eventually, the goal for ultimate corrosion protection would be to install cold spray nozzles immediately after the FSW equipment, which would allow minimal corrosion to occur before the protective layer is applied. (The current FSW process of these panels has a weld width of 1 inch and a travel speed of approximately 6 inches per minute.). Furthermore, the results from the last corrosion tests are yet to be received due to lack of time. Once this is done, final adjustments to the machining procedure before coating will be made if need be.

This thesis has opened many new research opportunities. They are listed below:

- The increase in coating thickness with substrate temperature is not fully understood. Although a theory was developed after several experiments were designed, executed and analyzed, this theory is yet to be confirmed by direct experimentation.
- In the same light, the tensile specimen theory is well under way, but lacks confirmatory experiments. Some conclusions could be made from the tensile specimens produced; however there were too many inconsistencies with the samples to be able to make authoritative statements. Once the new set of tensile samples are produced, a more comparative and definitive study will be performed.
- The nozzle design project has yet to manufacture a nozzle. The underlying theory and shape for the nozzle was established, and the nozzle design for manufacturing, assembly, disassembly and servicing was completed. All that remains it to build a nozzle and test the increase in performance.

11 References

[1] http://en.wikipedia.org/wiki/Boeing_787_Dreamliner, consulted on 11 Dec 2012

[2] http://www.boeing.com/commercial/787family/programfacts.html. consulted on 11 Dec 2012

[3] http://www.thefabricator.com/article/aluminumwelding/weldable-and-unweldable-aluminum-alloys Consulted on 11 dec 2012

[4] http://www.boeing.com/boeing/commercial/747family/pf/pf_facts.page, consulted on May 6th, 2013

[5] W. Polt, A little friction at Boeing, ,Boeing Frontier News, 3(5), 2004, Consulted March 2011, http://www.boeing.com/news/frontiers/archive/2004/september/i_tt.html

[6] T. DebRoy and H.K.D.H. Bhadeshia, Friction stir welding of dissimilar alloys - a perspective, *Science and Technology of Welding and Joining*, 15(4), 2010, 266-270

[7] A.P. Alkhimov, A.N. Papyrin, V.F. Dosarev, N.I. Nesterovich, and M.M. Shuspanov: U.S. Patent 5 302 414, 1994.

[8] A.Papyrin et.al., Cold Spray Technology, Elsevier, 2007

[9] E. Irissou et. al., Review on Cold Spray Process and Technology: Part I – Intellectual Property, *Journal of Thermal Spray Technology*, 17(4), 2008, 495-516

[10] B. Jodoin, Cold Spray Nozzle Mach Number Limitation, *Journal of Thermal Spray Technology*, 11(4), 2002, 496-507

[11] T. Hussain et.al., Bonding Mechanisms in Cold Spraying: the Contributions of Metallurgical and Mechanical Components, *Journal of Thermal Spray Technology*, 18(3), 2009, 364-379

[12] 14H. Assadi et. al., Bonding mechanisms of cold spray, *Acta Materialia*, 51 (2003), 4379-4394

[13] T Schmidt et.al., From Particle Acceleration to Impact and Bonding in Cold Spraying, *Journal of Thermal Spray Technology*, 18(5-6), 2009

[14] J.R. Davis, Ed., *Handbook of Thermal Spray Technology*, ASM International, 2004

[15] H. Herman, S. Sampath and R. McCune, Thermal Spray: Current status and Future Trends, *MRS Bulletin*, July 2000, 17-25

[16] R.S. Mishra, Z.Y. Ma, Friction stir welding and processing, *Mat. Sci. and Eng.,* R 50 (2005), 1-78

[17] http://www.twi.co.uk/technologies/welding-coating-and-material-processing/friction-stir-welding/

[18] http://en.wikipedia.org/wiki/Friction_stir_welding

[19] N.R. Mandal, *Aluminum Welding*, 2nd edition, ASM International, 2005, 168p. [ISBN 0-87180-826-4]

[20] C.B. Fuller et al., Evolution of microstructure and mechanical properties in naturally aged 7050 and 7075 Al friction stir welds, *Materials Science and Engineering A*, 527 (2010) , 2233-2240

[21] C.S. Paglia and R.G. Buchheit, A look in the corrosion of aluminum alloy friction stir welds, *Scripta Materialia,* 58 (2008), 383-387

[22] J.-F. LI et. Al., Mechanical properties, corrosion behaviours and microstructures of 7075 aluminum alloy with various aging treatments, *Trans. Nonferrous Met. Soc. China,* 18 (2008), 755-762.

[23] P. Cavaliere, A. Squillace, High temperature deformation of friction stir processed 7075 aluminum alloy, *Materials Characterization,* 55 (2005), 136-142

[24] H.B. Cary, S.C. Helzer, *Modern Welding Technology*, Prentice Hall, 2011, 715 pages

[25] K. Weman, *Welding Process Handbook*, St. Lucie Press, 2003, 208 pages

[26] ASM International, Handbook of Ternary Alloy Phase Diagrams, 1995

[27] ASTM B918/B918M-09, Standard Practice for Heat Treatment of Wrought Aluminum Alloys, *ASTM International*, 2009

[28] J.E. Hatch*, Aluminum Properties and Physical Metallurgy, ASM International, 1984, 397 pages*

[29] M.W. Mahoney et. Al., Properties of Friction-Stir Welded 7075 T651 Aluminum*, Metallurgical and Materials Transactions, 29A, 1998, 1955-1964*

[30] R.W.K. Honeycombe and R.W. Pethien*, Dynamic Recrystalization, Journal of Less-Common Metals, 28 (1972), 201-212*

[31] J.R. Davis*, Corrosion* – Understanding the Basics*, ASM International,* Materials Park*, OH, 2000*

[32] M. Pourbaix, Atlas of Electrochemical Equilibria in Aqueous Solution, *National Association of Corrosion Engineers,* Cebelcor, 1974

[33] O. Hatamleh, Corrosion susceptibility of peened friction stir welded 7075 aluminium alloy joints, *Corrosion Science*, 51(2009), 135-143

[34] M. Guerra et.al., Flow patterns during friction stir welding, *Materials Characterization*, 49 (2003), 95-101i

[35] K. Prasad Rao, G.D. Janaki Ram and B.E. Stucker, Improvement in corrosion resistance of *friction stir welded aluminum alloys with micro arc oxidation coatings, Scripta Materialia, 58 (2008), 998-1001*

[36] T.H. Van Steenkiste, J.R. Smith, R.E. Teets, Aluminum coatings via kinetic spray with relatively large powder particles, *Surface and Coatings Technology*, 154 (2002), 237-252

[37] Y. Tao et. al., Microstructure and corrosion performance of a cold sprayed aluminium coating on AZ91D magnesium alloy*, Corrosion Science*, 52 (2010), 3191-3197

[38] R. Ghelichi et. al., Microstructure and fatigue behaviour of cold spray coated Al5052*, Acta Materialia,* 60 (2012), 6555-6561

[39] Q. Wang, N. Birbilis, M.X. Zhang, Interfacial structure between particles in an aluminum deposit produced by cold spray, *Material Letters*, 65 (2011), 1576-1578

[40] A. Sova et. al., Preliminary study on deposition of aluminium and copper powders by cold spray micronozzle, *Surface and Coatings Technology*, 220 (2013), 98-101

[41] K. Spencer et. al., Residual stresses in cold spray Al coatings: The effect of alloying and of process parameters, *Surface and coatings technology*, 206 (2012), 4249-4255

[42] J.R. Davis, Corrosion of Aluminum and Aluminum Alloys, *ASM International*, 1999, 262 pages

[43] ASTM G85-11*,* Standard Practice for Modified Salt Spray (Fog) Testing, *ASTM International, 2011*

[44] ASTM B117-11*,* Standard Practice for Operating Salt Spray (Fog) Apparatus*, ASTM International, 2011*

[45] K. Surekha, B.S. Murthy and K. Prasad Rao, Microstructural characterization and corrosion behaviour of mulitpass friction stir processed AA2219 aluminium alloy, *Surface & Coatings Technology 202 (2008), 4057-4068*

[46] ASTM G110-92*,* Standard Practice for Evaluating Intergranular Corrosion Resistance of Heat Treatable Aluminum Alloys by Immersion in Sodium Chloride + Hydrogen Peroxide Solution, *ASTM International, 2009*

[47] C.S. Paglia and R.G. Buchheit*,* A look in the corrosion of aluminum alloy friction stir welds, *Scripta Materialia 58 (2008), 383-387*

[48] J. Kang et al*.,* In-situ investigation on the pitting corrosion behaviour of friction stir welded joint of AA2024-T3 aluminum alloy, *Corrosion Science, 52 (2010), 620-626*

[49] asm.matweb.com, consulted May 27th 2013

[50] MIL-C-5541 E, Chemical Conversion Coatings on Aluminum and Aluminum Alloys, Supersedes MIL-C-5541 D, *United States Department of Defence*, 30 November 1990

[51] ASTM G34-01*,* Standard Test Method for Exfoliation corrosion Susceptibility in 2xxx and 7xxx Series Aluminum Alloys (EXCO Test), *ASTM International, 2007*

[52] ASTM C-633-01, Standard test Method for Adhesion or Cohesion Strength of Thermal Spray Coatings, *ASTM International*, 2001

[53] S. Rech et. al., Mechanical property of multi-pass cold sprayed aluminium alloy coatings for repair application, *International Thermal Spray Conference Proceeding,* DVS 276 (2011), 252-257

[54] http://www.aalco.co.uk/datasheets/Aluminium-Alloy_5083-0~H111_149.ashx, consulted on May 27th, 2013

[55] ASTM E8/E8M-09, Standard Test Method for Tension Testing of Metallic Materials, *ASTM International*, 2009

[56] J.M. Roy, Development of Cold Gas Dynamic Spray Nozzle and Comparison of Oxidation Performance of Bond Coats for Aerospace Thermal Barrier Coatings at Temperatures of 1000°C and 1100°C*,* Master's Thesis, University of Ottawa, 2011

[57] G. S. Settles, Schlieren and Shadowgraph Techniques, 2nd Edition, *Springer*, 2006

[58] S. Tavoularis, Measurement in Fluid Mechanics, *Cambridge University Press*, 2005.

[59] A.F. Bicen, Refraction correction for LDA measurements in flows with curved optical boundaries, *TSI Quarterly*, 8(2):10-12, 1982

[60] A.J. Parry, M.J. Lalor, Y.D. Tridimas, and N.H. Woolley, Refraction corrections for laser-Doppler anemometry in a pipe bend, *Dantec Information*, No. 09 (September 1990): 4-6, 1990

[61] R. Budwig, Refractive index matching methods for liquid flow investigations, *Exp. Fluids*, 17:350-355, 1994.

[62] S. Kalpakjian and S.R. Schmid, Manufacturing Engineering Technology, 6th Edition, *Pearson Education*, Inc, 2010

[63] M. Nganbe, Chapter 6: Manufacture of superalloys and ceramic-metal matrix composites, MCG 5138 course, University of Ottawa

[64] R.C. Dykhuizen et. al., Impact of High Velocity Cold Spray Particles, *ASM International JTTEE*, 8(1999),559-564

Appendix A

Table 46. Vickers Hardness Test Grid Performed on a FSW Sample

X0	X1	X2	X3	X4	X5	X6	X7	X8	X9	X10	X11	X12	X13	X14	X15	X16
177	177	172	165	171	166	160	144	136	133	140	155	130	148	130	131	143
179	179	174	171	169	164	162	150	149	142	133	136	138	133	133	130	133
169	169	175	168	169	170	162	162	157	148	143	129	128	130	128	132	139
160	178	164	164	172	163	164	160	163	164	141	130	126	130	133	133	130
169	169	172	170	168	164	159	164	151	163	152	135	129	130	132	135	131
152	163	168	175	167	164	167	165	160	154	147	133	131	124	122	128	125
170	172	154	156	158	158	158	157	160	135	150	141	132	128	121	129	127
179	176	167	172	165	168	173	162	161	161	153	153	142	124	125	125	123
165	165	167	178	176	169	162	161	163	158	163	161	163	159	155	159	145
174	173	170	169	171	167	170	155	163	163	167	167	163	161	161	164	161
169	176	175	170	177	179	169	169	169	164	171	167	167	174	173	171	167
172	127	178	137	154	177	173	177	169	171	171	170	167	172	171	159	165
119	174	179	174	174	175	178	169	172	169	167	170	172	172	167	171	169

X17	X18	X19	X20	X21	X22	X23	X24	X25	X26	X27	X28	X29	X30	X31	X32
136	139	138	136	134	139	156	161	166	166	180	167	181	174	169	
132	136	130	132	136	150	156	157	159	166	170	174	173	168	175	171
131	135	136	134	145	158	153	161	158	166	169	165	178	178	176	171
139	129	126	140	154	158	160	154	166	161	168	165	170	173	175	170
137	137	136	151	150	151	162	156	163	164	159	172	166	166	167	141
131	136	130	152	145	163	159	163	168	162	167	171	168	174	177	164
125	127	138	139	151	150	153	156	166	152	154	170	161	168	156	154
127	142	158	160	164	165	153	158	170	169	175	177	164	173	179	171
152	156	163	161	168	164	170	173	161	165	170	163	171	176	166	149
156	159	170	159	161	168	172	168	168	170	166	158	174	149	173	170
168	163	166	172	166	172	174	170	171	174	177	182	168	168	170	170
170	173	169	168	178	179	169	168	172	173	181	175	168	179	171	176
175	169	169	173	171	172	185	178	179	177	180	175	179	182	182	153

Appendix B

Table 47. Dogbone Tension Test Results. Dogbone 4 Failed, 5 was Sprayed with SST-A0050 Powder and 16 was not Completed due to Powder Feeding Issues

Set #	DB #	UTS (MPa)	Elongation to Failure (%)
1	1	66	0.8
	2	66	0.7
	3	67	0.5
	10	94	1.2
2	6	65	1.1
	7	89	2.0
	8	99	2.0
	22	51	0.6
3	9	67	0.6
	11	85	1.6
	12	86	1.2
	20	67	0.8
4	13	94	0.8
	14	101	0.8
	15	74	0.7
	21	72	0.5
5	17	87	2.8
	18	83	2.7
	19	82	2.9